



Ductility prediction of metal sheets using the CPFEM method

Jianchang Zhu

► To cite this version:

Jianchang Zhu. Ductility prediction of metal sheets using the CPFEM method. Material chemistry. HESAM Université, 2020. English. NNT : 2020HESAE011 . tel-03025996

HAL Id: tel-03025996

<https://pastel.hal.science/tel-03025996>

Submitted on 26 Nov 2020

HAL is a multi-disciplinary open access archive for the deposit and dissemination of scientific research documents, whether they are published or not. The documents may come from teaching and research institutions in France or abroad, or from public or private research centers.

L'archive ouverte pluridisciplinaire **HAL**, est destinée au dépôt et à la diffusion de documents scientifiques de niveau recherche, publiés ou non, émanant des établissements d'enseignement et de recherche français ou étrangers, des laboratoires publics ou privés.

ÉCOLE DOCTORALE SCIENCES DES MÉTIERS DE L'INGÉNIEUR
[Laboratoire d'Étude des Microstructures et de Mécanique des Matériaux –
Campus de Metz]

THÈSE

présentée par : **Jianchang ZHU**

soutenue le : **15 Mai 2020**

pour obtenir le grade de : **Docteur d'HESAM Université**
préparée à : **École Nationale Supérieure d'Arts et Métiers**
Spécialité : **Mécanique - matériaux**

Ductility prediction of heterogeneous materials with periodic microstructure using multi-scale computational homogenization

THÈSE dirigée par :

M. Farid ABED-MERAIM

et co-encadrée par :

M. Mohamed BEN BETTAIEB

Jury

Mme. Anne-Marie HABRAKEN, Directrice de Recherche FNRS, MS²F, Université de Liège

Présidente

M. Laurent DELANNAY, Professeur, IMMC, Université Catholique de Louvain

Rapporteur

M. Jean-Claude MICHEL, Directeur de Recherche CNRS, LMA, Marseille

Rapporteur

M. Renald BRENNER, Directeur de Recherche CNRS, Institut d'Alembert, Sorbonne Université

Examinateur

M. Kostas DANAS, Chargé de Recherche CNRS, LMS, Ecole Polytechnique, Palaiseau

Examinateur

M. Farid ABED-MERAIM, Professeur, LEM3, ENSAM, Metz

Examinateur

M. Mohamed BEN BETTAIEB, Maître de Conférences, LEM3, ENSAM, Metz

Examinateur

To my beloved parents for their sacrifices

To my beloved brothers and sisters for their support

To my dear supervisors for their guidance

To all my dear friends for their help

Acknowledgment

First and foremost, I would like to express my sincere gratitude to my thesis director, Mr. Farid ABED-MERAIM, who kindly gave me this opportunity to study in France. I am deeply grateful for his encouragement, valuable advice and continuous guidance throughout my studies but more importantly for trusting me on this subject. I would like to thank my co-supervisor, Mr. Mohamed BEN BETTAIEB, for his responsible supervision, meticulous guidance and kind assistance. It was a really great pleasure for me to work with them for three years. Their expertise and personality will always be a form of inspiration for me in the future.

I also deeply thank Mrs. Anne-Marie HABRAKEN from Université de Liège for being the president of my Ph.D. thesis committee. I would like to express my gratitude to two reporters, Mr. Laurent DELANNAY from Université Catholique de Louvain and Mr. Jean-Claude MICHEL from LMA (Laboratoire de Mécanique et d'Acoustique), for their insightful comments and academic reports. I am grateful to Mr. Renald BRENNER from Sorbonne Université and Mr. Kostas DANAS from Ecole Polytechnique for accepting the invitation and spending their precious time to attend my thesis defense. I am honored to be able to invite these famous, charming and knowledgeable scholars as the referees. Their insightful, valuable and constructive comments are sincerely appreciated.

I would like to thank the organization-China Scholarship Council (CSC, Contract No. 201606020111), who supplied the scholarship to support my study in ENSAM.

I would also like to thank Mr. Mohamed JEBAHI for his helpful discussions on the developments in chapter 1 of this manuscript, and Mr. Hocine CHALAL for his help in understanding the user subroutines UMAT and UEL. I am grateful to Mr. Joseph PAUX for his abundant advices on the crystal plasticity modeling.

I would like to thank all my colleagues in our lab, Adil BENAARBIA, Boris POITROWSKI, El-Hadi TIKARROUCHINE, Fodil MERAGHNI, Holanyo AKPAMA, Nada MIQOI, Pascal POMAREDE, Paul DIDIER, Rabii CHEKKOUR, Soraya BARRAL, Theophile GROSS, Yessine JEDIDI, etc. and also my Chinese friends, Fengming QIANG, Yanfeng YANG, Bin JIA, Lei CAI, Yajun ZHAO, Qian WANG, Tian ZHANG, Xuan WU, Fan LI, Haitao TIAN, Xianqiong ZHAO, Qing XIA, Zhicheng HUANG, Peng WANG, Wenqing CHEN, Chi ZHANG. with whom I shared the most memorable moments.

Finally and more importantly, I express my deepest gratitude to my parents Junping ZHU and Huie WANG and to my younger brother Xiaochang ZHU for all their love and support, without whom I would not be able to complete my studies.

DUCTILITY PREDICTION OF METAL SHEETS USING CPFEM (CRYSTAL PLASTICITY FINITE ELEMENT METHOD)

RÉSUMÉ : Cette thèse a pour objectif de développer un outil numérique multi-échelles capable de prédire la ductilité des matériaux hétérogènes présentant une microstructure périodique. Tenant compte de la périodicité spatiale des milieux étudiées, la technique d'homogénéisation périodique est retenue pour assurer la transition entre les échelles microscopique et macroscopique. Cette technique, formulée sous l'hypothèse des grandes déformations, est couplée à l'approche de bifurcation de Rice pour prédire les limites de ductilité des matériaux étudiés. Pour assurer ce couplage, trois techniques numériques ont été implantées et comparées pour calculer le module tangent macroscopique. Ce couplage a été utilisé, entre autres, pour prédire la limite de ductilité des milieux poreux et polycristallins. L'étude menée sur les matériaux poreux a permis de bien analyser la compétition entre la coalescence des cavités et l'apparition du phénomène de localisation de la déformation plastique. D'un autre côté, l'étude portant sur les matériaux polycristallins a mis en évidence l'effet de plusieurs paramètres sur la perte de ductilité de ce type de matériaux.

Mots clés : milieux hétérogènes, homogénéisation périodique, ductilité, théorie de bifurcation, module tangent macroscopique.

ABSTRACT: The main objective of this PhD thesis is to develop a multi-scale numerical tool capable of predicting the ductility of heterogeneous materials displaying periodic microstructure. Considering the spatial periodicity of the studied media, the periodic homogenization technique is selected to ensure the transition between the microscopic and macroscopic scales. This technique, formulated under the large deformation assumption, is coupled with the Rice bifurcation approach to predict the ductility limits of the studied media. To ensure this coupling, three numerical techniques have been implemented and compared to compute the macroscopic tangent modulus. This coupling has been used, among other applications, to predict the ductility limit of porous and polycrystalline media. The study conducted on porous media has allowed the careful analysis of the competition between void coalescence and the onset of plastic strain localization phenomenon. On the other hand, the study carried out on polycrystalline materials has highlighted the effect of several parameters on the loss of ductility of this type of materials.

Keywords: heterogeneous media, periodic homogenization, ductility, bifurcation theory, macroscopic tangent modulus.

Table of Contents

Part I: English version

General introduction.....	13
Context of the thesis	13
Motivation and general framework of the study	13
Objectives of the thesis	15
Organization of the thesis	15
Conventions, notations and abbreviations	17
Chapter 1 Comparative study of three techniques for the computation of the macroscopic tangent moduli by periodic homogenization scheme.....	19
1.1. Introduction.....	19
1.2. Details on the finite element formulation in ABAQUS/Standard	23
1.3. Periodic homogenization problem	26
1.4. Computation of the macroscopic tangent modulus.....	29
1.4.1. Perturbation technique.....	30
1.4.2. Condensation technique.....	32
1.4.3. Fluctuation technique	37
1.5. Extension to symmetric microstructures.....	39
1.5.1. Perturbation technique.....	40
1.5.2. Condensation technique.....	42
1.6. Numerical results	44
1.6.1. Basic validations of the three techniques.....	44
1.6.2. More advanced validations of the three techniques.....	47
1.6.3. Numerical assessment of extended formulation of condensation technique in symmetric microstructures	51
1.7. Summary and conclusions	54
Chapter 2 Numerical investigation of necking in perforated sheets using the periodic homogenization approach	57
2.1. Introduction.....	57
2.2. Modeling of the mechanical behavior of perforated sheets	61

2.2.1. Multiscale transition problem.....	61
2.2.2. Constitutive relations at the microscale level	61
2.2.3. Numerical implementation of the multiscale transition scheme.....	64
2.2.4. Computation of the macroscopic tangent modulus.....	67
2.3. Necking criteria.....	68
2.3.1. Maximum Force Criterion	68
2.3.2. General Bifurcation Criterion.....	69
2.3.3. Rice Bifurcation criterion	69
2.4. Results and discussions.....	70
2.4.1. Results for homogeneous unit cell.....	70
2.4.2. Comparison with Tvergaard's results	73
2.4.3. Sensitivity study	76
2.5. Conclusions.....	88

Chapter 3 Investigation of the competition between void coalescence and macroscopic strain localization using the periodic homogenization multiscale scheme..... 91

3.1. Introduction.....	91
3.2. Micromechanical modeling of the unit cell	96
3.2.1. Multiscale transition problem.....	96
3.2.2. Constitutive model for the metal matrix	97
3.3. Periodic boundary conditions and macroscopic loading.....	99
3.3.1. Periodic boundary conditions	100
3.3.2. Proportional stressing	100
3.3.3. Proportional in-plane strain paths.....	105
3.4. Void coalescence and strain localization criteria	106
3.4.1. Maximum reaction force criterion	106
3.4.2. Maximum equivalent stress criterion.....	106
3.4.3. Energy-based criterion.....	107
3.4.4. Rice bifurcation criterion.....	107
3.5. Numerical predictions.....	109
3.5.1. Material parameters	109
3.5.2. Validity of the periodic boundary conditions	109
3.5.3. Proportional stressing	112

3.5.4. Proportional in-plane strain paths.....	119
3.6. Concluding remarks.....	126
Chapter 4 Prediction of the ductility limit of sheet metals based on CPFEM multiscale framework.....	129
4.1. Introduction.....	129
4.2. Plane-stress periodic homogenization problem	132
4.3. Single crystal modeling.....	134
4.3.1. Constitutive equations	134
4.3.2. Incremental integration.....	137
4.4. Bifurcation analysis	142
4.4.1. Bifurcation theory.....	142
4.4.2. Computation of the macroscopic tangent modulus.....	142
4.5. Numerical results	143
4.5.1. Mechanical response.....	146
4.5.2. Ductility limit predictions.....	150
4.6. Summary and conclusions	152
Conclusions and perspectives	153
Summary and conclusions	153
Perspectives	154
Part II: Résumé étendu en Français	
Introduction générale	159
Contexte de la thèse	159
Cadre général de l'étude	159
Objectifs de la thèse.....	160
Plan du résumé.....	161
Chapitre 1 Étude comparative de trois techniques pour le calcul du module tangent macroscopique par l'approche d'homogénéisation périodique.....	163
1.1. Introduction.....	163
1.2. Problème d'homogénéisation périodique.....	164
1.3. Calcul du module tangent macroscopique	167
1.3.1. Technique de perturbation	167

Table of contents

1.3.2. Technique de condensation	169
1.3.3. Technique de fluctuation	173
1.4. Validation de l'implantation des trois techniques.....	175
1.4.1. Validation basique.....	175
1.4.2. Validation avancée	177
1.5. Conclusions.....	179
Chapitre 2 Prédition des limites de ductilité de matériaux hétérogènes par la technique d'homogénéisation périodique.....	181
2.1. Introduction.....	181
2.2. Prédition de la limite de ductilité des matériaux poreux	181
2.2.1. Modélisation micromécanique du comportement de la cellule de base.....	182
2.2.2. Conditions aux limites et chargement macroscopique.....	186
2.2.3. Critères de coalescence et de localisation de la déformation plastique	190
2.2.4. Prédictions numériques.....	192
2.2.5. Bilan de l'étude.....	199
2.3. Prédition de la limite de ductilité des matériaux polycristallins.....	200
2.3.1. Adaptation de la technique d'homogénéisation périodique à un chargement en état plan de contraintes	200
2.3.2. Modélisation du comportement d'un monocristal élastoplastique	204
2.3.3. Résultats numériques.....	212
2.3.4. Bilan de l'étude.....	219
Appendix:	
Appendix A. Typical input file to output elementary stiffness matrices.....	221
Appendix B. Some sections of Python scripts.....	223
B.1. The perturbation technique.....	223
B.2. The condensation technique	224
B.3. The fluctuation technique.....	225
Appendix C. The numbering of the slip systems for FCC single crystals	227
Reference:	
References	229

List of figures

Fig. 1.1. Illustration of the PBCs between nodes M^- and M^+	29
Fig. 1.2. Basic algorithmic steps for the perturbation technique.....	31
Fig. 1.3. Node pairs in Z-direction.....	35
Fig. 1.4. RUC occupying the initial domain $\mathcal{V}_{r_0} = [0, \lambda_0 / 2] \times [0, \lambda_0 / 2] \times [0, \lambda_0 / 2]$ and its corresponding FUC assumed to be symmetric about three planes of symmetry ($x_{01} = 0$, $x_{02} = 0$ and $x_{03} = 0$).	40
Fig. 1.5. The finite element discretization of microstructure with centered layer: (a) Mesh 1; (b) Mesh 2.....	46
Fig. 1.6. The finite element discretization of microstructure with centered cylindrical fiber.	46
Fig. 1.7. Two typical composites discretized by finite elements: (a) Microstructure with cubic inclusion; (b) Microstructure with elliptical cylindrical fiber.....	48
Fig. 1.8. Evolution of the components of modulus $\mathbf{C}^{(PK1)}$ obtained by CT, FT, and PT for microstructure with a cubic inclusion: (a) $C_{1111}^{(PK1)}$; (b) $C_{2222}^{(PK1)}$; (c) $C_{1122}^{(PK1)}$; (d) $C_{1212}^{(PK1)}$	49
Fig. 1.9. Evolution of the components of modulus $\mathbf{C}^{(PK1)}$ obtained by CT, FT, and PT for microstructure with an elliptical cylindrical inclusion: (a) $C_{1111}^{(PK1)}$; (b) $C_{2222}^{(PK1)}$; (c) $C_{1122}^{(PK1)}$; (d) $C_{1212}^{(PK1)}$	51
Fig. 1.10. RUC with elliptical cylindrical fiber.....	52
Fig. 1.11. Mechanical responses for both unit cells: (a) Contour plot of the von Mises equivalent stress for the FUC; (b) Contour plot of the von Mises equivalent stress for the RUC; (c) Contour plot of the maximum principal logarithmic strain for the FUC; (d) Contour plot of the maximum principal logarithmic strain for the RUC.	53
Fig. 1.12. Evolution of the components of modulus $\mathbf{C}^{(PK1)}$ as predicted by the original CT with FUC and the extended CT with RUC: (a) $C_{1111}^{(PK1)}$; (b) $C_{2222}^{(PK1)}$; (c) $C_{1122}^{(PK1)}$; (d) $C_{1212}^{(PK1)}$	54
Fig. 2.1. Concept of the periodic homogenization approach.....	61
Fig. 2.2. Finite element discretization and boundary conditions applied to the unit cell.	65
Fig. 2.3. Illustration of the Rice bifurcation criterion.	70
Fig. 2.4. Prediction of necking, for three particular strain-path ratios, using the different necking criteria: (a) MFC; (b) GBC; (c) RBC.	72
Fig. 2.5. FLDs for a homogeneous sheet (without holes), as predicted by MFC, GBC, and RBC.	73
Fig. 2.6. Initial unit cell used for the comparisons with Tvergaard's results.	74
Fig. 2.7. Comparisons between the current numerical predictions and Tvergaard's results (in green color): (a) uniaxial tension state; (b) plane-strain tension state; (c) loading with proportional in-plane stressing $P_{22} / P_{11} = 2$	76
Fig. 2.8. Unit cells with different circular hole initial radii: (a) $R_0 / A_0 = 0.1$; (b) $R_0 / A_0 = 0.2$; (c) $R_0 / A_0 = 0.5$	77
Fig. 2.9. Effect of the hole radius on the FLDs predicted by: (a) MFC; (b) GBC; (c) RBC.	78
Fig. 2.10. Schematic evolution of the unit cell: (a) initial configuration; (b) current configuration for $\rho = -0.5$; (c) current configuration for $\rho = 1$	78

Fig. 2.11. Unit cells with different elliptical hole initial aspect ratios: (a) $b_0/a_0 = 1$; (b) $b_0/a_0 = 2$; (c) $b_0/a_0 = 3$.	79
Fig. 2.12. Effect of the hole aspect ratio on the FLDs predicted by: (a) MFC; (b) GBC; (c) RBC.....	80
Fig. 2.13. Unit cells with different elliptical hole initial orientations: (a) $\theta_0 = 0^\circ$; (b) $\theta_0 = 45^\circ$; (c) $\theta_0 = 90^\circ$	81
Fig. 2.14. Effect of the elliptical hole orientation on the FLDs predicted by: (a) MFC; (b) GBC; (c) RBC.....	82
Fig. 2.15. Unit cells with different initial hole shapes: (a) Circular; (b) Elliptical; (c) Square	82
Fig. 2.16. Effect of the hole shape on the FLDs predicted by: (a) MFC; (b) GBC; (c) RBC.....	83
Fig. 2.17. Effect of the plastic anisotropy of the metal matrix on the FLDs predicted by: (a) MFC; (b) GBC; (c) RBC.....	85
Fig. 2.18. Impact of the Lankford coefficients on the shape of the dense matrix yield surface.....	85
Fig. 2.19. Effect of the hardening exponent on: (a) the macroscopic stress-strain curves; (b) the FLDs predicted by the RBC.....	86
Fig. 2.20. Effect of initial yield strength on: (a) the macroscopic stress-strain curves; (b) the FLDs predicted by the RBC.....	87
Fig. 2.21. Effect of the macroscopic boundary conditions on: (a) the macroscopic stress-strain curves; (b) the FLDs predicted by the MFC and RBC.	88
Fig. 3.1. (a) Micromechanical model of a material layer composed of an arrangement of cubic voided unit cells; (b) a unit cell containing a centered, spherical void surrounded by a voided matrix.	96
Fig. 3.2. Illustration of the concept of periodic homogenization: (a) unit cell containing primary and secondary voids; (b) equivalent homogenized medium.	97
Fig. 3.3. Finite element mesh for one-half unit cell, for illustration.	97
Fig. 3.4. Unit cell subjected to triaxial macroscopic stress state without shear stresses.	101
Fig. 3.5. Schematic illustration of the multi-point constraints between the dummy node and the reference points (RP_1, RP_2, RP_3)	103
Fig. 3.6. (a) Thin metal sheet made of 2D array of voided unit cells; (b) unit cell subjected to in-plane strain path.	105
Fig. 3.7. The entire sheet with the prescribed boundary conditions.....	110
Fig. 3.8. Contour of microscopic fields obtained by classical finite element computations: (a) equivalent stress in the entire sheet; (b) equivalent stress in the central unit cell; (c) equivalent plastic strain in the entire sheet; (d) equivalent plastic strain in the central unit cell.	111
Fig. 3.9. Contour of microscopic fields obtained by multiscale computations: (a) equivalent stress obtained by PBCs; (b) equivalent plastic strain obtained by PBCs; (c) equivalent stress obtained by KBCs; (d) equivalent plastic strain obtained by KBCs.	111
Fig. 3.10. Effect of the boundary conditions on: (a) the evolution of the equivalent stress Σ_{eq} normalized by the initial yield stress σ_0 ; (b) the evolution of the critical equivalent strain E_{eq}^B	112
Fig. 3.11. Validation of the numerical implementation by comparing our predictions with results published in Liu et al. (2016): (a) evolution of ratio \dot{W}^e / \dot{W}^p ; (b) evolution of the macroscopic logarithmic strain components E_{11} , E_{22} and E_{33} ; (c) evolution of the macroscopic equivalent stress Σ_{eq} normalized by the initial stress σ_0	114

Fig. 3.12. Competition between void coalescence and macroscopic strain localization for proportional stressing configurations defined by $T=0.8; 1$ and 2 , with $L=1$: (a) evolution of the reaction force component α_3 of the dummy node normalized by the initial stress σ_0 ; (b) evolution of the equivalent stress Σ_{eq} normalized by the initial stress σ_0 ; (c) evolution of the cubic root of the determinant of the acoustic tensor $\vec{\mathcal{N}} \cdot \tilde{\mathbf{C}}^{(PK1)} \cdot \vec{\mathcal{N}}$; (d) evolution of ratio \dot{W}^e / \dot{W}^p	116
Fig. 3.13. Evolution of critical equivalent strains E_{eq}^S , E_{eq}^R , E_{eq}^B and E_{eq}^C over the range $0.7 \leq T \leq 3.0$ and for (a) $L=-1$; (b) $L=0$; (c) $L=1$	117
Fig. 3.14. Locus of limit strains E_{eq}^C and E_{eq}^B over the range $-1.0 \leq L \leq 1.0$ and for $T=0.8; 1.2; 1.6; 2.0; 2.4; 3.0$	119
Fig. 3.15. Study for strain-path ratios $\rho = -0.5; 0.0; 1.0$: (a) evolution of E_{33} versus E_{11} ; (b) distribution of the stress triaxiality ratio T and the Lode parameter L ; (c) evolution of volume fraction of the primary void f_p normalized by f_{p0}	121
Fig. 3.16. Dense sheet crossed by a narrow voided band.....	122
Fig. 3.17. Effect of the neighborhood of the unit cell on: (a) the evolution of the strain component in the thickness direction outside the band; (b) the growth of the primary void.....	123
Fig. 3.18. Geometric representation of three void shapes: (a) oblate void ($\mathcal{W}_0 = 1/3$); (b) spherical void; (c) prolate void ($\mathcal{W}_0 = 3$).....	124
Fig. 3.19. Effect of initial shape of the primary void on: (a) the predicted forming limit diagrams; (b) the shape of the macroscopic yield loci for the quadrant ($\Sigma_{11} \geq 0$ and $\Sigma_{22} \geq 0$).....	125
Fig. 3.20. Effect of the initial volume fraction of secondary voids on: (a) the predicted forming limit diagrams; (b) the evolution of the microscopic equivalent stress σ_{eq} normalized by the initial yield stress σ_0	126
Fig. 4.1. Polycrystalline aggregate: (a) selection of a unit cell from the bulk polycrystalline material; (b) finite element mesh of the unit cell generated by the Voronoi tessellation technique.....	133
Fig. 4.2. Schematic representation of the multiplicative decomposition of the deformation gradient: plastic slip and rigid rotation along with elastic distortion of the crystallographic lattice.	136
Fig. 4.3. Basic algorithmic steps of the perturbation technique under plane-stress condition.	143
Fig. 4.4. Microstructure of the different unit cell configurations: (a) UC50; (b) UC200; (c) UC500; (d) UC1000.	144
Fig. 4.5. Initial textures of the different unit cell configurations: (a) UC50; (b) UC200; (c) UC500; (d) UC1000.	145
Fig. 4.6. Evolutions of some components of the macroscopic first Piola-Kirchhoff stress tensor versus $F_{11}-1$: (a) Component P_{11} ; (b) Component P_{12}	147
Fig. 4.7. Contour plot of the von Mises microscopic stress: (a) $\rho = -0.5$; (b) $\rho = 0$; (c) $\rho = 0.5$	148
Fig. 4.8. Contour plot of the component 33 of the microscopic stress: (a) $\rho = -0.5$; (b) $\rho = 0$; (c) $\rho = 0.5$..	148
Fig. 4.9. Contour plot of the maximum microscopic logarithmic strain le_{max} : (a) $\rho = -0.5$; (b) $\rho = 0$; (c) $\rho = 0.5$	148

Fig. 4.10. Evolution of some components of the microscopic stress tensor versus $F_{11} - 1$: (a) first single crystal; (b) second single crystal.	149
Fig. 4.11. Evolution of the slips of the active slip systems: (a) first single crystal; (b) second single crystal.	150
Fig. 4.12. Evolution of some components of the in-plane tangent modulus versus $E_{11} = \ln(F_{11})$: (a) Component ${}^{IN}\tilde{C}_{1111}^{(PK1)}$; (b) Component ${}^{IN}\tilde{C}_{1212}^{(PK1)}$	151
Fig. 4.13. Prediction of the ductility limits: (a) evolution of the minimum of the determinant of the acoustic tensor $\vec{\mathcal{N}} \cdot {}^{IN}\tilde{\mathbf{C}}^{(PK1)} \cdot \vec{\mathcal{N}}$ as a function of $E_{11} = \ln(F_{11})$ for three different strain paths ($\rho = -0.5$, $\rho = 0$, and $\rho = 0.5$); (b) effect of the number of grains on the predicted FLDs.	152

List of tables

Table 1.1. Boundary conditions applied on the RUC	41
Table 1.2. Composition of sets Ψ , Ω required for the computation of the first and fourth columns of $\mathbf{C}^{(PK1)}$..	43
Table 1.3. Components of matrix \mathbf{Z} for the two meshes of the microstructure with centered layer.....	46
Table 1.4. Components of matrix \mathbf{Z} for the microstructure with centered cylindrical fiber.....	47
Table 1.5. Performance of the different techniques in terms of allocated space disk and CPU time for microstructure with cubic inclusion.	50
Table 1.6. Performance of the different techniques in terms of allocated space disk and CPU time for microstructure with elliptical cylindrical fiber.....	51
Table 1.7. Disk space and CPU time required for the use of CT with FUC and RUC.	54
Table 2.1. Elastic and hardening material parameters	70
Table 2.2. Lankford's coefficients.....	83
Table 3.1. Elastoplastic parameters of the dense matrix.....	109
Table 4.1. Elastic and hardening parameters.....	146

Part I: English version

General introduction

Context of the thesis

This work has been carried out within the research team ‘Méthodes Numériques, Instabilités et Vibrations’ of the laboratory ‘Laboratoire d’Étude des Microstructures et de Mécanique des Matériaux’ (LEM3) at ENSAM, Metz Campus. The main objective of this thesis is to develop a numerical tool based on the periodic homogenization approach to predict the ductility limits of heterogeneous materials (composites, polycrystalline aggregates, porous media...).

Motivation and general framework of the study

Sheet metals represent a significant part of the materials used for the manufacture of various components and finished products, particularly in industry and technology (automotive, rail, aeronautics, household appliances, electronics, etc.). The current climate and environmental standards require the producers and processors of metal sheets (steelmakers, automobile industry, etc.) to improve the production and the industrialization methods in order to meet new competitiveness challenges. Among these initiatives, one of the important innovations is to considerably lighten metal parts and products, while maintaining their strength. It is reported that reducing the mass of a vehicle by 25%, for example, reduces its fuel consumption by 15%. However, this lightening of the structures requires an advanced design of new metallic materials with optimal physical and mechanical properties (low mass density, high mechanical resistance, high ductility, high corrosion resistance, etc.). Nowadays, new generations of metallic materials, such as stainless steels, titanium alloys and new aluminum alloys emerge in succession. At the same time, the development of these new metallic materials often requires a deep understanding of the physical mechanisms involved in plastic deformation. Indeed, the application of sheet forming processes, such as stamping or deep drawing, can lead to the appearance of defects (related to plastic instabilities) on the formed parts. These instabilities can be classified into two main families: structural instabilities (buckling, wrinkling, springback, etc.) and material instabilities (diffuse and localized necking, damage, etc.). In this thesis, attention will be paid to the second type of instabilities, and more specifically to localized necking. This localized form of necking manifests itself as a very strong concentration of plastic deformation in a very narrow zone of the sheet, and is often preceded by diffuse necking, which flows and amplifies until precipitating in the localization of the deformation. The occurrence of localized necking represents the ductility limit of a metal sheet, since this phenomenon is often precursor to failure. The ductility (or formability) of a material is measured by its capability to undergo irreversible deformation without the occurrence of localized necking. To characterize the ductility of a material, the concept of forming limit diagram (FLD) is commonly used. To determine a FLD, the material is subjected to biaxial loadings according to different deformation paths, ranging from

uniaxial tension to equibiaxial stretching. For each applied loading path, the maximum principal deformations (in the plane of the sheet) measured at the occurrence of localized necking are determined. Thus, the obtained forming limit diagram separates the space of the principal deformations of the sheet in two zones: safe zone – the zone below the FLD, and failure zone – the zone above the FLD. Namely, the forming processes are therefore calibrated so that the associated principal deformations are located below the FLD, in order to obtain formed parts without defects. The first works devoted to the determination of FLDs are essentially experimental ([Keeler and Backofen, 1964](#); [Goodwin, 1968](#)). However, the experimental formability tests are sometimes limited by many practical difficulties, such as the high cost of implementing the experimental methods, and the absence of strict standardized measures which can thus lead to large variations in the results. To overcome these practical difficulties, numerous works have been devoted for several decades to the development of alternative methods based on theoretical approaches (analytical and / or numerical). These theoretical approaches are essentially based on the coupling of a localized necking criterion and a behavior model describing the mechanical response of the studied material. Among the strain localization criteria used in the literature, we can cite the bifurcation theory ([Rudnicki and Rice, 1975](#); [Rice, 1976](#)), the initial imperfection approach of Marciak-Kuczyński ([Marciak and Kuczyński, 1967](#); [Hutchinson and Neale, 1978](#)) and linearized perturbation stability analysis ([Dudzinski and Molinari, 1991](#); [Tóth et al., 1996](#)). The models used to describe the mechanical behavior of materials can be classified into two main families: phenomenological models and multiscale models. In earlier contributions, phenomenological models have been widely adopted to predict the FLDs. In this regard, Hill has developed the Hill's zero-extension instability criterion to predict the left-hand side of the FLD using a phenomenological isotropic rigid-plastic model ([Hill, 1952](#)). More recently, Marciak and Kuczyński have developed the initial imperfection approach and coupled it with an isotropic rigid-plastic model in order to predict the right-hand side of the FLD then to complete the Hill's effort ([Marciak and Kuczyński, 1967](#)). Despite their reliability and their wide application in the FLD predictions, phenomenological constitutive frameworks present some conceptual limitations such as their inability to accurately account for some key physical factors and phenomena, such as initial and induced textures and other microstructure-related parameters (grain morphology, crystallographic structure ...). These limitations have motivated the researchers to set up multiscale schemes for the predictions of FLDs. Contrary to phenomenological modeling, the multiscale approaches allow linking physical mechanisms and microstructure-induced properties to the macroscopic (or homogenized) mechanical behavior. Most recently, these multiscale strategies, such as the Taylor and the self-consistent schemes, have been coupled with several strain localization criteria, such as the bifurcation theory, the initial imperfection approach, and the perturbation method in order to predict necking limit strains. Our team has contributed to this field, where [Lorrain \(2005\)](#) and [Franz \(2008\)](#) have developed a strategy combining the self-consistent scheme with the bifurcation theory. Subsequently, [Akpama \(2016\)](#) extended the work of [Franz \(2008\)](#) by coupling the self-consistent scheme with the initial imperfection approach, and compared the predictions from this coupling to those from

the coupling of self-consistent scheme and bifurcation theory. Despite the substantial advances allowed by multiscale modeling strategy, the application of the previous multiscale approaches presents some limitations. These limitations are mainly due to the inability of these approaches to accurately take into consideration some important aspects in the constitutive modeling, such as a realistic description of the grains shapes, geometric and mechanical conditions over the boundary of the polycrystalline aggregate, grain boundaries, etc. Indeed, only the weight of the single crystals is considered in the Taylor model, without any additional information on grain morphology. By contrast, the single crystals are considered in the self-consistent scheme as ellipsoidal inclusions embedded within an infinite matrix. These simplifications sometimes lead to significant inaccuracies in the predictions. One of the goals of this thesis is to develop an alternative multiscale scheme, based on the Crystal Plasticity Finite Element Method (CPFEM), in order to predict the ductility of metal sheets. The use of this latter method allows overcoming the above-mentioned limitations in order to obtain more accurate predictions. Certainly, this multiscale scheme is flexible enough to be applied for a wide range of mechanical behavior modeling.

Objectives of the thesis

This thesis aims to develop a finite element based multiscale numerical strategy (a set of numerical tools) to predict the ductility limit of heterogeneous media (such as composites, voided materials, polycrystalline aggregates...) and then to investigate the effect of some microstructural parameters on ductility. This work is an extension of previous works carried out within our team. On the other hand, this numerical strategy can account for not only the multiscale models obviously also the phenomenological models. So that, in order to develop our numerical tools, the mechanical behavior is firstly described at the microscopic scale by either phenomenological modeling or crystal plasticity modeling (CPFEM). Then, the periodic homogenization technique will be adopted to determine the macroscopic mechanical behavior of heterogeneous media from that of their microscopic constituents. After that, the obtained macroscopic behavior model will be coupled with the bifurcation theory to predict localized necking in a number of heterogeneous materials, such as perforated sheets, voided materials and polycrystalline aggregates, etc.

Organization of the thesis

In order to apply the bifurcation theory for predicting the onset of localized necking, the macroscopic tangent modulus needs to be determined accurately and efficiently by the periodic homogenization scheme (Chapter 1). Then, the bifurcation theory will be coupled with some phenomenological models (in Chapter 2 and 3) followed by CPFEM models (in Chapter 4). So that, the manuscript is structured into four main chapters which are described as follows:

- Chapter 1 presents a comparative study of three numerical techniques for the computation of the macroscopic tangent moduli by periodic homogenization scheme: the perturbation technique, the condensation technique and the fluctuation technique. The practical implementations of these techniques within ABAQUS/Standard finite element (FE) code are specifically underlined. These implementations are based on the development of a set of Python scripts which are connected to the finite element computations to handle the computation of the tangent moduli. The extension of these techniques to mechanical problems exhibiting symmetry properties is also detailed in this chapter. The reliability, accuracy and ease of implementation of these techniques are evaluated through some typical numerical examples. Thus, this chapter provides valuable reference guidelines for efficiently applying our numerical tools in the following chapters.
- Chapter 2 employs the developed tools for the prediction of necking in perforated sheets. The results are thoroughly analyzed and compared with those predicted by two diffuse necking criteria: the maximum force criterion and the general bifurcation criterion. A sensitivity study is also conducted to numerically investigate the influence on the prediction of necking of the design parameters (dimension, aspect-ratio, orientation, and shape of the holes), the macroscopic boundary conditions and the metal matrix material parameters (plastic anisotropy, hardening).
- Chapter 3 applies the developed tools for the prediction of the occurrence of two failure mechanisms in ductile solid: void coalescence and macroscopic strain localization. In these predictions, the mechanical behavior modeling is coupled with several criteria (the Rice bifurcation approach, and an energy-based coalescence criterion among others). The occurrence of failure mechanisms is examined under two loading configurations: loadings under proportional stressing (classically used in unit cell computations to study the effect of stress state on void growth and coalescence), and loadings under proportional in-plane strain paths (traditionally used for predicting forming limit diagrams). Meanwhile, the relations between the two configurations of loading are carefully explained within these two failure mechanisms. The effect of secondary voids on the occurrence of macroscopic strain localization is also investigated.
- Chapter 4 is dedicated to the application of our numerical strategy to FCC polycrystals, where the CPFEM is used to characterize the mechanical behavior. The mechanical response at both single crystal and polycrystalline scales is highlighted through several simulations. Moreover, the crystal texture and hardening evolutions at the microscale as well as the formability of sheet metals at the macroscale are investigated. The effect of the number of grains on formability is also investigated.

Conventions, notations and abbreviations

The following conventions, notations and abbreviations are used throughout:

- Microscale (resp. macroscale) variables are denoted by lowercase (resp. capital) letters.
- Vectors and tensors are indicated by bold letters or symbols. However, scalar parameters and variables are designated by thin and *italic* letters or symbols.
- Einstein's convention of implied summation over repeated indices is adopted. The range of free (resp. dummy) index is given before (resp. after) the corresponding equation.
- $\dot{\bullet}$ time derivative of \bullet .
- \bullet^T transpose of \bullet .
- \bullet^{-1} inverse of \bullet .
- $\det(\bullet)$ determinant of \bullet .
- $\operatorname{sgn}(\bullet)$ sign of \bullet .
- $\operatorname{tr}(\bullet)$ trace of \bullet .
- e^\bullet exponential of \bullet .
- $\ln(\bullet)$ natural logarithm of \bullet .
- $\bullet \cdot \bullet$ simple contraction or contraction on one index (inner product).
- $\bullet : \bullet$ double contraction or contraction on two indices (inner product).
- $\bullet \otimes \bullet$ tensor product (external product).
- $\delta \bullet$ the virtual counterpart of field \bullet .
- δ_{ij} Kronecker delta.
- \mathbf{I}_2 second-order identity tensor.
- $\mathcal{D} \bullet$ iteration of field \bullet (within an incremental finite element computation).
- $\Delta \bullet$ small perturbation used for the differentiation of field \bullet .

- PT perturbation technique.
- CT condensation technique.
- FT fluctuation technique.
- FUC full unit cell (without or before application of symmetry restrictions).
- RUC reduced unit cell (after application of symmetry restrictions).
- UEL user element subroutine.
- UMAT user material subroutine.
- DOF degree of freedom.
- MPC multi-point constraints option (ABAQUS terminology).
- PBC (PBCs) periodic boundary conditions.
- KBC (KBCs) kinematic boundary conditions.
- MFC maximum force criterion.
- GBC general bifurcation criterion.
- RBC Rice bifurcation criterion.
- $\overset{\text{IN}}{\bullet}$ in-plane part of tensor \bullet equal to $\begin{pmatrix} \bullet_1 \\ \bullet_2 \end{pmatrix}$ if \bullet is a vector and $\begin{pmatrix} \bullet_{11} & \bullet_{12} \\ \bullet_{21} & \bullet_{22} \end{pmatrix}$ if \bullet is a second-order tensor, etc.
- $\bar{\bullet}$ the transport of \bullet in the intermediate configuration defined by the crystal lattice frame (equal to $\bar{\mathbf{r}}^T \cdot \bullet$ if \bullet is a vector and $\bar{\mathbf{r}}^T \cdot \bullet \cdot \bar{\mathbf{r}}$ if \bullet is a second-order tensor).
- $\check{\bullet}$ the transport of \bullet in the co-rotational frame (equal to $\check{\mathbf{r}}^T \cdot \bullet$ if \bullet is a vector and $\check{\mathbf{r}}^T \cdot \bullet \cdot \check{\mathbf{r}}$ if \bullet is a second-order tensor).

Chapter 1

Comparative study of three techniques for the computation of the macroscopic tangent moduli by periodic homogenization scheme

1.1. Introduction

The main objective of micromechanical multiscale approaches is to determine the effective (also called homogenized, overall or macroscopic) mechanical properties of heterogeneous media under some specific boundary conditions. In this context, [Hashin and Shtrikman \(1962\)](#) and [Hill \(1963\)](#) have analytically estimated the overall properties of reinforced composites made of linear elastic phases. As various nonlinear composites (composites containing at least one nonlinear phase) have attracted special interest for both academic and industrial communities, the earlier pioneering works have subsequently been extended to determine their effective properties. For instance, [Ponte Castaneda and Willis \(1988\)](#) have studied the mechanical behavior of nonlinear viscous composites. Suquet has derived in [Suquet \(1993\)](#) several analytical averaging relations for perfectly plastic composites. Teply and Dvorak have investigated in [Teply and Dvorak \(1988\)](#) the overall behavior of elastoplastic composites. A comprehensive review of analytical approaches, developed to estimate homogenized properties of heterogeneous composite materials, has been provided in several contributions (see, e.g., [Willis, 1981](#); [Mura et al., 1988](#); [Nemat-Nasser et al., 1996](#); [Mercier et al., 2012](#); [Ghossein and Lévesque, 2014](#)). Despite their wide use, analytical approaches are unable to give accurate effective properties for complex microstructures (random morphology and spatial distribution of constitutive phases...) exhibiting strong geometric and material nonlinearities. To overcome these limitations, some numerical approaches have

recently been developed, as alternative to analytical ones. In this regard, one may quote at least two types of commonly used approaches: those based on Fast Fourier Transforms (FFT), and those based on the Finite Element Method (FEM). As to the FFT methods, Moulinec and his coauthors ([Moulinec and Suquet, 1994, 1995, 2003; Moulinec and Silva, 2014](#)) have proposed a variety of multiscale schemes and compared their convergence rates for computing overall properties of both linear and nonlinear composites. From these investigations, it has been shown that the contrast between the mechanical properties in the phases significantly affects the convergence rate of the FFT-based computations. [Michel et al. \(1999\)](#) have demonstrated that FEM-based approaches converge more easily for composites with periodic microstructure and made of phases with infinite stiffness contrast (such as rigid inclusions or voids). Consequently, FEM-based approaches received more attention when dealing with more general heterogeneous materials, such as composites, polycrystalline aggregates and porous media. In this perspective, [Miehe \(2002\)](#) has developed a strain-driven homogenization approach for inelastic microstructures and composites based on an incremental variational formulation. This formulation can be used to compute the macroscopic response of elastoviscoplastic media under the three well-known boundary conditions: (i) linear deformation (LD), (ii) uniform traction (UT), and (iii) periodic boundary conditions (PBCs). A small strain formulation has been employed in [Miehe \(2002\)](#) to establish the multiscale relations as well as the constitutive equations of the different phases. The multiscale schemes presented in [Miehe \(2002\)](#) have been extended in [Miehe \(2003\)](#) to finite strain problems, where the Lagrange multiplier method has been employed to enforce the above boundary conditions on the microstructure. This extension has been achieved by generating a family of algorithms that allow deriving homogenized stress and tangent moduli for composites and polycrystalline aggregates. In this thesis, our attention is focused on the modeling of the mechanical behavior of heterogeneous media exhibiting a periodic or quasi-periodic distribution of heterogeneities (such as composite materials, voided media, or polycrystalline aggregates). Considering this spatial periodicity, the periodic homogenization approach turns out to be the more suitable scheme to ensure the transition between microscopic and macroscopic levels. The studied media are assumed to undergo large deformation. Consequently, a total Lagrangian formulation is adopted to formulate the governing equations of the periodic homogenization approach, where the deformation gradient and the first Piola–Kirchhoff stress tensor are selected as appropriate strain and stress measures, respectively. As first step for the application of the periodic homogenization approach, a unit cell assumed to be representative of the heterogeneous medium should be selected. Several studies, mainly based on some statistical techniques, have been carried out in the literature to evaluate the minimum size of the unit cell to ensure its representativeness of the heterogeneous medium. This step is not the object of the current chapter and the interested readers may refer to reference ([Kanit et al., 2003](#)). Once the unit cell is defined, the equations governing the periodic homogenization problem (namely, localization and homogenization relations, microscopic equilibrium equations, periodic boundary conditions) are solved by the finite element method. To this end, several academic finite element codes, such as Lagamine ([Ben Bettaieb et al., 2011](#)) or Zébulon

([Feyel, 1999](#)), have been extended by implementing some built-in tools and routines to automatically achieve the application of the macroscopic loading and PBCs and the computation of the macroscopic response. Analogous to most popular commercial finite element codes, such as ABAQUS/Standard, several plugin tools have been developed to easily apply the PBCs as well as the macroscopic loading (which can be strain-driven or stress-driven) and to compute the macroscopic response. Among these tools, one may quote the toolbox *Homtools* developed by [Lejeunes and Bourgeois \(2011\)](#), the *EasyPBC* tool proposed in [Omairey et al. \(2019\)](#) or the Python codes developed in [Tchalla et al. \(2013\)](#). Unfortunately, the above-mentioned tools are unable to achieve the automatic computation of the macroscopic tangent moduli. On the other hand, particular attention has been paid, in some contributions, to the efficient and accurate computation of these moduli for some engineering numerical applications using multiscale schemes. Indeed, the macroscopic tangent modulus is required for the prediction of the mechanical behavior of polycrystalline structures by the FE² method ([Ladevèze et al., 2001](#); [Terada and Kikuchi, 2001](#); [Matsui et al., 2004](#); [Asada and Ohno, 2007](#); [Miehe and Bayreuther, 2007](#); [Özdemir et al., 2008](#)). It is also needed for the prediction of the onset macroscopic material and structural instabilities by loss of ellipticity approaches ([Miehe et al., 2002c](#); [Michel et al., 2007](#); [Bruno et al., 2010](#); [Tadano et al., 2013](#)). In the literature, at least three FEM-based techniques have been developed to determine the macroscopic tangent modulus from the periodic homogenization computations:

- **The perturbation technique (PT):** this technique allows reducing the computation of the macroscopic tangent modulus to multiple macroscopic stress computations ([Temizer and Wriggers, 2008](#); [Tchalla et al., 2013](#)). By perturbing the macroscopic deformation gradient, the macroscopic tangent modulus is efficiently constructed by a forward difference of the macroscopic first Piola–Kirchhoff stress. To obtain the approximation of the *i-th* column of the macroscopic tangent modulus, a small perturbation of the *i-th* component of the macroscopic deformation gradient is needed (for 3D finite strain, where *i* ranges between 1 and 9). The *i-th* column of the macroscopic tangent modulus is equal to the forward difference between the perturbed and unperturbed macroscopic stress divided by the corresponding perturbation of the macroscopic deformation gradient. This method, widely adopted to numerically evaluate the tangent modulus for several phenomenological models ([Kiran and Khandelwal, 2014](#)), has been recently coupled with the periodic homogenization scheme in some investigations ([Temizer and Wriggers, 2008](#); [Tchalla et al., 2013](#)). This technique has the merit of being conceptually easy to understand, but generally requires a great deal of CPU time, as the finite element computation should be performed ten times for each increment (one time to compute the macroscopic unperturbed stress and nine times to construct the macroscopic tangent modulus).
- **The condensation technique (CT):** within this technique, the macroscopic tangent modulus is obtained by a condensation procedure of the global stiffness matrix. This method has initially been introduced for a small strain formulation ([Miehe and Koch, 2002](#)), and subsequently

extended to finite strain framework ([Miehe, 2003](#)). The practical application of this technique is based on the construction of a family of link-topology matrices to automatically represent the overall properties of discretized microstructures. The updated global stiffness matrix as well as the initial coordinates of the nodes on the boundary of the unit cell are required to compute the macroscopic tangent modulus by the condensation method.

- **The fluctuation technique (FT):** in this technique, the deformation gradient of each node of the FE discretization is additively decomposed into two parts: a homogeneous part associated with the macroscopic loading, and a nonhomogeneous part resulting from the periodic fluctuation contribution. As a result of this decomposition, the macroscopic tangent modulus can be written as the sum of the volume average of tangent moduli over the unit cell, and a fluctuation part, which depends on the global stiffness matrix and on a fluctuation matrix. The volume average of microscopic tangent moduli yields the well-known Taylor-type upper bound. The numerical procedures of this method at small strain and finite strain have been presented in [Miehe et al. \(2002b\)](#) and in [Miehe et al. \(2002a\)](#), respectively.

In this chapter, the above-discussed three techniques have been implemented in a set of Python scripts. In the developments of these scripts, some popular numerical packages, such as the NumPy and SciPy library, are used for scientific computing with Python. This choice is motivated by the fact that these libraries contain a powerful N-dimensional array object and useful linear algebra methods, thus enabling efficient matrix computations (reduced computation time and memory space). These python scripts are interpreted as post-processing of the finite element analysis, which is carried out within ABAQUS/Standard FE code. The toolbox *Homotools* ([Lejeunes and Bourgeois, 2011](#)) is used to automatically determine and generate the required boundary node sets, constraint equations, periodic boundary conditions, and post-processing calculations in order to compute the macroscopic response. Technical details, related to the connection between the ABAQUS/Standard FE code environment and the developed Python codes, will be provided in this investigation. A comparative study between the above-discussed three techniques will be given in the section corresponding to the numerical results. Thus, this chapter gives valuable reference guidelines to ABAQUS/Standard users for the determination of the homogenized tangent moduli. On the basis of this study, it is demonstrated that the condensation technique reveals to be the most efficient method (easy to implement, requires less CPU time and disk space). The computation of the tangent moduli corresponding to microstructures exhibiting symmetry properties is also detailed in this chapter. Note that such extension to symmetric problems allows considerably improving the computational performance.

The remainder of the chapter is organized as follows:

- Section 1.2 provides some technical details about the stress rates and associated tangent moduli adopted in ABAQUS/Standard FE code (built-in model or user-defined model) to formulate and

solve the weak form of the virtual work principle. These details are essential for the understanding of the subsequent sections.

- The formulation of the periodic homogenization problem at finite strain, and the practical aspects related to the solution of this problem are discussed in Section 1.3.
- The numerical aspects and the operational details related to the implementation of the three techniques for the computation of the tangent modulus (namely, the perturbation technique, the condensation technique, the fluctuation technique) are detailed in Section 1.4.
- Section 1.5 is dedicated to the adaptation of the perturbation and condensation techniques to the case of microstructures displaying symmetry properties.
- In Section 1.6, the implementation of the three techniques is validated by comparing their results with those published in [Miehe et al. \(2002b\)](#). The performances of these techniques are reported, discussed and compared through some numerical examples.

1.2. Details on the finite element formulation in ABAQUS/Standard

The majority of commercial finite element codes (such as ABAQUS, ANSYS, NASTRAN, LS-DYNA...) allow the accurate computation of the mechanical response of solids and structures exhibiting strong material and geometric nonlinearities (elastoplastic behavior, finite strain, finite rotation, contact...). Within the finite strain framework, there are several work-conjugate strain/stress measures classically used to formulate the virtual work principle, which is the basis of the finite element method. For instance, the ABAQUS/Standard built-in formulation¹ is based on the Jaumann rate of the Kirchhoff stress tensor, while NASTRAN is based on the Truesdell rate of the Cauchy stress tensor. The finite element simulation results must be independent of the choice of these strain/stress measures and the associated virtual work form. Hence, to ensure the accuracy and correctness of the finite element results, the specific stress rate and associated tangent modulus (relating the stress rate to the associated strain rate) should be properly chosen. The current section provides a brief overview of the relations between the different stress rates as well as the associated tangent moduli commonly used in ABAQUS/Standard code.

Starting with the formulation of the virtual work principle, the equilibrium equation is expressed in a rate form as follows:

$$\operatorname{div}_{x_0}(\dot{\mathbf{p}}) + \dot{\mathbf{b}}_0 = \mathbf{0}, \quad (1.1)$$

where:

¹ It is referred to ABAQUS/Standard formulation without user subroutines for nonlinear incremental analysis in this chapter. ABAQUS/Explicit adopts different fundamental solving technique, as well as the theoretical formulation.

- $\dot{\mathbf{p}}$ is the rate of the first Piola–Kirchhoff stress and $\text{div}_{\mathbf{x}_0}(\dot{\mathbf{p}})$ its divergence with respect to the reference coordinate system \mathbf{x}_0 .
- $\dot{\mathbf{b}}_0$ is the body force rate per unit volume in the reference configuration.

Multiplying Eq. (1.1) by a virtual velocity field $\delta \mathbf{v}$ and integrating over the volume of the reference configuration \mathcal{V}_0 yields:

$$\int_{\mathcal{V}_0} \delta \mathbf{v} \cdot [\text{div}_{\mathbf{x}_0}(\dot{\mathbf{p}}) + \dot{\mathbf{b}}_0] d\mathcal{V}_0 = 0. \quad (1.2)$$

Employing the chain rule and Gauss theorem, Eq. (1.2) can be reformulated as follows:

$$\int_{\mathcal{V}_0} \left[\frac{\partial \delta \mathbf{v}}{\partial \mathbf{x}_0} : \dot{\mathbf{p}} \right] d\mathcal{V}_0 = \int_{\mathcal{S}_0} \delta \mathbf{v} \cdot \dot{\mathbf{t}}_0 d\mathcal{S}_0 + \int_{\mathcal{V}_0} \delta \mathbf{v} \cdot \dot{\mathbf{b}}_0 d\mathcal{V}_0, \quad (1.3)$$

where \mathcal{S}_0 and $\dot{\mathbf{t}}_0$ denote the boundary surface of the reference configuration and the nominal traction rate prescribed on \mathcal{S}_0 , respectively. Vector $\dot{\mathbf{t}}_0$ is equal to $\dot{\mathbf{p}} \cdot \vec{\mathbf{n}}_0$, where $\vec{\mathbf{n}}_0$ is the outer normal to the boundary \mathcal{S}_0 .

The virtual work principle defined by Eq. (1.3) can be equivalently expressed in terms of the Kirchhoff stress $\boldsymbol{\tau}$ ($= \mathbf{p} \cdot \mathbf{f}^T$, where \mathbf{f} denotes the deformation gradient) and its objective derivatives $\tilde{\boldsymbol{\tau}}^{(m)}$ as follows (Ji et al., 2013):

$$\int_{\mathcal{V}_0} [\delta \mathbf{d} : \tilde{\boldsymbol{\tau}}^{(m)} - (2-m)\boldsymbol{\tau} : (\delta \mathbf{d} \cdot \mathbf{d}) + \boldsymbol{\tau} : (\delta \mathbf{g}^T \cdot \mathbf{g})] d\mathcal{V}_0 = \int_{\mathcal{S}_0} \delta \mathbf{v} \cdot \dot{\mathbf{t}}_0 d\mathcal{S}_0 + \int_{\mathcal{V}_0} \delta \mathbf{v} \cdot \dot{\mathbf{b}}_0 d\mathcal{V}_0, \quad (1.4)$$

where:

- \mathbf{g} is the velocity gradient, defined as $\partial \mathbf{v} / \partial \mathbf{x}$, and $\delta \mathbf{g}$ its virtual counterpart.
- \mathbf{d} is the strain rate, defined as the symmetric part of \mathbf{g} , and $\delta \mathbf{d}$ its virtual counterpart.
- m is a parameter that defines the different objective rates of the Kirchhoff stress. It is equal to 0, 1, and 2 for the Jaumann, Biot and Truesdell rates, respectively.

In ABAQUS/Standard built-in modeling, the Jaumann rate is employed. Hence, Eq. (1.4) is used with $m=0$:

$$\int_{\mathcal{V}_0} [\delta \mathbf{d} : \tilde{\boldsymbol{\tau}}^{(0)} - 2\boldsymbol{\tau} : (\mathbf{d} \cdot \delta \mathbf{d}) + \boldsymbol{\tau} : (\mathbf{g}^T \cdot \delta \mathbf{g})] d\mathcal{V}_0 = \int_{\mathcal{S}_0} \delta \mathbf{v} \cdot \dot{\mathbf{t}}_0 d\mathcal{S}_0 + \int_{\mathcal{V}_0} \delta \mathbf{v} \cdot \dot{\mathbf{b}}_0 d\mathcal{V}_0. \quad (1.5)$$

On the other hand, the Jaumann rate of the Kirchhoff stress $\tilde{\boldsymbol{\tau}}^{(0)}$ is related to the strain rate \mathbf{d} as follows:

$$\tilde{\boldsymbol{\tau}}^{(0)} = \mathbf{c}^{(0)} : \mathbf{d}, \quad (1.6)$$

where the tangent modulus $\mathbf{c}^{(0)}$ is expressed in terms of the jacobian matrix **DDSDDE** (using the terminology of ABAQUS/Standard FE code) and $j (= \det(\mathbf{f}))$ as follows:

$$\mathbf{c}^{(0)} = j \mathbf{DDSDDE}. \quad (1.7)$$

Utilizing finite element discretization, the velocity field \mathbf{v} and the strain rate \mathbf{d} can be obtained from the nodal displacement rate vector $\dot{\mathbf{q}}$ by the interpolation rule:

$$\mathbf{v} = \mathbf{N} \cdot \dot{\mathbf{q}} ; \quad \mathbf{d} = \frac{1}{2} (\mathbf{B} + \mathbf{B}^T) \cdot \dot{\mathbf{q}}, \quad (1.8)$$

with \mathbf{N} being the shape function vector, and \mathbf{B} its derivative with respect to \mathbf{x} .

The substitution of Eqs. (1.6) and (1.8) into the different components of Eq. (1.5) leads to:

$$\begin{cases} \int_{\mathcal{V}_0} [\delta \mathbf{d} : \tilde{\tau}^{(0)}] d\mathcal{V}_0 = \int_{\mathcal{V}_0} [\delta \mathbf{d} : \mathbf{c}^{(0)} : \mathbf{d}] d\mathcal{V}_0 = \delta \dot{\mathbf{q}}^T \left[\int_{\mathcal{V}_0} \mathbf{B}^T \cdot \mathbf{c}^{(0)} \cdot \mathbf{B} d\mathcal{V}_0 \right] \cdot \dot{\mathbf{q}} = \delta \dot{\mathbf{q}}^T \cdot \mathbf{K}_M \cdot \dot{\mathbf{q}}; \\ \int_{\mathcal{V}_0} [-2\boldsymbol{\tau} : (\mathbf{d} \cdot \delta \mathbf{d}) + \boldsymbol{\tau} : (\mathbf{g}^T \cdot \delta \mathbf{g})] d\mathcal{V}_0 = \delta \dot{\mathbf{q}}^T \cdot \mathbf{K}_{GNL} \cdot \dot{\mathbf{q}}; \\ \int_{\mathcal{S}_0} \dot{\mathbf{t}}_0 \cdot \delta \mathbf{v} d\mathcal{S}_0 + \int_{\mathcal{V}_0} \dot{\mathbf{b}}_0 \cdot \delta \mathbf{v} d\mathcal{V}_0 = \delta \dot{\mathbf{q}}^T \cdot \dot{\mathbf{r}}, \end{cases} \quad (1.9)$$

where:

- \mathbf{K}_M is the part of the global stiffness matrix associated with the mechanical behavior.
- \mathbf{K}_{GNL} is the part of the global stiffness matrix resulting from the geometric nonlinearities.
- $\dot{\mathbf{r}}$ is the residual vector.

Then, Eq. (1.5) can be written in the following discretized matrix form:

$$[\mathbf{K}_M + \mathbf{K}_{GNL}] \cdot \dot{\mathbf{q}} = \mathbf{K} \cdot \dot{\mathbf{q}} = \dot{\mathbf{r}}. \quad (1.10)$$

Equation (1.10) is strongly nonlinear, as stiffness matrix $\mathbf{K} (= [\mathbf{K}_M + \mathbf{K}_{GNL}])$ and vector $\dot{\mathbf{r}}$ depend on the nodal displacement rate vector $\dot{\mathbf{q}}$. Consequently, this equation is classically solved by an iterative scheme, such as the Newton–Raphson method.

For ABAQUS/Standard FE code, when the mechanical behavior is inelastic (elastoplastic, elastoviscoplastic...) and built-in material subroutines are used to model this behavior (i.e., without user material subroutine UMAT), Eq. (1.9)₁ is rearranged as follows:

$$\begin{aligned} \int_{\mathcal{V}_0} [\delta \mathbf{d} : \tilde{\tau}^{(0)}] d\mathcal{V}_0 &= \int_{\mathcal{V}_0} [\delta \mathbf{d} : \mathbf{c}^e : \mathbf{d}^e] d\mathcal{V}_0 \\ &= \int_{\mathcal{V}_0} [\delta \mathbf{d} : \mathbf{c}^e : (\mathbf{d} - \mathbf{d}^p)] d\mathcal{V}_0 \\ &= \delta \dot{\mathbf{q}}^T \cdot \left(\left[\int_{\mathcal{V}_0} [\mathbf{B}^T \cdot \mathbf{c}^e \cdot \mathbf{B}] d\mathcal{V}_0 \right] \cdot \dot{\mathbf{q}} - \int_{\mathcal{V}_0} [\mathbf{c}^e : \mathbf{d}^p] d\mathcal{V}_0 \right) \\ &= \delta \dot{\mathbf{q}}^T \cdot (\mathbf{K}_E \cdot \dot{\mathbf{q}} - \dot{\mathbf{r}}_p), \end{aligned} \quad (1.11)$$

where \mathbf{d}^e and \mathbf{d}^p are the elastic and plastic parts of the strain rate, and \mathbf{c}^e is the elasticity modulus, which contributes to the elastic stiffness \mathbf{K}_E . With this rearrangement, the global nonlinear equation system (1.10) is reformulated as follows:

$$[\mathbf{K}_E + \mathbf{K}_{GNL}] \cdot \dot{\mathbf{q}} = \dot{\mathbf{r}} + \dot{\mathbf{r}}_p. \quad (1.12)$$

Hence, when the ABAQUS/Standard built-in mechanical modeling is used, the global stiffness matrix is only constructed on the basis of the elastic contribution. However, when user material subroutines UMAT are used, the stiffness matrix is constructed on the basis of the **DDSDDE** tangent modulus, which obviously considers the effect of both elastic and inelastic behavior.

On the other hand, the rate of the first Piola–Kirchhoff stress $\dot{\mathbf{p}}$ is related to the rate of the deformation gradient $\dot{\mathbf{f}}$ by the tangent modulus $\mathbf{c}^{(PK1)}$:

$$\dot{\mathbf{p}} = \mathbf{c}^{(PK1)} : \dot{\mathbf{f}}. \quad (1.13)$$

The substitution of Eq. (1.13) into Eq. (1.3) leads to the following expression of the virtual work principle:

$$\int_{\mathcal{V}_0} [\delta \dot{\mathbf{f}} : \mathbf{c}^{(PK1)} : \dot{\mathbf{f}}] d\mathcal{V}_0 = \int_{\mathcal{S}_0} \delta \mathbf{v} \cdot \dot{\mathbf{t}}_0 d\mathcal{S}_0 + \int_{\mathcal{V}_0} \delta \mathbf{v} \cdot \dot{\mathbf{b}}_0 d\mathcal{V}_0. \quad (1.14)$$

Equation (1.14) can be considered as the total Lagrangian formulation of the virtual work principle. Forms (1.5) and (1.14) are strictly equivalent as long as the relationship between $\mathbf{c}^{(0)}$ and $\mathbf{c}^{(PK1)}$ is properly defined. To define this relationship, let us introduce tangent moduli $\mathbf{c}^{(2)}$ and $\mathbf{c}^{(PK2)}$ relating the Truesdell derivative of the Kirchhoff stress $\tilde{\tau}^{(2)}$ ($m=2$) to the strain rate \mathbf{d} , on the one hand, and the second Piola–Kirchhoff stress rate $\dot{\mathbf{s}}$ to the Green strain rate $\dot{\mathbf{e}}$, on the other hand:

$$\tilde{\tau}^{(2)} = \mathbf{c}^{(2)} : \mathbf{d} \quad ; \quad \dot{\mathbf{s}} = \mathbf{c}^{(PK2)} : \dot{\mathbf{e}}. \quad (1.15)$$

As demonstrated in Ji et al. (2013), $\mathbf{c}^{(0)}$ is linked to $\mathbf{c}^{(2)}$ through the following indicial form:

$$\forall i, j, k, l = 1, 2, 3: \quad c_{ijkl}^{(0)} = c_{ijkl}^{(2)} + \frac{1}{2} (\tau_{ik}\delta_{jl} + \tau_{jk}\delta_{il} + \tau_{il}\delta_{jk} + \tau_{ji}\delta_{ik}), \quad (1.16)$$

where δ_{ij} is the Kronecker delta.

Meanwhile, $\mathbf{c}^{(2)}$ and $\mathbf{c}^{(PK1)}$ are related to $\mathbf{c}^{(PK2)}$ by the following indicial forms (Ji et al., 2013):

$$\forall i, j, k, l = 1, 2, 3: \quad c_{ijkl}^{(2)} = f_{im} f_{jn} f_{kp} f_{lq} c_{mnpq}^{(PK2)} \quad ; \quad c_{inkq}^{(PK1)} = c_{mnpq}^{(PK2)} f_{im} f_{kp} + s_{nq} \delta_{ik}. \quad (1.17)$$

Equation (1.16) together with Eq. (1.17) define the relations between the different tangent modulus forms (namely, $\mathbf{c}^{(0)}$, $\mathbf{c}^{(2)}$, $\mathbf{c}^{(PK1)}$ and $\mathbf{c}^{(PK2)}$). If these relations are not strictly respected, the two forms of the virtual work principle (i.e., Eqs. (1.5) and (1.14)) become different, and this difference may lead to some work-conjugacy issues (convergence problems, errors associated with lack of energy conservation...).

1.3. Periodic homogenization problem

The periodic homogenization technique is used to ensure the transition between microscopic and macroscopic scales. Without loss of generality, we assume that the initial configuration of the unit cell

\mathcal{V}_0 occupies the domain $[-\lambda_0/2, \lambda_0/2] \times [-\lambda_0/2, \lambda_0/2] \times [-\lambda_0/2, \lambda_0/2]$. The studied unit cell is assumed to undergo finite strain and total Lagrangian formulation is used to formulate the periodic homogenization relations. Consequently, the deformation gradient and the first Piola–Kirchhoff stress tensor are used as appropriate work-conjugate strain and stress measures. For the sake of clarity, microscopic (resp. macroscopic) quantities will be denoted by small (resp. capital) characters and symbols.

The main equations governing the periodic homogenization scheme are outlined hereafter:

- The microscopic deformation gradient \mathbf{f} is additively decomposed into its macroscopic counterpart \mathbf{F} and a periodic fluctuation gradient \mathbf{f}_{per} :

$$\mathbf{f} = \mathbf{F} + \mathbf{f}_{per}. \quad (1.18)$$

The current position \mathbf{x} of a material point can be determined by spatial integration of Eq. (1.18):

$$\mathbf{x} = \mathbf{F} \cdot \mathbf{x}_0 + \mathbf{u}_{per}, \quad (1.19)$$

where \mathbf{x}_0 is the initial position of the material point, and \mathbf{u}_{per} is a periodic displacement over the initial configuration of the unit cell. The expression of the nodal velocity \mathbf{v} can be easily derived from Eq. (1.19):

$$\mathbf{v} = \dot{\mathbf{F}} \cdot \mathbf{x}_0 + \dot{\mathbf{u}}_{per} := \dot{\mathbf{F}} \cdot \mathbf{x}_0 + \mathbf{v}_{per}. \quad (1.20)$$

- The averaging relations linking the microscopic deformation gradient \mathbf{f} and the microscopic first Piola–Kirchhoff stress tensor \mathbf{p} to their macroscopic counterparts \mathbf{F} and \mathbf{P} :

$$\mathbf{F} = \frac{1}{|\mathcal{V}_0|} \int_{\mathcal{V}_0} \mathbf{f} d\mathcal{V}_0 \quad ; \quad \mathbf{P} = \frac{1}{|\mathcal{V}_0|} \int_{\mathcal{V}_0} \mathbf{p} d\mathcal{V}_0, \quad (1.21)$$

with $|\mathcal{V}_0|$ being the initial volume of the unit cell, which is equal here to $(\lambda_0)^3$.

Equation (1.21) can be equivalently expressed in the following rate form:

$$\dot{\mathbf{F}} = \frac{1}{|\mathcal{V}_0|} \int_{\mathcal{V}_0} \dot{\mathbf{f}} d\mathcal{V}_0 \quad ; \quad \dot{\mathbf{P}} = \frac{1}{|\mathcal{V}_0|} \int_{\mathcal{V}_0} \dot{\mathbf{p}} d\mathcal{V}_0, \quad (1.22)$$

- The microscopic static equilibrium equation in the absence of body forces:

$$\operatorname{div}_{\mathbf{x}_0}(\dot{\mathbf{p}}) = \mathbf{0}. \quad (1.23)$$

- The constitutive relation describing the microscopic as well as the macroscopic mechanical behavior can be summarized by the following generic form:

$$\dot{\mathbf{p}} = \mathbf{C}^{(PK1)} : \dot{\mathbf{f}} \quad ; \quad \dot{\mathbf{P}} = \mathbf{C}^{(PK1)} : \dot{\mathbf{F}}. \quad (1.24)$$

Compared to classic finite element problems, the periodic homogenization problem defined by Eqs. (1.18)–(1.24) presents two particular specificities: the nature of the loading to which the unit cell is

subjected, and the boundary conditions applied on the outer surfaces of the unit cell. These practical aspects will be clarified in the following developments. As a starting point for these developments, the virtual work principle given in Eq. (1.3) is reduced to the following form in the absence of body forces:

$$\int_{\mathcal{V}_0} \left[\frac{\partial \delta \mathbf{v}}{\partial \mathbf{x}_0} : \dot{\mathbf{p}} \right] d\mathcal{V}_0 = \int_{\mathcal{S}_0} \delta \mathbf{v} \cdot \dot{\mathbf{t}}_0 \, d\mathcal{S}_0. \quad (1.25)$$

Considering the decomposition in Eq. (1.20) and Eq. (1.22), the left-hand side of Eq. (1.25) can be written as follows:

$$\begin{aligned} \int_{\mathcal{V}_0} \left(\frac{\partial \delta \mathbf{v}}{\partial \mathbf{x}_0} : \dot{\mathbf{p}} \right) d\mathcal{V}_0 &= \int_{\mathcal{V}_0} \left(\left(\delta \dot{\mathbf{F}} + \frac{\partial \delta \mathbf{v}_{per}}{\partial \mathbf{x}_0} \right) : \dot{\mathbf{p}} \right) d\mathcal{V}_0 \\ &= \int_{\mathcal{V}_0} (\delta \dot{\mathbf{F}} : \dot{\mathbf{p}}) d\mathcal{V}_0 + \int_{\mathcal{S}_0} ((\delta \mathbf{v}_{per} \otimes \vec{\mathbf{n}}_0) : \dot{\mathbf{p}}) d\mathcal{S}_0. \end{aligned} \quad (1.26)$$

Considering the anti-periodicity of tensor $\delta \mathbf{v}_{per} \otimes \vec{\mathbf{n}}_0$ and the periodicity of $\dot{\mathbf{p}}^T$, one can easily show that:

$$\int_{\mathcal{S}_0} ((\delta \mathbf{v}_{per} \otimes \vec{\mathbf{n}}_0) : \dot{\mathbf{p}}) d\mathcal{S}_0 = \mathbf{0}. \quad (1.27)$$

Together with Eq. (1.27), Eq. (1.26) is reduced to the Hill-Mandel condition (Ben Bettaieb et al., 2012a):

$$\int_{\mathcal{V}_0} \left(\frac{\partial \delta \mathbf{v}}{\partial \mathbf{x}_0} : \dot{\mathbf{p}} \right) d\mathcal{V}_0 = |\mathcal{V}_0| \delta \dot{\mathbf{F}} : \dot{\mathbf{P}}. \quad (1.28)$$

As shown in some literatures (Debordes, 1986; Miehe and Bayreuther, 2006; Temizer and Wriggers, 2008) for the classical periodic homogenization technique within a total Lagrangian formulation, Eq. (1.26) enables to treat the macroscopic deformation gradient rate $\dot{\mathbf{F}}$ as macroscopic degrees of freedom associated with the nodal forces $|\mathcal{V}_0| \dot{\mathbf{P}}$. In practice, the application of macroscopic loading in combination with PBCs within ABAQUS is ensured by the use of the reference point technique (Lejeunes and Bourgeois, 2011). We detail in the following developments how the reference point technique manages the macroscopic loading and the PBCs in only one space direction (direction 1). The extension to the other directions can be done in a similar way.

If we consider two nodes M^- and M^+ belonging to faces \mathcal{S}_{01}^- and \mathcal{S}_{01}^+ and having identical coordinates in 2 and 3 directions (Fig. 1.1), the position of these two nodes can be determined from Eq. (1.19):

$$\mathbf{x}_{M^-} = \mathbf{F} \cdot \mathbf{x}_{0M^-} + \mathbf{u}_{M^-}^{per} \quad ; \quad \mathbf{x}_{M^+} = \mathbf{F} \cdot \mathbf{x}_{0M^+} + \mathbf{u}_{M^+}^{per}. \quad (1.29)$$

The PBCs require that $\mathbf{u}_{M^-}^{per} = \mathbf{u}_{M^+}^{per}$. Consequently, Eq. (1.29)₁ and Eq. (1.29)₂ can be combined to obtain:

$$\mathbf{x}_{M^+} - \mathbf{x}_{M^-} = \mathbf{F} \cdot (\mathbf{x}_{0M^+} - \mathbf{x}_{0M^-}). \quad (1.30)$$

On the other hand, the difference $\mathbf{x}_{M^+} - \mathbf{x}_{M^-}$ is defined as follows:

$$\mathbf{x}_{M^+} - \mathbf{x}_{M^-} = (\mathbf{u}_{M^+} - \mathbf{u}_{M^-}) + (\mathbf{x}_{0M^+} - \mathbf{x}_{0M^-}), \quad (1.31)$$

where \mathbf{u}_{M^+} and \mathbf{u}_{M^-} are the displacements of nodes M^+ and M^- , respectively. Considering the initial coordinates of nodes M^+ and M^- , the substitution of Eq. (1.31) into Eq. (1.30) leads to the following relation between displacements \mathbf{u}_{M^+} and \mathbf{u}_{M^-} :

$$\mathbf{u}_{M^+} - \mathbf{u}_{M^-} = (\mathbf{F} - \mathbf{I}_2) \cdot (\mathbf{x}_{0M^+} - \mathbf{x}_{0M^-}) = (\mathbf{F} - \mathbf{I}_2) \cdot \begin{bmatrix} \lambda_0 \\ 0 \\ 0 \end{bmatrix}. \quad (1.32)$$

Practically, the PBCs on the opposite faces \mathcal{S}_{01}^- and \mathcal{S}_{01}^+ and the macroscopic loading \mathbf{F} , summarized by Eq. (1.32), are applied by using the multi-point constraints (MPC) option of ABAQUS for each node pair (M^-, M^+) . The set of python scripts *Homtools* enables to automatically identify all the node pairs of faces \mathcal{S}_{01}^- and \mathcal{S}_{01}^+ and to apply the MPC between the nodes from the same node pair. To easily manage the application of the macroscopic loading and, more interestingly, to automatize the determination of the macroscopic mechanical response, a reference point (using the ABAQUS terminology), designated RP_1 , is created. The macroscopic loading is applied by imposing the following displacement on RP_1 : $(U_1 = (F_{11} - 1)\lambda_0; U_2 = 0; U_3 = 0)$. This reference point is connected with each node pair to apply the MPC represented by Eq. (1.32). The reaction forces induced by the displacement applied on RP_1 are equal to the components 11, 12 and 13 of the macroscopic Piola–Kirchhoff stress tensor \mathbf{P} multiplied by the initial volume of the unit cell $|\mathcal{V}_0|$ (Lejeunes and Bourgeois, 2011). Quite similar developments can be performed for the application of the PBCs on the other faces.

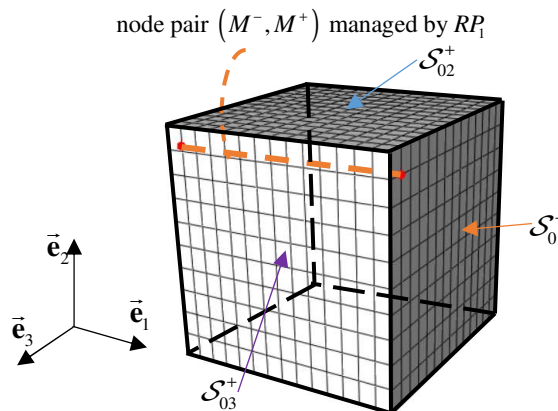


Fig. 1.1. Illustration of the PBCs between nodes M^- and M^+ .

1.4. Computation of the macroscopic tangent modulus

The practical aspects related to the solution of the periodic homogenization problem by the finite element method have been detailed in Section 1.3. This solution is conducted by using the *Homtools* capable of

handling the application of the PBCs and the macroscopic loading as well as the determination of the macroscopic response. To achieve this technical effort, we have developed a set of python scripts to automatically determine the numerical evolution of the macroscopic tangent modulus by using three FEM-based techniques. This is the main objective of the present section, where the theoretical concepts behind the three techniques are briefly revisited and the practical implementations of these techniques within ABAQUS/Standard FE code are extensively discussed.

1.4.1. Perturbation technique

1.4.1.1. Numerical concept

The macroscopic tangent modulus, denoted $\mathbf{C}^{(PK1)}$, links the rate of the macroscopic deformation gradient $\dot{\mathbf{F}}$ to the rate of the macroscopic first Piola–Kirchhoff stress tensor $\dot{\mathbf{P}}$. Hence, $\mathbf{C}^{(PK1)}$ can be obtained by the differentiation of the first Piola–Kirchhoff stress tensor with respect to the deformation gradient:

$$\dot{\mathbf{P}} = \mathbf{C}^{(PK1)} : \dot{\mathbf{F}} \Leftrightarrow \Delta\mathbf{P} \approx \mathbf{C}^{(PK1)} : \Delta\mathbf{F}, \quad (1.33)$$

where $\Delta \bullet$ is a very small perturbation applied to field \bullet .

Following the perturbation technique, each column of $\mathbf{C}^{(PK1)}$ is numerically constructed by perturbing the components of the macroscopic deformation gradient \mathbf{F} and using the associated perturbed response as follows:

$$\forall i, j, k, l = 1, 2, 3: C_{ijkl}^{(PK1)} \approx \frac{\Delta P_{ij}^{(\alpha)}}{\Delta F_{kl}^{(\alpha)}} \approx \frac{P_{ij}(\mathbf{F}_{kl}^{(\alpha)}) - P_{ij}(\mathbf{F})}{\alpha} \quad \text{with} \quad \mathbf{F}_{kl}^{(\alpha)} = \mathbf{F} + \Delta \mathbf{F}_{kl}^{(\alpha)} = \mathbf{F} + \alpha \vec{\mathbf{e}}_k \otimes \vec{\mathbf{e}}_l, \quad (1.34)$$

where $\vec{\mathbf{e}}_k$ and $\vec{\mathbf{e}}_l$ are respectively the k -th and l -th unit vector, and α is the perturbation magnitude (which typically ranges between 10^{-6} and 10^{-8}). For illustration, the matrix form of Eq. (1.34) corresponding to the perturbation tensor $\Delta \mathbf{F}_{11}^{(\alpha)} = \alpha \vec{\mathbf{e}}_1 \otimes \vec{\mathbf{e}}_1$ can be written as:

$$\begin{bmatrix} C_{1111}^{(PK1)} & C_{1122}^{(PK1)} & C_{1133}^{(PK1)} & C_{1112}^{(PK1)} & C_{1123}^{(PK1)} & C_{1113}^{(PK1)} & C_{1121}^{(PK1)} & C_{1132}^{(PK1)} & C_{1131}^{(PK1)} \\ C_{2211}^{(PK1)} & C_{2222}^{(PK1)} & C_{2233}^{(PK1)} & C_{2212}^{(PK1)} & C_{2223}^{(PK1)} & C_{2213}^{(PK1)} & C_{2221}^{(PK1)} & C_{2232}^{(PK1)} & C_{2231}^{(PK1)} \\ C_{3311}^{(PK1)} & C_{3322}^{(PK1)} & C_{3333}^{(PK1)} & C_{3312}^{(PK1)} & C_{3323}^{(PK1)} & C_{3313}^{(PK1)} & C_{3321}^{(PK1)} & C_{3332}^{(PK1)} & C_{3331}^{(PK1)} \\ C_{1211}^{(PK1)} & C_{1222}^{(PK1)} & C_{1233}^{(PK1)} & C_{1212}^{(PK1)} & C_{1223}^{(PK1)} & C_{1213}^{(PK1)} & C_{1221}^{(PK1)} & C_{1232}^{(PK1)} & C_{1231}^{(PK1)} \\ C_{2311}^{(PK1)} & C_{2322}^{(PK1)} & C_{2333}^{(PK1)} & C_{2312}^{(PK1)} & C_{2323}^{(PK1)} & C_{2313}^{(PK1)} & C_{2321}^{(PK1)} & C_{2332}^{(PK1)} & C_{2331}^{(PK1)} \\ C_{1311}^{(PK1)} & C_{1322}^{(PK1)} & C_{1333}^{(PK1)} & C_{1312}^{(PK1)} & C_{1323}^{(PK1)} & C_{1313}^{(PK1)} & C_{1321}^{(PK1)} & C_{1332}^{(PK1)} & C_{1331}^{(PK1)} \\ C_{2111}^{(PK1)} & C_{2122}^{(PK1)} & C_{2133}^{(PK1)} & C_{2112}^{(PK1)} & C_{2123}^{(PK1)} & C_{2113}^{(PK1)} & C_{2121}^{(PK1)} & C_{2132}^{(PK1)} & C_{2131}^{(PK1)} \\ C_{3211}^{(PK1)} & C_{3222}^{(PK1)} & C_{3233}^{(PK1)} & C_{3212}^{(PK1)} & C_{3223}^{(PK1)} & C_{3213}^{(PK1)} & C_{3221}^{(PK1)} & C_{3232}^{(PK1)} & C_{3231}^{(PK1)} \\ C_{3111}^{(PK1)} & C_{3122}^{(PK1)} & C_{3133}^{(PK1)} & C_{3112}^{(PK1)} & C_{3123}^{(PK1)} & C_{3113}^{(PK1)} & C_{3121}^{(PK1)} & C_{3132}^{(PK1)} & C_{3131}^{(PK1)} \end{bmatrix} \begin{Bmatrix} \alpha \\ 0 \\ 0 \\ 0 \\ 0 \\ 0 \\ 0 \\ 0 \\ 0 \end{Bmatrix} = \begin{Bmatrix} \Delta P_{11}^{(\alpha)} \\ \Delta P_{22}^{(\alpha)} \\ \Delta P_{33}^{(\alpha)} \\ \Delta P_{12}^{(\alpha)} \\ \Delta P_{23}^{(\alpha)} \\ \Delta P_{13}^{(\alpha)} \\ \Delta P_{21}^{(\alpha)} \\ \Delta P_{32}^{(\alpha)} \\ \Delta P_{31}^{(\alpha)} \end{Bmatrix}. \quad (1.35)$$

Thus, the first column of modulus $\mathbf{C}^{(PK1)}$ is computed as:

$$\forall i, j = 1, 2, 3: C_{ij11}^{(PK1)} \approx \frac{P_{ij}(\mathbf{F}_{11}^{(\alpha)}) - P_{ij}(\mathbf{F})}{\alpha}. \quad (1.36)$$

The eight other columns are obtained in the same way as for the first column.

1.4.1.2. Practical implementation

To determine the macroscopic tangent modulus $\mathbf{C}^{(PK1)}$ by the perturbation technique, ten FE computation steps are performed: one general computation step to compute the unperturbed tensor $\mathbf{P}(\mathbf{F})$, followed by nine perturbation steps to compute the perturbed tensors $\mathbf{P}(\mathbf{F}_{kl}^{(\alpha)})$ for $k, l = 1, 2, 3$.

The perturbation steps are achieved using the ABAQUS/Standard restart technique. In the general computation step, it is needed to specify the requested restart files in the input file. An analysis can be restarted only if the restart request is made for it. In ABAQUS/Standard, these files include the restart (.res), analysis database (.mdl and .stt), part (.prt), output database (.odb), and substructure database (.sim) files. Accordingly, based on these restart data at each specific restart time, the nine perturbation steps will restart the analysis with the perturbed macroscopic deformation gradient. It is worth noting that the general computation step can be linear or nonlinear, modeled via either built-in material model or user-defined material subroutine (UMAT). As to the perturbation computation steps, they are performed using the linear static perturbation analysis of ABAQUS/Standard. The algorithmic steps of the perturbation technique are illustrated in Fig. 1.2.

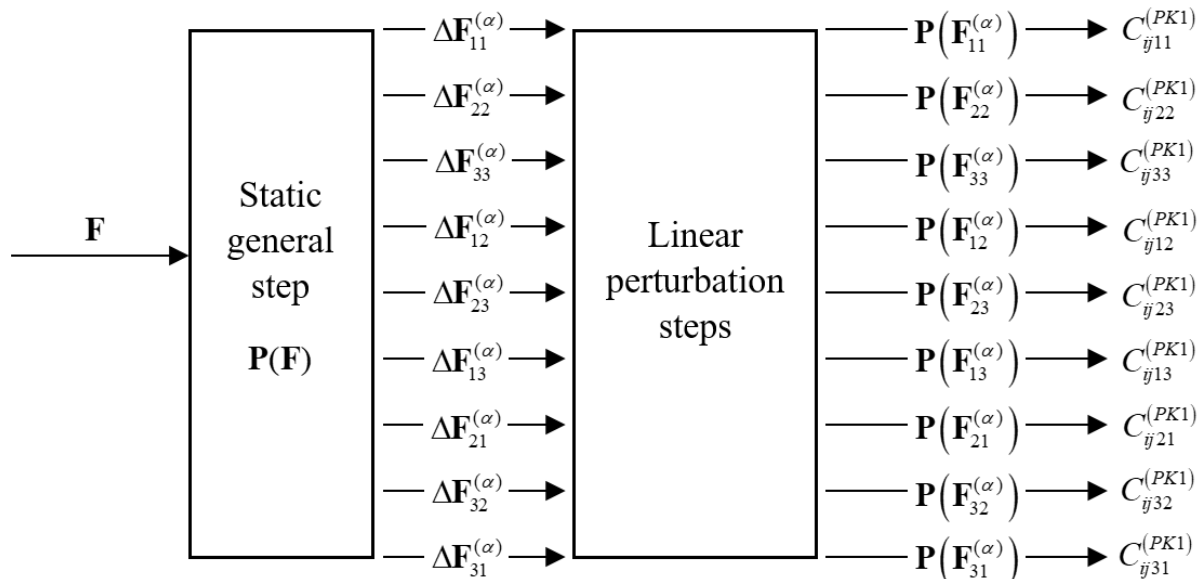


Fig. 1.2. Basic algorithmic steps for the perturbation technique.

Box 1. Main steps for the implementation of the perturbation technique.

The main steps for the implementation of the perturbation technique are summarized as follows:

- **Step 1:** run the general static step with addition of the option ‘*Restart, write, frequency=*n*’ in the ‘.inp’ file and then compute the unperturbed stress $\mathbf{P}(\mathbf{F})$ by the *Homotools*. Integer *n*, used as frequency parameter, specifies the increments at which restart information will be written. For example, frequency=2 is to write restart information at increments 2, 4, 6, etc.
- **Step 2:** create nine restart ‘.inp’ files with the option ‘*RESTART, READ, STEP=1, INC=*n*, END STEP’ to specify the step and the increment from which restart analysis continues (see Appendix B). In these files, static perturbation analysis step is used and the corresponding option is:

‘*STEP, PERTURBATION

*Static’

- **Step 3:** run these nine restart jobs with command ‘abaqus job=job-name oldjob=oldjob-name’, or ‘abaqus job=job-name oldjob=oldjob-name user=umat.f’ when a UMAT is used in Step 1.
- **Step 4:** output $\mathbf{P}(\mathbf{F}_{kl}^{(\alpha)})$ corresponding to $\mathbf{F}_{kl}^{(\alpha)}$ ($k, l = 1, 2, 3$) and construct the different columns of $\mathbf{C}^{(PK1)}$ by substituting $\mathbf{P}(\mathbf{F})$, computed in Step 1, and $\mathbf{P}(\mathbf{F}_{kl}^{(\alpha)})$ into the differential rule of Eq. (1.34).

We have developed a set of Python codes to automatically perform Steps 2→4. Our codes are devoted to managing the execution of the general and perturbed steps as well as the numerical construction of $\mathbf{C}^{(PK1)}$.

1.4.2. Condensation technique

1.4.2.1. Numerical concept

This technique is based on a condensation procedure of the global stiffness matrix \mathbf{K} introduced in Eq. (1.10). As previously explained in Section 1.2, when the ABAQUS/Standard built-in material models are used to describe the microscopic behavior, the material part \mathbf{K}_M of the stiffness matrix is constructed on the basis of the elastic tangent modulus. In this case, the condensation technique only gives the elastic macroscopic tangent modulus whether the mechanical behavior is elastic or inelastic. To avoid this problem, a UMAT should be used to implement the constitutive equations at the microscopic scale.

To apply the condensation technique, the nodes of the unit cell mesh shall be partitioned into two sets: set \mathcal{A} and set \mathcal{B} composed by the nodes in the interior and on the boundary of the unit cell, respectively. Let $N_{\mathcal{A}}$ and $N_{\mathcal{B}}$ denote the number of nodes of sets \mathcal{A} and \mathcal{B} , respectively. Following this partition, let us introduce the three link-topology matrices $\mathbb{D}_q \in \mathcal{R}^9 \times \mathcal{R}^3$, $\mathbb{Q}_q \in \mathcal{R}^9 \times \mathcal{R}^3$ and $\mathbb{H}_q \in \mathcal{R}^3 \times \mathcal{R}^{3N_{\mathcal{B}}}$ defined in the subsequent developments. The use of these matrices enables to simplify the algorithmic treatment and implementation of the condensation technique.

The topology matrix \mathbb{D}_q , associated with node q that belongs to the boundary of the unit cell, consists of the components x_{q01} , x_{q02} and x_{q03} of the initial coordinate vector \mathbf{x}_{q0} of node q as follows:

$$\forall q = 1, \dots, N_B : \quad \mathbb{D}_q = \begin{bmatrix} x_{q01} & 0 & 0 \\ 0 & x_{q02} & 0 \\ 0 & 0 & x_{q03} \\ x_{q02} & 0 & 0 \\ 0 & x_{q03} & 0 \\ x_{q03} & 0 & 0 \\ 0 & x_{q01} & 0 \\ 0 & 0 & x_{q02} \\ 0 & 0 & x_{q01} \end{bmatrix}. \quad (1.37)$$

Matrix \mathbb{D}_q is introduced in order to rewrite Eq. (1.30) in a matrix form that is more suitable for algorithmic implementation:

$$\forall q = 1, \dots, N_p : \quad \mathbf{x}_{q^+} - \mathbf{x}_{q^-} = (\mathbb{D}_{q^+}^T - \mathbb{D}_{q^-}^T) \cdot \mathbf{F} := \mathbb{Q}_q^T \cdot \mathbf{F}, \quad (1.38)$$

with N_p being the total number of node pairs.

As to matrix \mathbb{H}_q , it is built to link the current coordinate vector of the nodes on the boundary of the unit cell \mathbf{x}_b to the current coordinate vector $\mathbf{x}_q = \mathbf{x}_{q^+} - \mathbf{x}_{q^-}$ of node pair q :

$$\forall q = 1, \dots, N_p : \quad \mathbf{x}_q = \mathbb{H}_q \cdot \mathbf{x}_b. \quad (1.39)$$

The components of matrix \mathbb{H}_q take one of the following values: 0, -1 or 1.

Using matrices \mathbb{H}_q and \mathbb{Q}_q , Eq. (1.38) can be re-expressed in a more compact form:

$$\forall q = 1, \dots, N_p : \quad \mathbb{H}_q \cdot \mathbf{x}_b = \mathbb{Q}_q^T \cdot \mathbf{F}. \quad (1.40)$$

Thus, all the periodic constraints of the unit cell can be assembled in the global notation:

$$\mathbb{H} \cdot \mathbf{x}_b = \mathbb{Q}^T \cdot \mathbf{F}, \quad (1.41)$$

where global matrices \mathbb{H} and \mathbb{Q} are constructed by concatenation of their nodal counterparts \mathbb{H}_q and \mathbb{Q}_q ($1 \leq q \leq N_p$):

$$\mathbb{H} := \begin{bmatrix} \mathbb{H}_1 \\ \vdots \\ \mathbb{H}_q \\ \vdots \\ \mathbb{H}_{N_p} \end{bmatrix}; \quad \mathbb{Q}^T := \begin{bmatrix} \mathbb{Q}_1^T \\ \vdots \\ \mathbb{Q}_q^T \\ \vdots \\ \mathbb{Q}_{N_p}^T \end{bmatrix}. \quad (1.42)$$

On the other hand, following the partition of the whole node set into subsets \mathcal{A} and \mathcal{B} , Eq. (1.10) can be restated in the following form (after permutation of lines and columns of matrix \mathbf{K} and the corresponding components of vectors $\dot{\mathbf{q}}$ and $\dot{\mathbf{r}}$):

$$\begin{bmatrix} \mathbf{K}_{\mathcal{A}\mathcal{A}} & \mathbf{K}_{\mathcal{A}\mathcal{B}} \\ \mathbf{K}_{\mathcal{B}\mathcal{A}} & \mathbf{K}_{\mathcal{B}\mathcal{B}} \end{bmatrix} \cdot \begin{Bmatrix} \dot{\mathbf{q}}_{\mathcal{A}} \\ \dot{\mathbf{q}}_{\mathcal{B}} \end{Bmatrix} = \begin{Bmatrix} \dot{\mathbf{r}}_{\mathcal{A}} \\ \dot{\mathbf{r}}_{\mathcal{B}} \end{Bmatrix}. \quad (1.43)$$

As a consequence of the microscopic equilibrium equation (1.23), the internal force vector $\dot{\mathbf{r}}_{\mathcal{A}}$ is equal to $\mathbf{0}$ at the convergence of the FE computations. Hence, Eq. (1.43) becomes:

$$\begin{bmatrix} \mathbf{K}_{\mathcal{A}\mathcal{A}} & \mathbf{K}_{\mathcal{A}\mathcal{B}} \\ \mathbf{K}_{\mathcal{B}\mathcal{A}} & \mathbf{K}_{\mathcal{B}\mathcal{B}} \end{bmatrix} \cdot \begin{Bmatrix} \dot{\mathbf{q}}_{\mathcal{A}} \\ \dot{\mathbf{q}}_{\mathcal{B}} \end{Bmatrix} = \begin{Bmatrix} \mathbf{0} \\ \dot{\mathbf{r}}_{\mathcal{B}} \end{Bmatrix}. \quad (1.44)$$

The elimination of $\dot{\mathbf{q}}_{\mathcal{A}}$ from Eq. (1.44) allows deriving the condensed (or reduced) stiffness matrix $\tilde{\mathbf{K}}_{\mathcal{B}\mathcal{B}}$ relating the boundary displacement rate $\dot{\mathbf{q}}_{\mathcal{B}}$ to $\dot{\mathbf{r}}_{\mathcal{B}}$:

$$\tilde{\mathbf{K}}_{\mathcal{B}\mathcal{B}} \cdot \dot{\mathbf{q}}_{\mathcal{B}} = \dot{\mathbf{r}}_{\mathcal{B}} \quad \text{with} \quad \tilde{\mathbf{K}}_{\mathcal{B}\mathcal{B}} = \mathbf{K}_{\mathcal{B}\mathcal{B}} - \mathbf{K}_{\mathcal{B}\mathcal{A}} \cdot \mathbf{K}_{\mathcal{A}\mathcal{A}}^{-1} \cdot \mathbf{K}_{\mathcal{A}\mathcal{B}}. \quad (1.45)$$

At the convergence of incremental analysis, the macroscopic tangent modulus $\mathbf{C}^{(PK1)}$ is computed in terms of the condensed stiffness matrix $\tilde{\mathbf{K}}_{\mathcal{B}\mathcal{B}}$, matrices \mathbb{H} and \mathbb{Q} as follows (Miehe, 2003; Geers et al., 2017):

$$\mathbf{C}^{(PK1)} = \frac{1}{|\mathcal{V}_0|} \mathbb{Q} \cdot \left[\mathbb{H} \cdot \tilde{\mathbf{K}}_{\mathcal{B}\mathcal{B}}^{-1} \cdot \mathbb{H}^T \right]^{-1} \cdot \mathbb{Q}^T. \quad (1.46)$$

Considering expression (1.45) of $\tilde{\mathbf{K}}_{\mathcal{B}\mathcal{B}}$, the macroscopic tangent modulus $\mathbf{C}^{(PK1)}$ can be expressed as:

$$\mathbf{C}^{(PK1)} = \frac{1}{|\mathcal{V}_0|} \mathbb{Q} \cdot \left[\mathbb{H} \cdot \left(\mathbf{K}_{\mathcal{B}\mathcal{B}} - \mathbf{K}_{\mathcal{B}\mathcal{A}} \cdot \mathbf{K}_{\mathcal{A}\mathcal{A}}^{-1} \cdot \mathbf{K}_{\mathcal{A}\mathcal{B}} \right)^{-1} \cdot \mathbb{H}^T \right]^{-1} \cdot \mathbb{Q}^T. \quad (1.47)$$

For sake of brevity, only the final result of the condensation technique is given in Eq. (1.47). The interested readers may refer to references (Miehe, 2003) and (Geers et al., 2017) for further details on how Eq. (1.47) is obtained. Analogous developments will be carried out in Section 1.5 to determine the macroscopic tangent modulus $\mathbf{C}^{(PK1)}$ by the condensation method for the particular case of symmetric problems.

1.4.2.2. Practical implementation

As presented in Section 1.4.2.1, the macroscopic modulus $\mathbf{C}^{(PK1)}$ is obtained by a condensation procedure of the global stiffness matrix \mathbf{K} , which is assembled from the elementary stiffness matrices \mathbf{K}_{el} . The requested option to output the elementary stiffness matrices is ‘*Element Matrix Output’, which needs to be added in the input file. To illustrate the operational aspects, a brief example of an input file is provided in Appendix A. After achieving the finite element computation, the elementary

stiffness matrices will be stored in an external file with ‘.mtx’ extension (e.g. ‘myMatrix.mtx’ as in the example of Appendix A). This file is the input of the Python codes developed to assemble and handle the global stiffness matrix \mathbf{K} . Recalling that all the nodes of the unit cell mesh are grouped into two sets \mathcal{A} and \mathcal{B} ; hence, a node q belongs to set \mathcal{B} if at least one of the following conditions hold:

$$x_{q01} = -\lambda_0 / 2 \text{ or } \lambda_0 / 2 ; \quad x_{q02} = -\lambda_0 / 2 \text{ or } \lambda_0 / 2 ; \quad x_{q03} = -\lambda_0 / 2 \text{ or } \lambda_0 / 2, \quad (1.48)$$

otherwise, it belongs to set \mathcal{A} .

In order to construct topology matrices \mathbb{Q} and \mathbb{H} , the set of node pairs as well as the corresponding initial coordinates need to be identified. As illustrated in Fig. 1.3, nodes i and j make up a node pair in the Z -direction.

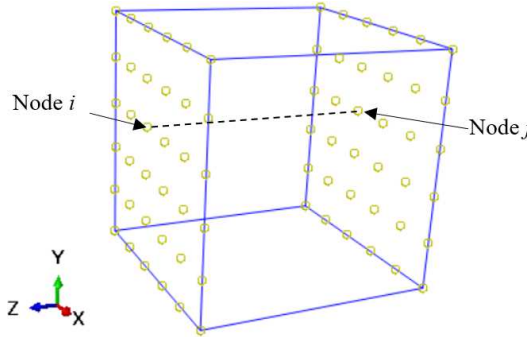


Fig. 1.3. Node pairs in Z -direction.

To identify all the node pairs in node set \mathcal{B} , the following algorithm is developed and implemented into the Python code.

Nodes i and j represent a node pair in X -direction, if:

$$x_{i01} - x_{j01} = \pm \lambda_0 \text{ and } x_{i02} = x_{j02} \text{ and } x_{i03} = x_{j03}.$$

Nodes i and j represent a node pair in Y -direction, if:

$$x_{i02} - x_{j02} = \pm \lambda_0 \text{ and } x_{i01} = x_{j01} \text{ and } x_{i03} = x_{j03}.$$

Nodes i and j represent a node pair in Z -direction, if:

$$x_{i03} - x_{j03} = \pm \lambda_0 \text{ and } x_{i01} = x_{j01} \text{ and } x_{i02} = x_{j02}.$$

The components of matrix $\mathbb{H} \in \mathcal{R}^{3N_p} \times \mathcal{R}^{3N_B}$ take one of three possible values: 0, -1 or 1. These components can be determined as follows, once all the node pairs detected:

If Nodes i and j form a node pair (with $i < j$), the distribution of values 1 and -1 in \mathbb{H} can be summarized as:

$$\begin{aligned} \mathbb{H}_{3i-2,3i-2} &= 1 & \mathbb{H}_{3i-2,3j-2} &= -1, \\ \mathbb{H}_{3i-1,3i-1} &= 1 & \mathbb{H}_{3i-1,3j-1} &= -1, \\ \mathbb{H}_{3i,3i} &= 1 & \mathbb{H}_{3i,3j} &= -1. \end{aligned} \quad (1.49)$$

The other components of matrix \mathbb{H} , not defined by Eq. (1.49), are set to 0.

Matrix $\mathbb{D} \in \mathcal{R}^9 \times \mathcal{R}^{3N_B}$ is assembled from matrices $\mathbb{D}_q \in \mathcal{R}^9 \times \mathcal{R}^3$, defined in Eq. (1.37), as follows:

$$\mathbb{D} = \begin{bmatrix} & \mathbb{D}_i & & \mathbb{D}_j & \\ & \begin{array}{|ccc|} \hline & x_{i01} & 0 & 0 \\ & 0 & x_{i02} & 0 \\ & 0 & 0 & x_{i03} \\ & x_{i02} & 0 & 0 \\ & 0 & x_{i03} & 0 \\ & x_{i03} & 0 & 0 \\ & 0 & x_{i01} & 0 \\ & 0 & 0 & x_{i02} \\ & 0 & 0 & x_{i01} \\ \hline \end{array} & \cdots & \begin{array}{|ccc|} \hline & x_{j01} & 0 & 0 \\ & 0 & x_{j02} & 0 \\ & 0 & 0 & x_{j03} \\ & x_{j02} & 0 & 0 \\ & 0 & x_{j03} & 0 \\ & x_{j03} & 0 & 0 \\ & 0 & x_{j01} & 0 \\ & 0 & 0 & x_{j02} \\ & 0 & 0 & x_{j01} \\ \hline \end{array} & \cdots \end{bmatrix}. \quad (1.50)$$

Once matrix \mathbb{D} constructed, matrix \mathbb{Q} can be determined by the following matrix multiplication:

$$\mathbb{Q} = \mathbb{D} \cdot \mathbb{H}^T. \quad (1.51)$$

With the labels of nodes belonging to sets \mathcal{A} and \mathcal{B} , one can easily extract the four submatrices $\mathbf{K}_{\mathcal{AA}}$, $\mathbf{K}_{\mathcal{AB}}$, $\mathbf{K}_{\mathcal{BA}}$ and $\mathbf{K}_{\mathcal{BB}}$ from the global matrix \mathbf{K} , as stated in Eq. (1.43). Thus far, all the ingredients needed to compute $\mathbf{C}^{(PK1)}$ are prepared.

Box 2. Main steps for the implementation of the condensation technique.

The main steps for the implementation of the condensation technique are summarized as follows:

- **Step 1:** add the option ‘*Element Matrix Output’ in the input file; run the finite element computation with a user subroutine UMAT, the elementary stiffness matrices \mathbf{K}_{el} will be outputted in a ‘.mtx’ file.
- **Step 2:** assemble the global stiffness matrix \mathbf{K} from elementary stiffness matrices stored in the ‘.mtx’ file by using the connectivity of the different nodes of the elements; partition \mathbf{K} into four submatrices $\mathbf{K}_{\mathcal{AA}}$, $\mathbf{K}_{\mathcal{AB}}$, $\mathbf{K}_{\mathcal{BA}}$ and $\mathbf{K}_{\mathcal{BB}}$, after permutation of its lines and columns as stated in Eq. (1.43).
- **Step 3:** compute the condensed matrix $\tilde{\mathbf{K}}_{\mathcal{BB}}$ from submatrices $\mathbf{K}_{\mathcal{AA}}$, $\mathbf{K}_{\mathcal{AB}}$, $\mathbf{K}_{\mathcal{BA}}$ and $\mathbf{K}_{\mathcal{BB}}$ on the basis of Eq. (1.45).
- **Step 4:** construct matrices \mathbb{H} and \mathbb{Q} by using Eqs. (1.49) and (1.51), respectively.
- **Step 5:** compute the macroscopic tangent modulus $\mathbf{C}^{(PK1)}$ by using Eq. (1.47).

We have developed a set of Python scripts to automatically manage Steps 2→5. To improve the efficiency of the condensation method, the developed scripts are parallelized with multiple processors (see Appendix B for more details). The execution of Step 5 inflicts high CPU and memory costs. These costs are mainly due to the double matrix-inversion required in Eq. (1.47). To efficiently optimize this execution, these inversion operations are performed by using the functions ‘linalg.solve’ and ‘linalg.pinvh’ of the NumPy library.

1.4.3. Fluctuation technique

1.4.3.1. Numerical concept

Considering Eqs. (1.26) and (1.27), the following condition should be fulfilled at the convergence of the finite element iterations:

$$G := \int_{\mathcal{V}_0} \left[\frac{\partial \delta \mathbf{v}_{per}}{\partial \mathbf{x}_0} : \dot{\mathbf{p}} \right] d\mathcal{V}_0 = 0. \quad (1.52)$$

The linearization of Eq. (1.52), classically used in finite element computations, takes the form:

$$G + \mathcal{D}G = 0, \quad (1.53)$$

where $\mathcal{D}\bullet$ is the iteration of field \bullet (in the finite element sense). Higher-order terms are neglected in the linearized form given by Eq. (1.53).

The linearized form (1.53) requires that $G \rightarrow 0$ and $\mathcal{D}G \rightarrow 0$ at the convergence of the finite element computation. Hence, the following iterative form can be derived from Eq. (1.52):

$$\mathcal{D}G = \int_{\mathcal{V}_0} \left[\frac{\partial \delta \mathbf{v}_{per}}{\partial \mathbf{x}_0} : \mathbf{c}^{(PK1)} : \left(\mathcal{D}\dot{\mathbf{F}} + \mathcal{D} \frac{\partial \mathbf{v}_{per}}{\partial \mathbf{x}_0} \right) \right] d\mathcal{V}_0 = 0. \quad (1.54)$$

After finite element discretization, the periodic velocity \mathbf{v}_{per} can be obtained from the interpolation rule (similar to the one used in Eq. (1.8)):

$$\mathbf{v}_{per} = \mathbf{N} \cdot \dot{\mathbf{q}}_{per}. \quad (1.55)$$

The substitution of Eq. (1.55) into Eq. (1.54) leads to the following linear algebraic system:

$$\mathbf{K} \cdot \mathcal{D}\dot{\mathbf{q}}_{per} = -\hat{\mathbf{K}} \cdot \mathcal{D}\dot{\mathbf{F}}, \quad (1.56)$$

where the global stiffness matrix \mathbf{K} and a fluctuation matrix $\hat{\mathbf{K}}$ are defined as:

$$\mathbf{K} = \bigcup_{el=1}^n \int_{\mathcal{V}_0^{el}} \mathbf{B}^T \cdot \mathbf{c}^{(PK1)} \cdot \mathbf{B} d\mathcal{V}_0^{el} \quad ; \quad \hat{\mathbf{K}} = \bigcup_{el=1}^n \int_{\mathcal{V}_0^{el}} \mathbf{B}^T \cdot \mathbf{c}^{(PK1)} d\mathcal{V}_0^{el}, \quad (1.57)$$

where $\bigcup_{el=1}^n$ denotes the finite element assembly operator when the unit cell is discretized by n finite elements el . It is worth noting that the global stiffness matrix \mathbf{K} defined by Eq. (1.57)₁ is exactly the same as the one introduced in Eq. (1.10) and equal to $[\mathbf{K}_M + \mathbf{K}_{GNL}]$ (as long as the relations between the microscopic tangent moduli $\mathbf{c}^{(0)}$, $\mathbf{c}^{(2)}$, $\mathbf{c}^{(PK1)}$ and $\mathbf{c}^{(PK2)}$ are correctly defined).

Vector $\mathcal{D}\dot{\mathbf{q}}_{per}$ can be obtained by solving Eq. (1.56):

$$\mathcal{D}\dot{\mathbf{q}}_{per} = -\mathbf{K}^{-1} \cdot \hat{\mathbf{K}} \cdot \mathcal{D}\dot{\mathbf{F}}, \quad (1.58)$$

and then iteration $\mathcal{D}\dot{\mathbf{f}}_{per}$ can be obtained from Eq. (1.58) by:

$$\mathcal{D}\dot{\mathbf{f}}_{per} = \mathbf{B} \cdot \mathcal{D}\dot{\mathbf{q}}_{per} = -\mathbf{B} \cdot \mathbf{K}^{-1} \cdot \hat{\mathbf{K}} \cdot \mathcal{D}\dot{\mathbf{F}}. \quad (1.59)$$

On the other hand, we have the following relation:

$$\mathcal{D}\dot{\mathbf{P}} = \frac{1}{|\mathcal{V}_0|} \int_{\mathcal{V}_0} \mathcal{D}\dot{\mathbf{p}} d\mathcal{V}_0 = \frac{1}{|\mathcal{V}_0|} \int_{\mathcal{V}_0} \mathbf{c}^{(PK1)} : (\mathcal{D}\dot{\mathbf{F}} + \mathcal{D}\dot{\mathbf{f}}_{per}) d\mathcal{V}_0. \quad (1.60)$$

The combination of Eqs. (1.59) and (1.60) yields:

$$\mathcal{D}\dot{\mathbf{P}} = \frac{1}{|\mathcal{V}_0|} \int_{\mathcal{V}_0} \mathcal{D}\dot{\mathbf{p}} d\mathcal{V}_0 = \frac{1}{|\mathcal{V}_0|} \int_{\mathcal{V}_0} \mathbf{c}^{(PK1)} : (\mathcal{D}\dot{\mathbf{F}} - \mathbf{B} \cdot \mathbf{K}^{-1} \cdot \hat{\mathbf{K}} \cdot \mathcal{D}\dot{\mathbf{F}}) d\mathcal{V}_0. \quad (1.61)$$

As iteration $\mathcal{D}\dot{\mathbf{F}}$ is homogeneous over the volume \mathcal{V}_0 of the unit cell, Eq. (1.61) can be reformulated as:

$$\mathcal{D}\dot{\mathbf{P}} = \frac{1}{|\mathcal{V}_0|} \int_{\mathcal{V}_0} \mathcal{D}\dot{\mathbf{p}} d\mathcal{V}_0 = \frac{1}{|\mathcal{V}_0|} \left(\int_{\mathcal{V}_0} \mathbf{c}^{(PK1)} d\mathcal{V}_0 - \hat{\mathbf{K}}^T \cdot \mathbf{K}^{-1} \cdot \hat{\mathbf{K}} \right) : \mathcal{D}\dot{\mathbf{F}}. \quad (1.62)$$

By comparing Eqs. (1.33) and (1.62), one can easily deduce that:

$$\mathbf{C}^{(PK1)} = \frac{1}{|\mathcal{V}_0|} \left(\int_{\mathcal{V}_0} \mathbf{c}^{(PK1)} d\mathcal{V}_0 - \hat{\mathbf{K}}^T \cdot \mathbf{K}^{-1} \cdot \hat{\mathbf{K}} \right). \quad (1.63)$$

1.4.3.2. Practical implementation

As stated by Eq. (1.63), the macroscopic tangent modulus $\mathbf{C}^{(PK1)}$ consists of two main parts: the volume average of the microscopic moduli $\mathbf{c}^{(PK1)}$ and a fluctuation part dependent on the global stiffness matrix \mathbf{K} and on a global fluctuation matrix $\hat{\mathbf{K}}$. Global matrices \mathbf{K} and $\hat{\mathbf{K}}$ are obtained from their elementary counterparts \mathbf{K}_{el} and $\hat{\mathbf{K}}_{el}$ by the assembly rules given by Eq. (1.57). Elementary matrices \mathbf{K}_{el} and $\hat{\mathbf{K}}_{el}$ are dependent on $\mathbf{c}^{(PK1)}$. Hence, to ensure the accurate computation of the macroscopic tangent modulus $\mathbf{C}^{(PK1)}$, the microscopic tangent moduli $\mathbf{c}^{(PK1)}$ should be correctly defined and implemented. Furthermore, to determine the different ingredients required for the computation of $\mathbf{C}^{(PK1)}$ by the fluctuation technique, a user element (UEL) subroutine needs to be used. To achieve this task, we have used the UEL developed in [Salahouelhadj et al. \(2012\)](#), after some modifications and additions. Indeed, the virtual work principle has been slightly modified to consider the Jaumann derivative of the Kirchhoff stress instead of the Truesdell derivative used in the initial version. After these modifications, the elementary stiffness matrix \mathbf{K}_{el} has been correctly computed in the UEL by adding the contribution of the geometric nonlinearities \mathbf{K}_{GNLel} (see Eq. (1.9)₂) to the contribution due to material behavior $\mathbf{K}_{M el}$ (see Eq. (1.9)₁). As to $\mathbf{c}^{(PK1)}$, which is associated with each integration point, it is determined from the jacobian matrix **DDSDDE** (an output of the corresponding UMAT) by using Eqs. (1.7), (1.16) and (1.17). Once matrices $\mathbf{c}^{(PK1)}$ are determined for all the integration points of the element, the elementary

contribution to the volume average of the microscopic moduli $\int_{\mathcal{V}_0^{el}} \mathbf{c}^{(PK1)} d\mathcal{V}_0^{el}$ can be determined by an easy integration operation, and the elementary stiffness matrix \mathbf{K}_{el} and fluctuation matrix $\hat{\mathbf{K}}_{el}$ can be computed by the following relations:

$$\mathbf{K}_{el} = \int_{\mathcal{V}_0^{el}} \mathbf{B}^T \cdot \mathbf{c}^{(PK1)} \cdot \mathbf{B} d\mathcal{V}_0^{el} ; \quad \hat{\mathbf{K}}_{el} = \int_{\mathcal{V}_0^{el}} \mathbf{B}^T \cdot \mathbf{c}^{(PK1)} d\mathcal{V}_0^{el}. \quad (1.64)$$

The different elementary contributions should be outputted and stored in separate files.

Box 3. Main steps for the implementation of the fluctuation technique.

The main steps for the implementation of the fluctuation technique are summarized as follows:

- **Step 1:** compute the microscopic tangent moduli $\mathbf{c}^{(PK1)}$ from jacobian matrix **DDSDDE** by using Eqs. (1.7), (1.16) and (1.17).
- **Step 2:** compute the elementary contributions (namely, \mathbf{K}_{el} , $\hat{\mathbf{K}}_{el}$ and $\int_{\mathcal{V}_0^{el}} \mathbf{c}^{(PK1)} d\mathcal{V}_0^{el}$) and store them in external files.
- **Step 3:** read the external files and use the connectivity of the different nodes to assemble the various elementary contributions and to obtain the global counterparts.
- **Step 4:** once the global counterparts determined, the macroscopic tangent modulus $\mathbf{C}^{(PK1)}$ can be easily computed by Eq. (1.63).

A set of Python codes has been developed to perform Steps 3→4. The algorithm of the codes can be found in Appendix B.

1.5. Extension to symmetric microstructures

In some applications, the studied heterogeneous media are made of unit cells exhibiting symmetry properties (composite materials, porous media...). Hence, it is essential to examine whether these symmetry properties can be efficiently exploited to speed up the computation of the overall properties of heterogeneous media. A heterogeneous unit cell has symmetry properties if the geometric distribution of the different phases is symmetric (see Fig. 1.4) and the behavior of each phase exhibits material symmetries (isotropic or orthotropic). Without loss of generality, we consider a 3D unit cell occupying the initial domain $\mathcal{V}_0 = [-\lambda_0 / 2, \lambda_0 / 2] \times [-\lambda_0 / 2, \lambda_0 / 2] \times [-\lambda_0 / 2, \lambda_0 / 2]$. This unit cell is assumed to be symmetric about three planes of symmetry ($x_{01} = 0$, $x_{02} = 0$ and $x_{03} = 0$), as displayed in Fig. 1.4. In this case, the study of one eighth of the unit cell, occupying the initial domain $\mathcal{V}_0 = [0, \lambda_0 / 2] \times [0, \lambda_0 / 2] \times [0, \lambda_0 / 2]$, is sufficient to determine the mechanical response of the full unit cell only if the boundary conditions on the planes of symmetry ($x_{01} = 0$, $x_{02} = 0$ and $x_{03} = 0$) and on the outer surfaces ($x_{01} = \lambda_0 / 2$, $x_{02} = \lambda_0 / 2$ and $x_{03} = \lambda_0 / 2$) are correctly defined. Otherwise, the

results of such analyses could mislead. The use of one eighth of the unit cell (shortly called RUC, as reduced unit cell), instead of the full one (denoted as FUC), allows dividing the number of mesh elements by 8 (for the same computation accuracy), thus considerably reducing the CPU time required for the computation of the macroscopic tangent modulus. The current section is focalized on the theoretical extension of the perturbation and condensation techniques for the determination of the overall moduli of RUCs. The practical aspects related to the implementation of these extended techniques in this particular case are quite similar to those developed for the general case (Sections 1.4.1.2 and 1.4.2.2). These practical aspects are omitted for the sake of brevity.

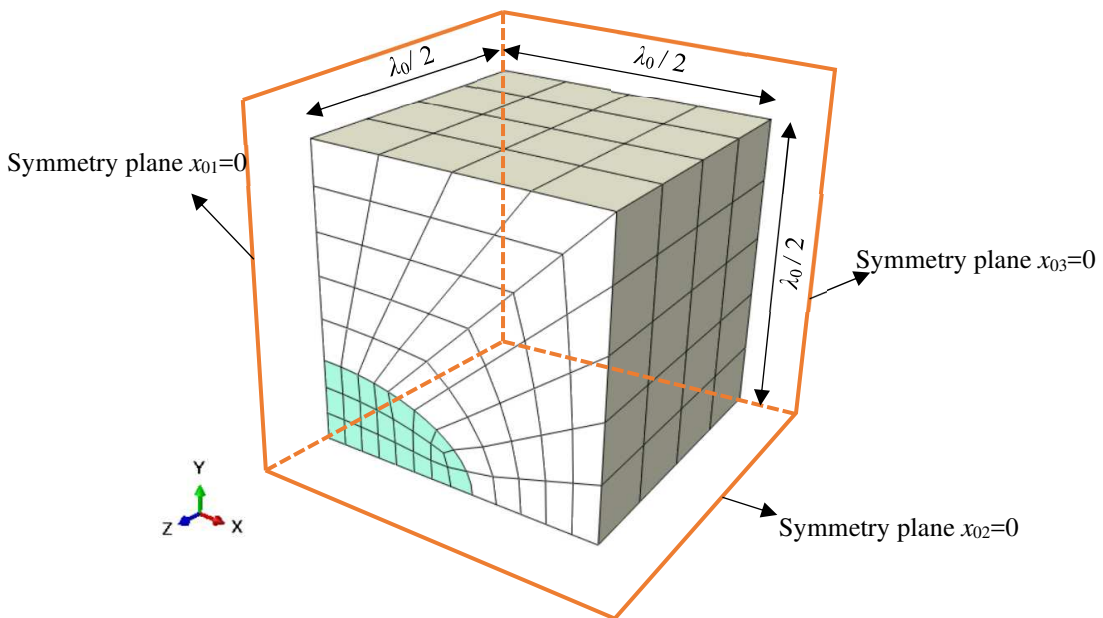


Fig. 1.4. RUC occupying the initial domain $\mathcal{V}_0 = [0, \lambda_0 / 2] \times [0, \lambda_0 / 2] \times [0, \lambda_0 / 2]$ and its corresponding FUC assumed to be symmetric about three planes of symmetry ($x_{01} = 0$, $x_{02} = 0$ and $x_{03} = 0$).

1.5.1. Perturbation technique

The suitable boundary conditions to be applied on the RUC to ensure the same mechanical response as that of the whole unit cell have been initially established by Léné (1984) for media undergoing small strain. The developments achieved by Léné (1984) are extended in this chapter to the finite strain framework, and these extensions are used to construct the overall tangent modulus by the perturbation technique. The prescribed boundary conditions, under the perturbed steps, are dependent on the applied perturbation. The details are given in Table 1.1 (with α being the magnitude of the perturbation introduced in Section 1.4.1.1). As shown in this table, the boundary conditions applied on the different degree of freedoms (DOFs) are categorized into two main families:

- DOFs subjected to a small linear displacement increment $\Delta u_i = (\Delta \mathbf{F}_{kl}^{(\alpha)} \cdot \mathbf{x}_0)_i$ (where \mathbf{x}_0 is the initial position of the associated node and $(\Delta \mathbf{F}_{kl}^{(\alpha)} \cdot \mathbf{x}_0)_i$ is the i -th component of vector $\Delta \mathbf{F}_{kl}^{(\alpha)} \cdot \mathbf{x}_0$);

- DOFs free from any displacement constraint (Δu_i free). In this case, the associated reaction force is obviously equal to zero.

To better explain these boundary conditions, let us detail them for the perturbation $\Delta \mathbf{F}_{11}^{(\alpha)}$:

- On face $x_{01} = 0$: $\Delta u_1 = (\Delta \mathbf{F}_{11}^{(\alpha)} \cdot \mathbf{x}_0)_1 = 0$, while the other DOFs are free.
- On face $x_{01} = \lambda_0 / 2$: $\Delta u_1 = (\Delta \mathbf{F}_{11}^{(\alpha)} \cdot \mathbf{x}_0)_1 = \alpha \lambda_0 / 2$, while the other DOFs are free.
- On faces $x_{02} = 0$ and $\lambda_0 / 2$: $\Delta u_2 = (\Delta \mathbf{F}_{11}^{(\alpha)} \cdot \mathbf{x}_0)_2 = 0$, while the other DOFs are free.
- On faces $x_{03} = 0$ and $\lambda_0 / 2$: $\Delta u_3 = (\Delta \mathbf{F}_{11}^{(\alpha)} \cdot \mathbf{x}_0)_3 = 0$, while the other DOFs are free.

The perturbed stress tensors $\mathbf{P}(\mathbf{F}_{kl}^{(\alpha)})$, corresponding to the various perturbations $\Delta \mathbf{F}_{kl}^{(\alpha)}$ and required to construct the macroscopic tangent modulus $\mathbf{C}^{(PK1)}$ column by column, are derived from the reaction forces applied on the boundary of the reduced unit cell \mathcal{S}_{r0} :

$$\mathbf{P}(\mathbf{F}_{kl}^{(\alpha)}) = \frac{1}{|\mathcal{V}_{r0}|} \int_{\mathcal{V}_{r0}} \mathbf{p}(\mathbf{F}_{kl}^{(\alpha)}) d\mathcal{V}_{r0} = \frac{1}{|\mathcal{V}_{r0}|} \int_{\mathcal{S}_{r0}} \mathbf{t}_0(\mathbf{F}_{kl}^{(\alpha)}) \otimes \mathbf{x}_0 d\mathcal{S}_{r0}. \quad (1.65)$$

To define the different perturbation steps, the nine restart ‘.inp’ files described in Step 2 of Box 1 need to be modified to integrate the difference in the boundary conditions from one perturbation step to another.

Table 1.1. Boundary conditions applied on the RUC.

Perturbed components	Boundary conditions		
	faces $x_{01} = 0$ and $\lambda_0 / 2$	faces $x_{02} = 0$ and $\lambda_0 / 2$	faces $x_{03} = 0$ and $\lambda_0 / 2$
$kk = 11; 22; 33$	$\Delta u_1 = (\Delta \mathbf{F}_{kk}^{(\alpha)} \cdot \mathbf{x}_0)_1$; Δu_2 free ; Δu_3 free	Δu_1 free ; $\Delta u_2 = (\Delta \mathbf{F}_{kk}^{(\alpha)} \cdot \mathbf{x}_0)_2$; Δu_3 free	Δu_1 free ; Δu_2 free ; $\Delta u_3 = (\Delta \mathbf{F}_{kk}^{(\alpha)} \cdot \mathbf{x}_0)_3$
12	Δu_1 free ; $\Delta u_2 = (\Delta \mathbf{F}_{12}^{(\alpha)} \cdot \mathbf{x}_0)_2$; $\Delta u_3 = (\Delta \mathbf{F}_{12}^{(\alpha)} \cdot \mathbf{x}_0)_3$	$\Delta u_1 = (\Delta \mathbf{F}_{12}^{(\alpha)} \cdot \mathbf{x}_0)_1$; Δu_2 free ; $\Delta u_3 = (\Delta \mathbf{F}_{12}^{(\alpha)} \cdot \mathbf{x}_0)_3$	Δu_1 free ; Δu_2 free ; $\Delta u_3 = (\Delta \mathbf{F}_{12}^{(\alpha)} \cdot \mathbf{x}_0)_3$
21	Δu_1 free ; $\Delta u_2 = (\Delta \mathbf{F}_{21}^{(\alpha)} \cdot \mathbf{x}_0)_2$; $\Delta u_3 = (\Delta \mathbf{F}_{21}^{(\alpha)} \cdot \mathbf{x}_0)_3$	$\Delta u_1 = (\Delta \mathbf{F}_{21}^{(\alpha)} \cdot \mathbf{x}_0)_1$; Δu_2 free ; $\Delta u_3 = (\Delta \mathbf{F}_{21}^{(\alpha)} \cdot \mathbf{x}_0)_3$	Δu_1 free ; Δu_2 free ; $\Delta u_3 = (\Delta \mathbf{F}_{21}^{(\alpha)} \cdot \mathbf{x}_0)_3$
23	$\Delta u_1 = (\Delta \mathbf{F}_{23}^{(\alpha)} \cdot \mathbf{x}_0)_1$; Δu_2 free ; Δu_3 free	$\Delta u_1 = (\Delta \mathbf{F}_{23}^{(\alpha)} \cdot \mathbf{x}_0)_1$; Δu_2 free ; $\Delta u_3 = (\Delta \mathbf{F}_{23}^{(\alpha)} \cdot \mathbf{x}_0)_3$	$\Delta u_1 = (\Delta \mathbf{F}_{23}^{(\alpha)} \cdot \mathbf{x}_0)_1$; $\Delta u_2 = (\Delta \mathbf{F}_{23}^{(\alpha)} \cdot \mathbf{x}_0)_2$; Δu_3 free
32	$\Delta u_1 = (\Delta \mathbf{F}_{32}^{(\alpha)} \cdot \mathbf{x}_0)_1$; Δu_2 free ; Δu_3 free	$\Delta u_1 = (\Delta \mathbf{F}_{32}^{(\alpha)} \cdot \mathbf{x}_0)_1$; Δu_2 free ; $\Delta u_3 = (\Delta \mathbf{F}_{32}^{(\alpha)} \cdot \mathbf{x}_0)_3$	$\Delta u_1 = (\Delta \mathbf{F}_{32}^{(\alpha)} \cdot \mathbf{x}_0)_1$; $\Delta u_2 = (\Delta \mathbf{F}_{32}^{(\alpha)} \cdot \mathbf{x}_0)_2$; Δu_3 free

13	Δu_1 free ; $\Delta u_2 = (\Delta \mathbf{F}_{13}^{(\alpha)} \cdot \mathbf{x}_0)_2$; $\Delta u_3 = (\Delta \mathbf{F}_{13}^{(\alpha)} \cdot \mathbf{x}_0)_3$	Δu_1 free ; $\Delta u_2 = (\Delta \mathbf{F}_{13}^{(\alpha)} \cdot \mathbf{x}_0)_2$; Δu_3 free	$\Delta u_1 = (\Delta \mathbf{F}_{13}^{(\alpha)} \cdot \mathbf{x}_0)_1$; $\Delta u_2 = (\Delta \mathbf{F}_{13}^{(\alpha)} \cdot \mathbf{x}_0)_2$; Δu_3 free
31	Δu_1 free ; $\Delta u_2 = (\Delta \mathbf{F}_{31}^{(\alpha)} \cdot \mathbf{x}_0)_2$; $\Delta u_3 = (\Delta \mathbf{F}_{31}^{(\alpha)} \cdot \mathbf{x}_0)_3$	Δu_1 free ; $\Delta u_2 = (\Delta \mathbf{F}_{31}^{(\alpha)} \cdot \mathbf{x}_0)_2$; Δu_3 free	$\Delta u_1 = (\Delta \mathbf{F}_{31}^{(\alpha)} \cdot \mathbf{x}_0)_1$; $\Delta u_2 = (\Delta \mathbf{F}_{31}^{(\alpha)} \cdot \mathbf{x}_0)_2$; Δu_3 free

1.5.2. Condensation technique

The development of a condensation technique pertaining to unit cells exhibiting symmetry properties is presented hereafter. This development follows the general idea behind the same technique for full unit cells (without symmetry properties), summarized in Section 1.4.2.1, with some main adaptations that are essential to account for the particularities of RUCs. The perturbation technique presented in Section 1.5.1 is of great use to ensure the theoretical extension of the condensation technique. Unlike the original condensation technique, where the different columns of the overall tangent modulus $\mathbf{C}^{(PK1)}$ are simultaneously determined in a single matrix operation, the columns of the tangent modulus corresponding to the RUC are computed separately, through successive iterations. Indeed, the starting point of the original condensation technique consists in the partition of nodes into two different sets \mathcal{A} and \mathcal{B} . The composition of these node sets is independent of the boundary conditions applied on the unit cell. Then, the same sets can be used to compute all the columns of $\mathbf{C}^{(PK1)}$. For the extended condensation technique, the partition of DOF sets depends on the boundary conditions, as shown in Table 1.1. Therefore, it is not possible to simultaneously construct all the columns of $\mathbf{C}^{(PK1)}$ by using the same DOF partition, and thus the computation of the columns of $\mathbf{C}^{(PK1)}$ in successive iterations (one iteration for each column) is unavoidable.

In what follows, we detail how a column of $\mathbf{C}^{(PK1)}$ can be determined, and the same algorithm could be used to compute the other columns.

As a starting point of this algorithm, the DOFs of the nodes of the RUC mesh should be partitioned into two sets:

- set Ψ : the set of DOFs on which the reaction forces are zero. This set includes the DOFs of all the nodes in the interior of the RUC as well as the DOFs of the nodes on the boundary, which are free from any displacement constraint (see Table 1.2 for illustration). Then, set Ψ is defined by the following equation at the convergence:

$$\dot{\mathbf{r}}_\Psi = \mathbf{0}, \quad (1.66)$$

where $\dot{\mathbf{r}}_\Psi$ is the residual rate vector corresponding to DOFs in set Ψ .

- set Ω : the set of DOFs on the boundary of the RUC that are subjected to a linear displacement. Consequently, the vector of displacement rates corresponding to DOFs in Ω , denoted $\dot{\mathbf{q}}_\Omega$, is related to the rate of the macroscopic deformation gradient $\dot{\mathbf{F}}$ by the following matrix form (more suitable for algorithmic treatment):

$$\dot{\mathbf{q}}_\Omega - \mathbb{S}^T \cdot \dot{\mathbf{F}} = \mathbf{0}, \quad (1.67)$$

where the topology matrix \mathbb{S} is constructed in the same manner as matrix \mathbb{D}_q introduced in Eq. (1.37), but with DOFs in set Ω .

The residual rate vector corresponding to DOFs in set Ω , denoted $\dot{\mathbf{r}}_\Omega$, can be related to the rate of the macroscopic Piola–Kirchhoff stress tensor $\dot{\mathbf{P}}$ (see Eq. (1.65) to understand this matrix form):

$$\dot{\mathbf{P}} - \frac{1}{|\mathcal{V}_{r0}|} \mathbb{S} \cdot \dot{\mathbf{r}}_\Omega = \mathbf{0}. \quad (1.68)$$

The partition into sets Ψ and Ω is illustrated in Table 1.2 for the construction of the first and fourth columns of $\mathbf{C}^{(PK1)}$.

Table 1.2. Composition of sets Ψ , Ω required for the computation of the first and fourth columns of $\mathbf{C}^{(PK1)}$.

Column of $\mathbf{C}^{(PK1)}$	Set Ψ	Set Ω
First column	- the DOFs of all the nodes in the interior of the RUC; - the second and the third DOF of nodes belonging to faces $x_{01} = 0$ and $\lambda_0 / 2$; - the first and the third DOF of nodes belonging to faces $x_{02} = 0$ and $\lambda_0 / 2$; - the first and the second DOF of nodes belonging to faces $x_{03} = 0$ and $\lambda_0 / 2$	- the first DOF of nodes belonging to faces $x_{01} = 0$ and $\lambda_0 / 2$; - the second DOF of nodes belonging to faces $x_{02} = 0$ and $\lambda_0 / 2$; - the third DOF of nodes belonging to faces $x_{03} = 0$ and $\lambda_0 / 2$
Fourth column	- the DOFs of all the nodes in the interior of the RUC; - the first DOF of nodes belonging to faces $x_{01} = 0$ and $\lambda_0 / 2$; - the second DOF of nodes belonging to faces $x_{02} = 0$ and $\lambda_0 / 2$; - the first and the second DOF of nodes belonging to faces $x_{03} = 0$ and $\lambda_0 / 2$	- the second and the third DOF of nodes belonging to faces $x_{01} = 0$ and $\lambda_0 / 2$; - the first and the third DOF of nodes belonging to faces $x_{02} = 0$ and $\lambda_0 / 2$; - the third DOF of nodes belonging to faces $x_{03} = 0$ and $\lambda_0 / 2$

Considering this partition rule, the matrix form of the equilibrium equation associated with the RUC can be written in the following form (very similar to Eq. (1.43)):

$$\begin{bmatrix} \mathbf{K}_{\Psi\Psi} & \mathbf{K}_{\Psi\Omega} \\ \mathbf{K}_{\Omega\Psi} & \mathbf{K}_{\Omega\Omega} \end{bmatrix} \begin{bmatrix} \dot{\mathbf{q}}_\Psi \\ \dot{\mathbf{q}}_\Omega \end{bmatrix} = \begin{bmatrix} \dot{\mathbf{r}}_\Psi \\ \dot{\mathbf{r}}_\Omega \end{bmatrix}. \quad (1.69)$$

The linearization of Eqs. (1.66), (1.67) and (1.68), required for finite element iterations, yields:

$$\begin{cases} \dot{\mathbf{r}}_\psi + \mathcal{D}\dot{\mathbf{r}}_\psi = \mathbf{0}; \\ \dot{\mathbf{q}}_\Omega - \mathbb{S}^T \cdot \dot{\mathbf{F}} + \mathcal{D}\dot{\mathbf{q}}_\Omega - \mathbb{S}^T \cdot \mathcal{D}\dot{\mathbf{F}} = \mathbf{0}; \\ \dot{\mathbf{P}} - \frac{1}{|\mathcal{V}_{r0}|} \mathbb{S} \cdot \dot{\mathbf{r}}_\Omega + \mathcal{D}\dot{\mathbf{P}} - \frac{1}{|\mathcal{V}_{r0}|} \mathbb{S} \cdot \mathcal{D}\dot{\mathbf{r}}_\Omega = \mathbf{0}. \end{cases} \quad (1.70)$$

Using Eq. (1.69), equation system (1.70) can be further elaborated:

$$\begin{cases} \dot{\mathbf{r}}_\psi + \mathbf{K}_{\psi\psi} \cdot \mathcal{D}\dot{\mathbf{q}}_\psi + \mathbf{K}_{\psi\Omega} \cdot \mathcal{D}\dot{\mathbf{q}}_\Omega = \mathbf{0}; \\ \dot{\mathbf{q}}_\Omega - \mathbb{S}^T \cdot \dot{\mathbf{F}} + \mathcal{D}\dot{\mathbf{q}}_\Omega - \mathbb{S}^T \cdot \mathcal{D}\dot{\mathbf{F}} = \mathbf{0}; \\ \dot{\mathbf{P}} - \frac{1}{|\mathcal{V}_{r0}|} \mathbb{S} \cdot \dot{\mathbf{r}}_\Omega + \mathcal{D}\dot{\mathbf{P}} - \frac{1}{|\mathcal{V}_{r0}|} \mathbb{S} \cdot (\mathbf{K}_{\Omega\psi} \cdot \mathcal{D}\dot{\mathbf{q}}_\psi + \mathbf{K}_{\Omega\Omega} \cdot \mathcal{D}\dot{\mathbf{q}}_\Omega) = \mathbf{0}. \end{cases} \quad (1.71)$$

Equation (1.71)₁ allows us to express $\mathcal{D}\dot{\mathbf{q}}_\psi$ as:

$$\mathcal{D}\dot{\mathbf{q}}_\psi = -\mathbf{K}_{\psi\psi}^{-1} \cdot (\dot{\mathbf{r}}_\psi + \mathbf{K}_{\psi\Omega} \cdot \mathcal{D}\dot{\mathbf{q}}_\Omega). \quad (1.72)$$

At the equilibrium state, we have $\dot{\mathbf{r}}_\psi = \mathbf{0}$. Therefore, Eq. (1.72) can be reduced to the following form:

$$\mathcal{D}\dot{\mathbf{q}}_\psi = -\mathbf{K}_{\psi\psi}^{-1} \cdot \mathbf{K}_{\psi\Omega} \cdot \mathcal{D}\dot{\mathbf{q}}_\Omega. \quad (1.73)$$

Insertion of Eq. (1.73) into Eqs. (1.71)_{2,3} leads to the reduced equation system:

$$\begin{cases} \dot{\mathbf{q}}_\Omega - \mathbb{S}^T \cdot \dot{\mathbf{F}} + \mathcal{D}\dot{\mathbf{q}}_\Omega - \mathbb{S}^T \cdot \mathcal{D}\dot{\mathbf{F}} = \mathbf{0}; \\ \dot{\mathbf{P}} - \frac{1}{|\mathcal{V}_{r0}|} \mathbb{S} \cdot \dot{\mathbf{r}}_\Omega + \mathcal{D}\dot{\mathbf{P}} - \frac{1}{|\mathcal{V}_{r0}|} \mathbb{S} \cdot (\mathbf{K}_{\Omega\Omega} - \mathbf{K}_{\Omega\psi} \cdot \mathbf{K}_{\psi\psi}^{-1} \cdot \mathbf{K}_{\psi\Omega}) \cdot \mathcal{D}\dot{\mathbf{q}}_\Omega = \mathbf{0}. \end{cases} \quad (1.74)$$

Together with equation system (1.70), the equilibrium state of (1.74) requires:

$$\begin{cases} \mathcal{D}\dot{\mathbf{q}}_\Omega - \mathbb{S}^T \cdot \mathcal{D}\dot{\mathbf{F}} = \mathbf{0}; \\ \mathcal{D}\dot{\mathbf{P}} - \frac{1}{|\mathcal{V}_{r0}|} \mathbb{S} \cdot (\mathbf{K}_{\Omega\Omega} - \mathbf{K}_{\Omega\psi} \cdot \mathbf{K}_{\psi\psi}^{-1} \cdot \mathbf{K}_{\psi\Omega}) \cdot \mathcal{D}\dot{\mathbf{q}}_\Omega = \mathbf{0}. \end{cases} \quad (1.75)$$

The elimination of $\mathcal{D}\dot{\mathbf{q}}_\Omega$ in (1.75) allows us to obtain:

$$\mathcal{D}\dot{\mathbf{P}} - \frac{1}{|\mathcal{V}_{r0}|} \mathbb{S} \cdot (\mathbf{K}_{\Omega\Omega} - \mathbf{K}_{\Omega\psi} \cdot \mathbf{K}_{\psi\psi}^{-1} \cdot \mathbf{K}_{\psi\Omega}) \cdot \mathbb{S}^T \cdot \mathcal{D}\dot{\mathbf{F}} = \mathbf{0}. \quad (1.76)$$

The expression of the overall tangent modulus $\mathbf{C}^{(PK1)}$ can be easily identified from Eq. (1.76):

$$\mathbf{C}^{(PK1)} = \frac{1}{|\mathcal{V}_{r0}|} \mathbb{S} \cdot (\mathbf{K}_{\Omega\Omega} - \mathbf{K}_{\Omega\psi} \cdot \mathbf{K}_{\psi\psi}^{-1} \cdot \mathbf{K}_{\psi\Omega}) \cdot \mathbb{S}^T. \quad (1.77)$$

1.6. Numerical results

1.6.1. Basic validations of the three techniques

To validate the implementation of the three techniques (namely, CT, FT, and PT), the numerical predictions obtained by these techniques are compared with those given by Miehe et al. (2002b).

Consistently, two plane composite microstructures are considered (width/length=1/1). Each microstructure is made of a soft matrix reinforced by a stiff inclusion. The behavior of each phase is assumed to be isotropic linear elastic with the following elasticity parameters:

- Matrix: $E_m = 2081.06 \text{ MPa}$; $\nu_m = 0.3007$.
- Inclusion: $E_i = 10 E_m$; $\nu_i = \nu_m$.

For the first microstructure, the inclusion is a layer centered in the middle of the composite and occupying 1/3 of the total volume (Fig. 1.5). As to the second microstructure, the associated inclusion is centered cylindrical fiber and its volume fraction is equal to 12.56% (Fig. 1.6).

To compute the macroscopic tangent moduli by the different techniques, a plane-strain loading has been applied on the two analyzed microstructures (the same as the one defined in Miehe et al., 2002b). In this case, we report and compare the in-plane components of the macroscopic moduli $\mathbf{C}^{(PK1)}$ stored in matrix \mathbf{Z} :

$$\mathbf{Z} = \begin{bmatrix} C_{1111}^{(PK1)} & C_{1122}^{(PK1)} & 0 \\ C_{2211}^{(PK1)} & C_{2222}^{(PK1)} & 0 \\ 0 & 0 & C_{1212}^{(PK1)} \end{bmatrix}. \quad (1.78)$$

The difference between the results from (Miehe et al., 2002b) and our predictions obtained by the three techniques is quantified by a scalar indicator m defined as:

$$m = \|\mathbf{Z}\| / \|\mathbf{Z}^{Ref}\| = \left(\sum_{i=1}^3 \sum_{j=1}^3 (Z_{ij})^2 \right)^{1/2} / \left(\sum_{i=1}^3 \sum_{j=1}^3 (Z_{ij}^{Ref})^2 \right)^{1/2}, \quad (1.79)$$

where \mathbf{Z}^{Ref} and \mathbf{Z} denote the overall modulus determined in reference (Miehe et al., 2002b) and that computed by our predictions, respectively.

1.6.1.1. Microstructure with centered layer

To investigate the effect of mesh discretization on the prediction of the tangent modulus, this microstructure is discretized by two different meshes: Mesh 1 made of 36 finite elements, as displayed in Fig. 1.5a, and Mesh 2 composed of 144 finite elements, as shown in Fig. 1.5b.

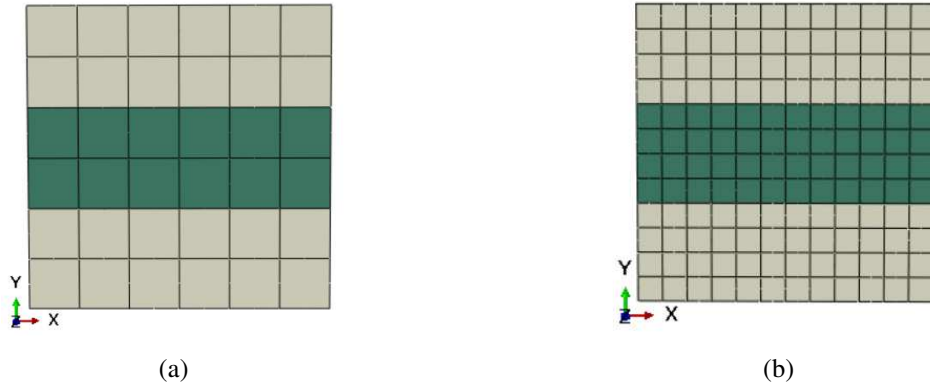


Fig. 1.5. The finite element discretization of microstructure with centered layer: (a) Mesh 1; (b) Mesh 2.

The components of \mathbf{Z} obtained by the different techniques (namely, CT, FT, and PT) with the two meshes (Mesh 1 and Mesh 2) are reported in [Table 1.3](#). For the three techniques, the predictions are almost insensitive to the mesh density, thus confirming the earlier observations made in reference ([Miehe et al., 2002b](#)). Moreover, the three techniques provide the same results with indicator m very close to 1, thus implying that our predictions are very close to those given in [Miehe et al. \(2002b\)](#).

Table 1.3. Components of matrix \mathbf{Z} for the two meshes of the microstructure with centered layer.

Reference (Miehe et al., 2002b)	CT		FT		PT	
	Mesh1	Mesh2	Mesh1	Mesh2	Mesh1	Mesh2
Z_{11}	78682.6	78682.6	78564.6	78564.4	78564.6	78564.4
Z_{22}	4204.0	4204.0	4189.5	4189.5	4189.5	4189.5
Z_{12}	1815.9	1815.9	1801.5	1801.5	1801.5	1801.5
Z_{33}	1194.0	1194.0	1194.0	1194.0	1194.0	1194.0
m	1.000	1.000	0.998	0.998	0.998	0.998

1.6.1.2. Microstructure with centered cylindrical fiber

In this case, the unit cell is discretized by 700 elements ([Fig. 1.6](#)).

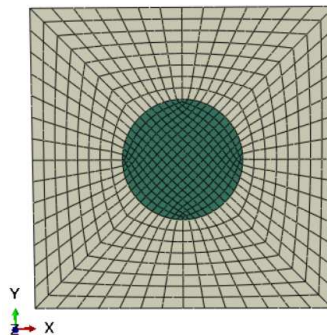


Fig. 1.6. The finite element discretization of microstructure with centered cylindrical fiber.

As reported in [Table 1.4](#), the results obtained by CT, FT, and PT are almost identical and very close to the reference values. These results provide additional validation of our implementations.

Table 1.4. Components of matrix \mathbf{Z} for the microstructure with centered cylindrical fiber.

Reference (Miehe et al., 2002b)	CT	FT	PT
Z_{11}	3413.1	3400.7	3400.7
Z_{22}	3413.1	3400.8	3400.8
Z_{12}	1415.1	1407.2	1407.2
Z_{33}	960.1	958.8	958.9
m	1.000	0.996	0.996

1.6.2. More advanced validations of the three techniques

In the previous section, some basic validations of the three techniques have been conducted by comparing our predictions with the results presented in Miehe et al. (2002b). It appears from this preliminary study that all of the three techniques accurately predict the macroscopic tangent modulus. Thus, the accuracy and reliability of the implementation of the three techniques are partially validated. In this section, attention is focused on evaluating the computational performances of the three techniques, by considering two microstructure examples:

- Microstructure with cubic inclusion: the geometry is characterized by a cube containing a stiff cubic inclusion in the center, which occupies 20 % of the total volume (Fig. 1.7a). This microstructure is discretized by 1000 finite elements.
- Microstructure with elliptical cylindrical fiber: the geometry is characterized by a cube containing a stiff elliptical cylindrical fiber in the center, which occupies 12.6 % of the total volume (Fig. 1.7b). The fiber is aligned in the Z-direction and its cross section is an ellipse with aspect ratio (long axis/short axis) equal to 2. This microstructure is discretized by 2176 finite elements.

For the two cases, the mechanical behavior of the matrix and the inclusion are assumed to be elastoplastic and linear elastic, respectively:

- The matrix elasticity and hardening parameters are:

$$E_m = 210 \text{ GPa} ; \quad \nu_m = 0.3 ; \quad \text{isotropic hardening law : } \sigma_y = 362.99(0.008 + \varepsilon_{eq}^p)^{0.184}.$$

- The inclusion elasticity parameters are:

$$E_i = 10 E_m ; \quad \nu_i = \nu_m.$$

The two microstructures are subjected to the following deformation history:

$$\text{initial state : } \mathbf{F}(0) = \begin{bmatrix} 1 & 0 & 0 \\ 0 & 1 & 0 \\ 0 & 0 & 1 \end{bmatrix} \rightarrow \text{final state : } \mathbf{F}(t_f) = \begin{bmatrix} 1.2 & 0 & 0 \\ 0 & 0.91287 & 0 \\ 0 & 0 & 0.91287 \end{bmatrix}, \quad (1.80)$$

with t_f corresponding to the end of the loading history, and the deformation gradient \mathbf{F} is assumed to evolve linearly between $\mathbf{F}(0)$ and $\mathbf{F}(t_f)$.

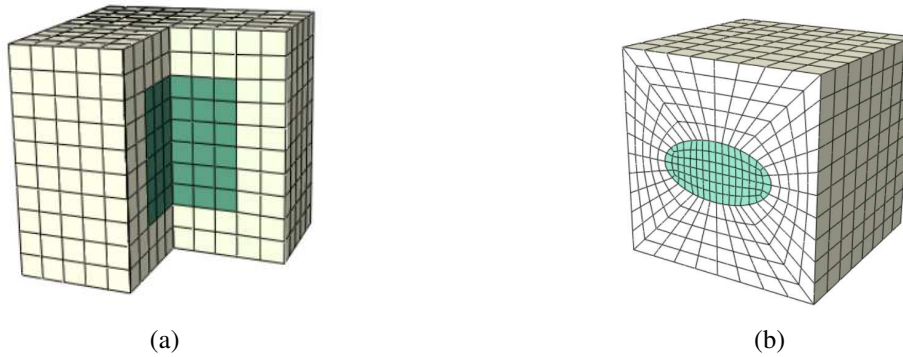


Fig. 1.7. Two typical composites discretized by finite elements: (a) Microstructure with cubic inclusion; (b) Microstructure with elliptical cylindrical fiber.

During the general finite element computations, the external files required to compute the overall tangent moduli are automatically created and filled. Based on these external files, the developed Python scripts are executed. For CT, the required external file is the ‘.mtx’ file, which contains the elementary stiffness matrices \mathbf{K}_{el} at each n converged increments (with n being the record frequency, as shown in Appendix A). For FT, besides this ‘.mtx’ file, two other ‘.txt’ files are required, which contain the micro tangent moduli $\mathbf{c}^{(PK1)}$ for all the integration points and the elementary fluctuation matrices $\hat{\mathbf{K}}_{el}$. For PT, the external files are the database needed to conduct the restart analysis. This data includes the ‘.res’, ‘.mdl’ and ‘.stt’, ‘.prt’, ‘.odb’ files, as well as the ‘.sim’ files. Some practical aspects related to the execution of the Python scripts can be found in Section 1.4 and in the appendices. Note that the disk space allocated for the generated external files and the CPU time spent for the tangent modulus computations increase with the complexity of the studied microstructures. Therefore, the evaluation of the computational efficiency is twofold: the required disk space and CPU time. These computations were made on 8 parallelized cores allocated in cluster computer.

1.6.2.1. Microstructure with a cubic inclusion

The mechanical behavior of the two phases is assumed to be isotropic (for both elasticity and plasticity), and the von Mises yield function is used to compute the equivalent stress from the stress tensor. The evolution of the components $C_{1111}^{(PK1)}$, $C_{2222}^{(PK1)}$, $C_{1122}^{(PK1)}$, and $C_{1212}^{(PK1)}$ obtained by CT, FT, and PT are reported in Fig. 1.8. It is clear from this figure that the three techniques give identical results, thus providing additional validation of our implementation.

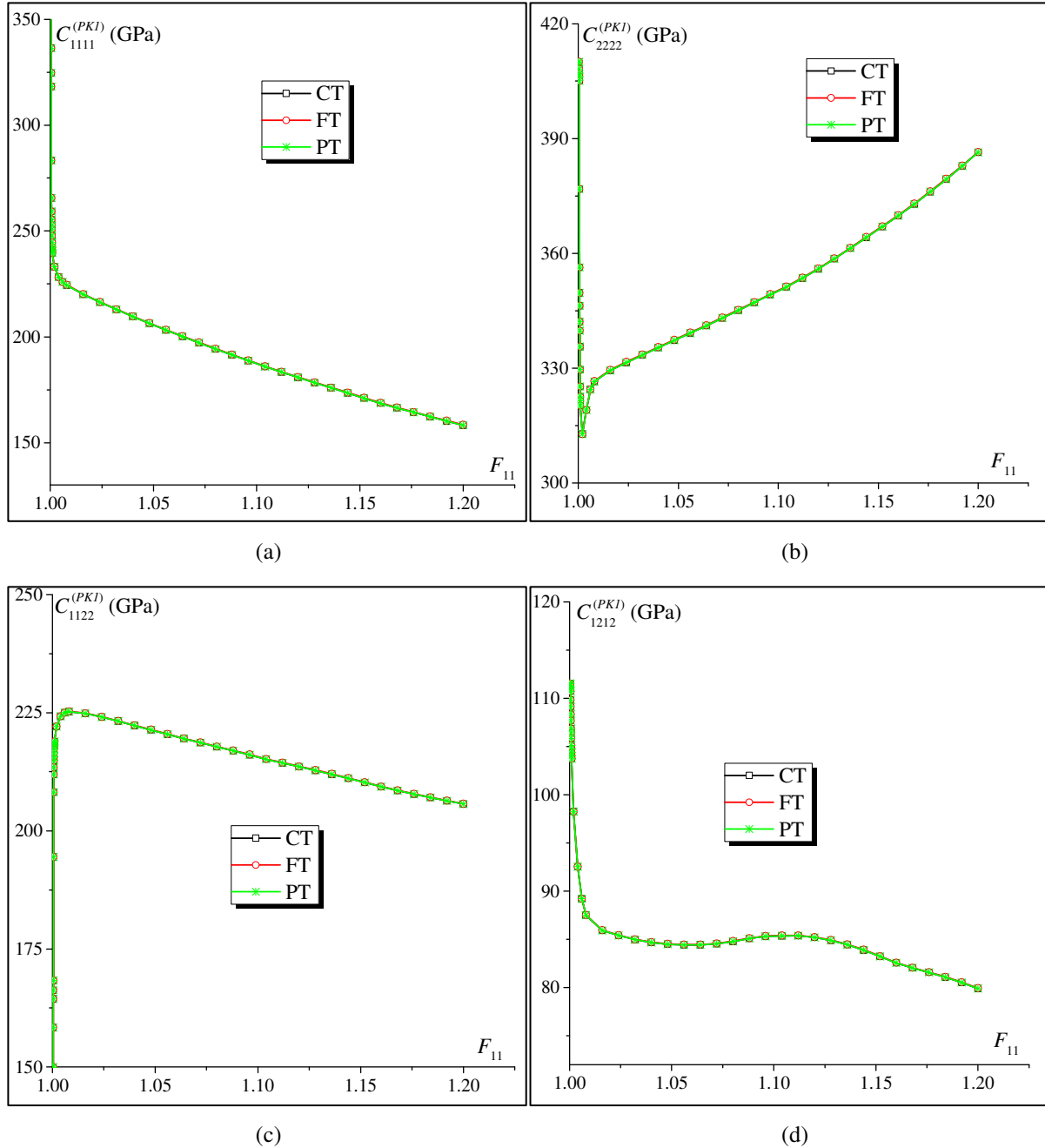


Fig. 1.8. Evolution of the components of modulus $\mathbf{C}^{(PK1)}$ obtained by CT, FT, and PT for microstructure with a cubic inclusion: (a) $C_{1111}^{(PK1)}$; (b) $C_{2222}^{(PK1)}$; (c) $C_{1122}^{(PK1)}$; (d) $C_{1212}^{(PK1)}$.

The overall modulus $\mathbf{C}^{(PK1)}$ is evaluated at each $\Delta t = 0.01t_f$ (see Eq. (1.80)). Then, $\mathbf{C}^{(PK1)}$ is computed 100 times during the loading history. As shown in Table 1.5, PT consumes more disk space and CPU time than CT and FT. This result is expectable considering the fact that ten finite element computations are required when the PT is used, against only a single computation for the other techniques. Despite the fact that the nine finite element steps required to numerically construct the overall tangent modulus by the PT are linear (hence, relatively quick to be run), the CPU time consumed by the computations in this case remains relatively high. Even though there is no much difference between the CPU times consumed

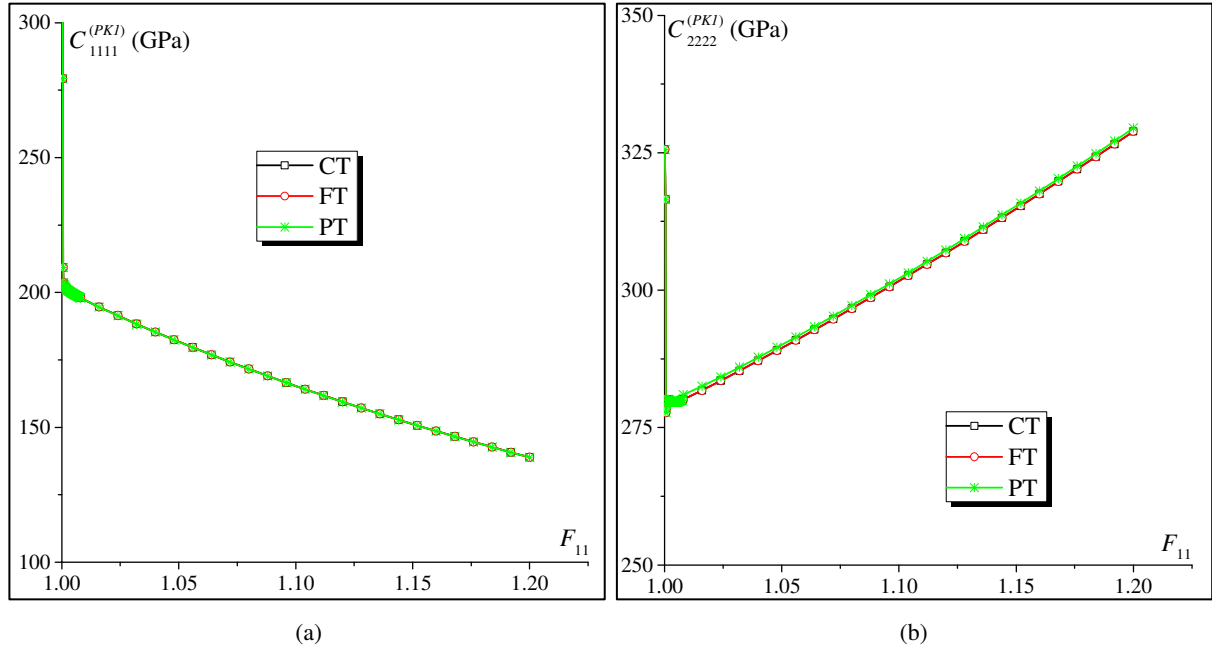
by CT and FT, the external file size required by FT is almost twice that required by CT. This result is also expectable considering the amount of data to be outputted when the FT is applied.

Table 1.5. Performance of the different techniques in terms of allocated space disk and CPU time for microstructure with cubic inclusion.

	CT	FT	PT
External files (GB)	3.979	7.654	11.087
CPU time (Minutes)	82	85.1	111.64

1.6.2.2. Microstructure with elliptical cylindrical fiber

In this case, the plastic behavior of the matrix is assumed to be anisotropic and it is modeled by the Hill'48 yield function with Lankford coefficients $r_0 = 0.585$; $r_{45} = 0.571$; and $r_{90} = 0.766$. The evolutions of the components $C_{1111}^{(PKI)}$, $C_{2222}^{(PKI)}$, $C_{1122}^{(PKI)}$, and $C_{1212}^{(PKI)}$ obtained by the three implemented techniques are plotted in Fig. 1.9. This figure confirms once again that the three techniques provide identical results.



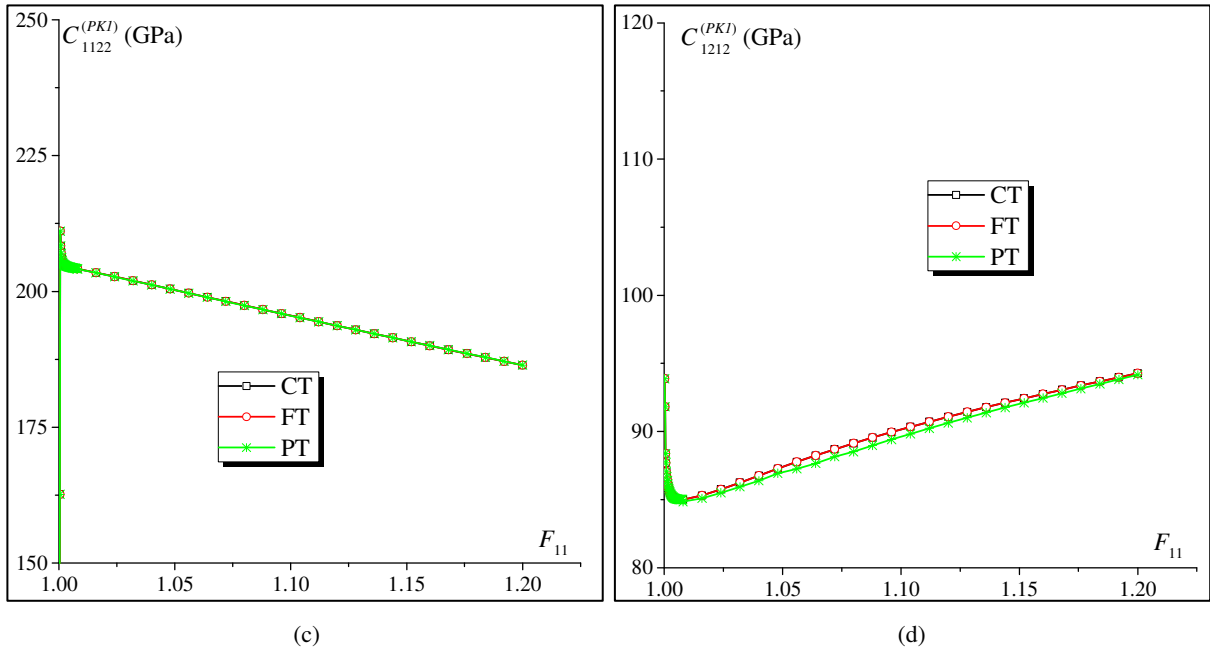


Fig. 1.9. Evolution of the components of modulus $C^{(PK1)}$ obtained by CT, FT, and PT for microstructure with an elliptical cylindrical inclusion: (a) $C_{1111}^{(PK1)}$; (b) $C_{2222}^{(PK1)}$; (c) $C_{1122}^{(PK1)}$; (d) $C_{1212}^{(PK1)}$.

The overall tangent modulus is evaluated at each $\Delta t = 0.04 t_f$ (see Eq. (1.80)). As shown in Table 1.6, PT consumes much more CPU time and requires the largest disk space. Also, as previously shown, CT appears to be the most efficient in terms of CPU times and external files.

Table 1.6. Performance of the different techniques in terms of allocated space disk and CPU time for microstructure with elliptical cylindrical fiber.

	CT	FT	PT
External files (<i>GB</i>)	2.064	3.977	4.48
CPU time (<i>Minutes</i>)	24	26.7	40.5

1.6.3. Numerical assessment of extended formulation of condensation technique in symmetric microstructures

We have presented in Section 1.5 the extended formulations of CT as well as of PT for the case of symmetric microstructures. In the same way as in the previous Section 1.6.2, the comparison between the performances of extended CT and PT has been conducted for reduced unit cells (RUC). The results of such a comparison (not shown here for brevity) reveal that the performance difference between CT and PT is similar to the case of original formulations with full unit cells (FUC) (which have been reported in Table 1.5 and Table 1.6). Consequently, attention is confined in this section to the performance analysis of the extended CT. The objective is to compare the performance of the extended formulation with RUC to the performance of the original formulation with FUC.

To assess the performance of the extension of CT to problems exhibiting symmetry properties (Section 1.5), let us consider the microstructure with elliptical cylindrical fiber. The RUC is discretized by 272

elements (Fig. 1.10) versus 2176 elements for FUC (Fig. 1.7b). The material parameters of both phases (matrix and inclusion) are the same as those provided in Section 1.6.2.

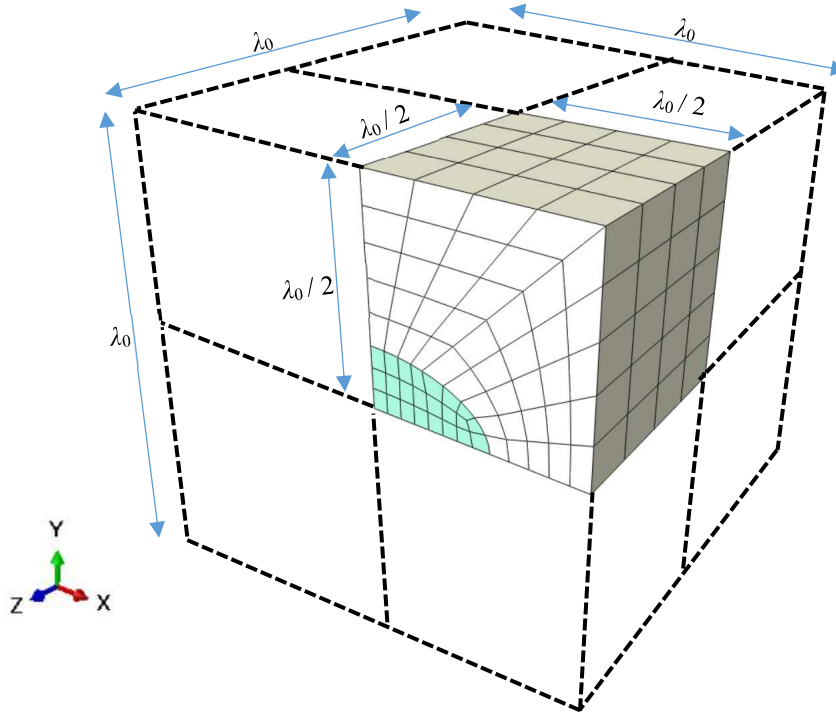


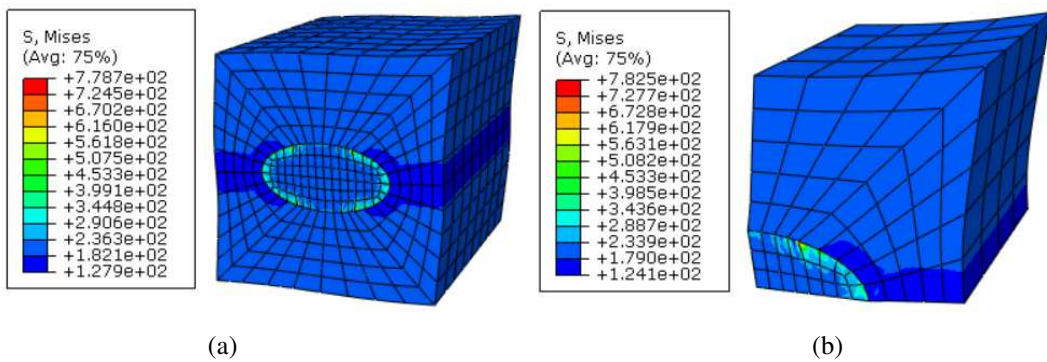
Fig. 1.10. RUC with elliptical cylindrical fiber.

Both FUC and RUC are subjected to the following deformation history:

$$\text{initial state: } \mathbf{F}(0) = \begin{bmatrix} 1 & 0 & 0 \\ 0 & 1 & 0 \\ 0 & 0 & 1 \end{bmatrix} \rightarrow \text{final state: } \mathbf{F}(t_f) = \begin{bmatrix} 1. & 0.2 & 0 \\ 0 & 1. & 0 \\ 0 & 0 & 1. \end{bmatrix}, \quad (1.81)$$

which corresponds to a simple shear test.

The distribution of the von Mises equivalent stress and the maximum principal logarithmic strain obtained for both unit cells (namely FUC and RUC) at the end of the loading are displayed in Fig. 1.11. As clearly shown in this figure, the two unit cell configurations give very close mechanical responses. These results prove the reliability and accuracy of the boundary conditions applied on the boundary of the RUC, as summarized in Table 1.1.



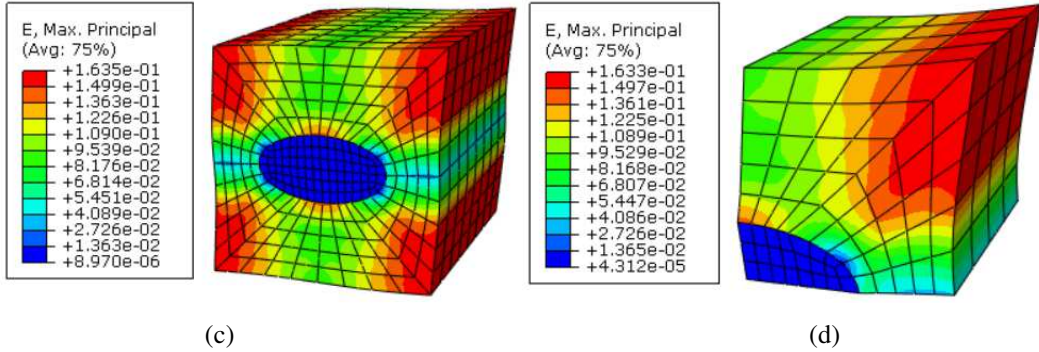
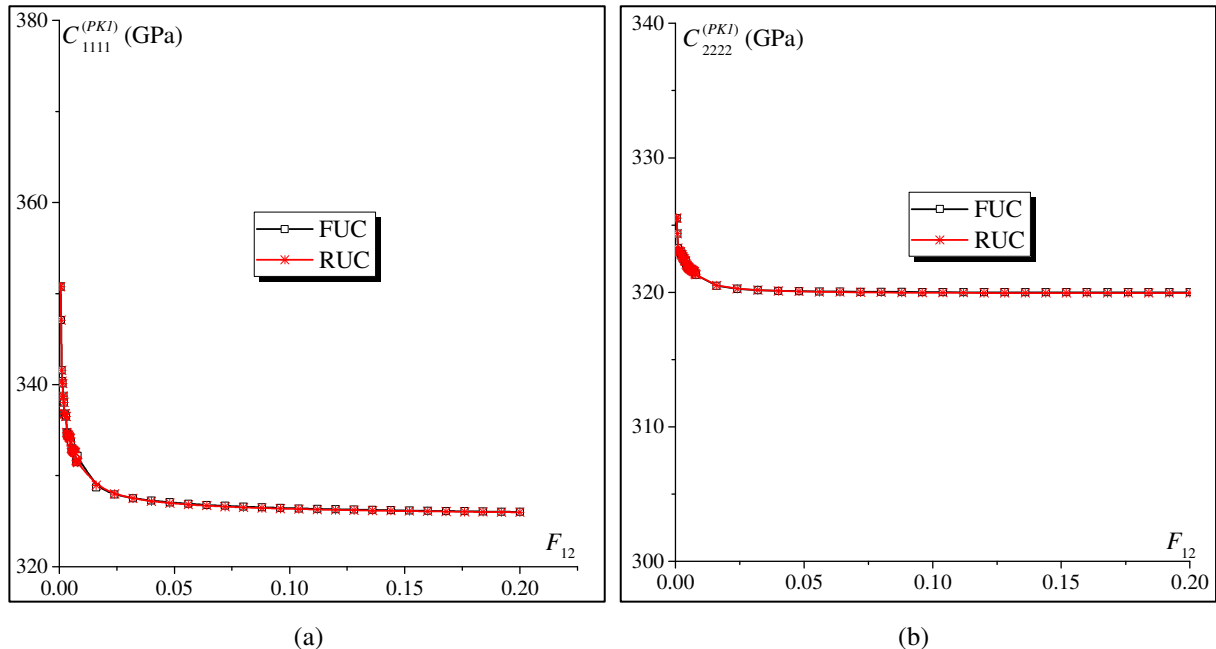


Fig. 1.11. Mechanical responses for both unit cells: (a) Contour plot of the von Mises equivalent stress for the FUC; (b) Contour plot of the von Mises equivalent stress for the RUC; (c) Contour plot of the maximum principal logarithmic strain for the FUC; (d) Contour plot of the maximum principal logarithmic strain for the RUC.

Fig. 1.12 provides the evolution of components $C_{1111}^{(PK1)}$, $C_{2222}^{(PK1)}$, $C_{122}^{(PK1)}$, and $C_{1212}^{(PK1)}$ as predicted by both the original CT with FUC and the extended CT version with RUC. The perfect agreement between the predictions observed in this figure clearly demonstrates that the extended condensation technique is correctly implemented and is reliable.



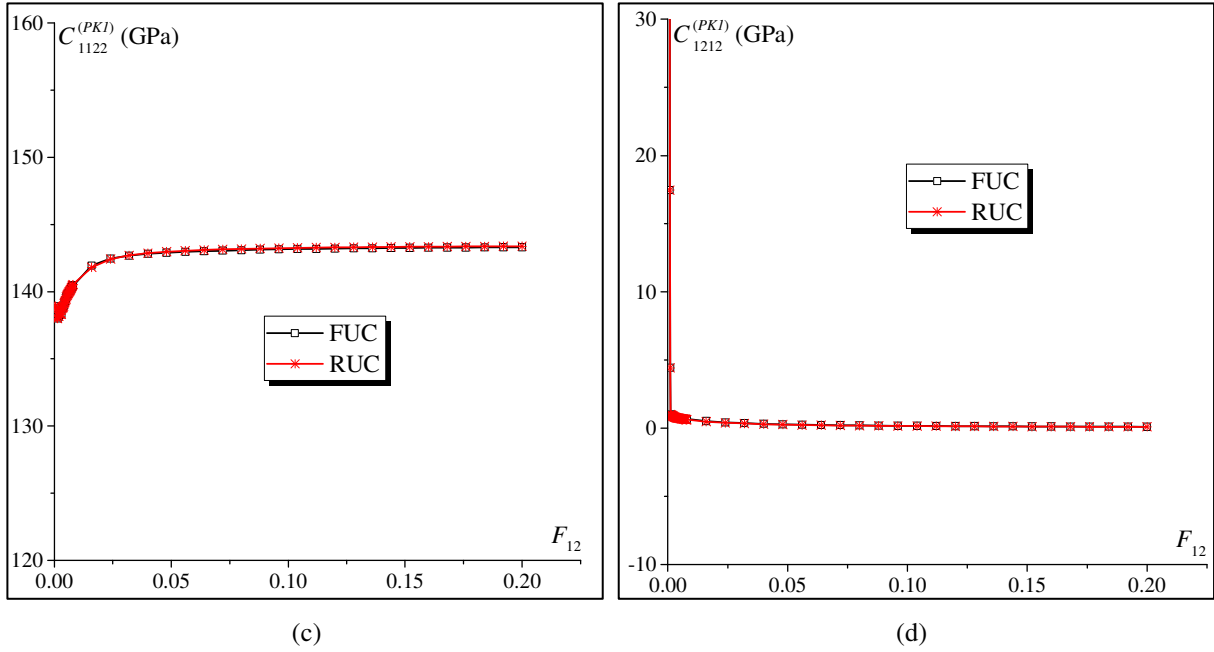


Fig. 1.12. Evolution of the components of modulus $\mathbf{C}^{(PK1)}$ as predicted by the original CT with FUC and the extended CT with RUC: (a) $C_{1111}^{(PK1)}$; (b) $C_{2222}^{(PK1)}$; (c) $C_{1122}^{(PK1)}$; (d) $C_{1212}^{(PK1)}$.

The overall tangent modulus is evaluated at each $\Delta t = 0.04 t_f$. As shown in Table 1.7, the use of the RUC instead of the FUC for the computation of the macroscopic tangent modulus allows dividing the size of external files by 8 and the CPU time by 13. This means that the RUC model greatly improves the computational efficiency. It is worth noting that, for CT, the CPU time is essentially consumed by the process of inverting large matrices. In the present comparative study, the element number used for the RUC model is reduced by a factor of 8, compared to the FUC model, which leads to a strong reduction in the stiffness matrix dimension (reduction by a factor of 43.84 in the current model). This strong size reduction induces a significant decrease in the computational effort. This comparison highlights the great interest of using the RUC model when the microstructure exhibits symmetry properties.

Table 1.7. Disk space and CPU time required for the use of CT with FUC and RUC.

	FUC	RUC
External files (GB)	2.064	0.26
CPU time (Minutes)	24	1.8

1.7. Summary and conclusions

In this chapter, three numerical techniques used to compute the overall tangent moduli for periodic unit cells have been briefly presented and implemented within ABAQUS/Standard by developing a set of Python scripts. Several conclusions can be drawn on the basis of the study conducted to compare the different techniques:

- The perturbation technique can be carried out by using only the *Homtools* (for the application of the periodic boundary conditions and the macroscopic loading) and the Python scripts that we

have developed. Hence, additional subroutines or tools (such as UMAT or UEL) are not essential for the computation of the overall tangent moduli by this technique. The numerical predictions reveal that PT is the most expensive both in terms of CPU time and external file storage. The high CPU time is attributable to the necessity to perform ten finite element computation steps (1 general step and 9 perturbation steps) for each computation of the tangent modulus.

- To implement and run the fluctuation technique, a user element (UEL) subroutine needs to be used. This limits the potential use of this method by the ABAQUS users' community. Furthermore, even though this technique does not consume excessive CPU time, the disk space occupied by the external files generated by this method remains relatively large as compared to the case of the condensation method.
- Compared to the latter techniques, the condensation technique seems to be easier to operate and reveals to be timesaving. To use this technique in conjunction with inelastic behavior, a user material (UMAT) subroutine should be used. Moreover, this technique has been successfully extended to explore microstructures exhibiting symmetry properties, and the interest of this extension has been highlighted through some numerical predictions.

Thus, this chapter provides valuable reference guidelines to ABAQUS/Standard users for the determination of the homogenized tangent moduli of linear or nonlinear heterogeneous materials, such as composites, polycrystalline aggregates and porous solids. The techniques and tools developed in this chapter could be used, in the following chapters, for the implementation of multiscale transition.

Chapter 2

Numerical investigation of necking in perforated sheets using the periodic homogenization approach

2.1. Introduction

Due to their lightness and aesthetic attractiveness, perforated sheets have been increasingly used in various industrial fields, including automotive, architecture, agriculture, pollution control, and mining ([IPA., 2015](#)). Additionally, the variety of patterns and perforation shapes makes them quite versatile. To accurately design and manufacture press-formed products, in-depth knowledge of the mechanical behavior and the conditions of occurrence of plastic instabilities in this kind of sheets remains a crucial task for both scientific and technological communities. The theoretical and numerical modeling of the mechanical behavior of perforated sheets has been widely investigated in several previous contributions in the literature. The various developed models have as objectives to predict the geometric distribution of the relevant mechanical fields (stress, plastic strain, ...) or to derive an effective (macroscopic) constitutive model representative of the mechanical behavior of the perforated medium as well as the corresponding mechanical parameters (elasticity parameters, anisotropy parameters, hardening parameters). Among these investigations, one can quote the pioneering work of [O'Donnell and Langer \(1962\)](#), who have developed a theoretical method for calculating the stress distribution and effective mechanical properties of perforated plates with triangular penetration pattern. In [O'Donnell and Langer \(1962\)](#), the mechanical behavior of the dense matrix is assumed to be linear elastic. More recently, [Krajcinovic et al. \(1992\)](#) have applied the percolation theory to determine the stress state and distribution

in a two-dimensional elastic medium containing randomly distributed circular voids. The effect of plastic behavior of the dense matrix on the effective properties of perforated sheets has been widely studied in several contributions. In these contributions, the effective (macroscopic) plastic behavior has been generally determined by defining a yield criterion and the corresponding evolution of the yield stress (macroscopic hardening). [Chen \(1993\)](#) has performed finite element simulations and experimental tensile tests to propose a yield criterion and the associated flow rules for perforated sheets with circular holes in hexagonal or equilateral triangular patterns. In [Chen \(1993\)](#), both von Mises and Hill'48 yield functions have been used to characterize the plasticity of the dense matrix. A similar methodology has been followed in [Baik et al. \(1997\)](#) to determine a yield criterion for perforated sheets with a uniform triangular pattern of round holes. In the latter contribution, the plastic anisotropy of the metal matrix has been modeled by the von Mises and Hosford yield functions. It should be noted that in the previous works ([Chen, 1993; Baik et al., 1997](#)), the classical finite element method has mainly been used to determine the effective mechanical behavior of a representative volume element (RVE) of the studied perforated sheet. Concretely, to build a typical yield function, a monotonically increasing loading combination is applied on the RVE. This loading is assumed to be linear in the macroscopic stress space (the ratio of the major to minor average stresses is kept constant during loading), while the shear stress is set to zero. During this loading, the homogenized stress-strain data are recorded. The yield point is determined from the plot of the effective (macroscopic) equivalent stress as a function of the effective equivalent plastic strain. The numerical modeling of the mechanical behavior of perforated sheets has been significantly improved by coupling the classical finite element analysis to multiscale approaches. These multiscale approaches are based on the concept of substituting a heterogeneous medium with an equivalent macroscopically homogeneous one. In this context, perforated sheets are viewed as heterogeneous media made of two main phases: the hole and the metal dense matrix (which may be itself made of several metallurgical phases). Such a multiscale strategy has been used by several authors to characterize equivalent mechanical behavior of perforated sheets. For instance, [van Rens et al. \(1998\)](#) have used a numerical homogenization approach to determine the initial yield function and its evolution for a RVE of perforated sheets with square pattern of circular holes. More recently, [Khatam and Pindera \(2011\)](#) have employed a finite-volume direct averaging micromechanics (FVDAM) theory to accurately determine the homogenized response of perforated sheets with hexagonal arrays of circular holes, and to establish the relation of homogenized response to yield and limit surfaces. In this chapter, we have adopted the multiscale strategy to study the mechanical behavior of perforated sheets with periodically distributed holes (in the two directions of the plane of the sheet). Considering this periodic distribution, the periodic homogenization technique already detailed in Chapter 1 has been used to determine the overall mechanical behavior of one square pattern, which is selected to be the unit cell representative of the studied sheet. It is worth noting that the mechanical behavior of perforated shells and plates has been extensively studied by using the asymptotic homogenization approach in several contributions ([Kalamkarov, 1992, 2014; Kalamkarov and Kolpakov, 1997; Andrianov et al., 2012a, 2012b;](#)

[Kalamkarov et al., 2012](#)). By contrast to the above references, which are mainly focused on the derivation of the macroscopic behavior of perforated thin structures (determination of the effective macroscopic elastic properties...), our contribution aims to investigate the onset of plastic instability in perforated sheets. As such instability usually occurs in the finite strain range, a total Lagrangian framework is adopted to express the assumptions and equations governing the periodic homogenization approach. Within this framework, the deformation gradient (resp. the first Piola–Kirchhoff stress tensor) is used as strain (resp. stress) measure. The periodic homogenization scheme is based on the assumption of spatial periodicity of the microscopic mechanical fields (namely, the microscopic deformation gradient and the microscopic first Piola–Kirchhoff stress) over the boundary of the unit cell. The equations governing the periodic homogenization technique are solved by the finite element method. To achieve this task, the Python scripts *Homtools* described in Chapter 1, has been used to easily apply the periodic boundary conditions (PBCs) and to determine the macroscopic first Piola–Kirchhoff stress tensor associated with the prescribed macroscopic deformation gradient.

Despite the large number of contributions dedicated to the modeling of the mechanical behavior of perforated sheets and to the determination of their effective macroscopic properties (effective elastoplastic parameters, shape of the macroscopic yield surface and its evolution), theoretical investigations on the necking and formability of perforated sheets are still seldom and not very extensive. It is however well recognized that the initiation of plastic instability in this kind of sheets is essentially dependent on the mechanical behavior of the dense matrix and on the morphology (size and form) of patterns and holes. In the majority of past studies related to this particular issue, perforated sheets are considered as thin media containing periodic array of cylindrical voids. [Tvergaard \(1981\)](#) is one of the first authors who extensively studied the onset of plastic strain localization in voided sheets under several mechanical states, such as uniaxial and biaxial plane-strain tension. In the latter reference, plastic strain localization is viewed as a bifurcation from the fundamental solution path, and Hill's theory of uniqueness ([Hill, 1958](#)) has been used to numerically predict bifurcation. To apply this analysis, the incremental form of the virtual work principle has been established on the basis of the incremental equilibrium equations. At each stage of the loading history, an approximate solution to this incremental form has been obtained by the finite element method. Bifurcation occurs when the determinant of the global stiffness matrix vanishes. In [Tvergaard \(1981\)](#), the limit strains given by bifurcation theory have been compared with their counterparts obtained by the maximum nominal traction criterion (diffuse necking criterion). More recently ([Tvergaard, 2015](#)), the previous study has been extended to void-sheets subjected to simple shear and pure shear states. It is to be noted that Tvergaard's investigations ([Tvergaard, 1981, 2015](#)) have been restricted to the following particular choices and assumptions: only some specific strain and stress states are studied, the form of voids is taken to be solely circular, and the plane-strain condition is assumed in the thickness direction of the sheet. In addition to these investigations, the necking occurrence in perforated sheets has also been analyzed through the classical

concept of forming limit diagrams (FLDs). As the studied sheets are assumed to be thin, FLD predictions have been legitimately based on the plane-stress assumption in the thickness of the sheet ([Hutchinson et al., 1978](#)). Furthermore, a wide range of strain paths (from uniaxial tension state to equibiaxial tension state) is covered when the FLD approach is used. The concept of forming limit diagrams has been first applied to perforated sheets in [Iseki et al. \(1989\)](#). In this chapter, a diffuse necking criterion has been used to predict the onset of necking. According to this criterion, the necking limit is reached when the product of external force and displacement rate reaches a maximum value. The effect of hole shape (circular, elliptical, square) on the formability limit has been particularly highlighted in [Iseki et al. \(1989\)](#). It has been found from this study that perforated sheets with square holes have the best formability limit. Iseki's formability criterion ([Iseki et al., 1989](#)) has been subsequently used by [Chiba et al. \(2015\)](#) to predict the FLDs of perforated aluminum sheets with square holes. In this analysis, both phenomenological material models (based on Hill'48 and von Mises yield functions) and a crystal plasticity model have been used to describe the mechanical behavior of the dense matrix. In the above-cited contributions ([Tvergaard, 1981, 2015; Iseki et al., 1989; Chiba et al., 2015](#)), finite element analyses have been combined with the different necking criteria to predict the onset of necking. In the present chapter, we have coupled the periodic homogenization approach with some diffuse and localized necking criteria to predict the forming limits of perforated sheets. The onset of diffuse necking is predicted by the maximum force criterion ([Considère, 1885](#)) and the general bifurcation criterion ([Drucker, 1950, 1956; Hill, 1958](#)). As to localized necking, its occurrence is determined by the loss of ellipticity criterion ([Rudnicki and Rice, 1975](#)). To apply both bifurcation criteria, the analytical tangent modulus, which relates the macroscopic first Piola–Kirchhoff stress rate to the macroscopic deformation gradient rate (as a total Lagrangian formulation is adopted), needs to be determined. To compute this tangent modulus, we have used the condensation technique detailed in Chapter 1. The different necking criteria have been implemented in the form of Python scripts.

A brief outline of the present chapter is as follows:

- Section 2.2 details the modeling of the mechanical behavior of the perforated sheets.
- Section 2.3 gives the main lines of the adopted necking criteria.
- The numerical results of the current study are reported in Section 2.4. Our numerical results are firstly compared with the numerical predictions of [Tvergaard \(1981\)](#). Secondly, a sensitivity study is conducted to analyze the effect of several mechanical and design parameters on the shape and the level of forming limit diagrams.
- Section 2.5 closes this chapter by summarizing some conclusions and future work.

2.2. Modeling of the mechanical behavior of perforated sheets

2.2.1. Multiscale transition problem

We consider a thin perforated sheet with a large number of holes, which are periodically distributed in the two directions of the plane of the sheet as depicted in Fig. 2.1a. This perforated sheet may be viewed as a heterogeneous medium made of two main phases: the hole and the metal matrix. Consequently, the mechanical behavior of this perforated sheet could be modeled by using a multiscale scheme. The metal matrix is assumed to be homogeneous, as microscopic heterogeneities between the different metallurgical phases are neglected in this study. The first step in the application of this multiscale process consists of the selection of a RVE, such that duplicating it provides sufficient accuracy for representing the material larger scales. In the current chapter, we have chosen a RVE with square pattern containing a unique hole located in the center of the RVE (Fig. 2.1b). The second step concerns the choice of the most relevant multiscale scheme to determine the homogenized behavior of this RVE. Considering the periodicity of the hole arrangement, the periodic homogenization technique (Miehe, 2003) is selected for this purpose. The use of this homogenization technique allows us to replace the heterogeneous RVE (called also unit cell in the context of periodic homogenization) by an equivalent homogenized medium with the same effective mechanical properties (Fig. 2.1c).

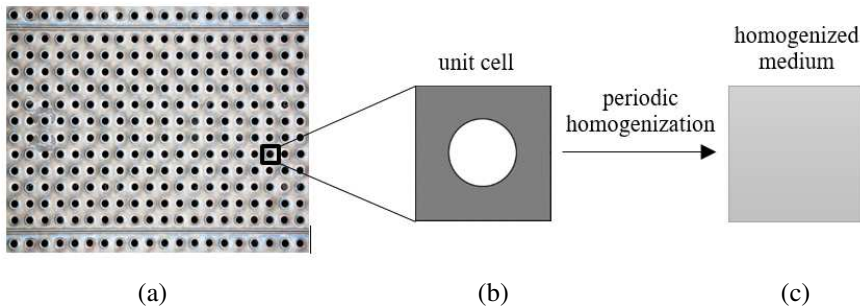


Fig. 2.1. Concept of the periodic homogenization approach.

In what follows, capital (resp. small) letters and symbols will be used to denote macroscale (resp. microscale) quantities and variables. The constitutive relations that describe the mechanical behavior of the dense matrix, which will be detailed in Section 2.2.2. The equations governing periodic homogenization scheme presented in Section 1.3 (Chapter 1) are adapted into the plane-stress state. The main lines of this adaptation are introduced in Section 2.2.3.

2.2.2. Constitutive relations at the microscale level

As the metal matrix is assumed to be homogeneous, a phenomenological constitutive framework is sufficient to describe the mechanical behavior of a microscopic material point from this matrix. To simplify the notations in the following developments, reference to the current position of the microscopic material point \mathbf{x} in the different mechanical fields will be omitted. Perforated sheets are generally

manufactured from cold-rolled products, which exhibit non negligible plastic anisotropy. Hence, a plastically anisotropic and rate-independent framework is chosen to model the mechanical behavior of the metal dense matrix. To develop the constitutive equations governing the mechanical behavior of the dense matrix, it is more convenient to use an Eulerian formulation. In this formulation, the velocity gradient \mathbf{g} and the Cauchy stress tensor $\boldsymbol{\sigma}$ are used as strain and stress measures. These tensors are related to their Lagrangian counterparts \mathbf{f} and \mathbf{p} by the following classical relations:

$$\mathbf{g} = \dot{\mathbf{f}} \cdot \mathbf{f}^{-1} ; \quad \mathbf{p} = j \boldsymbol{\sigma} \cdot \mathbf{f}^{-T} \quad \text{with} \quad j = \det(\mathbf{f}), \quad (2.1)$$

where \mathbf{f}^{-T} denotes the transpose of the inverse of tensor \mathbf{f} .

The microscopic velocity gradient \mathbf{g} is additively decomposed into its symmetric and skew-symmetric parts, denoted \mathbf{d} and \mathbf{w} , respectively:

$$\mathbf{g} = \mathbf{d} + \mathbf{w}. \quad (2.2)$$

To satisfy the objectivity principle (i.e., frame invariance), objective derivatives for tensor variables should be used. A practical approach, used to ensure frame invariance while maintaining simple forms of the constitutive equations, consists in reformulating these equations in terms of rotation-compensated variables. In the present work, a co-rotational approach based on the Jaumann objective rate is used. Accordingly, tensor quantities are expressed in a rotating frame so that simple material time derivatives can be used in the constitutive equations. The rotation \mathbf{r} of this rotating frame, with respect to the fixed one, is derived from the spin tensor \mathbf{w} (skew-symmetric part of \mathbf{g}) by the following relation:

$$\dot{\mathbf{r}} \cdot \mathbf{r}^T = \mathbf{w}. \quad (2.3)$$

In the remainder of the current section (Section 2.2.2), all tensor variables will be expressed in the rotating frame (called co-rotational frame), that is to say, using rotation-compensated variables. Consequently, time derivatives are involved in the constitutive equations, making them identical in form to a small-strain formulation.

The strain rate \mathbf{d} is itself split into its elastic part \mathbf{d}^e and plastic part \mathbf{d}^p :

$$\mathbf{d} = \mathbf{d}^e + \mathbf{d}^p. \quad (2.4)$$

The stress rate is described with a hypoelastic law:

$$\dot{\boldsymbol{\sigma}} = \mathbf{c}^e : \mathbf{d}^e, \quad (2.5)$$

where \mathbf{c}^e denotes the fourth-order elasticity tensor. Here, elasticity is assumed to be isotropic and is defined by two material parameters: the Young modulus E and the Poisson ratio ν .

The plastic strain rate \mathbf{d}^p is assumed to be normal to the yield surface, and the following normality law is adopted:

$$\mathbf{d}^p = \dot{\lambda} \frac{\partial \Phi}{\partial \boldsymbol{\sigma}}, \quad (2.6)$$

where $\dot{\lambda}$ denotes the plastic multiplier, and Φ is the yield function defined as the difference between the equivalent stress σ_{eq} and the microscopic yield stress σ_y . In this chapter, the Hill'48 criterion is used as equivalent stress measure (Hill, 1948), while hardening is assumed to be isotropic and is modeled by the Swift law. Consequently, σ_{eq} and σ_y are defined by the following expressions:

$$\sigma_{eq} = \sqrt{\boldsymbol{\sigma} : \mathbf{H} : \boldsymbol{\sigma}} \quad ; \quad \sigma_y = K \left(\varepsilon_0 + \varepsilon_{eq}^p \right)^n, \quad (2.7)$$

where:

- K , ε_0 and n are hardening parameters.
- ε_{eq}^p is the equivalent plastic strain.
- \mathbf{H} is the Hill'48 orthotropic matrix, whose components are expressed in terms of three Lankford coefficients (r_0, r_{45}, r_{90}) that measure the degree of plastic anisotropy.

The activation of the plastic deformation is governed by the well-known Kuhn–Tucker constraints:

$$\Phi = (\sigma_{eq} - \sigma_y) \leq 0 \quad ; \quad \dot{\lambda} \geq 0 \quad ; \quad \Phi \dot{\lambda} = 0. \quad (2.8)$$

The Cauchy stress rate $\dot{\boldsymbol{\sigma}}$ is related to the strain rate \mathbf{d} by the elastoplastic continuum tangent matrix \mathbf{c}^{ep} :

$$\dot{\boldsymbol{\sigma}} = \mathbf{c}^{ep} : \mathbf{d}. \quad (2.9)$$

The expression of this elastoplastic tangent modulus can be obtained by combining the different constitutive equations (2.2)–(2.9). One can obtain after classical computations the following expression for \mathbf{c}^{ep} (Haddag et al., 2007):

$$\mathbf{c}^{ep} = \mathbf{c}^e - \left(\frac{\left(\mathbf{c}^e : \frac{\partial \Phi}{\partial \boldsymbol{\sigma}} \right) \otimes \left(\frac{\partial \Phi}{\partial \boldsymbol{\sigma}} : \mathbf{c}^e \right)}{\frac{\partial \Phi}{\partial \boldsymbol{\sigma}} : \mathbf{c}^e : \frac{\partial \Phi}{\partial \boldsymbol{\sigma}} + \frac{\partial \sigma_y}{\partial \varepsilon_{eq}^p}} \right). \quad (2.10)$$

As demonstrated by Mansouri et al. (2014), the microscopic tangent modulus $\mathbf{c}^{(PKI)}$ is related to the elastoplastic tangent modulus \mathbf{c}^{ep} by the following relationship:

$$\forall i, j, k, l = 1, 2, 3: \quad c_{ijkl}^{(PKI)} = c_{ijkl}^{ep} + \ell_{ijkl}^1 - \ell_{ijkl}^2 - \ell_{ijkl}^3, \quad (2.11)$$

where ℓ_{ijkl}^1 , ℓ_{ijkl}^2 , ℓ_{ijkl}^3 are respectively the index forms of fourth-order tensors ℓ^1 , ℓ^2 and ℓ^3 that originate from the large strain framework and which are given by:

$$\forall i, j, k, l = 1, 2, 3: \quad \ell_{ijkl}^1 = \sigma_{ij} \delta_{kl} \quad ; \quad \ell_{ijkl}^2 = \frac{1}{2} (\sigma_{jl} \delta_{ik} + \sigma_{jk} \delta_{il}) \quad ; \quad \ell_{ijkl}^3 = \frac{1}{2} (\sigma_{ik} \delta_{jl} - \sigma_{il} \delta_{jk}). \quad (2.12)$$

2.2.3. Numerical implementation of the multiscale transition scheme

As demonstrated in Chapter 1, the *Homtools* has been used to easily define the PBCs and the average loadings over the unit cells as well as to determine the average response. As a first step in solving the periodic homogenization problem, the unit cell occupying an initial volume $\mathcal{V}_0 = [0, l_0] \times [0, l_0] \times [0, 0.1l_0]$ is discretized by finite elements (Fig. 2.2). 3D finite elements (C3D20) have been used in this chapter, in spite of the small thickness of the studied sheets. As the numerical strategy (introduced in Section 2.1) is used to predict forming limit diagrams, the unit cell is submitted to biaxial stretching along the 1st and 2nd directions, while under a plane-stress state in the third direction (Fig. 2.2). This loading is represented by the following generic macroscopic fields:

$$\mathbf{F} = \begin{pmatrix} F_{11} & 0 & ? \\ 0 & F_{22} & ? \\ ? & ? & ? \end{pmatrix} ; \quad \mathbf{P} = \begin{pmatrix} ? & ? & 0 \\ ? & ? & 0 \\ 0 & 0 & 0 \end{pmatrix}, \quad (2.13)$$

where the components denoted by ‘?’ are the unknown components that need to be determined.

Under plane-stress state, the kinematic relations of periodic homogenization (1.19) and (1.20) are respectively adapted into the in-plane forms:

$${}^{IN}\mathbf{x} = {}^{IN}\mathbf{F} \cdot {}^{IN}\mathbf{x}_0 + {}^{IN}\mathbf{u}_{per}, \quad (2.14)$$

and

$${}^{IN}\mathbf{v} = {}^{IN}\dot{\mathbf{F}} \cdot {}^{IN}\mathbf{x}_0 + {}^{IN}\dot{\mathbf{u}}_{per} := {}^{IN}\dot{\mathbf{F}} \cdot {}^{IN}\mathbf{x}_0 + {}^{IN}\mathbf{v}_{per}, \quad (2.15)$$

where ${}^{IN}\bullet$ are the reduced in-plane forms of vector and tensor fields \bullet .

The other equations related to periodic homogenization are the same as those presented in Section 1.3 (namely, Eqs. (1.21)–(1.24)). For the sake of brevity, these equations are not recalled here.

With the in-plane relations, the unit cell is technically submitted to the following boundary conditions:

- On the boundary surfaces \mathcal{S}_{01}^- and \mathcal{S}_{01}^+ : a reference point RP_1 (following the ABAQUS terminology) is created to apply the components F_{11} , $F_{12}(=0)$ and $F_{13}(=\text{free})$ of the macroscopic deformation gradient \mathbf{F} . Furthermore, for the current position of the two corresponding nodes ${}^{IN}\mathbf{x}_{0q}^-$ and ${}^{IN}\mathbf{x}_{0q}^+$ with identical coordinates in 2 and 3 directions on surfaces \mathcal{S}_{01}^- and \mathcal{S}_{01}^+ , the following constraint equation is imposed:

$${}^{IN}\mathbf{x}_q^+ - {}^{IN}\mathbf{x}_q^- = {}^{IN}\mathbf{F} \cdot \left({}^{IN}\mathbf{x}_{0q}^+ - {}^{IN}\mathbf{x}_{0q}^- \right). \quad (2.16)$$

Constraint equation (2.16) is the in-plane form of Eq. (1.30) presented in Section 1.3.

- On the boundary surfaces \mathcal{S}_{02}^- and \mathcal{S}_{02}^+ : a reference point RP_2 is created to apply the components $F_{21}(=0)$, F_{22} and $F_{23}(=\text{free})$ of \mathbf{F} . Furthermore, a periodic constraint, similar to the one imposed to the nodes of surfaces \mathcal{S}_{01}^- and \mathcal{S}_{01}^+ , is applied.
- On the boundary surfaces \mathcal{S}_{03}^- and \mathcal{S}_{03}^+ : a reference point RP_3 is created to enforce the macroscopic stress components $P_{31} = P_{32} = P_{33} = 0$.

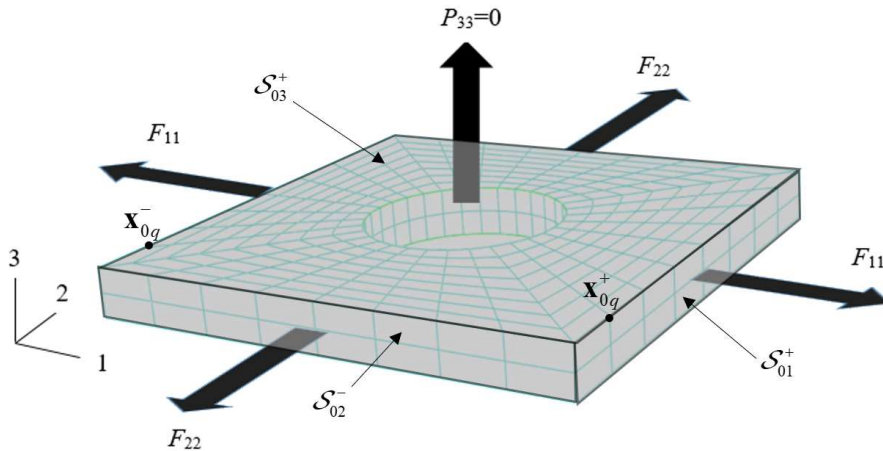


Fig. 2.2. Finite element discretization and boundary conditions applied to the unit cell.

The above macroscopic loading in terms of displacement on the reference points can be summarized briefly:

$$\begin{aligned} RP_1 : U_{11} &= (F_{11} - 1)l_0 ; \quad U_{12} = 0 ; \quad P_{13} = 0 ; \\ RP_2 : U_{21} &= 0 ; \quad U_{22} = ((F_{11})^\rho - 1)l_0 ; \quad P_{23} = 0 ; \\ RP_3 : P_{31} &= 0 ; \quad P_{32} = 0 ; \quad P_{33} = 0 . \end{aligned} \quad (2.17)$$

More details about the practical aspects of applying Eq. (2.17) can be found in Section 1.3.

Meanwhile, the macroscopic force R_i applied on the boundary surfaces \mathcal{S}_{01}^- and \mathcal{S}_{01}^+ is obtained by multiplying the component P_{ii} by the initial surface \mathcal{S}_{01} of boundaries \mathcal{S}_{01}^- or \mathcal{S}_{01}^+ , namely:

$$R_i = P_{ii} \mathcal{S}_{01} . \quad (2.18)$$

A similar relationship can be defined between the force R_2 applied on \mathcal{S}_{02}^- and \mathcal{S}_{02}^+ and P_{22} .

As discussed in Section 1.3, by using the *Homotools*, it is allowed to treat the macroscopic deformation gradient \mathbf{F} as macroscopic degrees of freedom associated with the nodal reaction forces $|\mathcal{V}_0| \mathbf{P}$ at the reference points. It is worth noting that the demonstration in Section 1.3 is also suitable for the plane-stress case in this chapter, which are specified in the following.

As a departure, we recall the virtual work principle expressed in Eq. (1.25):

$$\int_{\mathcal{V}_0} \left[\frac{\partial \delta \mathbf{v}}{\partial \mathbf{x}_0} : \dot{\mathbf{p}} \right] d\mathcal{V}_0 = \int_{\mathcal{S}_0} \delta \mathbf{v} \cdot \dot{\mathbf{t}}_0 d\mathcal{S}_0. \quad (2.19)$$

where $\mathcal{S}_0 (= \mathcal{S}_{01}^- \cup \mathcal{S}_{01}^+ \cup \mathcal{S}_{02}^- \cup \mathcal{S}_{02}^+ \cup \mathcal{S}_{03}^- \cup \mathcal{S}_{03}^+)$ and $\dot{\mathbf{t}}_0$ denote, respectively, the boundary surface of the initial configuration and the nominal traction rate prescribed on \mathcal{S}_0 . Vector $\dot{\mathbf{t}}_0$ is equal to $\dot{\mathbf{p}} \cdot \vec{\mathbf{n}}_0$, where $\vec{\mathbf{n}}_0$ is the outer normal to the boundary \mathcal{S}_0 .

To solve Eq. (2.19), the Hill-Mandel condition could be used after validating it for the plane-stress state. This condition states the incremental internal energy equivalence between the micro and macroscales as:

$$\int_{\mathcal{V}_0} \left[\frac{\partial \delta \mathbf{v}}{\partial \mathbf{x}_0} : \dot{\mathbf{p}} \right] d\mathcal{V}_0 - |\mathcal{V}_0| \delta \dot{\mathbf{F}} : \dot{\mathbf{P}} = 0. \quad (2.20)$$

To prove equality (2.20), the left-hand side of the latter can be recasted as:

$$\int_{\mathcal{V}_0} \left[\frac{\partial \delta \mathbf{v}}{\partial \mathbf{x}_0} : \dot{\mathbf{p}} \right] d\mathcal{V}_0 - |\mathcal{V}_0| \delta \dot{\mathbf{F}} : \dot{\mathbf{P}} = \int_{\mathcal{S}_0} [\delta \mathbf{v} - \delta \dot{\mathbf{F}} \cdot \mathbf{x}_0] \cdot [\dot{\mathbf{t}}_0 - \dot{\mathbf{P}} \cdot \vec{\mathbf{n}}_0] d\mathcal{S}_0. \quad (2.21)$$

Following the decomposition of the whole boundary of the unit cell \mathcal{S}_0 into six faces, the right-hand side of Eq. (2.21) could be expanded as:

$$\begin{aligned} \int_{\mathcal{S}_0} [\delta \mathbf{v} - \delta \dot{\mathbf{F}} \cdot \mathbf{x}_0] \cdot [\dot{\mathbf{t}}_0 - \dot{\mathbf{P}} \cdot \vec{\mathbf{n}}_0] d\mathcal{S}_0 &= \int_{\mathcal{S}_{01}^- \cup \mathcal{S}_{01}^+ \cup \mathcal{S}_{02}^- \cup \mathcal{S}_{02}^+} [\delta \mathbf{v} - \delta \dot{\mathbf{F}} \cdot \mathbf{x}_0] \cdot [\dot{\mathbf{t}}_0 - \dot{\mathbf{P}} \cdot \vec{\mathbf{n}}_0] d\mathcal{S}_0 \\ &\quad + \int_{\mathcal{S}_{03}^- \cup \mathcal{S}_{03}^+} [\delta \mathbf{v} - \delta \dot{\mathbf{F}} \cdot \mathbf{x}_0] \cdot [\dot{\mathbf{t}}_0 - \dot{\mathbf{P}} \cdot \vec{\mathbf{n}}_0] d\mathcal{S}_0. \end{aligned} \quad (2.22)$$

Making use of the kinematic relationship under plane-stress condition, the first part of the right-hand side of Eq. (2.22) may be transformed as:

$$\begin{aligned} &\int_{\mathcal{S}_{01}^- \cup \mathcal{S}_{01}^+ \cup \mathcal{S}_{02}^- \cup \mathcal{S}_{02}^+} [\delta \mathbf{v} - \delta \dot{\mathbf{F}} \cdot \mathbf{x}_0] \cdot [\dot{\mathbf{t}}_0 - \dot{\mathbf{P}} \cdot \vec{\mathbf{n}}_0] d\mathcal{S}_0 \\ &= \int_{\mathcal{S}_{01}^- \cup \mathcal{S}_{01}^+ \cup \mathcal{S}_{02}^- \cup \mathcal{S}_{02}^+} [{}^{IN} \delta \mathbf{v} - {}^{IN} \delta \dot{\mathbf{F}} \cdot {}^{IN} \mathbf{x}_0] \cdot [{}^{IN} \dot{\mathbf{t}}_0 - {}^{IN} \dot{\mathbf{P}} \cdot {}^{IN} \vec{\mathbf{n}}_0] d\mathcal{S}_0 \\ &= \int_{\mathcal{S}_{01}^- \cup \mathcal{S}_{01}^+ \cup \mathcal{S}_{02}^- \cup \mathcal{S}_{02}^+} {}^{IN} \delta \mathbf{v}_{per} \cdot [{}^{IN} \dot{\mathbf{t}}_0 - {}^{IN} \dot{\mathbf{P}} \cdot {}^{IN} \vec{\mathbf{n}}_0] d\mathcal{S}_0, \end{aligned} \quad (2.23)$$

with ${}^{IN} \bullet$ being the reduced in-plane forms of vector and tensor fields \bullet . The periodicity of vector ${}^{IN} \delta \mathbf{v}_{per}$ and the anti-periodicity of vector $[{}^{IN} \dot{\mathbf{t}}_0 - {}^{IN} \dot{\mathbf{P}} \cdot {}^{IN} \vec{\mathbf{n}}_0]$ over the set of faces $\mathcal{S}_{01}^- \cup \mathcal{S}_{01}^+ \cup \mathcal{S}_{02}^- \cup \mathcal{S}_{02}^+$ lead to the following boundary integral constraint:

$$\int_{\mathcal{S}_{01}^- \cup \mathcal{S}_{01}^+ \cup \mathcal{S}_{02}^- \cup \mathcal{S}_{02}^+} {}^{IN} \delta \mathbf{v}_{per} \cdot [{}^{IN} \dot{\mathbf{t}}_0 - {}^{IN} \dot{\mathbf{P}} \cdot {}^{IN} \vec{\mathbf{n}}_0] d\mathcal{S}_0 = 0. \quad (2.24)$$

On the other hand, the second part of the right-hand side of Eq. (2.22) can thereby be naturally reduced to 0 considering the plane-stress condition:

$$\text{over } \mathcal{S}_{03}^- \cup \mathcal{S}_{03}^+ : [\dot{\mathbf{t}}_0 - \dot{\mathbf{P}} \cdot \vec{\mathbf{n}}_0] = \vec{0} \Rightarrow \int_{\mathcal{S}_{03}^- \cup \mathcal{S}_{03}^+} [\delta \mathbf{v} - \delta \dot{\mathbf{F}} \cdot \mathbf{x}_0] \cdot [\dot{\mathbf{t}}_0 - \dot{\mathbf{P}} \cdot \vec{\mathbf{n}}_0] d\mathcal{S}_0 = 0. \quad (2.25)$$

Considering Eqs. (2.24) and (2.25), the Hill-Mandel condition of Eq. (2.20) is validated for the plane-stress state.

2.2.4. Computation of the macroscopic tangent modulus

The application of the bifurcation criteria presented in Section 2.3 requires the computation of the macroscopic tangent modulus $\mathbf{C}^{(PKI)}$ introduced in Eq. (1.24)₂. To determine this tangent modulus from the finite element outputs, the condensation technique presented in Chapter 1 has been adopted, after its adaptation to the kinematics of the plane-stress state. For completeness, the main steps of this technique will be recalled in the following developments. Further information about this technique can be found in Section 1.4.2 and reference (Miehe, 2003).

- *Step 1:* at the convergence of the finite element method, ABAQUS offers the possibility to save the elementary stiffness matrices \mathbf{K}^{el} in a ‘.mtx’ file by using the command ‘*Element Matrix Output*’. A classical assembly procedure has been implemented to determine the global stiffness matrix \mathbf{K} from the elementary ones \mathbf{K}^{el} and by taking into account the connectivity of the different nodes of the mesh:

$$\mathbf{K} = \bigcup_{el=1}^{el=Nel} \mathbf{K}^{el}, \quad (2.26)$$

where Nel refers to the total number of finite elements in the mesh.

- *Step 2:* the nodes of the mesh are partitioned into two sets (Fig. 2.2): set \mathcal{B} made of nodes located on the boundary surfaces $\mathcal{S}_{01}^- \cup \mathcal{S}_{01}^+ \cup \mathcal{S}_{02}^- \cup \mathcal{S}_{02}^+$ where periodicity constraints are applied, and set \mathcal{A} which is composed of the other nodes of the mesh. By using this partition, the lines and columns of the global stiffness matrix \mathbf{K} are rearranged (permuted) to obtain the following decomposition:

$$\mathbf{K} = \begin{bmatrix} \mathbf{K}_{AA} & \mathbf{K}_{AB} \\ \mathbf{K}_{BA} & \mathbf{K}_{BB} \end{bmatrix}. \quad (2.27)$$

- *Step 3:* matrices \mathbb{H} and \mathbb{Q} are computed by following the numerical procedure detailed in Section 1.4.2.
- *Step 4:* the macroscopic tangent modulus is computed by using the following relation:

$$\mathbf{C}^{(PKI)} = \frac{1}{|\mathcal{V}_0|} \mathbb{Q} \cdot \left[\mathbb{H} \cdot \left(\mathbf{K}_{BB} - \mathbf{K}_{BA} \cdot \mathbf{K}_{AA}^{-1} \cdot \mathbf{K}_{BB} \right)^{-1} \cdot \mathbb{H}^T \right]^{-1} \cdot \mathbb{Q}^T. \quad (2.28)$$

The constitutive equations used to model the mechanical behavior of the dense matrix have been integrated by using an Euler explicit algorithm and implemented as a UMAT subroutine in ABAQUS. As the integration algorithm is explicit, the consistent elastoplastic tangent modulus used to construct the stiffness matrix \mathbf{K} coincides with the analytical one given by Eq. (2.10), as

explained in [Simo \(1998\)](#). As demonstrated in [Temizer and Wriggers \(2008\)](#), the condensation technique allows us to obtain an analytical macroscopic tangent modulus if the microscopic one, used to compute the global stiffness matrix \mathbf{K} , is itself analytical. Consequently, $\mathbf{C}^{(PK1)}$ is an analytical tangent modulus, which can be used without any modification in the subsequent bifurcation analyses.

2.3. Necking criteria

To predict the occurrence of necking in thin perforated sheets, and represent the prediction results in terms of forming limit diagrams, the applied macroscopic deformation gradient given in Eq. (2.13) is defined by the following in-plane components:

$$F_{11} = e^{E_{11}} \quad ; \quad F_{22} = e^{E_{22}} \quad \text{with} \quad E_{22} = \rho E_{11}. \quad (2.29)$$

To cover the whole range of strain paths, relevant for the plot of forming limit diagrams, the strain-path ratio ρ is varied between $-1/2$ (uniaxial tensile state) and 1 (equibiaxial tensile state).

To predict the onset of necking in the unit cell, the macroscopic first Piola–Kirchhoff stress tensor \mathbf{P} and the corresponding analytical tangent modulus $\mathbf{C}^{(PK1)}$ are used as inputs for three necking criteria: the Maximum Force Criterion (MFC), the General Bifurcation Criterion (GBC), and the Rice Bifurcation Criterion (RBC). Considering the plane-stress assumption, $\mathbf{C}^{(PK1)}$ will be used as its in-plane form ${}^{\text{IN}}\mathbf{C}^{(PK1)}$ in those necking criteria, where ${}^{\text{IN}}\mathbf{C}^{(PK1)}$ can be deduced by:

$$\forall i, j, k, l = 1, 2: \quad {}^{\text{IN}}C_{ijkl}^{(PK1)} = C_{ijkl}^{(PK1)} - \frac{C_{ij33}^{(PK1)} C_{33kl}^{(PK1)}}{C_{3333}^{(PK1)}}. \quad (2.30)$$

These necking criteria will be briefly presented in the following Sections (2.3.1; 2.3.2 and 2.3.3).

2.3.1. Maximum Force Criterion

[Swift \(1952\)](#) proposed a diffuse necking condition for stretched metal sheets submitted to biaxial loading, as depicted in [Fig. 2.2](#). This condition can be mathematically expressed as:

$$\dot{R}_1 = 0 \quad \text{and} \quad \dot{R}_2 = 0. \quad (2.31)$$

Condition (2.31) suggests that diffuse necking occurs when components R_1 and R_2 reach their maximum values simultaneously. However, the satisfaction of this simultaneous condition is only possible for two particular strain paths (uniaxial and equibiaxial strain paths), as it has been experimentally and theoretically demonstrated in [Habbar \(1994\)](#) and [Abed-Meraim et al. \(2014\)](#). Accordingly, to be able to predict the onset of diffuse necking for the whole range of strain paths, we only consider the first condition in Eq. (2.31), namely:

$$\dot{R}_1 = 0. \quad (2.32)$$

As the component P_{11} of tensor \mathbf{P} is proportional to force R_1 , condition (2.32) can be equivalently rewritten as:

$$\dot{P}_{11} = 0. \quad (2.33)$$

2.3.2. General Bifurcation Criterion

Diffuse necking is also predicted by the general bifurcation criterion (GBC). This criterion states that plastic instability occurs when the second-order work vanishes (Drucker, 1950, 1956; Hill, 1958). According to the GBC, diffuse necking is predicted when at least one eigenvalue of the symmetric part of ${}^{IN}\mathbf{C}^{(PK1)}$ (called hereafter ${}^{IN}\mathbf{C}_{sym}^{(PK1)}$) becomes negative. Further details about the development of this criterion are provided in Bouktir et al. (2018).

2.3.3. Rice Bifurcation criterion

In the approach proposed by Rudnicki and Rice (1975), material instability corresponds to a bifurcation associated with admissible jumps for strain and stress rates across a localization band, as illustrated in Fig. 2.3. In a Lagrangian formulation, the kinematic condition for the strain rate jump writes:

$${}^{IN}\llbracket \dot{\mathbf{F}} \rrbracket = {}^{IN}\dot{\mathbf{F}}^+ - {}^{IN}\dot{\mathbf{F}}^- = {}^{IN}\vec{\dot{\mathcal{C}}} \otimes {}^{IN}\vec{\mathcal{N}}, \quad (2.34)$$

where ${}^{IN}\llbracket \dot{\mathbf{F}} \rrbracket$ is the jump of the in-plane velocity gradient field ${}^{IN}\dot{\mathbf{F}}$ across the discontinuity band, while ${}^{IN}\vec{\dot{\mathcal{C}}}$ is the in-plane jump vector, and ${}^{IN}\vec{\mathcal{N}}$ is the in-plane unit vector normal to the localization band in the initial configuration equal to $(\cos\theta, \sin\theta)$, where θ is the inclination of vector ${}^{IN}\vec{\mathcal{N}}$ (see Fig. 2.3).

On the other hand, the continuity condition for the force equilibrium across the band is expressed as:

$${}^{IN}\llbracket \dot{\mathbf{P}} \rrbracket \cdot {}^{IN}\vec{\mathcal{N}} = \vec{0}. \quad (2.35)$$

The combination of Eqs. (2.34) and (2.35) with the macroscopic constitutive law (1.24) leads to the following equation:

$$\left({}^{IN}\mathbf{C}^{(PK1)} : {}^{IN}\vec{\dot{\mathcal{C}}} \otimes {}^{IN}\vec{\mathcal{N}} \right) \cdot {}^{IN}\vec{\mathcal{N}} = \vec{0}, \quad (2.36)$$

which can be written in index form:

$$\forall i=1,2,: \quad \left({}^{IN}\mathcal{N}_j {}^{IN}C_{ijkl}^{(PK1)} {}^{IN}\mathcal{N}_l \right) {}^{IN}\dot{\mathcal{C}}_k = 0, \quad j,k,l=1,2,. \quad (2.37)$$

By introducing matrix ${}^{IN}\tilde{\mathbf{C}}^{(PK1)}$, defined as the transpose of matrix ${}^{IN}\mathbf{C}^{(PK1)}$ by permutation of the first two indices (${}^{IN}\tilde{\mathbf{C}}_{ijkl}^{(PK1)} = {}^{IN}C_{jikl}^{(PK1)}$), condition (2.37) can be rewritten as follows:

$$\forall j=1,2: \quad \left({}^{IN}\mathcal{N}_i {}^{IN}\tilde{\mathbf{C}}_{ijkl}^{(PK1)} {}^{IN}\mathcal{N}_l \right) {}^{IN}\dot{\mathcal{C}}_k = 0, \quad i,k,l=1,2,. \quad (2.38)$$

which is equivalent to:

$$\left({}^{\text{IN}}\vec{\mathbf{N}} \cdot {}^{\text{IN}}\tilde{\mathbf{C}}^{(\text{PK1})} \cdot {}^{\text{IN}}\vec{\mathbf{N}} \right) \cdot {}^{\text{IN}}\dot{\vec{\mathbf{C}}} = \vec{0}. \quad (2.39)$$

Tensor ${}^{\text{IN}}\vec{\mathbf{N}} \cdot {}^{\text{IN}}\tilde{\mathbf{C}}^{(\text{PK1})} \cdot {}^{\text{IN}}\vec{\mathbf{N}}$ is the so-called acoustic tensor. As long as this tensor is invertible, the jump vector ${}^{\text{IN}}\dot{\vec{\mathbf{C}}}$ remains equal to zero, thus precluding any discontinuity (bifurcation) in the deformation field. However, when the acoustic tensor becomes singular, there exists non-zero jump vectors that satisfy Eq. (2.39), and this can be seen as indicator of effective bifurcation. Therefore, strain localization occurs when the acoustic tensor is no longer invertible:

$$\det\left({}^{\text{IN}}\vec{\mathbf{N}} \cdot {}^{\text{IN}}\tilde{\mathbf{C}}^{(\text{PK1})} \cdot {}^{\text{IN}}\vec{\mathbf{N}} \right) = 0. \quad (2.40)$$

The bifurcation criterion given by Eq. (2.40) is implemented in the set of Python codes by following the algorithm developed in [Ben Bettaieb and Abed-Meraim \(2015\)](#).

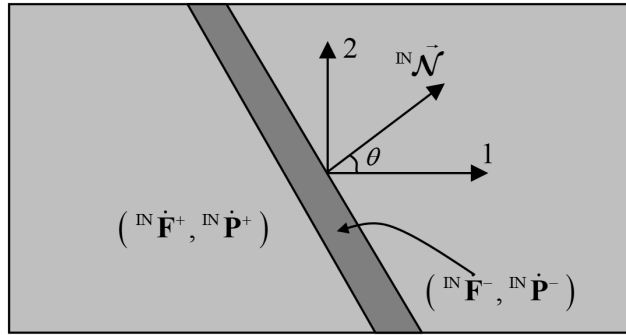


Fig. 2.3. Illustration of the Rice bifurcation criterion.

2.4. Results and discussions

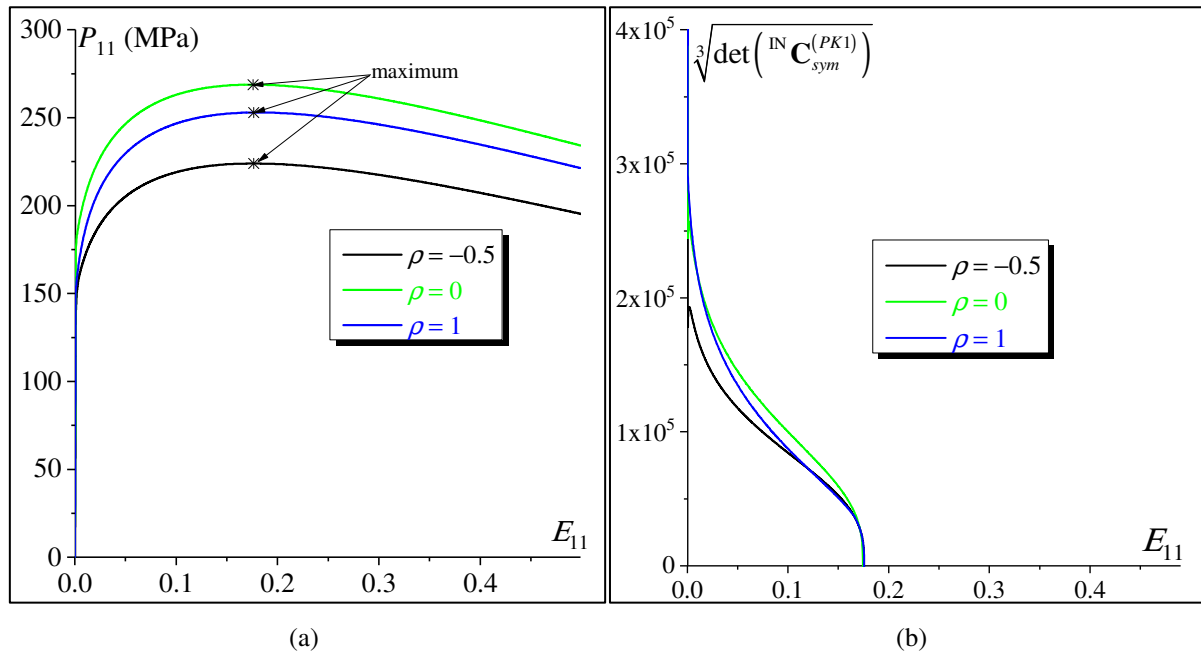
2.4.1. Results for homogeneous unit cell

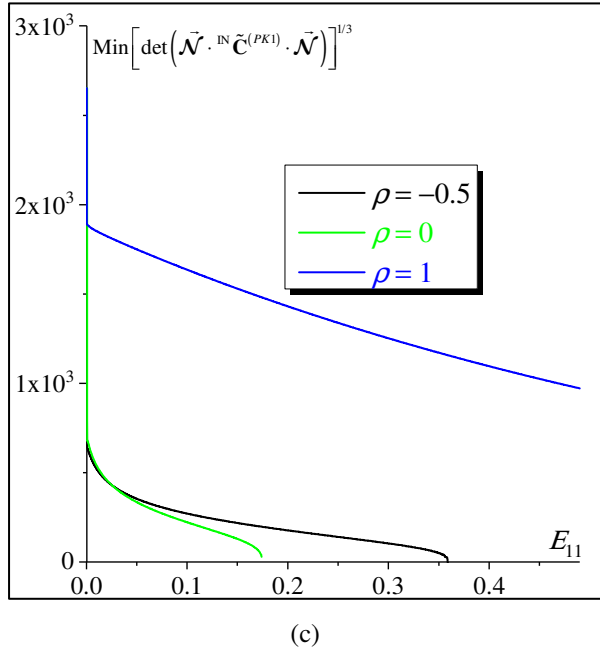
To provide a first validation to the developed numerical tools, attention is confined here to the prediction of the occurrence of necking in a homogeneous unit cell (without holes). For this simulation, the mechanical behavior is assumed to be plastically isotropic, following the von Mises yield function. In this context, the Lankford coefficients r_0 , r_{45} and r_{90} used in the Hill'48 yield function are set to 1. Elastic and isotropic hardening parameters (Eq. (2.7)) are reported in [Table 2.1](#). These parameters correspond to the aluminum alloy AA5052-O.

Table 2.1. Elastic and hardening material parameters

Elastic parameters		Isotropic hardening parameters		
E (GPa)	ν	K (MPa)	ε_0	n
210	0.3	363	0.008	0.184

The prediction of the onset of necking using the above-described diffuse and localized necking criteria is illustrated in Fig. 2.4 for three particular strain paths: $\rho = -0.5$, $\rho = 0$, and $\rho = 1$. In Fig. 2.4a, the evolution of the component P_{11} is plotted as a function of E_{11} ($= \ln(F_{11})$). For MFC, the moment when P_{11} reaches its maximum value is considered as indicator of the onset of diffuse necking. For the three strain-path ratios considered, the corresponding stress-strain curves are clearly distinct, but the maximum values for P_{11} are reached at the same strain level, which is equal to $n - \varepsilon_0$ (≈ 0.176). The evolution of the cubic root of the determinant of the symmetric part ${}^{\text{IN}}\mathbf{C}_{\text{sym}}^{(\text{PK1})}$ of ${}^{\text{IN}}\mathbf{C}^{(\text{PK1})}$ is plotted as a function of E_{11} in Fig. 2.4b. The onset of necking starts, according to the GBC, when the smallest eigenvalue of ${}^{\text{IN}}\mathbf{C}_{\text{sym}}^{(\text{PK1})}$ vanishes, or in an equivalent way, when ${}^{\text{IN}}\mathbf{C}_{\text{sym}}^{(\text{PK1})}$ becomes singular (as ${}^{\text{IN}}\mathbf{C}_{\text{sym}}^{(\text{PK1})}$ is positive definite before it becomes singular). As clearly shown in this figure, the predicted limit strains E_{11} are strictly the same (equal to $n - \varepsilon_0 \approx 0.176$) for the three different strain-path ratios considered. The predictions based on RBC are reported in Fig. 2.4c, where the evolution of the cubic root of the minimum of the determinant of the acoustic tensor, over all possible orientations ${}^{\text{IN}}\vec{\mathcal{N}}$ for the localization band, is plotted as a function of E_{11} . It can be seen that, irrespective of the selected strain path, the minimum of that determinant abruptly drops during the transition from elastic to plastic regime. This determinant vanishes for the strain-path ratios $\rho = -0.5$ and $\rho = 0$ at strain levels equal to $2(n - \varepsilon_0)$ and $n - \varepsilon_0$, respectively. By contrast, this determinant remains strictly positive, even for very large strain levels, for the equibiaxial tension state ($\rho = 1$). Consequently, localized necking cannot be predicted by RBC for this particular strain-path ratio.





(c)

Fig. 2.4. Prediction of necking, for three particular strain-path ratios, using the different necking criteria: (a) MFC; (b) GBC; (c) RBC.

Fig. 2.5 provides the FLDs predicted by using the three different necking criteria. As can be seen, the forming limit curve given by MFC reveals to be a horizontal line, which also coincides with the predictions given by GBC for the three particular strain-path ratios: $\rho = -0.5$; $\rho = 0$, and $\rho = 1$ (see, e.g., [Abed-Meraim et al., 2014](#)). The RBC is able to determine limit strains at localized necking only in the range of negative strain-path ratios. In the latter range, the FLD takes the form of a straight line, along which $E_{11}(\rho)$ is equal to $(n - \varepsilon_0)/(1 + \rho)$. This result may be viewed as an extension of the results demonstrated for the particular case of rigid-plastic behavior. Indeed, the adopted elastoplastic behavior model can be reduced to a rigid-plastic one by setting ε_0 to 0. In this limiting case of rigid-plasticity, [Hill \(1952\)](#) has demonstrated that $E_{11}(\rho)$ is equal to $n/(1 + \rho)$ in the left-hand side of the FLD. This classical result has also been confirmed by the recent numerical investigations reported in [Ben Bettaieb and Abed-Meraim \(2015\)](#). For the positive strain-path ratios, the limit strains predicted by RBC are so unrealistically high that they cannot be represented in Fig. 2.5. It is also clearly shown from Fig. 2.5 that the three necking criteria provide the same limit strain for the plane-strain state ($\rho = 0$). As a preliminary conclusion, the results given in Fig. 2.5 represent a first partial validation for the developed numerical tools.

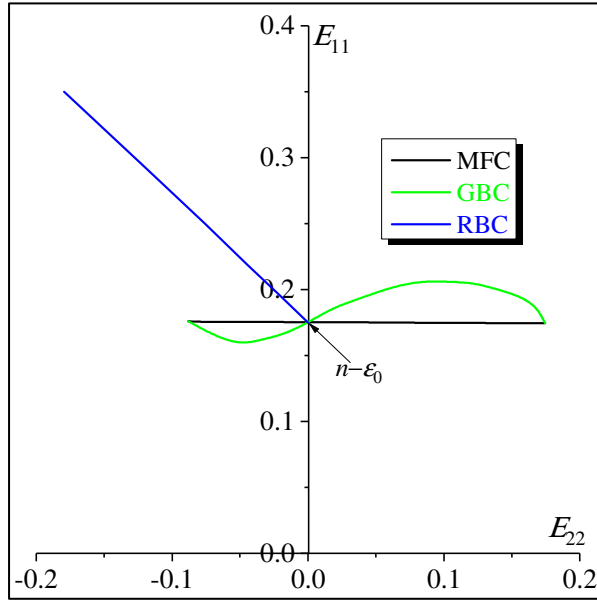


Fig. 2.5. FLDs for a homogeneous sheet (without holes), as predicted by MFC, GBC, and RBC.

2.4.2. Comparison with Tvergaard's results

To further validate the developed numerical approach, our numerical predictions have been compared with those published in [Tvergaard \(1981\)](#). To this aim, our numerical tools have been slightly modified and adapted to be conformal with the simulations performed in [Tvergaard \(1981\)](#). For instance, the plane-strain condition is applied in the thickness direction of the sheet, instead of the plane-stress condition commonly adopted so far. Accordingly, the component F_{33} is set to 1 all along the loading ([Fig. 2.6](#)). Also, the material parameters and the finite element mesh discretization used in these comparisons coincide with those considered in [Tvergaard \(1981\)](#). In these comparisons, three different loading states have been considered:

- Uniaxial tension state: for this loading, the component P_{22} is set to 0 ([Fig. 2.6](#)). Consequently, F_{22} is left free. The loading is applied in direction 1, where component F_{11} increases monotonically from 1 (which corresponds to $E_{11} = 0$) to 2.
- Plane-strain tension state: for this loading, the component F_{22} is set to 1 ([Fig. 2.6](#)). Consequently, P_{22} is left free, and component F_{11} increases monotonically from 1 (which corresponds to $E_{11} = 0$) to 2.
- Proportional in-plane stressing: for this loading, the ratio P_{22} / P_{11} of the in-plane components of the first Piola–Kirchhoff stress tensor is set to 2 ([Fig. 2.6](#)). To apply this loading, component F_{22} increases monotonically from 1 to 2. The application of this proportional in-plane stressing has required further numerical developments. Indeed, the toolbox *Homtools* used to apply the macroscopic boundary conditions allows us to easily manage strain-driven boundary conditions.

However, for stress-driven boundary conditions, some improvements and extensions are needed. In fact, the application of proportional stressing has been made possible by implementing in ABAQUS a procedure based on the coupling of the *Homtools* and the user-subroutine MPC (*Multi-point constraints*). The use of the MPC subroutine allows us to update the value of component F_{11} in order to ensure that ratio P_{22} / P_{11} remains equal to 2 during the loading. The interested reader may refer to Chapter 3 to better understand how proportional stressing is applied on the unit cell. The new results further confirm the previous and current trends showing the perfect agreement between our numerical predictions and those obtained in Tvergaard (1981).

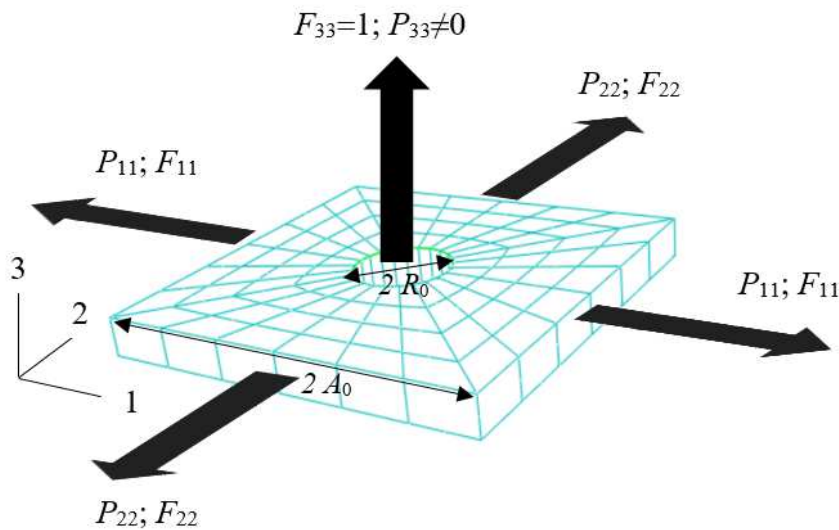


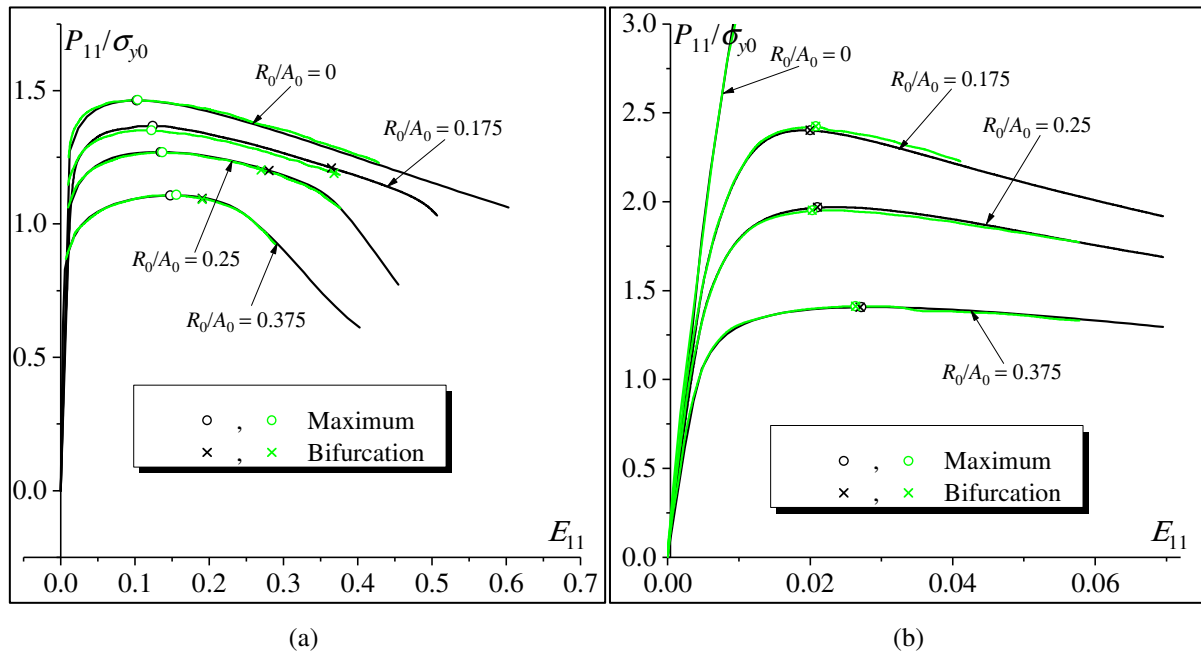
Fig. 2.6. Initial unit cell used for the comparisons with Tvergaard's results.

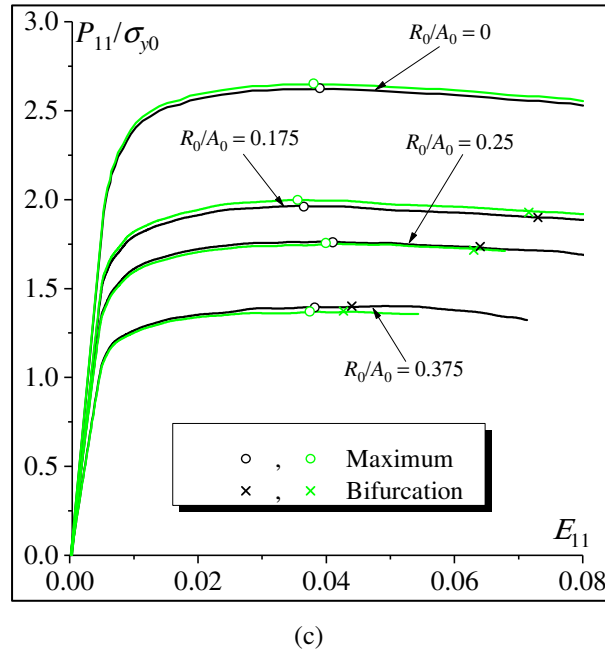
The comparisons between our predictions (in black color) and Tvergaard's results (in green color) are given in Fig. 2.7. In this figure, the component P_{11} normalized by the initial yield stress is plotted as a function of E_{11} . To analyze the effect of the hole radius on the instability predictions (such as shear band bifurcation), four values for the ratio R_0 / A_0 are taken (Fig. 2.6): 0 (which corresponds to homogeneous unit cell); 0.175; 0.25 and 0.375. From Fig. 2.7, the following conclusions can be drawn:

- The plots in Fig. 2.7 show that the level of the maximum stress P_{11} is significantly reduced when increasing the hole diameter. This observed general trend is common to all of the simulations and for both loading situations (i.e., uniaxial tension state, and plane-strain tension state).
- All of our predictions agree very well with those published in Tvergaard (1981). Indeed, the $P_{11} - E_{11}$ curves are perfectly superposed. Furthermore, the bifurcation points that we predict here by using the RBC are identically the same as those predicted in Tvergaard (1981) based on bifurcation theory with instability modes in the form of shear band localization.
- For the uniaxial tensile state (Fig. 2.7a), the strains corresponding to the maximum nominal stress and those associated with bifurcation exhibit opposite evolution with the increase of the ratio

R_0 / A_0 . Indeed, while the strains corresponding to the maximum nominal stress increase when increasing the void volume fraction, the opposite trend is observed for the bifurcation critical strains.

- For the plane-strain tension state (Fig. 2.7b), when the void volume fraction is set to zero (i.e., homogeneous sheet), the nominal stress does not reach a maximum, and also bifurcation is not predicted. In this case, the strain components E_{22} and E_{33} remain equal to 0 and the sheet is deformed with a very small volume change, which is entirely due to elastic compressibility (as plastic deformation is taken to be without volume change). Consequently, a very important stress P_{11} is required to slightly deform the sheet, and this stress level cannot decrease. For the other ratios ($R_0 / A_0 \neq 0$), maximum nominal stress and bifurcation are more easily reached, as the volume change of the perforated sheet is allowed by the evolution of the hole volume. For this plane-strain tension state, maximum nominal stress occurs simultaneously with bifurcation when $R_0 > 0$.
- The results provided in Fig. 2.7c show that bifurcation cannot be reached for homogeneous sheet (i.e., when ratio R_0 / A_0 is set to zero) with $P_{22} / P_{11} = 2$. This result is quite expectable considering the fact that for this loading, the strain-path ratio is positive (but not constant). For the other unit cells, the limit strains at bifurcation decrease when the hole radius increases. On the other hand, the strains corresponding to the maximum nominal stress are less sensitive to the hole radius, as shown in Fig. 2.7c.





(c)

Fig. 2.7. Comparisons between the current numerical predictions and Tvergaard's results (in green color): (a) uniaxial tension state; (b) plane-strain tension state; (c) loading with proportional in-plane stressing $P_{22} / P_{11} = 2$.

2.4.3. Sensitivity study

In this section, a sensitivity study is conducted to analyze the effect of several design and mechanical parameters on the onset of necking in perforated sheets. When not explicitly specified, the material parameters of the dense matrix are the same as those given in Table 2.1. A preliminary sensitivity analysis has been performed to investigate the influence of the selected finite element mesh on the necking predictions. The choice of mesh discretization has been mainly dictated by seeking good compromise between the CPU time required for the computations and the accuracy of the predictions. For the sake of conciseness, the details of this preliminary study are not discussed in the current chapter.

2.4.3.1. Effect of the hole radius

In this subsection, the hole is assumed to be initially circular and the influence of its initial radius R_0 on the forming limit diagrams is analyzed (Fig. 2.8). The results of this analysis are shown in Fig. 2.9. Contrary to the case of zero void volume fraction (i.e., homogeneous unit cell without holes, see Fig. 2.5), localized necking for perforated unit cell is predicted at realistic (finite) limit strains, even in the range of positive strain-path ratios (see right-hand side of the FLDs in Fig. 2.9c). Indeed, the presence of holes induces some softening, which allows promoting the occurrence of localized necking (Tvergaard, 1981; Koplik and Needleman, 1988). Clearly, the necking limit strains decrease on the whole when increasing the size of the holes, which corresponds to larger void volume fraction. As clearly shown in Fig. 2.9, the effect of the hole radius on the necking limit strains is much more pronounced in the range of positive strain-path ratios. This common trend, which is observed for the three adopted necking criteria (see Fig. 2.9), is directly attributable to the hole growth, which is mainly dependent on

the applied loading path as shown in Fig. 2.10. To further explain this point, let us introduce the surface growth factor $\Delta S = S - S_0$, with S_0 and S denoting the initial and current hole surface in the plane of the sheet, respectively. One can easily derive the following expression for ΔS :

$$\Delta S = \left(e^{(1+\rho)E_{11}} - 1 \right) S_0. \quad (2.41)$$

Hence, the surface growth factor increases with the strain-path ratio (and also with the triaxiality factor). For negative strain-path ratios (especially near the uniaxial tensile state, as illustrated in Fig. 2.10b), ΔS is relatively small and the loading path is characterized more by a change in the hole shape than a change in the hole surface. By contrast, for equibiaxial tensile state, the hole remains circular and the loading path exhibits the largest surface growth factor (Fig. 2.10c).

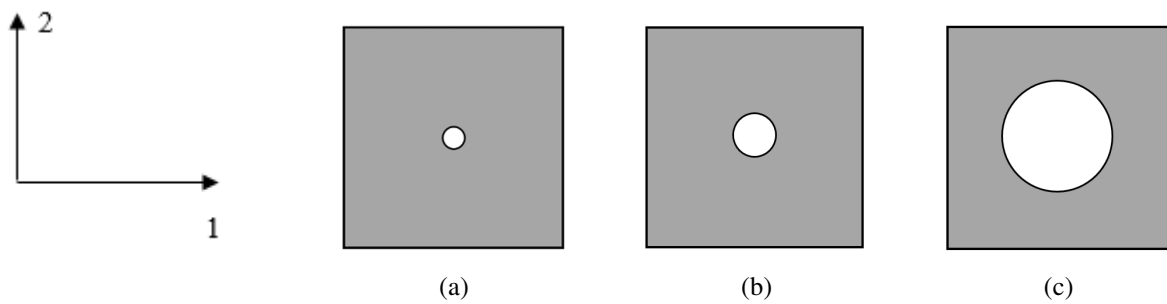
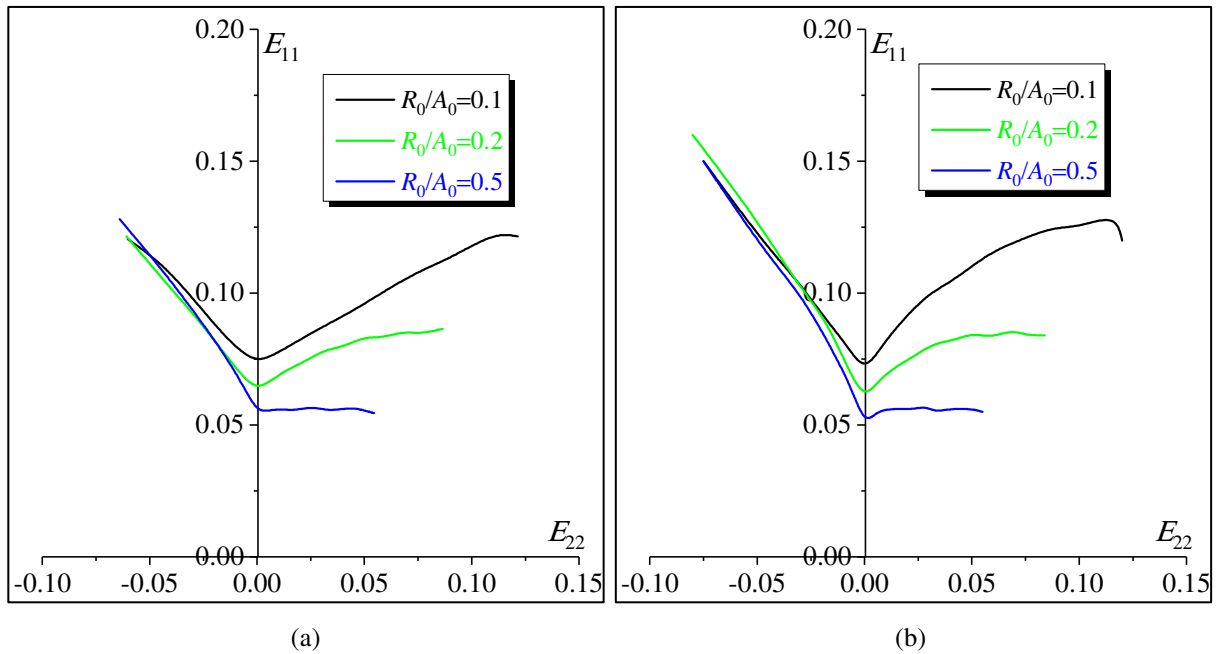
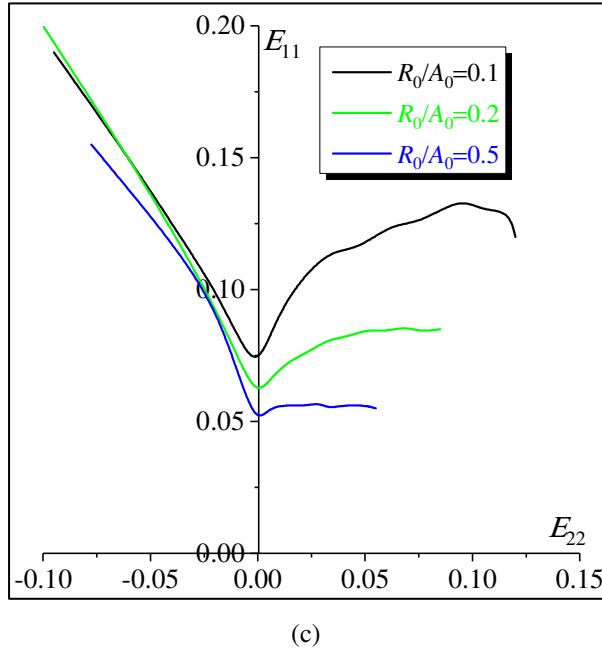


Fig. 2.8. Unit cells with different circular hole initial radii: (a) $R_0 / A_0 = 0.1$; (b) $R_0 / A_0 = 0.2$; (c) $R_0 / A_0 = 0.5$.





(c)

Fig. 2.9. Effect of the hole radius on the FLDs predicted by: (a) MFC; (b) GBC; (c) RBC.

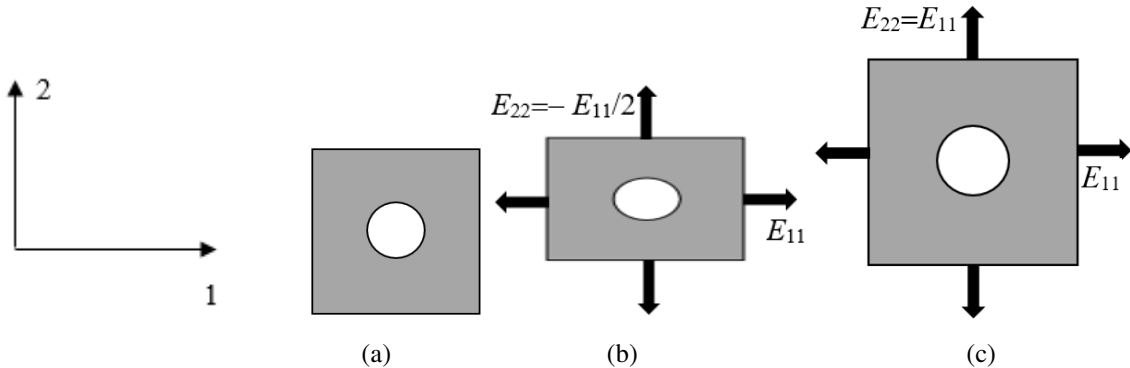


Fig. 2.10. Schematic evolution of the unit cell: (a) initial configuration; (b) current configuration for $\rho = -0.5$; (c) current configuration for $\rho = 1$.

2.4.3.2. Effect of the elliptical hole aspect ratio

It is expected that the hole shape has a significant impact on the mechanical behavior and on the development of necking in perforated sheets. To investigate this aspect, our interest is firstly centered on perforated sheets with elliptical holes. We assume that the minor (resp. major) axis of the hole is aligned with the direction of major (resp. minor) strain E_{11} (resp. E_{22}), as illustrated in Fig. 2.11. The initial hole shape is characterized by the initial aspect ratio b_0 / a_0 , where b_0 (resp. a_0) is the major (resp. minor) radius of the hole. In the current simulations, we have used three different values for the ratio b_0 / a_0 : 1 (which corresponds to a circular hole), 2 and 3 (see Fig. 2.11). The initial radii a_0 and b_0 are determined in such a way that the hole initial surface is the same for the three different configurations. From Fig. 2.12, it is clearly shown that the necking limit strains decrease with an increase in the initial aspect ratio b_0 / a_0 . This result also confirms the trends observed in several pioneering

studies, devoted to 3D voided materials and focused on some particular loading paths, which state that void-induced softening is mainly dependent on the ellipsoidal void aspect ratio (see for instance, Pardoen and Hutchinson, 2000; Keralavarma and Benzerga, 2010). These studies have revealed that the increase in void aspect ratio induces accelerated void growth, thus resulting in earlier occurrence of softening.

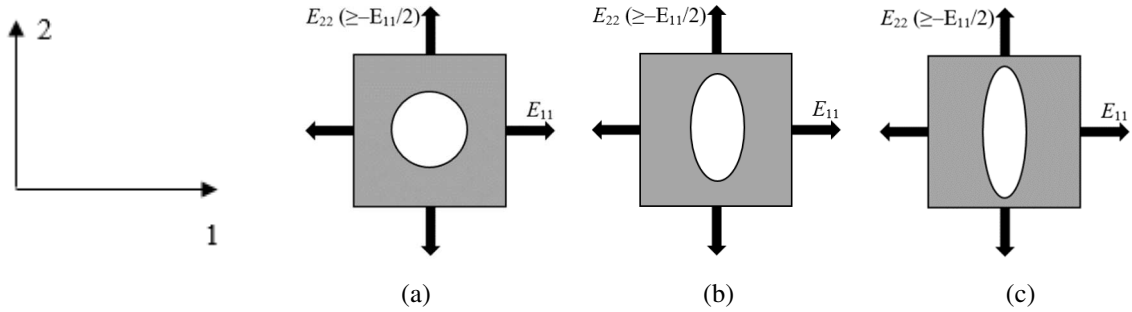
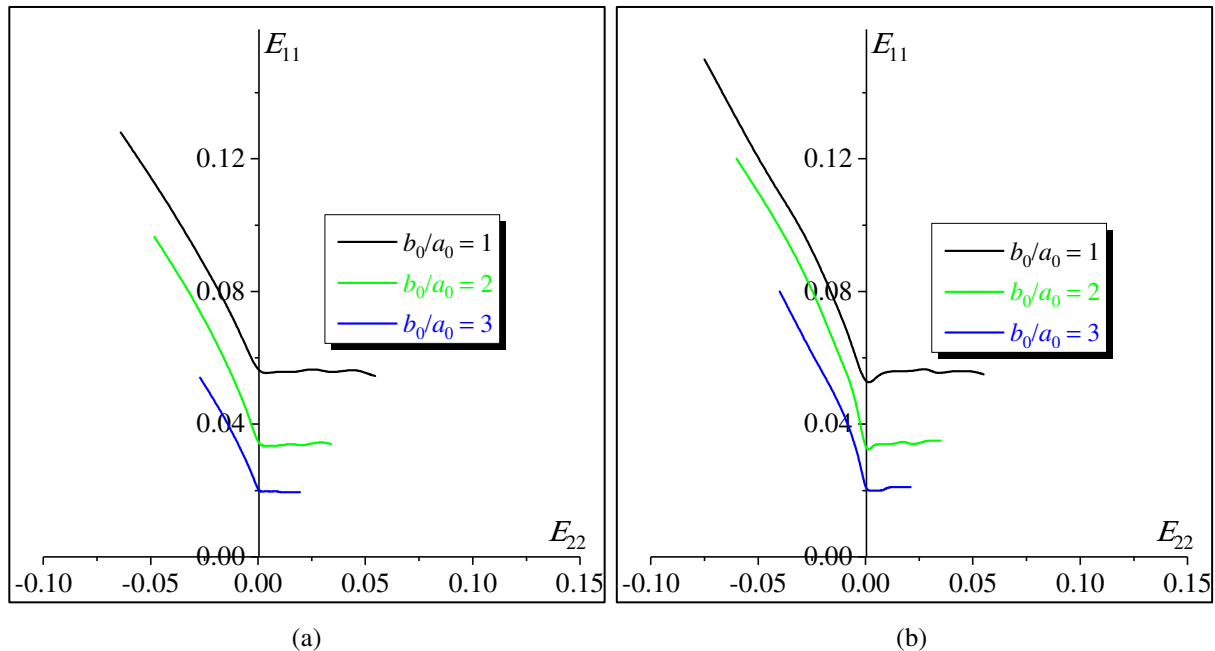
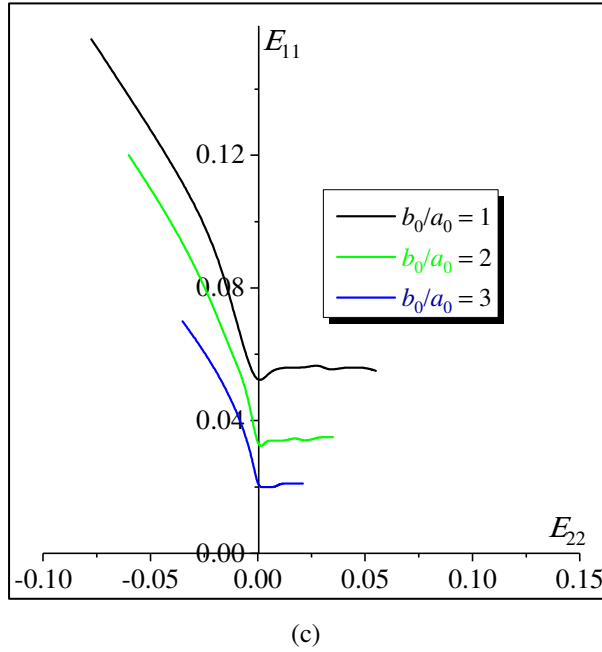


Fig. 2.11. Unit cells with different elliptical hole initial aspect ratios: (a) $b_0/a_0 = 1$; (b) $b_0/a_0 = 2$; (c) $b_0/a_0 = 3$.





(c)

Fig. 2.12. Effect of the hole aspect ratio on the FLDs predicted by: (a) MFC; (b) GBC; (c) RBC.

2.4.3.3. Effect of the elliptical hole orientation

In the current subsection, the effect of the elliptical hole orientation on the necking predictions is investigated. To this end, the initial orientation θ_0 , defined by the angle between the major axis of the hole and the major strain direction, is varied with three values considered for θ_0 : 0° (Fig. 2.13a), 45° (Fig. 2.13b) and 90° (Fig. 2.13c). Note that the initial shape and aspect ratio of the hole are kept the same for all of the simulations in this subsection. By analyzing the results of Fig. 2.14, the following conclusions can be drawn:

- The most favorable hole orientation, in terms of necking resistance, is 45° . This result may be explained by the fact that, for this orientation, the applied loading leads to a change in the hole shape and orientation without significant growth. Indeed, in this case, the hole is subject to shear-type loading, as its principal axes are oriented at 45° with respect to the principal strain directions. Consequently, necking is delayed with significant improvement in the necking limit.
- The hole orientation at 0° results in higher necking limit strains than those obtained with the orientation at 90° , as demonstrated in Fig. 2.14. This result can be easily understood through the analysis conducted in Section 2.4.3.2. In fact, holes with initial orientations at 0° and 90° may be viewed as elliptical holes with aspect ratio b_0/a_0 equal to $1/2$ and 2 , respectively (see the analysis in Section 2.4.3.2).
- For the particular case of equibiaxial tension strain path, the necking limit strains predicted by bifurcation (i.e., GBC and RBC) are the same for orientations 0° and 90° , as shown in Fig. 2.14b

and Fig. 2.14c. This result is obvious considering that these two orientations are equivalent, as E_{11} is equal to E_{22} . This is obviously not the case when the MFC is used.

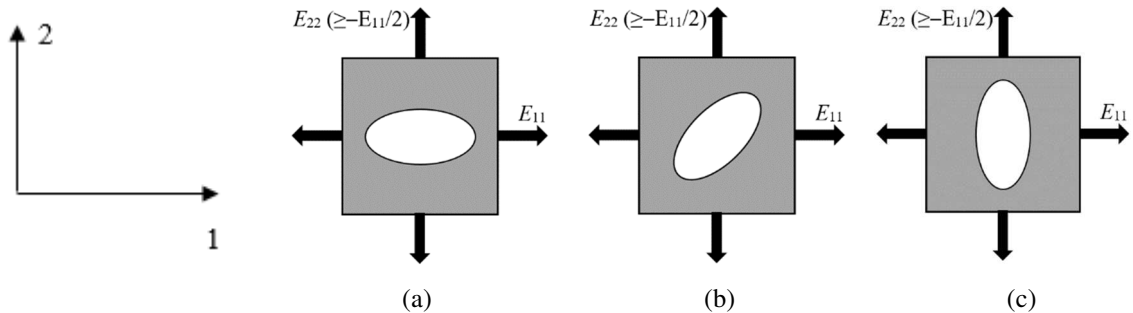


Fig. 2.13. Unit cells with different elliptical hole initial orientations: (a) $\theta_0 = 0^\circ$; (b) $\theta_0 = 45^\circ$; (c) $\theta_0 = 90^\circ$.

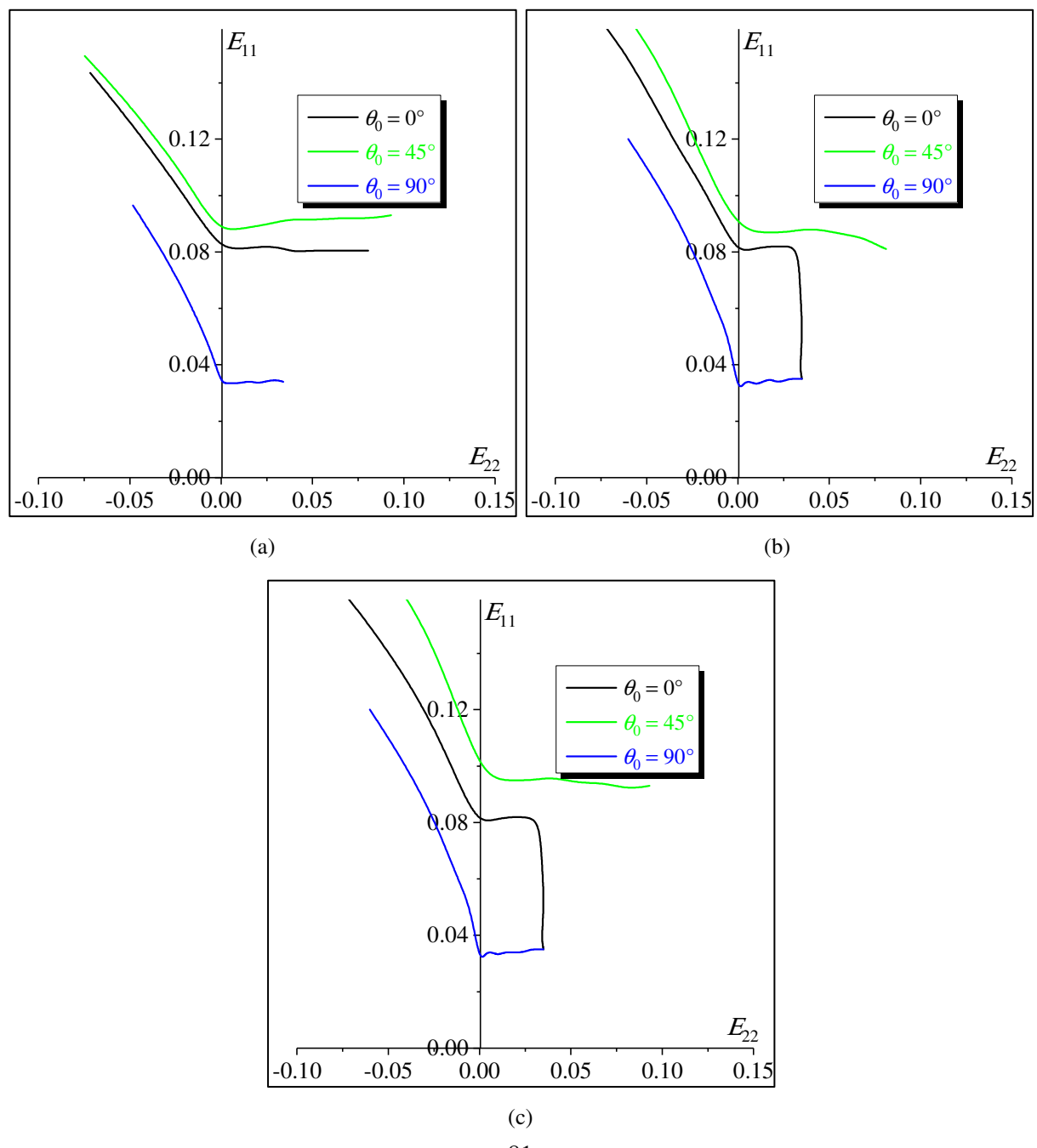


Fig. 2.14. Effect of the elliptical hole orientation on the FLDs predicted by: (a) MFC; (b) GBC; (c) RBC.

2.4.3.4. Effect of the hole shape

In the current subsection, the effect of the hole shape on the prediction of necking is numerically investigated. To this aim, three initial hole shapes are used and compared in the simulations: circular, elliptical and square (see illustration in Fig. 2.15). In these simulations, the initial hole surface is taken the same for the different unit cells. The initial aspect ratio b_0 / a_0 of the elliptical hole is set to 2. The results reported in Fig. 2.16 reveal that the necking limit strains predicted for the unit cell with square hole are the highest, regardless of the adopted necking criterion and of the strain-path ratio considered. These necking predictions are consistent with the numerical results obtained by Jia et al. (2002) and Iseki et al. (1989) and confirming the excellent formability of perforated sheets with square holes, as compared to those with circular or elliptical holes for the same hole surface.

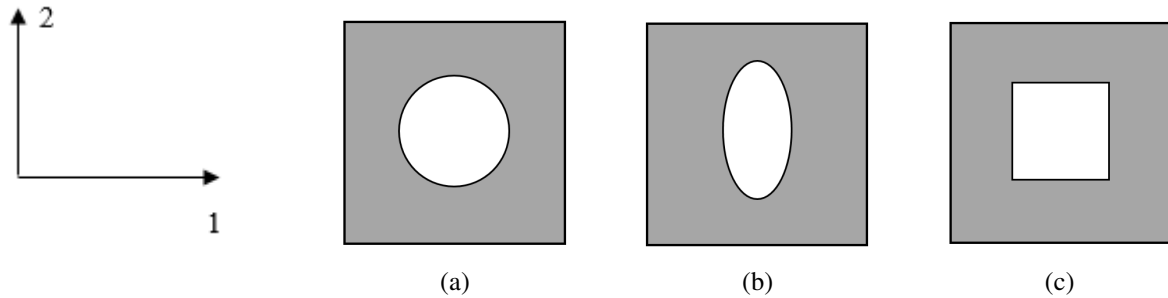
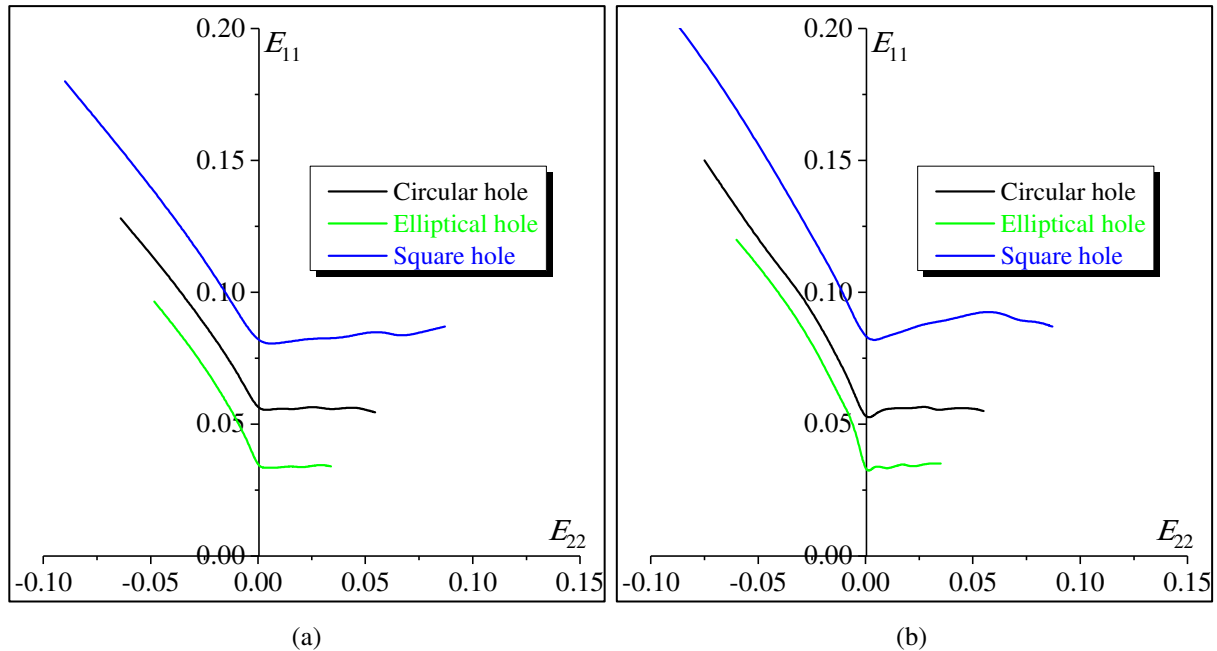
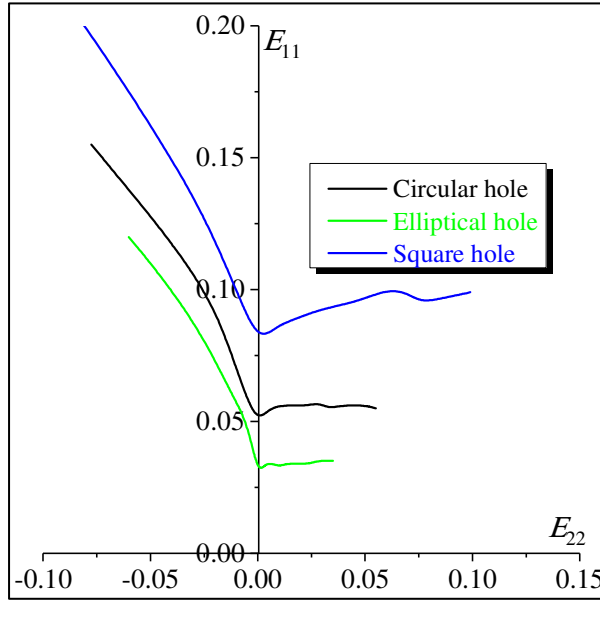


Fig. 2.15. Unit cells with different initial hole shapes: (a) Circular; (b) Elliptical; (c) Square.





(c)

Fig. 2.16. Effect of the hole shape on the FLDs predicted by: (a) MFC; (b) GBC; (c) RBC.

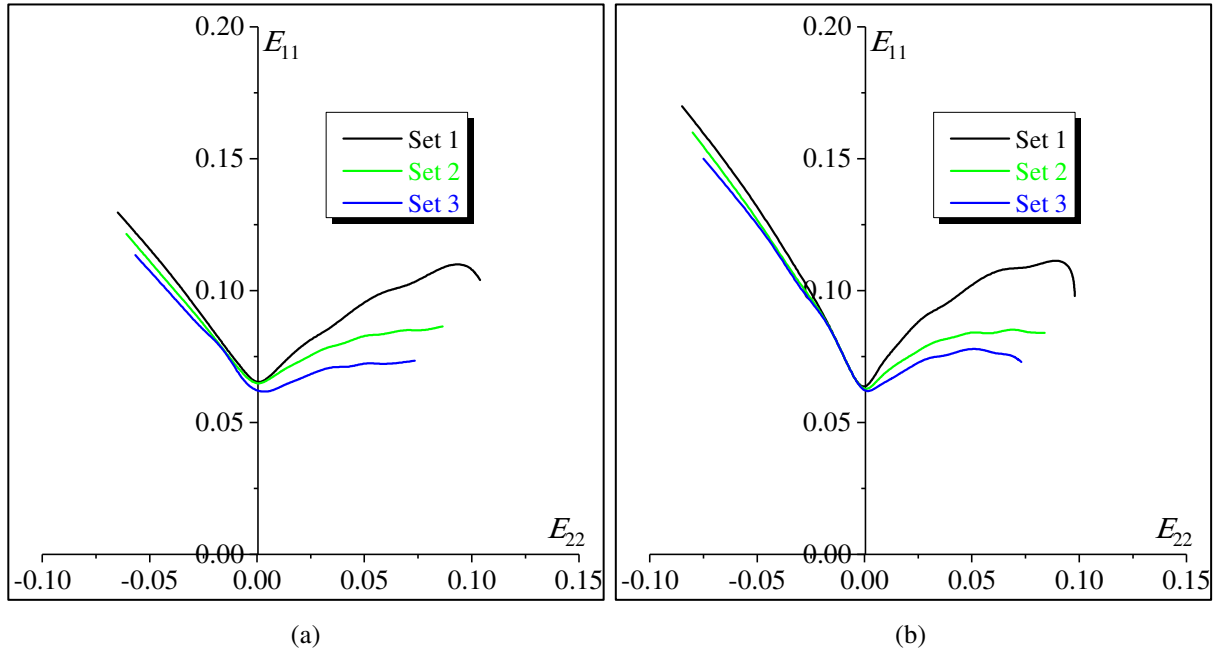
2.4.3.5. Effect of the plastic anisotropy of the metal matrix

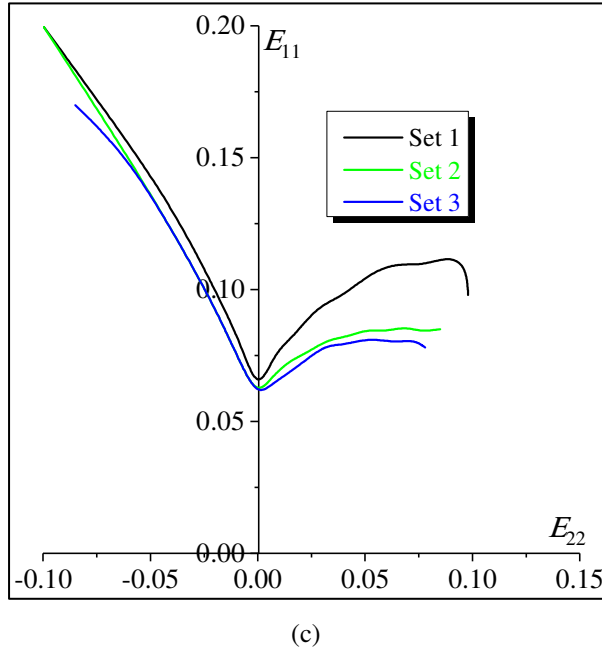
In the previous subsections (2.4.3.1 to 2.4.3.4) attention has been focused on the analysis of the effect of the hole geometric characteristics on the onset of necking in perforated sheets. In those subsections the plasticity of the dense matrix has been assumed to be isotropic, and described by the von Mises yield function. On the other hand, it is well recognized that plastic anisotropy has a significant effect on the necking limit strains of metal sheets (without perforation), especially in the range of positive strain-path ratios (see, e.g., Barlat, 1987). The objective of this subsection is to numerically analyze the effect of the plastic anisotropy of the metal matrix on the occurrence of necking in perforated sheets. To this end, the Hill'48 yield function is used to model the metal matrix plastic anisotropy with three different sets of Lankford's coefficients (r_0, r_{45}, r_{90}), as reported in Table 2.2. The rolling direction of the metal sheet is assumed to coincide with the major strain direction. Set 1 typically corresponds to plastic anisotropy of aluminum alloys (Chiba et al., 2015). By contrast, set 2 corresponds to an isotropic dense matrix. As to the parameters of set 3, the latter are virtual and are chosen purposely to better understand the effect of plastic anisotropy on the predicted necking limit strains. The impact of these different sets of anisotropy parameters on the shape of the metal matrix yield surface is shown in Fig. 2.17.

Table 2.2. Lankford's coefficients

	r_0	r_{45}	r_{90}
set 1	0.585	0.571	0.766
set 2	1	1	1
set 3	1.5	1.5	1.5

All of the simulations in this subsection pertain to unit cells with circular hole, where the ratio R_0 / A_0 is set to 0.2. Fig. 2.17 illustrates the effect of the Lankford coefficients on the prediction of forming limit diagrams. As revealed in this figure, the necking limit strains predicted by the different necking criteria are not very sensitive to the values of the Lankford coefficients in the range of negative strain-path ratios. By contrast, this sensitivity to plastic anisotropy is more pronounced in the range of positive strain-path ratios. Furthermore, it is clear from Fig. 2.17 that *set 1* of Lankford's coefficients results in higher necking limit strains than *set 2*, which in turn leads to necking limit strains higher than those predicted by *set 3*. These numerical predictions of necking are likely to be correlated with the sharpness of the associated yield surfaces. To further assess such a correlation, we plot in Fig. 2.18 the yield surfaces of the metal matrix that correspond to the above-defined sets of Lankford coefficients. Similar to some studies in the literature (see, e.g., Wu et al., 2004), these yield surfaces are normalized by their corresponding equibiaxial yield stresses ($\sigma_{11} = \sigma_{22}$), in order to emphasize their differences in terms of sharpness. In accordance with several literature results, a correlation between the overall level of the FLDs, in the neighborhood of equibiaxial tension, and the degree of sharpness of the associated yield surfaces may be clearly established. The sharper the yield surface, the lower the corresponding FLD. The FLD predictions reported in Fig. 2.17 are consistent with the above discussion on the sharpness of the yield surface (see Fig. 2.18), and confirm once again the important role of material anisotropy in the modeling of forming limits of perforated sheets.





(c)

Fig. 2.17. Effect of the plastic anisotropy of the metal matrix on the FLDs predicted by: (a) MFC; (b) GBC; (c) RBC.

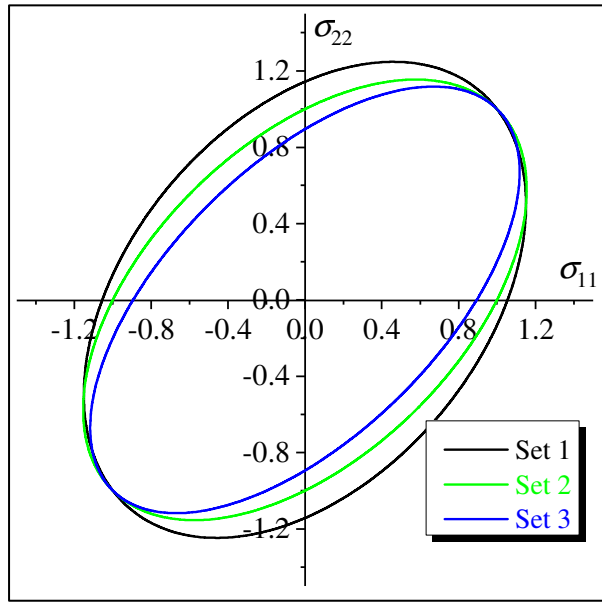


Fig. 2.18. Impact of the Lankford coefficients on the shape of the dense matrix yield surface.

2.4.3.6. Effect of the hardening parameters of the metal matrix

In this subsection, we investigate the effect of the isotropic hardening parameters (the hardening exponent n and the initial yield strength σ_{y0} / E) of the dense matrix on the mechanical behavior of the perforated sheets (stress-strain curves and ductility limits). All the simulations presented in this section are made for unit cells with circular holes, where the ratio R_0 / A_0 is set to 0.2 and the plastic behavior of the dense matrix is assumed to be isotropic (i.e. $r_0 = r_{45} = r_{90} = 1$). The objective of this section is twofold. Firstly, it aims to better validate the proposed approach by comparing our predictions

(black color) with the results published in Tvergaard (1981) (green color). The results presented in Fig. 2.19a and Fig. 2.20a confirm again the good agreement between the two sets of results. This further validates the developed approach. Secondly, this section analyzes the effect of the hardening parameters on the level and the shape of forming limit diagrams. On the one hand, it is clearly shown in Fig. 2.19b that the ductility limits, obtained by the different necking criteria, strongly increase when increasing the hardening exponent n (see Eq. (2.7)). In connection with Fig. 2.19b, some numerical investigations (see, e.g., Hutchinson et al., 1978; Ben Bettaieb and Abed-Meraim, 2015) also support the trend according to which low hardening materials are more prone to plastic instabilities. On the other hand, the effect of initial yield stress of the dense matrix on the ductility of the unit cell seems to be relatively small and dependent on the applied strain path, as demonstrated in Fig. 2.20b.

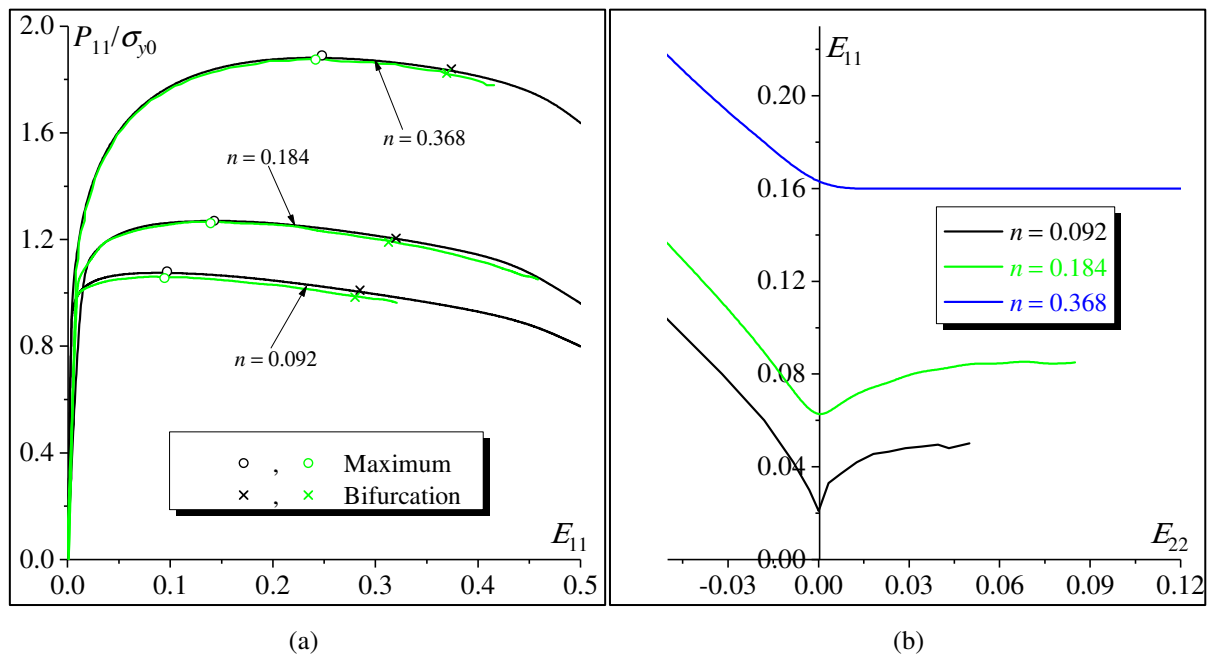


Fig. 2.19. Effect of the hardening exponent on: (a) the macroscopic stress–strain curves; (b) the FLDs predicted by the RBC.

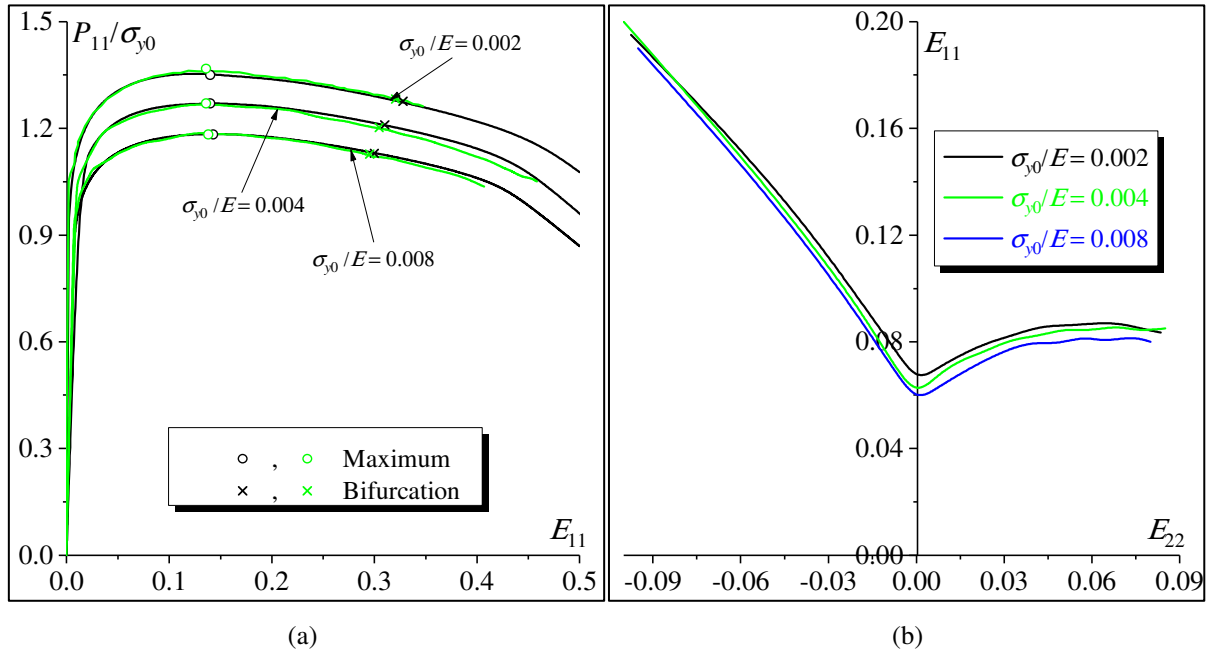


Fig. 2.20. Effect of initial yield strength on: (a) the macroscopic stress–strain curves; (b) the FLDs predicted by the RBC.

2.4.3.7. Effect of the macroscopic boundary conditions

In order to investigate the effect of the macroscopic boundary conditions on the mechanical behavior (stress–strain curves and ductility limits) of perforated sheets, the results obtained by the periodic boundary conditions (briefly called PBCs) are compared with those obtained by the application of the kinematic boundary conditions (briefly designated KBCs). It must be noted that the KBCs can be viewed as a particular case of the PBCs, where the periodic displacement field \mathbf{u}_{per} (see Eq. (1.19)) is set to $\mathbf{0}$.

Consequently, the deformation gradient on the boundary of the unit cell is assumed to be homogeneous ($\mathbf{f} = \mathbf{F}$ over the boundary of the unit cell). Also, the KBCs (or mixed with PBCs) have been usually adopted in the study of the mechanical behavior of voided materials (see, e.g., Liu et al., 2016). However, the different boundary conditions lead to different macroscopic responses and consequently different evolutions of the macroscopic tangent modulus. To couple the homogenization approach based on the KBCs with the bifurcation approach, the condensation procedure, which has been presented in Section 2.2.4 and Section 1.4.2 and used to derive the macroscopic tangent modulus, has been modified. More details about these modifications are provided in Miehe (2003). The results displayed in Fig. 2.21 highlight the effect of these boundary conditions on the strain–stress curves as well as on the level and the shape of the forming limit diagrams. Especially, one can observe that the ductility limits predicted by using the KBCs are higher than their counterparts determined by the PBCs. To plot the curves of Fig. 2.21, the hole is assumed to be circular, with the ratio R_0 / A_0 set to 0.2, and the metal matrix material parameters are taken to be the same as those reported in Section 2.4.1.

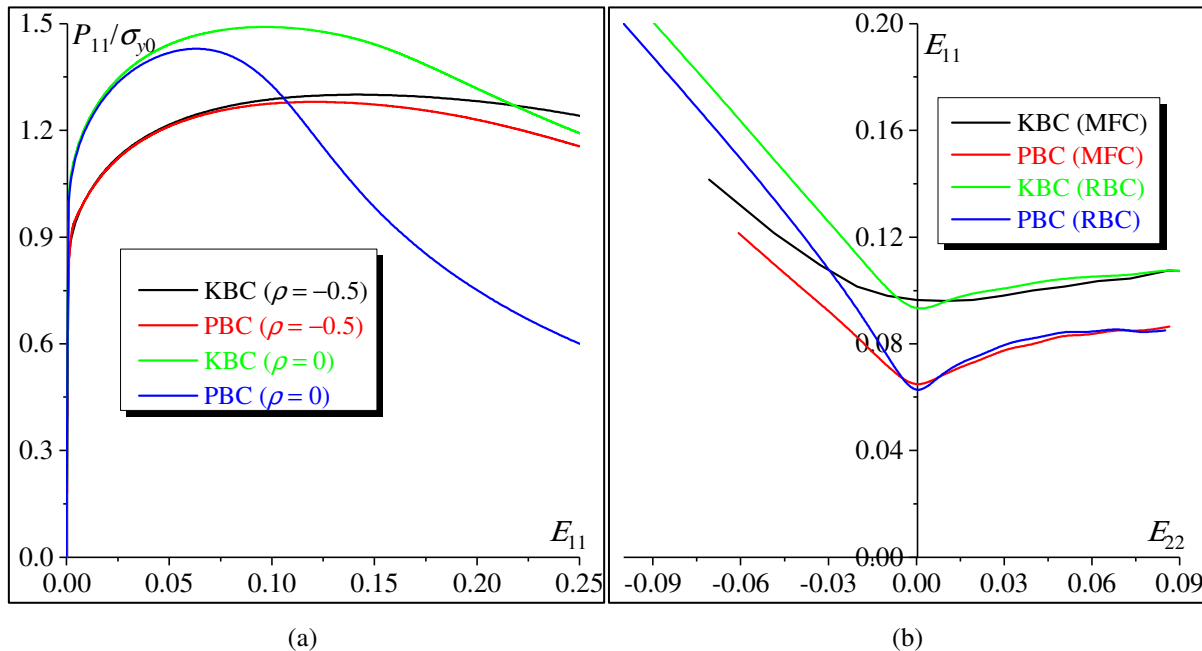


Fig. 2.21. Effect of the macroscopic boundary conditions on: (a) the macroscopic stress–strain curves; (b) the FLDs predicted by the MFC and RBC.

2.4.3.8. Conclusions common to the various sensitivity studies

In addition to the conclusions revealed in the previous subsections, which are specific to each sensitivity study, more common conclusions (valid for the various sensitivity studies) can be drawn:

- For all of the strain paths of the FLD (aside from the particular plane-strain tension state), RBC predicts limit strains that are strictly higher than those predicted by MFC and GBC. This confirms the statement, widely recognized in thin sheet metals without holes, according to which diffuse necking occurs prior to localized necking, and extends this result to perforated sheets.
- For the particular strain path of plane-strain tension ($\rho = 0$), the three necking criteria investigated predict the same limit strains for perforated sheets, which is a well-admitted result in thin sheet metals without holes.
- The impact of hole perforation on the reduction of necking limit strains is more drastic in the range of positive strain-path ratios. This result may be explained by the fact that in this range of positive strain-path ratios, the hole growth phenomenon is more important than in the range of negative strain-path ratios.

2.5. Conclusions

In this chapter, several numerical tools have been developed to predict the occurrence of diffuse and localized necking in perforated sheets. These tools are based on the coupling between the periodic homogenization technique, used to numerically model the mechanical behavior of a representative volume element of the studied sheet, and three necking criteria. Various sensitivity studies have been

conducted to analyze the effect of some design and mechanical parameters on the onset of necking in thin perforated metal sheets. From all of the sensitivity studies, it appears that the geometric characteristics of the holes (size of radius, elliptical aspect ratio, orientation, shape) significantly influence the predicted necking limit strains. Furthermore, when the void volume fraction is reduced to zero (i.e., sheet metals without holes), localized necking is not predicted in the range of positive strain-path ratios, which confirms the central role of pre-existing voids as key destabilizing factor. It is also demonstrated that the hardening parameters and the plastic anisotropy of the dense metal matrix have a significant impact on the forming limit diagrams of perforated sheets. Such sensitivity studies and others may be advantageously used to select the optimal design and mechanical parameters leading to improved ductility and formability characteristics. In this sense, the developed numerical tools will be helpful in the design and the manufacture of perforated sheets as well as other heterogeneous materials (for example, the composite materials). Additionally, by using these developed tools, it will be more attractive to explore the ductile failure of voided materials (presented in Chapter 2) and polycrystalline aggregates (presented in Chapter 3).

Chapter 3

Investigation of the competition between void coalescence and macroscopic strain localization using the periodic homogenization multiscale scheme

3.1. Introduction

The ductility of thin metal sheets is often limited by the onset of ductile failure. Therefore, this phenomenon is central in structural integrity assessment together with corrosion and fatigue. Several possible failure scenarios may occur during plastic forming operations. In this field, one can quote at least three main scenarios. The first one takes place only for very pure metals. In this case, material fails without damage occurrence, owing to the absence of void nucleation sites. In such circumstances, the deformation state is homogeneous at the beginning of the loading, and the deformation starts concentrating in narrow bands at a certain limit strain. The initiation of such bands marks the development of localized necking in the material. The second scenario corresponds to the localization of plastic strain into narrow bands due to various possible softening mechanisms. Ultimately, following the accumulation of large plastic strains and the increase of stress triaxiality in the necked regions, voids nucleate, grow and coalesce to lead to final material failure. The third mechanism involves damage initiation within the material prior to plastic strain localization. The softening induced by the accumulated porosity is sufficient to counteract the strain hardening capacity of the material, which leads to plastic strain localization in narrow bands. An exhaustive analysis of the different failure mechanisms and the competition between them has been reported in [Teko\u0111lu et al. \(2015\)](#). It is now well known that

the initiation of ductile failure and the competition between void coalescence and plastic strain localization are sensitively dependent on the stress state applied to the metal sheets. To thoroughly analyze these fundamental aspects, various experiments have been designed in several pioneering contributions. In this area, one can quote [Bao and Wierzbicki \(2004\)](#), who have experimentally highlighted that void growth is the dominant failure mode for high stress triaxiality, while failure for low stress triaxiality is mainly governed by the combination of shear and void growth modes. These observations have been confirmed by [Barsoum and Faleskog \(2007\)](#), who have experimentally established that the onset of ductile failure is additionally dependent on the Lode parameter L , and not only on the stress triaxiality ratio T , especially for low values of T . The combined effect of stress triaxiality ratio and Lode parameter on the failure behavior has also been confirmed by the experimental program conducted by [Driemeier et al. \(2010\)](#). Although some observations have been ascertained by quantitative experimental testing, the comprehensive information about the underlying mechanisms, such as void growth, detection of localization in the specimens, and onset of void coalescence is still difficult to reach. To overcome this difficulty, profound knowledge on ductile failure in voided materials can mainly be acquired through theoretical approaches. These theoretical approaches can be classified into two main families: micromechanical models and numerical approaches based on unit cell computations.

The class of micromechanical models has been initiated by the pioneering work of [Gurson \(1977\)](#), who has derived, on the basis of limit-analysis theory, a plastic potential describing the plastic flow of a representative volume element defined by a spherical void embedded in a rigid perfectly plastic matrix. The original Gurson model is based on several restrictive assumptions such as: only the effect of void growth on the mechanical behavior is considered, the voids are initially spherical and remain spherical during the growth process, and the metal matrix is dense. These restrictive assumptions limit the Gurson model capability of providing accurate predictions of the mechanical behavior. Consequently, the original Gurson model has been largely extended in the literature. The most widely-known extension has been developed in [Tvergaard and Needleman \(1984\)](#) to consider the effect of nucleation of new voids and coalescence of existing voids on the mechanical behavior. In this extension, referred to as the GTN model, the final material failure has been predicted by using an empirical coalescence criterion. The numerical predictions based on the GTN model have been favorably compared with various experimental results ([Tvergaard and Needleman, 1984](#)). To analyze the competition between void coalescence and strain localization, the GTN model has been coupled in [Mansouri et al. \(2014\)](#) and [Chalal and Abed-Merai \(2015\)](#) with the Rice bifurcation theory ([Rudnicki and Rice, 1975; Rice, 1976](#)). This theory is based on the loss of ellipticity of the governing equations. Hence, to predict strain localization via the Rice bifurcation theory, the expression of the analytical tangent modulus needs to be derived from the constitutive equations. Despite their well-recognized interest, the extended versions of the Gurson model present some limitations and drawbacks in the analysis of the different metal failure scenarios (e.g., by void coalescence or strain localization). In fact, these models are generally based on

heuristic extensions of the original Gurson model without sound physical foundations. Furthermore, they involve additional material parameters to better reproduce the experimental results (such as parameters q_1 , q_2 and q_3 , or the threshold coalescence parameter f_c , introduced in the GTN model), and the identification of these parameters is not always easy and often questionable. Moreover, and despite the significant progress made in this area, these extended models are still unable to accurately consider relatively complicated situations, such as complex loadings (as these models are mainly based on axisymmetric loading), or realistic void shapes (as these models only consider spherical or ellipsoidal voids).

To overcome the above-mentioned drawbacks, a number of numerical approaches, based on unit cell finite element computations, have been developed in the literature. In these models, the ductile solid is represented by a spatially periodic arrangement of identical unit cells. Therefore, to describe the mechanical behavior of the whole solid, it is sufficient to consider a single unit cell, to which are applied relevant boundary conditions that accurately account for the effect of neighboring unit cells on the mechanical behavior (generally periodic or kinematic boundary conditions or a combination of them). Thanks to its reliability and flexibility, unit cell analysis has been widely employed to investigate the mechanical response of voided materials as well as the competition between the phenomena of void coalescence and strain localization. To thoroughly analyze this competition, it is essential to couple unit cell computations with relevant theoretical criteria and indicators that are able to accurately predict such material instability phenomena. Several indicators have been adopted in some contributions as void coalescence criteria, while in other contributions as strain localization criteria. Indeed, the distinction between the two phenomena and the corresponding criteria has not been clearly established in early investigations. These criteria can be categorized into four main families:

- *Initial imperfection criteria*: this approach, following the same spirit as the Marciak and Kuczyński method ([Marciak and Kuczyński, 1967](#)), assumes that strain localization occurs when the ratio η of the deformation gradient rate inside the unit cell to that outside the unit cell becomes sufficiently large. It has been first introduced by [Needleman and Tvergaard \(1992\)](#) within unit cell computations to predict the onset of strain localization. This indicator has subsequently been adopted by [Dunand and Mohr \(2014\)](#), [Dæhli et al. \(2017\)](#) and [Zhu et al. \(2018\)](#) to predict the onset of void coalescence. In [Dunand and Mohr \(2014\)](#) and [Dæhli et al. \(2017\)](#), the critical value of parameter η has been set to 5.0. However, [Zhu et al. \(2018\)](#) have set the critical value of η to 10.0 by following the work of [Barsoum and Faleskog \(2011\)](#). The above investigations reveal the difficulty in defining a unified and consistent threshold value for η . Moreover, the associated numerical predictions are generally sensitive to the mesh refinement, and this approach is not able to predict void coalescence for high stress triaxiality, and when the Lode parameter is close to 0, as demonstrated in [Barsoum and Faleskog \(2011\)](#). A very similar

criterion has been used in [Teko\u0111lu et al. \(2015\)](#) to predict the onset of strain localization in voided ductile solids.

- *Maximum load criteria:* this class of criteria has been initiated by [Tvergaard \(2012\)](#) and recently used by [Teko\u0111lu et al. \(2015\)](#), who have assumed that strain localization occurs when the equivalent macroscopic stress reaches its maximum value. More recently, [Guo and Wong \(2018\)](#) have proposed a strain localization indicator, which assumes that strain localization is met when the macroscopic force applied on the unit cell reaches its maximum value. The same authors have demonstrated that this criterion is equivalent to the Rice bifurcation approach ([Rudnicki and Rice, 1975; Rice, 1976](#)). It is interesting to note that this approach is somehow similar to the maximum force criterion developed by [Swift \(1952\)](#) to predict the occurrence of diffuse necking in thin metal sheets.
- *Energy-based criterion:* this approach, which has been initiated by [Wong and Guo \(2015\)](#), is exclusively adopted to predict the onset of void coalescence. It defines void coalescence as the point along the straining history where the ratio of overall elastic to plastic work rates of the unit cell attains a negative minimum value. This energy-based criterion has recently been utilized in several investigations to predict the onset of void coalescence ([Liu et al., 2016; D\u00e6hli et al., 2017; Guo and Wong, 2018; Luo and Gao, 2018](#)).
- *Void growth type criteria:* this family of criteria assumes that void coalescence occurs when void growth exhibits abrupt acceleration. [Teko\u0111lu et al. \(2015\)](#) have developed an indicator by closely following the same concept, which assumes that the onset of void coalescence is reached when the ratio of the maximum to the minimum effective plastic strain rate at the void surface first exceeds 15.0.

It is well known that the competition between the phenomena of macroscopic strain localization and void coalescence is generally dependent on the stress state, especially the stress triaxiality ratio T and the Lode parameter L . [Teko\u0111lu et al. \(2015\)](#) have demonstrated that macroscopic strain localization occurs prior to void coalescence at high stress triaxiality, while at lower stress triaxiality, the two phenomena occur simultaneously. Motivated by this latter investigation, [Guo and Wong \(2018\)](#) have shown that the onset of macroscopic strain localization and that of void coalescence are distinct, and that macroscopic strain localization plays a precursor role to void coalescence. Furthermore, they demonstrate that the difference in the strain levels corresponding to the onset of strain localization and void coalescence, respectively, decreases as stress triaxiality T increases, suggesting that both phenomena may occur simultaneously for sufficiently large T . These latter results are at variance with the trends obtained by [Teko\u0111lu et al. \(2015\)](#). This apparent contradiction is likely to be attributable to the difference between the void coalescence and strain localization criteria used in both investigations. For the considered ranges of stress triaxiality ($0.7 \leq T \leq 2.0$) and Lode parameter ($-1.0 \leq L \leq 1.0$), [Guo and Wong \(2018\)](#) have enumerated three possible scenarios associated with different ranges of T and

L : both macroscopic strain localization and void coalescence are possible (for $1.0 \leq T \leq 2.0$, independently of the value of L); macroscopic strain localization is possible, but void coalescence is not possible (for $0.8 \leq T \leq 0.9$ and $-1.0 \leq L \leq 0.4$); both macroscopic strain localization and void coalescence are not possible (for $T = 0.7$ and $-1.0 \leq L \leq 1.0$).

In the present chapter, unit cell computations are performed to investigate the competition between macroscopic strain localization and void coalescence for a wide range of loading states. The unit cell is subjected to fully periodic boundary conditions (PBCs), allowing for the accurate modeling of the interaction between the studied unit cell and the neighboring ones. This point represents the first main theoretical originality of the developed approach, as compared to the earlier ones. The periodic homogenization multiscale scheme is used for determining the macroscopic behavior of the unit cell. This multiscale scheme is coupled with the condensation technique, detailed in Chapter 1, to numerically evaluate the macroscopic tangent modulus relating the macroscopic first Piola-Kirchhoff stress rate to the rate of macroscopic deformation gradient. The determination of the macroscopic tangent modulus allows rigorously applying the Rice bifurcation criterion for the prediction of the onset of macroscopic strain localization. This accurate application of the bifurcation criterion constitutes the second main theoretical originality of our approach, as the earlier numerical approaches were not able to determine the macroscopic tangent modulus. The competition between the onset of strain localization predicted by the Rice bifurcation theory and the ductility limits predicted by other existing criteria is investigated. To analyze this competition, attention is focused on two main configurations of loading states. Firstly, loadings under proportional stressing (or constant stress paths) are considered, where the stress triaxiality ratio T ranges between 0.7 and 3.0, and the Lode parameter L is comprised between -1.0 and 1.0. For this first loading configuration, our numerical predictions are found to be consistent with the classical published trends: strain localization occurs prior to void coalescence, both being predicted at realistic strain levels for the whole ranges of T and L . Moreover, the trends obtained in [Guo and Wong \(2018\)](#), stating that the difference between the strain levels corresponding to the onset of strain localization and void coalescence decreases as stress triaxiality T increases, are confirmed by our numerical predictions. The second loading configuration covers the in-plane strain paths used for predicting the forming limit diagrams (applied to the perforated sheets in Chapter 2). Although of major importance in the context of forming processes (formability of thin metal sheets), this second loading configuration has not been sufficiently investigated in the early studies based on unit cell computations. Our numerical predictions reveal that only plastic strain localization may occur for this second configuration of loading, as void coalescence cannot be reached. The developed approach, based on the coupling between the periodic homogenization scheme and the strain localization and coalescence criteria, is also used for investigating the effects of void shape and secondary population of voids on the ductility limit of thin metal sheets.

This chapter is organized as follows:

- Section 3.2 details the micromechanical approach used to model the unit cell behavior.
- Section 3.3 presents the boundary conditions and the two macroscopic loading configurations applied in the unit cell computations.
- The adopted strain localization and void coalescence criteria are described in Section 3.4.
- The numerical results of the current study are reported and extensively discussed in Section 3.5.
- Section 3.6 closes this chapter by summarizing some conclusions and future works.

3.2. Micromechanical modeling of the unit cell

We consider a ductile solid defined as an array of cubic unit cells containing a void at their center, as shown in Fig. 3.1a. Each unit cell may be regarded as a heterogeneous medium composed of two main phases: the primary void and the metal matrix, which is itself assumed to be voided to account for the possible effect of secondary population of voids (Fig. 3.1b). The initial shape of the primary void is assumed to be spherical or ellipsoidal, while all the secondary voids are assumed to be spherical. A Cartesian frame $(\vec{e}_1, \vec{e}_2, \vec{e}_3)$ is introduced to define the coordinates of the material points, where vectors \vec{e}_i are normal to the faces of the unit cell in the initial configuration. The origin of this coordinate system is located at the center of the unit cell. Hence, the initial unit cell occupies the domain $[-l_0/2, l_0/2] \times [-l_0/2, l_0/2] \times [-l_0/2, l_0/2]$, as shown in Fig. 3.1b (with $l_0 = 1\text{mm}$).

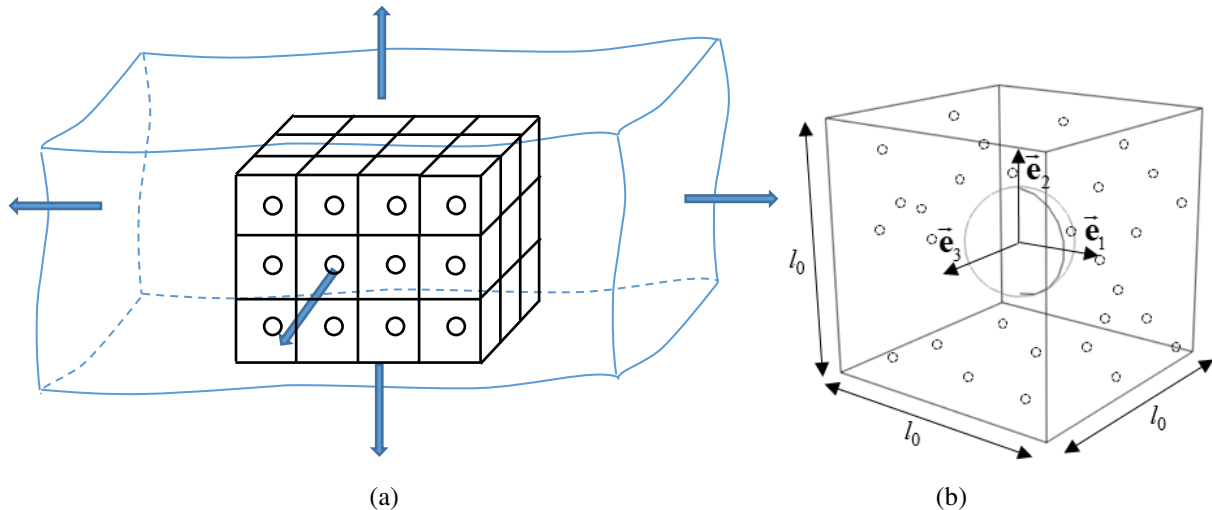


Fig. 3.1. (a) Micromechanical model of a material layer composed of an arrangement of cubic voided unit cells; (b) a unit cell containing a centered, spherical void surrounded by a voided matrix.

3.2.1. Multiscale transition problem

Considering the periodicity of the void arrangement (Fig. 3.1a), the periodic homogenization seems to be a suitable multiscale scheme to determine the homogenized behavior of the unit cell (Miehe, 2003; Zhu et al., 2020). The use of this homogenization technique allows substituting the heterogeneous unit cell by an equivalent homogenized medium with the same effective mechanical properties (Fig. 3.2).

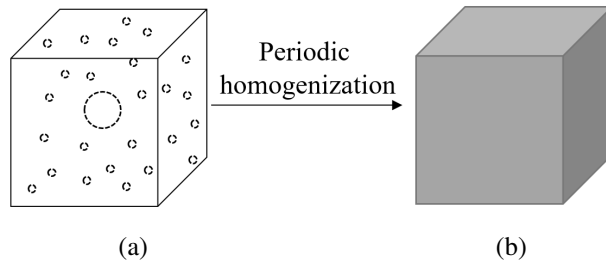


Fig. 3.2. Illustration of the concept of periodic homogenization: (a) unit cell containing primary and secondary voids; (b) equivalent homogenized medium.

The equations governing periodic homogenization scheme are presented in Section 1.3 (for the general 3D cases) and Section 2.2.3 (for the plane-stress cases), they are not recalled here for brevity. Further details on the practical aspects related to the application of the PBCs on the outer surfaces of the unit cell can also be found in Section 1.3 and Section 2.2.3. The developments of Sections 3.3.2 and 3.3.3 provide more details on how to apply the corresponding macroscopic loadings. The constitutive relations describing the mechanical behavior of the metal matrix, will be detailed in Section 3.2.2.

3.2.2. Constitutive model for the metal matrix

To account for the effect of secondary population of voids, the mechanical behavior of the metal matrix is modeled by the original Gurson porous model ([Gurson, 1977](#)). The same methodology can be applied for any other constitutive framework (for instance, the GTN model to include void nucleation and coalescence). A typical finite element mesh for the unit cell is presented in [Fig. 3.3](#).

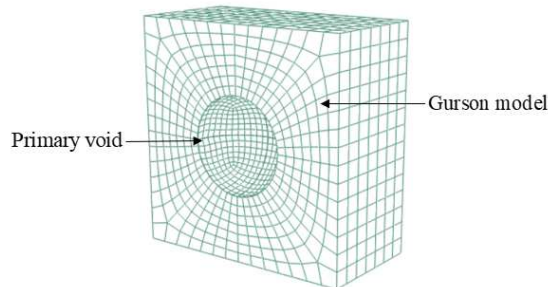


Fig. 3.3. Finite element mesh for one-half unit cell, for illustration.

At the microscopic level, a relationship has been derived by combining the constitutive relations of the metal matrix:

$$\dot{\mathbf{p}} = \mathbf{c}^{(PK1)} : \dot{\mathbf{f}} \quad (3.1)$$

The expression of the microscopic analytical tangent modulus $\mathbf{c}^{(PK1)}$ is determined from the following developments. As a departure point for these developments, the strain rate \mathbf{d} is expressed as the symmetric part of the microscopic velocity gradient \mathbf{g} (see also Eq. (2.2)):

$$\mathbf{d} = \frac{1}{\gamma} (\mathbf{g} + \mathbf{g}^T). \quad (3.2)$$

Meanwhile, the strain rate \mathbf{d} is itself split into its elastic and plastic parts \mathbf{d}^e and \mathbf{d}^p :

$$\mathbf{d} = \mathbf{d}^e + \mathbf{d}^p. \quad (3.3)$$

In a co-rotational material frame (we adopt here the co-rotational frame associated with the Jaumann objective rate), the Cauchy stress rate is described with the following hypoelastic law:

$$\dot{\mathbf{\sigma}} = \mathbf{c}^e : \mathbf{d}^e, \quad (3.4)$$

where \mathbf{c}^e is the fourth-order elasticity tensor.

The plastic strain rate \mathbf{d}^p is determined by the normality rule:

$$\mathbf{d}^p = \dot{\lambda} \frac{\partial \Phi}{\partial \mathbf{\sigma}}, \quad (3.5)$$

with $\dot{\lambda}$ denoting the plastic multiplier, and Φ the Gurson yield function defined as:

$$\Phi = \left(\frac{\sigma_{eq}}{\sigma_y} \right)^2 + 2f_s \cosh \left(\frac{3\sigma_h}{2\sigma_y} \right) - \left(1 + f_s^2 \right) \leq 0, \quad (3.6)$$

where

- σ_{eq} is the von Mises equivalent stress, equal to $(3\mathbf{\sigma}_{dev} : \mathbf{\sigma}_{dev} / 2)^{1/2}$.
- $\mathbf{\sigma}_{dev}$ and $\sigma_h = \text{tr}(\mathbf{\sigma}) / 3$ are the deviatoric and hydrostatic parts of the Cauchy stress tensor $\mathbf{\sigma}$, respectively.
- σ_y is the yield stress of the dense metal matrix, defined by the Swift hardening law:

$$\sigma_y = K \left(\varepsilon_0 + \bar{\varepsilon}^p \right)^n, \quad (3.7)$$

where K , ε_0 and n are hardening parameters, and $\bar{\varepsilon}^p$ is the equivalent plastic strain of the dense metal matrix.

Note that setting $f_s = 0$, one recovers the conventional J_2 flow theory with isotropic hardening. This particular case will be used when the metal matrix is assumed to be fully dense.

In the current chapter, only growth of secondary voids is considered (i.e., the effects of nucleation of new secondary voids and coalescence between existing voids are neglected). By neglecting the elastic volume change, the rate of the secondary void volume fraction reads:

$$\dot{f}_s = (1 - f_s) \text{tr}(\mathbf{d}^p). \quad (3.8)$$

The equivalent plastic strain rate $\dot{\bar{\varepsilon}}^p$ is obtained from the equivalence principle in terms of rate of plastic work for the metal matrix and its dense part:

$$(1 - f_s) \sigma_y \dot{\bar{\varepsilon}}^p = \mathbf{\sigma} : \mathbf{d}^p \Leftrightarrow \dot{\bar{\varepsilon}}^p = \frac{\mathbf{\sigma} : \mathbf{d}^p}{(1 - f_s) \sigma_y}. \quad (3.9)$$

The activation of plastic flow is governed by the application of the Kuhn–Tucker constraints:

$$\begin{aligned} \text{elastic loading / unloading: } & \Phi \leq 0 ; \dot{\Phi} < 0 ; \dot{\lambda} = 0 ; \\ \text{elastoplastic loading: } & \Phi = 0 ; \dot{\Phi} = 0 ; \dot{\lambda} > 0 . \end{aligned} \quad (3.10)$$

In the case of elastoplastic loading, condition $\dot{\Phi} = 0$ can be expanded as follows:

$$\dot{\Phi} = \mathbf{V}_\sigma : \dot{\boldsymbol{\sigma}} + V_{\sigma_y} \dot{\sigma}_y + V_{f_s} \dot{f}_s = 0 , \quad (3.11)$$

where:

$$\begin{aligned} \mathbf{V}_\sigma &= \frac{\partial \Phi}{\partial \boldsymbol{\sigma}} = \frac{1}{\sigma_y} \left[3 \frac{\boldsymbol{\sigma}_{dev}}{\sigma_y} + f_s \cosh \left(\frac{3\sigma_h}{2\sigma_y} \right) \mathbf{I}_2 \right] ; \\ V_{\sigma_y} &= \frac{\partial \Phi}{\partial \sigma_y} = -\frac{1}{\sigma_y} \left[2 \left(\frac{\sigma_{eq}}{\sigma_y} \right)^2 + 3 f_s \sinh \left(\frac{3\sigma_h}{2\sigma_y} \right) \right] ; \\ V_{f_s} &= \frac{\partial \Phi}{\partial f_s} = 2 \cosh \left(\frac{3\sigma_h}{2\sigma_y} \right) - 2 f_s . \end{aligned} \quad (3.12)$$

The substitution of Eqs. (3.3), (3.5) and (3.12)₁ into Eq. (3.4) leads to the following expression for $\dot{\boldsymbol{\sigma}}$:

$$\dot{\boldsymbol{\sigma}} = \mathbf{c}^e : (\mathbf{d} - \mathbf{d}^p) = \mathbf{c}^e : (\mathbf{d} - \dot{\lambda} \mathbf{V}_\sigma) = \mathbf{c}^{ep} : \mathbf{d} . \quad (3.13)$$

The combination of the above equations allows us to obtain the following expression for the plastic multiplier $\dot{\lambda}$:

$$\dot{\lambda} = \frac{\mathbf{V}_\sigma : \mathbf{c}^e : \mathbf{d}}{H_\lambda} \quad \text{where} \quad H_\lambda = \mathbf{V}_\sigma : \mathbf{c}^e : \mathbf{V}_\sigma - \frac{V_{\sigma_y}}{(1-f_s)} \frac{(\boldsymbol{\sigma} : \mathbf{V}_\sigma) \partial \sigma_y}{\partial \varepsilon^p} . \quad (3.14)$$

The expression of the elastoplastic tangent modulus \mathbf{c}^{ep} can be derived by combining Eqs. (3.13) and (3.14):

$$\mathbf{c}^{ep} = \mathbf{c}^e - \alpha \frac{(\mathbf{c}^e : \mathbf{V}_\sigma) \otimes (\mathbf{V}_\sigma : \mathbf{c}^e)}{H_\lambda} , \quad (3.15)$$

where $\alpha = 0$ for elastic loading or unloading, and $\alpha = 1$ for elastoplastic loading.

The relation between moduli \mathbf{c}^{ep} and $\mathbf{c}^{(PK1)}$ can be found in Section 2.2.2.

3.3. Periodic boundary conditions and macroscopic loading

The periodic homogenization problem briefly recalled in Section 3.2.1 is solved within the ABAQUS/Standard finite element software. The main steps of this solution strategy are summarized hereafter:

- Discretization of the unit cell by finite elements: to this end, the C3D20 quadratic solid element is used, with a higher mesh density around the primary void (to avoid potential element distortion).

A user-defined material (UMAT) subroutine is used for implementing the Gurson constitutive equations describing the mechanical behavior of the metal matrix.

- Application of the periodic boundary conditions (PBCs): this task is automatically managed by using the set of python scripts *Homtools* (as described in Chapter 1 and 2). These PBCs are applied on the six (resp., four) outer faces of the unit cell, when this unit cell is subjected to proportional stressing (resp., proportional in-plane strain path), as will be detailed in Sections 3.3.2 and 3.3.3. Further practical details on the application of the PBCs were provided in Section 1.3 and Section 2.2.3.
- Application of macroscopic loading: in the current chapter, the unit cell may be subjected to two different loading configurations. Firstly, macroscopic proportional stressing (i.e., proportional stress paths) to investigate the effect of the stress triaxiality ratio T and Lode parameter L on the competition between void coalescence and macroscopic plastic strain localization. Secondly, macroscopic proportional in-plane strain paths to predict forming limit diagrams (FLDs) of thin voided sheets. To apply the first loading configuration, some extensions of the set of python scripts *Homtools* are required. However, the application of the second loading configuration is easily achieved by using the *Homtools* (see Section 2.2.3). Further details on the first and second loading configuration will be given in Sections 3.3.2 and 3.3.3, respectively.
- Computation of the macroscopic mechanical response: the *Homtools* enables to readily and automatically manage this task.

3.3.1. Periodic boundary conditions

The fully PBCs are practically applied on the outer faces of the unit cells. The developments presented in Section 1.3 have detailed how to apply PBCs in one space direction. For the two following macroscopic loadings, these developments will be performed in 2 directions (direction 1 and direction 2) for proportional in-plane strain paths while in 3 directions for proportional stressing.

3.3.2. Proportional stressing

As previously stated, loadings under macroscopic proportional stressing (i.e., proportional stress paths) are applied to investigate the effect of the stress triaxiality ratio T and Lode parameter L on the competition between void coalescence and macroscopic plastic strain localization. In this case, the unit cell is subjected to a diagonal triaxial macroscopic stress state (without shear stresses) as illustrated in Fig. 3.4.

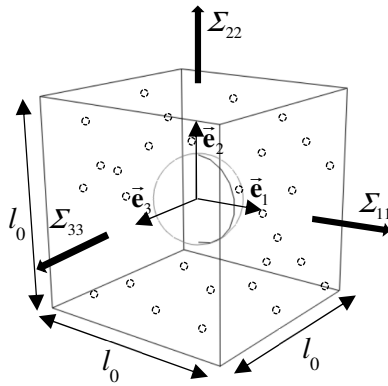


Fig. 3.4. Unit cell subjected to triaxial macroscopic stress state without shear stresses.

Proportional stress state requires that the stress ratios β_1 and β_2 defined as:

$$\beta_1 = \frac{\Sigma_{11}}{\Sigma_{33}}; \quad \beta_2 = \frac{\Sigma_{22}}{\Sigma_{33}}, \quad (3.16)$$

should be kept constant during the deformation history. In Eq. (3.16), Σ_{11} , Σ_{22} and Σ_{33} designate the diagonal components of the macroscopic Cauchy stress tensor Σ , which is related to its microscopic counterpart σ through the following averaging rule:

$$\Sigma = \frac{1}{|\mathcal{V}|} \int_{\mathcal{V}} \sigma(\mathbf{x}) d\mathcal{V}, \quad (3.17)$$

where \mathcal{V} is the cell volume of the current configuration.

The macroscopic hydrostatic stress Σ_h and the macroscopic equivalent (von Mises) stress Σ_{eq} are obtained from components Σ_{11} , Σ_{22} and Σ_{33} as:

$$\Sigma_h = \frac{\Sigma_{11} + \Sigma_{22} + \Sigma_{33}}{3}; \quad \Sigma_{eq} = \frac{1}{\sqrt{2}} \sqrt{(\Sigma_{11} - \Sigma_{22})^2 + (\Sigma_{11} - \Sigma_{33})^2 + (\Sigma_{22} - \Sigma_{33})^2}. \quad (3.18)$$

Assuming that $\Sigma_{11} \geq \Sigma_{22} \geq \Sigma_{33}$, the macroscopic stress triaxiality ratio T and Lode parameter L can be expressed in terms of the stress ratios β_1 and β_2 (Liu et al., 2016):

$$\begin{cases} T = \frac{\Sigma_h}{\Sigma_{eq}} = \frac{\sqrt{2}(1+\beta_1+\beta_2)}{3\sqrt{(1-\beta_1)^2+(1-\beta_2)^2+(\beta_1-\beta_2)^2}} \operatorname{sgn}(\Sigma_{33}); \\ L = \frac{(2\beta_2 - \beta_1 - 1)}{\beta_1 - 1}, \quad -1 \leq L \leq 1. \end{cases} \quad (3.19)$$

Stress triaxiality ratio T and Lode parameter L characterize the spherical and deviatoric parts of the macroscopic stress state, respectively. Ratios T and L are kept constant during the deformation history by prescribing constant values for β_1 and β_2 . By inverting Eq. (3.19), β_1 and β_2 can be expressed as functions of T and L :

$$\beta_1 = \frac{3T\sqrt{3+L^2} + 3 - L}{3T\sqrt{3+L^2} - 3 - L} ; \quad \beta_2 = \frac{3T\sqrt{3+L^2} + 2L}{3T\sqrt{3+L^2} - 3 - L}. \quad (3.20)$$

It is worthwhile to note that this inversion is not unique, as multiple combinations of β_1 and β_2 can be obtained for the same values of T and L (Wong and Guo, 2015). The influence of this non-uniqueness on void coalescence can be found in Section 5 of Wong and Guo (2015). By following Liu et al. (2016), the solution for β_1 and β_2 given by Eq. (3.20) is adopted for all the predictions of Section 3.5.3. Meanwhile, we have adopted the following sign convention for L : the extreme values of $L = +1, -1, 0$ refer to the stress state case of generalized compression, generalized tension and pure shear, superimposed with hydrostatic stress, respectively (Liu et al., 2016). Note that an opposite sign convention, $L = +1, -1$, is adopted in numerous studies (Dunand and Mohr, 2014; Wong and Guo, 2015; Guo and Wong, 2018) for generalized tension and generalized compression, resectively.

To apply proportional triaxial stressing, 3D periodic boundary conditions shall be imposed on the six outer faces of the unit cell (two by two faces), following the concept presented in Section 1.3. In this case, three reference points RP_1 , RP_2 and RP_3 are created by using the *Homtools* to manage these boundary conditions and the macroscopic loading. These reference points are defined by the following displacements:

$$\begin{aligned} RP_1 : U_{11} &= (F_{11} - 1)l_0 ; U_{12} = 0 ; U_{13} = 0 ; \\ RP_2 : U_{21} &= 0 ; U_{22} = (F_{22} - 1)l_0 ; U_{23} = 0 ; \\ RP_3 : U_{31} &= 0 ; U_{32} = 0 ; U_{33} = (F_{33} - 1)l_0 . \end{aligned} \quad (3.21)$$

Components F_{11} , F_{22} and F_{33} of the macroscopic deformation gradient \mathbf{F} should be prescribed in such a way that the stress triaxiality ratio T and the Lode parameter L hold constant during the entire deformation history. Such prescription is not possible to be directly operated on the displacements of the reference points RP_1 , RP_2 and RP_3 . To overcome this inconvenience, an extra dummy (or ‘ghost’) node is introduced into the finite element model. The DOFs of this dummy node and the associated reaction forces are denoted (U_1^*, U_2^*, U_3^*) and $(\alpha_1, \alpha_2, \alpha_3)$, respectively. A user subroutine MPC (Abaqus, 2014) has been developed to connect the dummy node to the three reference points RP_1 , RP_2 and RP_3 (and further to the unit cell). In this subroutine, the reference points serve as slave nodes, while the dummy node serves as master node wherein the loading is imposed. The master node transmits the imposed loading through the multi-point constraints to the reference points as stated by Eq. (3.22):

$$\begin{bmatrix} U_{11} \\ U_{22} \\ U_{33} \end{bmatrix} = \mathcal{T} \begin{bmatrix} U_1^* \\ U_2^* \\ U_3^* \end{bmatrix}. \quad (3.22)$$

where \mathcal{T} is a functional to be determined in order to ensure that the displacements U_{11} , U_{22} , and U_{33} applied on the reference points lead to the prescribed ratios β_1 and β_2 between the different macroscopic stress components. A simplified illustration of the MPC subroutine is shown in Fig. 3.5.

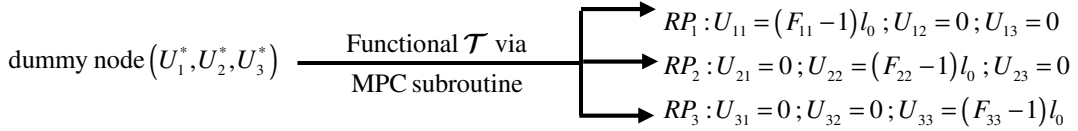


Fig. 3.5. Schematic illustration of the multi-point constraints between the dummy node and the reference points (RP_1, RP_2, RP_3) .

We next detail the derivation of the expression of functional \mathcal{T} . In this aim, the work rate equivalence between the dummy node and the unit cell shall be used (Liu et al., 2016):

$$\boldsymbol{\alpha}^T \cdot \dot{\mathbf{U}}^* = |\mathcal{V}| \tilde{\Sigma}^T \cdot \tilde{\mathbf{G}}, \quad (3.23)$$

where \mathbf{U}^* and $\boldsymbol{\alpha}$ are the displacement and the associated reaction force vectors of the dummy node, respectively. As to $\tilde{\Sigma}$ and $\tilde{\mathbf{G}}$, they represent the storage vectors for the diagonal components of the macroscopic Cauchy stress and the macroscopic velocity gradient associated with the unit cell, respectively:

$$\boldsymbol{\alpha} = \begin{bmatrix} \alpha_1 \\ \alpha_2 \\ \alpha_3 \end{bmatrix}; \quad \mathbf{U}^* = \begin{bmatrix} U_1^* \\ U_2^* \\ U_3^* \end{bmatrix}; \quad \tilde{\Sigma} = \begin{bmatrix} \Sigma_{11} \\ \Sigma_{22} \\ \Sigma_{33} \end{bmatrix}; \quad \tilde{\mathbf{G}} = \begin{bmatrix} G_{11} \\ G_{22} \\ G_{33} \end{bmatrix}. \quad (3.24)$$

Vectors $\dot{\mathbf{U}}^*$ and $\tilde{\mathbf{G}}$ may be linked by a transformation matrix \mathcal{R} belonging to $\mathcal{SO}(3)^2$ (Wong and Guo, 2015):

$$\begin{bmatrix} G_{11} \\ G_{22} \\ G_{33} \end{bmatrix} = \mathcal{R} \cdot \begin{bmatrix} \dot{U}_1^* \\ \dot{U}_2^* \\ \dot{U}_3^* \end{bmatrix}. \quad (3.25)$$

In the present contribution, we have adopted the form of \mathcal{R} given by Liu et al. (2016):

$$\mathcal{R} = \begin{bmatrix} \sin^2 \varphi_1 + \cos \varphi_2 \cos^2 \varphi_1 & \cos \varphi_2 \cos \varphi_1 \sin \varphi_1 - \cos \varphi_1 \sin \varphi_1 & \cos \varphi_1 \sin \varphi_2 \\ \cos \varphi_2 \cos \varphi_1 \sin \varphi_1 - \cos \varphi_1 \sin \varphi_1 & \cos \varphi_2 \sin^2 \varphi_1 + \cos^2 \varphi_1 & \sin \varphi_2 \sin \varphi_1 \\ -\cos \varphi_1 \sin \varphi_2 & -\sin \varphi_1 \sin \varphi_2 & \cos \varphi_2 \end{bmatrix}. \quad (3.26)$$

The form (3.26) of the transformation matrix \mathcal{R} is valid for $\Sigma_{33} > 0$ (i.e., $\text{sgn}(\Sigma_{33}) = 1$). This condition is obviously ensured for the loadings studied in Section 3.5.3, where $0.7 \leq T \leq 3$ and $-1 \leq L \leq 1$, which corresponds to positive stress ratios β_1 and β_2 . The expressions of the rotation angles φ_1 and φ_2 used to define matrix \mathcal{R} will be derived in the subsequent developments.

² Matrix \mathcal{R} belongs to $\mathcal{SO}(3)$ if \mathcal{R} is orthogonal (i.e., $\mathcal{R}^{-1} = \mathcal{R}^T$) and $\det(\mathcal{R}) = 1$.

The external loading is applied on the dummy node and the transformation matrix is used to suitably transfer this loading on the different reference points. We apply a linear displacement on only the third DOF of the dummy node with $\dot{U}_3^* = 1$. The first two DOFs are left free. Consequently, the corresponding reaction forces are equal to zero (namely, $\alpha_1 = \alpha_2 = 0$). With this particular loading, Eq. (3.23) reduces to:

$$\alpha_3 \dot{U}_3^* = |\mathcal{V}| (\Sigma_{11} G_{11} + \Sigma_{22} G_{22} + \Sigma_{33} G_{33}). \quad (3.27)$$

Without dwelling into the mathematical details, which have been extensively discussed in Wong and Guo (2015) and Liu et al. (2016), the expression of α_3 can be derived as a function of $|\mathcal{V}|$ and the components of the macroscopic stress Σ_{11} , Σ_{22} and Σ_{33} as follows:

$$\alpha_3 = |\mathcal{V}| \sqrt{(\Sigma_{11})^2 + (\Sigma_{22})^2 + (\Sigma_{33})^2}. \quad (3.28)$$

By involving Eqs. (3.16), Eq. (3.28) can be rewritten as follows:

$$\alpha_3 = |\mathcal{V}| \sqrt{(\Sigma_{11})^2 + (\Sigma_{22})^2 + (\Sigma_{33})^2} = |\mathcal{V}| \left(\sqrt{(\beta_1)^2 + (\beta_2)^2 + 1} \right) \Sigma_{33}, \quad (3.29)$$

Using the fact that $\alpha_1 = \alpha_2 = 0$, the rotation angles φ_1 and φ_2 , which define the rotation matrix \mathcal{R} introduced in Eq. (3.26), can be obtained by the following relationships (Liu et al., 2016):

$$\varphi_1 = \tan^{-1} \left(\frac{\beta_2}{\beta_1} \right) ; \quad \varphi_2 = \tan^{-1} \left(\sqrt{(\beta_1)^2 + (\beta_2)^2} \right). \quad (3.30)$$

The substitution of Eqs. (3.30) into Eq. (3.26) leads to the following expression of the transformation matrix \mathcal{R} :

$$\mathcal{R} = \begin{bmatrix} \frac{(\beta_1)^2 \mu + (\beta_2)^2}{(\beta_1)^2 + (\beta_2)^2} & \frac{\beta_1 \beta_2 (\mu - 1)}{(\beta_1)^2 + (\beta_2)^2} & \beta_1 \mu \\ \frac{\beta_1 \beta_2 (\mu - 1)}{(\beta_1)^2 + (\beta_2)^2} & \frac{(\beta_1)^2 + (\beta_2)^2 \mu}{(\beta_1)^2 + (\beta_2)^2} & \beta_2 \mu \\ -\beta_1 \mu & -\beta_2 \mu & \mu \end{bmatrix} \quad \text{with} \quad \mu = \frac{1}{\sqrt{(\beta_1)^2 + (\beta_2)^2 + 1}}. \quad (3.31)$$

For proportional stressing, the transformation matrix \mathcal{R} holds constant during the loading (as ratios β_1 and β_2 do not change). Hence, the integration of Eq. (3.25) leads to the following expression:

$$\begin{bmatrix} E_{11} \\ E_{22} \\ E_{33} \end{bmatrix} = \mathcal{R} \cdot \begin{bmatrix} U_1^* \\ U_2^* \\ U_3^* \end{bmatrix}, \quad (3.32)$$

where \mathbf{E} is the macroscopic logarithmic strain tensor defined as:

$$\mathbf{E} = \int_0^t \mathbf{G} dt = \ln(\mathbf{F}). \quad (3.33)$$

The combination of Eqs. (3.21), (3.32) and (3.33) yields:

$$\begin{cases} F_{11} = (U_{11} / l_0) + 1 = e^{(\mathcal{R}_{11} U_1^* + \mathcal{R}_{12} U_2^* + \mathcal{R}_{13} U_3^*)}; \\ F_{22} = (U_{22} / l_0) + 1 = e^{(\mathcal{R}_{21} U_1^* + \mathcal{R}_{22} U_2^* + \mathcal{R}_{23} U_3^*)}; \\ F_{33} = (U_{33} / l_0) + 1 = e^{(\mathcal{R}_{31} U_1^* + \mathcal{R}_{32} U_2^* + \mathcal{R}_{33} U_3^*)}. \end{cases} \quad (3.34)$$

The expression of functional \mathcal{T} can be readily identified from Eq. (3.34). Thus, the relations between the DOFs of the dummy node and those of the three reference points to be implemented in the MPC user subroutine are summarized by Eqs. (3.34). The PBCs together with constraints (3.34) determine the boundary value problem of the unit cell, and the proportional stressing applied during the loading history.

3.3.3. Proportional in-plane strain paths

We consider a thin metal sheet made of 2D array of voided unit cells (a single unit cell in the thickness direction), as depicted in Fig. 3.6a. Loading under macroscopic proportional in-plane strain paths is classically adopted to predict forming limit diagrams (FLDs) of thin metal sheets. In this case, the unit cell is subjected to biaxial stretching in the 1 and 2 directions (Fig. 3.6b). Additionally, the out-of-plane components of the macroscopic first Piola-Kirchhoff stress \mathbf{P} (and thus Σ): $P_{13}, P_{23}, P_{31}, P_{32}$ and P_{33} are set to zero. The strain-path ratio $\rho = E_{11} / E_{22}$ is kept constant during the loading, and it ranges between $-1/2$ (uniaxial tension state) and 1 (equibiaxial tension state). The other in-plane components of the macroscopic logarithmic strain (E_{12}, E_{21}) are set to zero. In this case, PBCs are only applied on the faces normal to directions 1 and 2 (Fig. 3.6b). However, faces normal to direction 3 are free from any boundary condition. This specific choice enables to ensure the macroscopic plane-stress state in the third direction.

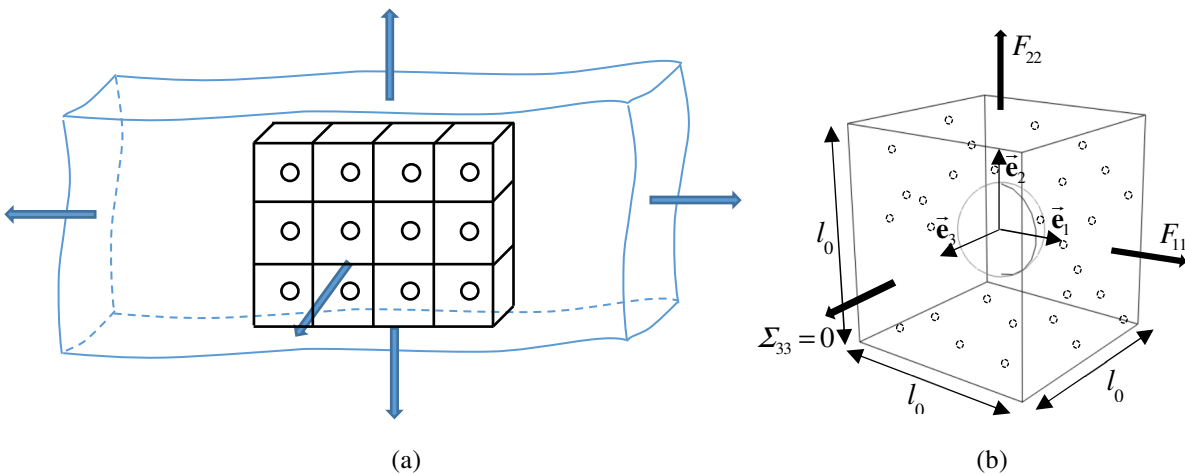


Fig. 3.6. (a) Thin metal sheet made of 2D array of voided unit cells; (b) unit cell subjected to in-plane strain path.

Recalling that the macroscopic loading takes the following form (the same as the loading in Section 2.2.3):

$$\mathbf{F} = \begin{bmatrix} F_{11} & 0 & ? \\ 0 & (F_{11})^\rho & ? \\ ? & ? & ? \end{bmatrix}; \quad \mathbf{P} = \begin{bmatrix} ? & ? & 0 \\ ? & ? & 0 \\ 0 & 0 & 0 \end{bmatrix}, \quad (3.35)$$

where components marked by ‘?’ are unknown and need to be determined. Components F_{13} , F_{31} , F_{23} , F_{32} and F_{33} are calculated by making use of the plane-stress conditions:

$$P_{13} = P_{31} = P_{23} = P_{32} = P_{33} = 0. \quad (3.36)$$

To apply the 2D periodic boundary conditions and the macroscopic loading of Eq. (3.35), three reference points RP_1 , RP_2 and RP_3 should be created. The prescribed boundary conditions should be applied on the reference points (a displacement on RP_1 and RP_2 , and a force on RP_3) to comply with Eq. (3.35), are the same as Eq. (2.17) (in Section 2.2.3).

3.4. Void coalescence and strain localization criteria

In the present work, attention is directed towards the prediction of ductile failure by using four indicators, which will be presented hereafter: the first three ones have been used in previous contributions (but without rigorous coupling with the periodic homogenization multiscale scheme), while the last one is applied for the first time herein. These different indicators will be classified for the loading case under proportional stressing.

3.4.1. Maximum reaction force criterion

This indicator has been adopted in [Guo and Wong \(2018\)](#) to predict the onset of strain localization. With this criterion, strain localization is attained when the reaction force component α_3 applied on the dummy node and defined by Eq. (3.28) reaches its maximum value, or equivalently:

$$\dot{\alpha}_3 = 0. \quad (3.37)$$

The critical equivalent strain predicted at the moment when this criterion is verified will be denoted E_{eq}^R .

3.4.2. Maximum equivalent stress criterion

This indicator, initiated by [Tvergaard \(2012\)](#), states that material failure occurs when the macroscopic equivalent stress Σ_{eq} reaches its maximum value. For triaxial proportional stressing, the macroscopic Cauchy stress tensor takes the general form:

$$\Sigma = \begin{bmatrix} \Sigma_{11} & 0 & 0 \\ 0 & \Sigma_{22} & 0 \\ 0 & 0 & \Sigma_{33} \end{bmatrix} = \Sigma_{33} \begin{bmatrix} \beta_1 & 0 & 0 \\ 0 & \beta_2 & 0 \\ 0 & 0 & 1 \end{bmatrix}. \quad (3.38)$$

In this case, the macroscopic equivalent stress Σ_{eq} can be expressed as follows:

$$\Sigma_{eq} = \sqrt{\frac{(\Sigma_{11} - \Sigma_{22})^2 + (\Sigma_{11} - \Sigma_{33})^2 + (\Sigma_{22} - \Sigma_{33})^2}{2}} = \sqrt{(\beta_1)^2 + (\beta_2)^2 - \beta_1\beta_2 - \beta_1 - \beta_2 + 1} |\Sigma_{33}|. \quad (3.39)$$

The critical equivalent strain predicted at the moment when this criterion is verified will be denoted E_{eq}^S .

3.4.3. Energy-based criterion

The energy-based criterion has been proposed by Wong and Guo (2015) and is based on the fact that void coalescence involves localization of plastic deformation between neighboring voids, with the material outside the localization band undergoing elastic unloading (Pardoen and Hutchinson, 2000). To apply this criterion, elastic and plastic work rates should be computed:

$$\dot{W}^e = \int_V \boldsymbol{\sigma} : \mathbf{d}^e dV ; \quad \dot{W}^p = \int_V \boldsymbol{\sigma} : \mathbf{d}^p dV, \quad (3.40)$$

where $\boldsymbol{\sigma}$ is the microscopic Cauchy stress tensor, \mathbf{d}^e and \mathbf{d}^p are respectively the elastic and plastic parts of the deformation rate tensor. The sign of the ratio \dot{W}^e / \dot{W}^p implies three different loading states: $\dot{W}^e / \dot{W}^p > 0$ for a state of elastoplastic loading, $\dot{W}^e / \dot{W}^p < 0$ for a state of elastic unloading, $\dot{W}^e / \dot{W}^p = 0$ for a state of neutral loading. Following Wong and Guo (2015), the onset of void coalescence is deemed to occur when the ratio \dot{W}^e / \dot{W}^p attains a minimum and is negative.

The critical equivalent strain predicted at the moment when this criterion is verified will be denoted E_{eq}^C .

3.4.4. Rice bifurcation criterion

In this chapter, the Rice bifurcation criterion is adopted to predict the macroscopic strain localization under both loading configurations: proportional stressing (3D stress configuration) and in-plane proportional strain paths (plane-stress condition). The in-plane formulation of this criterion has been presented in Section 2.3.3. In the following, we present the formula in 3D stress configuration.

Following the Rice approach (Rudnicki and Rice, 1975; Rice, 1976), the onset of strain localization may be mathematically related to the loss of ellipticity of the macroscopic governing equations. The kinematic condition for the strain path jump reads in a Lagrangian framework:

(3.41)

where:

- $\llbracket \dot{\mathbf{F}} \rrbracket$ is the jump of the velocity gradient field $\dot{\mathbf{F}}$ across the localization band equal to the difference between velocity gradient outside the band $\dot{\mathbf{F}}^O$ and its counterpart inside the band $\dot{\mathbf{F}}^I$,
- $\dot{\mathcal{C}}$ is the jump vector,

- $\vec{\mathcal{N}}$ is the unit vector normal to the localization band in the initial configuration equal to $(\sin\theta_2\cos\theta_1, \sin\theta_2\sin\theta_1, \cos\theta_2)$, where θ_1 ($0 \leq \theta_1 < 2\pi$), θ_2 ($0 \leq \theta_2 \leq \pi$) is the inclination of vector $\vec{\mathcal{N}}$.

The continuity condition of the in-plane force equilibrium through the band writes:

$$[\![\dot{\mathbf{P}}]\!] \cdot \vec{\mathcal{N}} = \vec{0}. \quad (3.42)$$

Combining Eqs. (3.41), (3.42) and (1.24)₂, one can deduce the following condition:

$$\left(\mathbf{C}^{(PK1)} : (\dot{\mathcal{C}} \otimes \vec{\mathcal{N}}) \right) \cdot \vec{\mathcal{N}} = \vec{0}, \quad (3.43)$$

which can be equivalently expressed in its index form:

$$\forall i=1,2,3: \left(\mathcal{N}_j C_{ijkl}^{(PK1)} \mathcal{N}_l \right) \dot{C}_k = 0, \quad j,k,l=1,2,3. \quad (3.44)$$

Introducing $\tilde{\mathbf{C}}^{(PK1)}$ as the transpose of macroscopic tangent modulus $\mathbf{C}^{(PK1)}$ (see also Section 2.3.3):

$$\forall i,j,k,l=1,2,3: \tilde{C}_{ijkl}^{(PK1)} = C_{jikl}^{(PK1)}. \quad (3.45)$$

Condition (3.44) is written as:

$$\forall j=1,2,3: \left(\mathcal{N}_i \tilde{C}_{jikl}^{(PK1)} \mathcal{N}_l \right) \dot{C}_k = 0, \quad i,k,l=1,2,3, \quad (3.46)$$

This criterion corresponds to the singularity of the macroscopic acoustic tensor $\vec{\mathcal{N}} \cdot \tilde{\mathbf{C}}^{(PK1)} \cdot \vec{\mathcal{N}}$:

$$\det(\vec{\mathcal{N}} \cdot \tilde{\mathbf{C}}^{(PK1)} \cdot \vec{\mathcal{N}}) = 0. \quad (3.47)$$

This condition will be reduced into its in-plane form (2.40) when the plane-stress condition is considered.

The practical details about the implementation of the condensation technique for computing $\mathbf{C}^{(PK1)}$ can be found in Section 1.4.2 and in Zhu et al. (2020). As presented in box 2 of Section 1.4.2, step 2 requires that all the nodes of the mesh are partitioned into two categories: set \mathcal{B} made of the nodes located on the boundary surfaces where periodic constraints are imposed and set \mathcal{A} composed of the other nodes. So that, set \mathcal{B} is made of the nodes located on $\mathcal{S}_{01}^- \cup \mathcal{S}_{01}^+ \cup \mathcal{S}_{02}^- \cup \mathcal{S}_{02}^+ \cup \mathcal{S}_{03}^- \cup \mathcal{S}_{03}^+$ (see Fig. 1.1) when proportional stressing is applied, and $\mathcal{S}_{01}^- \cup \mathcal{S}_{01}^+ \cup \mathcal{S}_{02}^- \cup \mathcal{S}_{02}^+$ when proportional in-plane strain path is applied (the same situation addressed in Chapter 2).

The critical equivalent strain predicted at the moment when this criterion is verified will be denoted E_{eq}^B .

3.5. Numerical predictions

The material parameters used in the simulations reported in Sections 3.5.2, 3.5.3 and 3.5.4 are summarized in Section 3.5.1. Then, the validity of the periodic conditions applied on the boundary of the unit cell is examined in Section 3.5.2 by assessing its degree of accuracy and effectiveness in reproducing the behavior of the macroscopic medium. Afterward, the predictions performed under proportional stressing are presented in 3.5.3, where some of our numerical predictions are favorably compared with existing results published in the literature. The competition between void coalescence and macroscopic plastic strain localization is carefully analyzed in this section. Finally, Section 3.5.4 focuses on the predictions of forming limit diagrams for thin voided metal sheets by using the developed numerical approach.

3.5.1. Material parameters

The initial volume fraction of the primary void f_{p0} is set to 0.04 in all the simulations presented hereafter. The metal matrix is assumed to be fully dense for all the simulations of Sections 3.5.1 and 3.5.2. The effect of the secondary void population is investigated in Section 3.5.3 by varying the value of f_{s0} . The mechanical behavior of the dense part of the metal matrix is assumed to be elastically and plastically isotropic. For consistent comparisons with Liu et al. (2016), the elasticity and hardening parameters provided in Table 3.1 are used in the different simulations.

Table 3.1. Elastoplastic parameters of the dense matrix.

Elasticity		Hardening		
E (GPa)	ν	K (MPa)	ε_0	n
210	0.3	958.8	0.0025	0.1058

The initial yield stress σ_0 of the dense matrix can be deduced from the parameters given in Table 3.1:

$$\sigma_0 = K (\varepsilon_0)^n. \quad (3.48)$$

3.5.2. Validity of the periodic boundary conditions

One of the most important issues in terms of ensuring that a homogenization multiscale scheme is accurate and effective is how the boundary conditions are treated. It is well known that uniform boundary conditions (kinematic or uniform force) require a large representative volume element to accurately capture microscopic properties and phenomena. By contrast, PBCs can provide better evaluations of the microscopic fields and thus of the macroscopic response than uniformly distributed conditions, even for non-periodic geometries (Terada et al., 2000; Kanit et al., 2003; Henyš et al., 2019). Despite its major importance, the effect of boundary conditions on the onset of void coalescence or macroscopic strain localization has not been analyzed in earlier investigations. In fact, a large majority of these

investigations use KBCs (Liu et al., 2016) or a mixture of KBCs and PBCs (Barsoum and Faleskog, 2011; Wong and Guo, 2015; Guo and Wong, 2018; Zhu et al., 2018), and a very limited number of contributions is based on fully PBCs. In the present section, we investigate the effect of the applied boundary conditions on the distribution of the microscopic fields and on the onset of strain localization, as predicted by the Rice bifurcation approach. In this aim, we consider a 2D voided thin sheet made of 5×5 unit cells. This sheet is subjected to classical equibiaxial loading until 1% of deformation in each direction (Fig. 3.6).

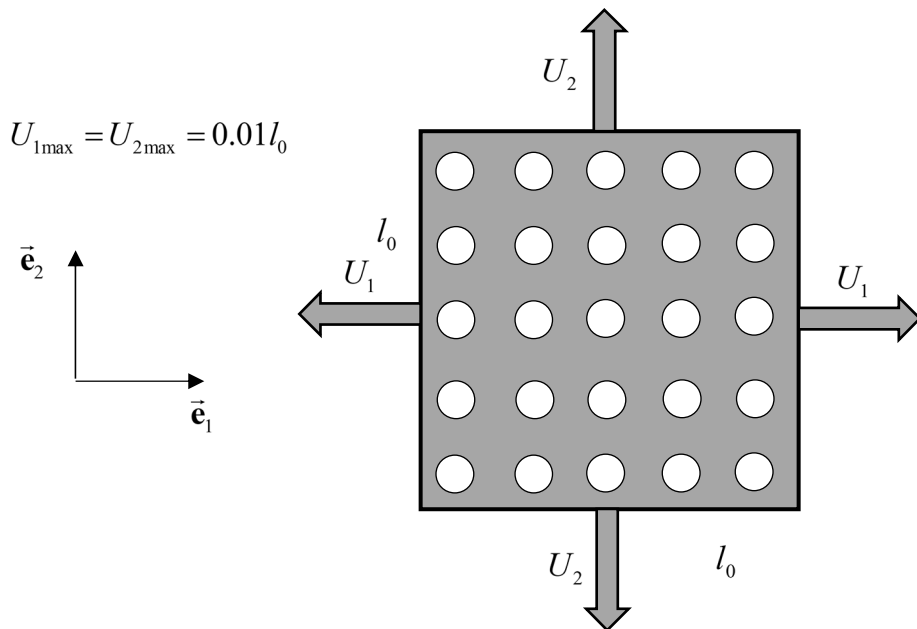
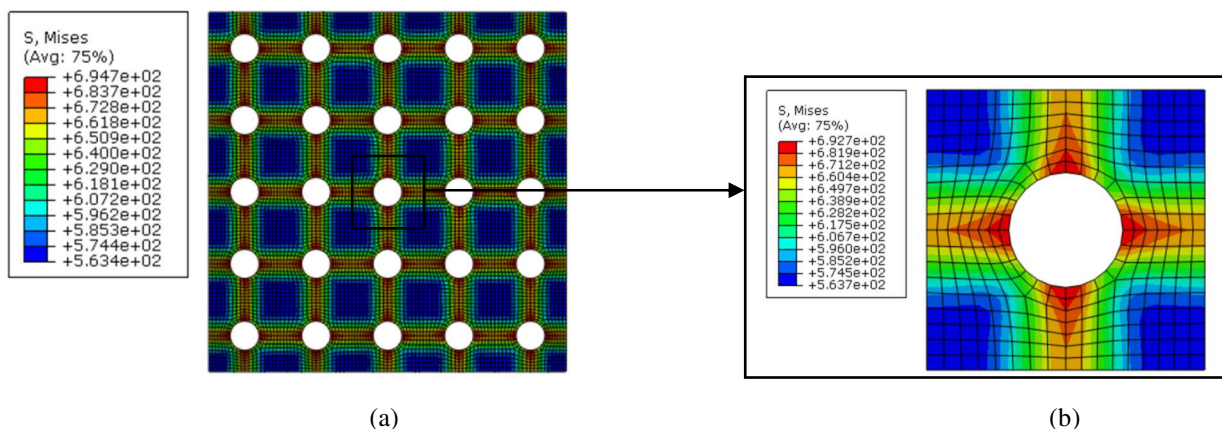


Fig. 3.7. The entire sheet with the prescribed boundary conditions.

The distributions of the microscopic equivalent (von Mises) stress and plastic strain at the end of the loading with a focus on the central unit cell are shown in Fig. 3.8. This figure highlights the heterogeneity of the microscopic fields, especially around the voids.



(a)

(b)

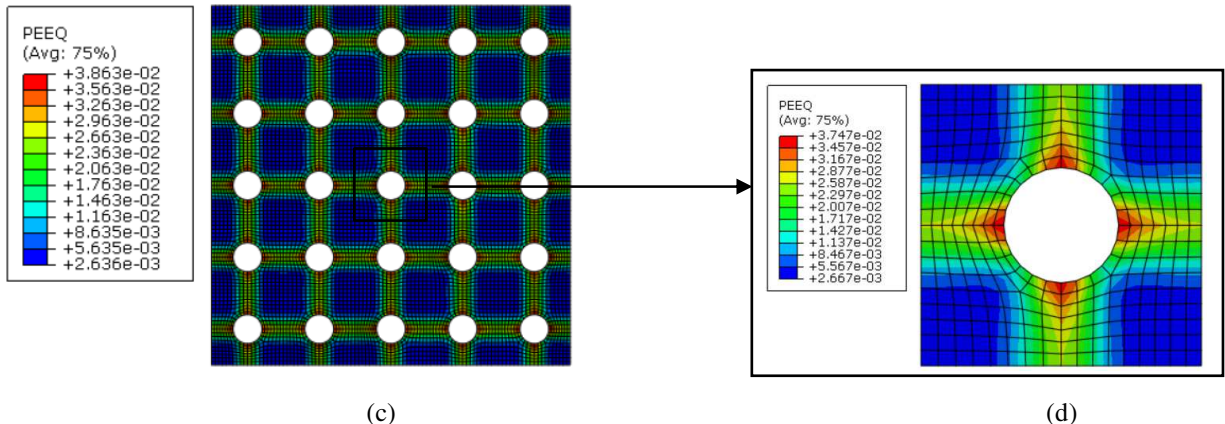


Fig. 3.8. Contour of microscopic fields obtained by classical finite element computations: (a) equivalent stress in the entire sheet; (b) equivalent stress in the central unit cell; (c) equivalent plastic strain in the entire sheet; (d) equivalent plastic strain in the central unit cell.

The central unit cell is now isolated and subjected to the same loading as the entire sheet. PBCs and KBCs are successively applied on the boundary of the isolated unit cell. The *Homtools* are used for applying the macroscopic loading and the different boundary conditions. The results of these computations in terms of distribution of microscopic equivalent stress and plastic strain fields are depicted in Fig. 3.9. The comparison between Fig. 3.9a and c, on the one hand, and Fig. 3.9b and d, on the other hand, clearly shows the important effect of the applied boundary conditions on the microscopic mechanical response. Furthermore, the comparison between Fig. 3.8 and Fig. 3.9 reveals that the results obtained from the unit cell with PBCs are in good agreement with those of the entire sheet. This agreement confirms the reliability of PBCs compared to KBCs in the prediction of the mechanical behavior of the unit cell.

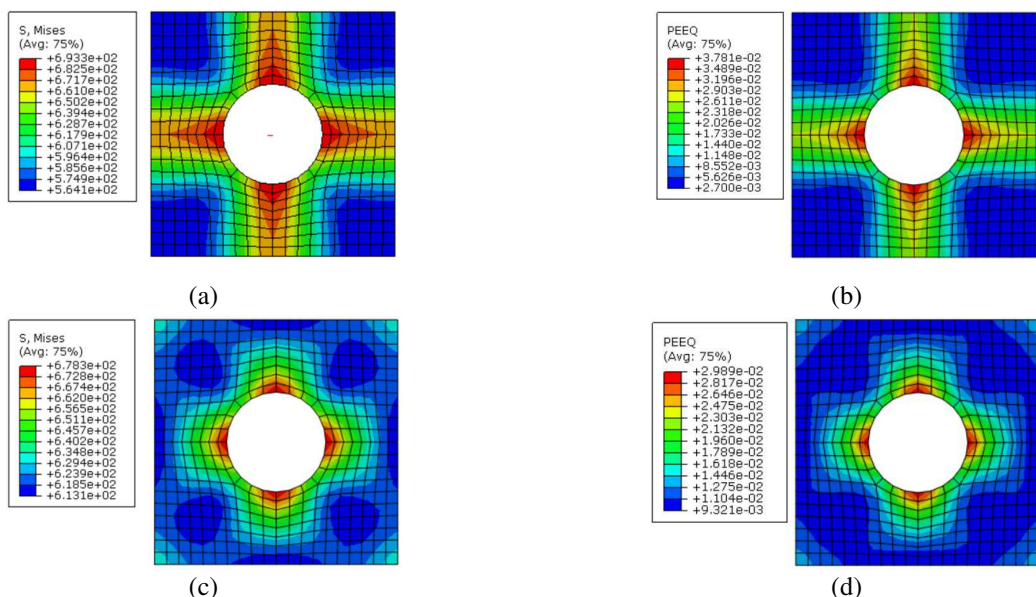


Fig. 3.9. Contour of microscopic fields obtained by multiscale computations: (a) equivalent stress obtained by PBCs; (b) equivalent plastic strain obtained by PBCs; (c) equivalent stress obtained by KBCs; (d) equivalent plastic strain obtained by KBCs.

As shown in Fig. 3.10a, a rapid drop in equivalent stress occurs as the equivalent strain reaches the critical value E_{eq}^B indicated by full circles when the PBCs are used (unlike the curves obtained by the KBCs). Consequently, strain localization predicted by using KBCs is expected to occur much later than that obtained by PBCs. To check this point, the onset of macroscopic strain localization, predicted by bifurcation theory, is simulated for a 3D unit cell subjected to several proportional stressing states ($L = -1$, $T = 0.7; 1.0; 2.0$). To perform these predictions, the initial void volume fractions f_{p0} and f_{s0} are set to 0.04 and 0.0, respectively. The results of these predictions are displayed in Fig. 3.10b, where the critical equivalent strain E_{eq}^B is plotted versus the macroscopic stress triaxiality ratio T . This figure shows that E_{eq}^B obtained by KBCs is three times higher than that obtained by PBCs. This figure also demonstrates that KBCs lead to a strong overestimation of the macroscopic equivalent strain at the onset of strain localization.

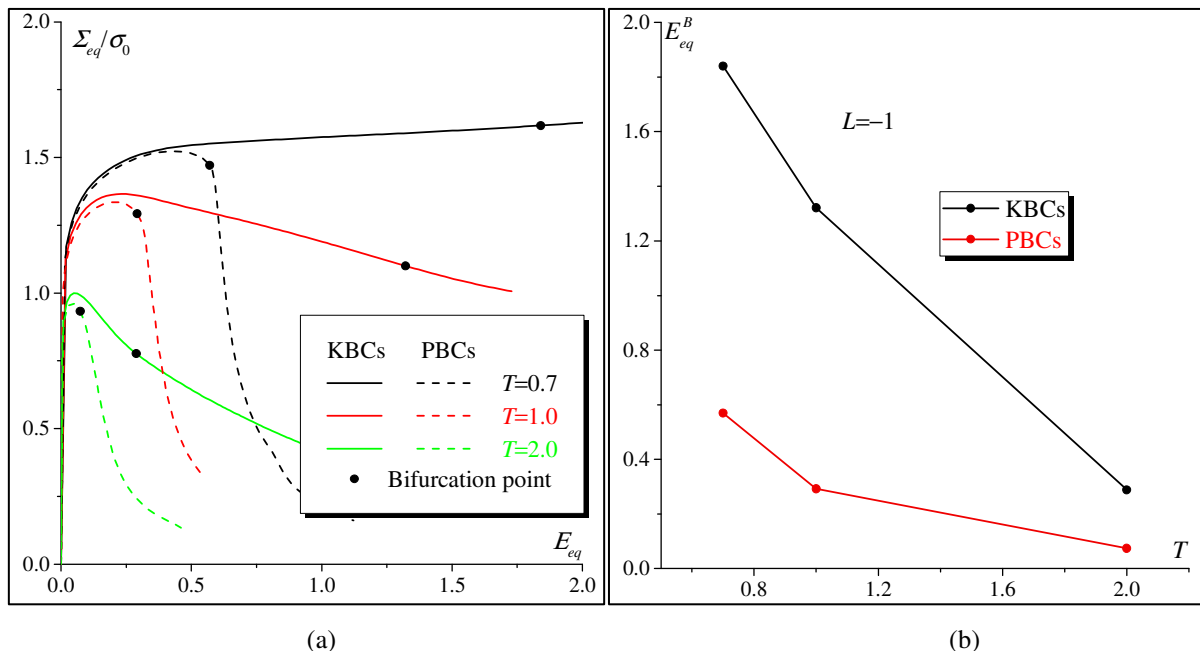


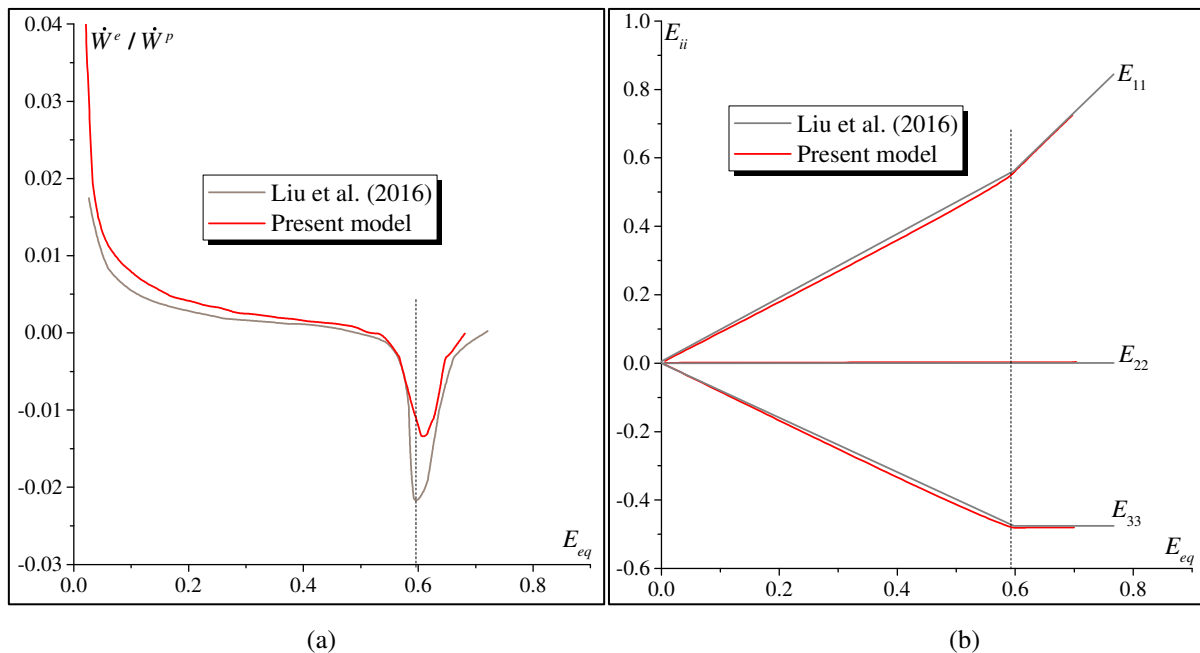
Fig. 3.10. Effect of the boundary conditions on: (a) the evolution of the equivalent stress Σ_{eq} normalized by the initial yield stress σ_0 ; (b) the evolution of the critical equivalent strain E_{eq}^B .

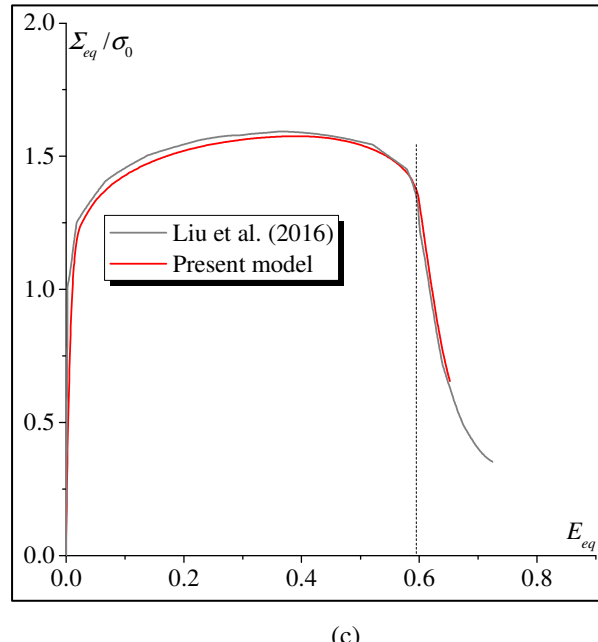
3.5.3. Proportional stressing

3.5.3.1. Comparison with results of Liu et al. (2016)

To validate the developed approach, our numerical predictions are compared with those published in Liu et al. (2016). For this purpose, KBCs are applied, instead of PBCs, on the boundary of the unit cell. This unit cell is proportionally stressed, where the stress state is taken to be of $T = 1.0$ and $L = 0.0$. The onset of void coalescence is predicted by the energy-based criterion presented in Section 3.4.3. The evolutions of the ratio \dot{W}^e / \dot{W}^p , the macroscopic logarithmic strain components (E_{11} , E_{22} , E_{33}) and the

macroscopic equivalent stress Σ_{eq} are plotted as functions of the macroscopic equivalent strain E_{eq} in Fig. 3.11a, b and c, respectively. Among these plots, our numerical predictions are marked by red curves and those published in Liu et al. (2016) by grey curves. The evolution of the principal logarithmic strains and the equivalent stress-strain response are in very good agreement with those reported in Liu et al. (2016). This is also the case for the predicted value of the critical strain for void coalescence E_{eq}^C ($E_{eq}^C = 0.597$ in Liu et al., 2016 versus $E_{eq}^C = 0.605$ in the current model). However, the magnitude of \dot{W}^e / \dot{W}^p when void coalescence occurs is not in perfect agreement. This difference is likely to be attributable to the type of the finite element used in the simulations. In fact, the C3D8R element (eight-node reduced-integration solid element) is used in Liu et al. (2016), while in the present investigation, the unit cell is discretized by using the C3D8 solid element (with full integration). One can observe from the curves of Fig. 3.11a that, as the unit cell deforms plastically, the energy ratio undergoes a state of decrease up to a point where ratio \dot{W}^e / \dot{W}^p becomes equal to zero. This means that the loading state applied on the unit cell changes from elastoplastic loading to elastic unloading. As further increase in deforming, ratio \dot{W}^e / \dot{W}^p will reach a minimum value where the maximum elastic unloading occurs. This point is identified as the onset of void coalescence. Beyond this point, ratio \dot{W}^e / \dot{W}^p will increase from negative to positive. This change means that the mechanical state in the unit cell recovers to elastoplastic loading from elastic unloading. Together with Fig. 3.11a, Fig. 3.11b shows a shift of the principal logarithmic strains when void coalescence occurs. It is observed that the cell straining mode shifts from triaxial to uniaxial strain state with $\dot{E}_{22} = \dot{E}_{33} = 0$ (Koplik and Needleman, 1988). It is worth noting that the straining mode shifts and the minimum of \dot{W}^e / \dot{W}^p always occurs simultaneously and corresponds to the onset of void coalescence.





(c)

Fig. 3.11. Validation of the numerical implementation by comparing our predictions with results published in Liu et al. (2016): (a) evolution of ratio \dot{W}^e / \dot{W}^p ; (b) evolution of the macroscopic logarithmic strain components E_{11} , E_{22} and E_{33} ; (c) evolution of the macroscopic equivalent stress Σ_{eq} normalized by the initial stress σ_0 .

3.5.3.2. Competition between void coalescence and macroscopic strain localization

To start the analysis of the competition between void coalescence and macroscopic strain localization, three proportional stressing configurations are simulated. For these loadings, the Lode parameter L is set to 1.0 and three values for the stress triaxiality ratio T are considered: 0.8; 1.0 and 2.0. The matrix of the unit cell is assumed to be fully dense (hence, $f_{s0} = 0$) and the initial volume fraction of the primary void f_{p0} is set to 0.04. The evolution of some macroscopic quantities, relevant to study the competition between void coalescence and macroscopic strain localization, are plotted in Fig. 3.12. In unit cell computations, the equivalent strain E_{eq} is often used as a measure of material ductility. Therefore, a critical equivalent strain, predicted by each indicator, has also been used to denote material failure. For comparison purposes, four symbols are marked in each curve of Fig. 3.12 to designate the level of the macroscopic equivalent strain corresponding to each criterion:

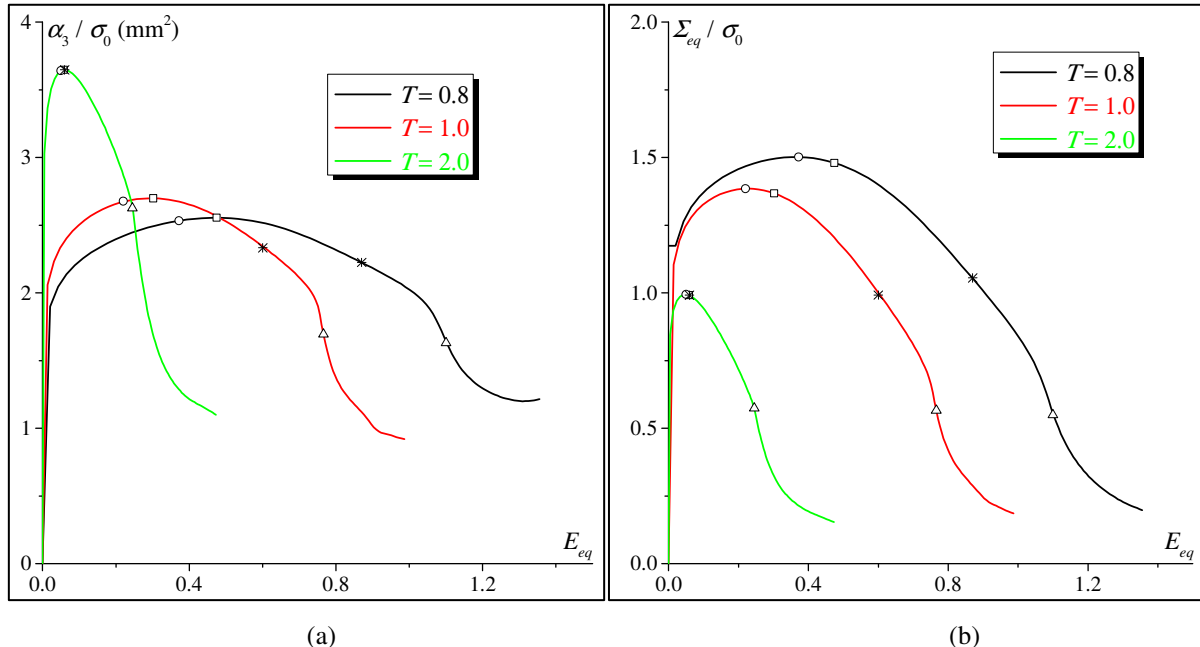
- A square (\square) to designate E_{eq}^R (when the reaction force component α_3 of the dummy node reaches its maximum value).
- A circle (\circlearrowleft) to designate E_{eq}^S (when the equivalent stress Σ_{eq} reaches its maximum value).
- A star ($*$) to designate E_{eq}^B (when the determinant of the acoustic tensor $\vec{\mathcal{N}} \cdot \tilde{\mathbf{C}}^{(PK1)} \cdot \vec{\mathcal{N}}$ vanishes).
- An up triangle (\triangle) to designate E_{eq}^C (when ratio \dot{W}^e / \dot{W}^p reaches its minimum and negative value).

In view of the curves in Fig. 3.12, some conclusions can be drawn:

- For all of the stress triaxiality ratios considered, the critical equivalent strains predicted by the different criteria are classified as follows:

$$E_{eq}^S < E_{eq}^R < E_{eq}^B < E_{eq}^C. \quad (3.49)$$
- As expected, the different critical equivalent strains (namely, E_{eq}^S , E_{eq}^R , E_{eq}^B and E_{eq}^C) decrease with the increase of stress triaxiality ratio T , reflecting the loss of ductility. Moreover, the dependency of the different critical equivalent strains on T is more pronounced in the low stress triaxiality range and saturates as T increases to a high level.
- The difference between the various critical equivalent strains decreases when the stress triaxiality ratio increases. For instance, the difference between E_{eq}^S and E_{eq}^C decreases from 0.73 for $T=0.8$ to 0.20 for $T=2.0$.

The effect of the stress triaxiality ratio on the onset of ductile failure will be further investigated in Section 3.5.3.3, where a wide range of T will be considered and not only three particular values.



(a)

(b)

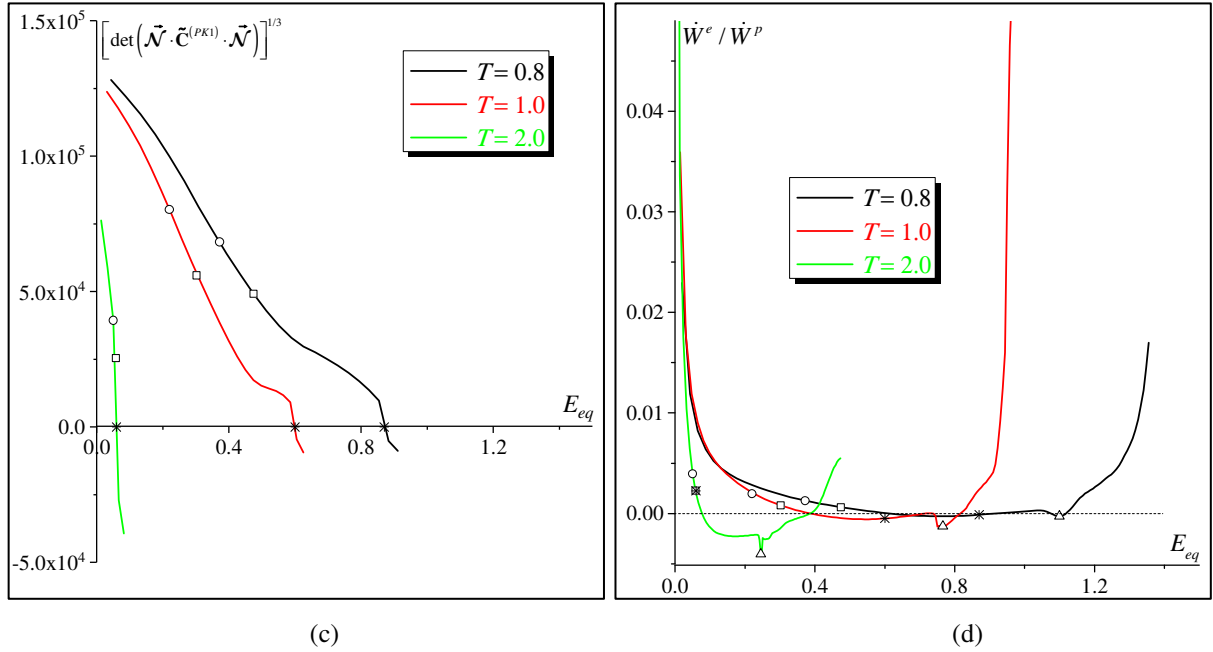


Fig. 3.12. Competition between void coalescence and macroscopic strain localization for proportional stressing configurations defined by $T=0.8; 1$ and 2 , with $L=1$: (a) evolution of the reaction force component α_3 of the dummy node normalized by the initial stress σ_0 ; (b) evolution of the equivalent stress Σ_{eq} normalized by the initial stress σ_0 ; (c) evolution of the cubic root of the determinant of the acoustic tensor $\det(\vec{\mathcal{N}} \cdot \tilde{\mathbf{C}}^{(PK1)} \cdot \vec{\mathcal{N}})^{1/3}$; (d) evolution of ratio \dot{W}^e / \dot{W}^p .

3.5.3.3. Effect of the stress triaxiality ratio on ductile failure

An overview of the competition between void coalescence and strain localization is provided in Fig. 3.13, where the evolutions of the critical equivalent strains E_{eq}^S , E_{eq}^R , E_{eq}^B and E_{eq}^C are plotted against T for the range $(0.7 \leq T \leq 3.0)$ and for three L values ($-1; 0$ and 1.0). As one can see, all of the four limit strains decrease as T increases for the different values of L . By examining the evolution of E_{eq}^C and E_{eq}^B for a given range of T , one can observe that $E_{eq}^B < E_{eq}^C$ regardless the value of L . Namely, localization bifurcation occurs before the attainment of void coalescence predicted by the energy-based criterion for the full range of T . For $T < 2.0$, the limit strains E_{eq}^B , E_{eq}^R and E_{eq}^S are attained with $E_{eq}^S < E_{eq}^R < E_{eq}^B$, and the difference between these limit strains decreases as T increases for the various values of L . For higher values of T , notably $T > 2.0$, the curves corresponding to E_{eq}^B , E_{eq}^R and E_{eq}^S are almost indistinguishable. This result means that for high stress triaxiality levels, the maximum of the reaction force of the dummy node, the maximum equivalent stress and the bifurcation are reached at approximatively the same moment. This latter conclusion is fully consistent with the predictions obtained by Guo and Wong (2018), where it has been demonstrated that the maximum reaction force of the dummy node (used as strain localization criterion) and the maximum equivalent stress are simultaneously attained for high values of T (typically higher than 1.5). On the other hand, the

bifurcation criterion (used in this thesis as a rigorous macroscopic strain localization criterion) appears to be less conservative than the criterion of maximum reaction force on the dummy node (used as strain localization criterion in [Guo and Wong, 2018](#)) for the range of low triaxiality ($T < 2.0$), and this is more remarkable for $L = 1.0$. Whatever the adopted macroscopic strain localization criterion, defined as the maximum equivalent stress in [Bomarito and Warner \(2015\)](#) and [Tekoglu et al. \(2015\)](#) or as the maximum reaction force in [Guo and Wong \(2018\)](#), the bifurcation criterion presented herein leads to relatively higher limit strains for $T < 2.0$. For higher stress triaxiality ($2.0 < T < 3.0$), all three strain localization criteria predict almost the same results.

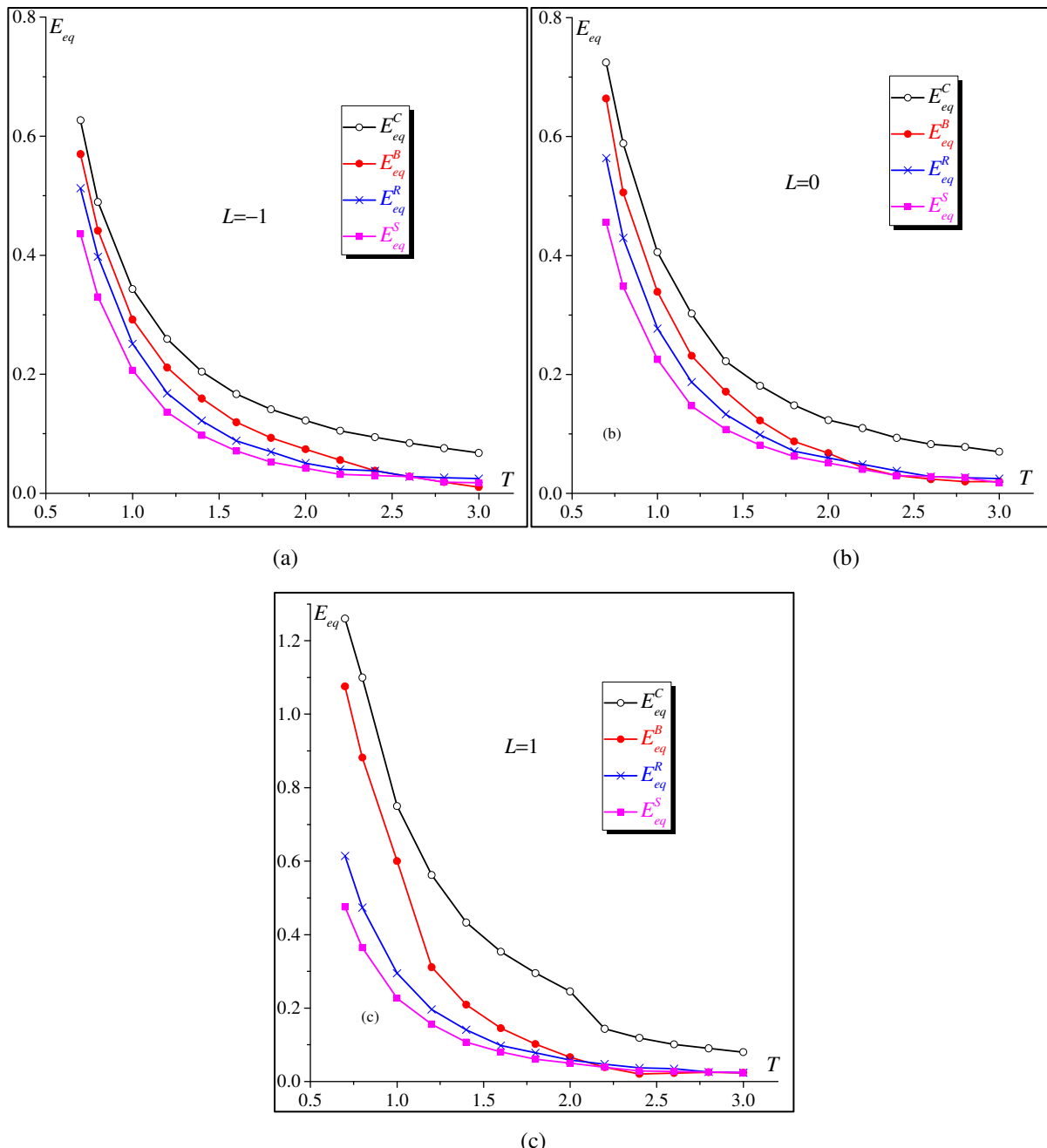


Fig. 3.13. Evolution of critical equivalent strains E_{eq}^S , E_{eq}^R , E_{eq}^B and E_{eq}^C over the range $0.7 \leq T \leq 3.0$ and for (a) $L = -1$; (b) $L = 0$; (c) $L = 1$.

3.5.3.4. Effect of the Lode parameter on ductile failure

Special attention is now paid to the analysis of the effect of the Lode parameter L on macroscopic strain localization and void coalescence. The evolutions of the critical equivalent strains E_{eq}^C and E_{eq}^B are plotted in Fig. 3.14 over the range $-1.0 \leq L \leq 1.0$ and for some particular T values (0.8; 1.2; 1.6; 2.0; 2.4 and 3.0). The loci of E_{eq}^C and E_{eq}^B are denoted by solid and dash lines, respectively. At first glance, it is clear that E_{eq}^C is larger than E_{eq}^B for the full range of L . For low to moderate levels of T , both E_{eq}^C and E_{eq}^B increase with L , especially for $0 \leq L \leq 1.0$, with different increase rates. Moreover, the difference between E_{eq}^C and E_{eq}^B increases with L in the range $0 \leq L \leq 1.0$ for relatively low triaxiality levels. For high stress triaxiality levels (e.g., $T = 2.4$ and $T = 3.0$), E_{eq}^C and E_{eq}^B are quasi linear and almost constant for the full range of L . In other words, the effect of Lode parameter is more pronounced when the stress triaxiality is low. Regarding the effect of L , Barsoum and Faleskog (2011) and Dunand and Mohr (2014) have found that E_{eq}^C performs a convex and non-symmetric function of L ($-1.0 < L < 1.0$) by following the coalescence criterion developed in Needleman and Tvergaard (1992). This trend has been confirmed by Luo and Gao (2018) using a sandwiched unit cell model, but seems to be inconsistent with that observed in our investigation. This apparent inconsistency is explained by the convention adopted to determine T and L from β_1 and β_2 (see Section 3.3.2). In fact, several families of stress states (β_1, β_2) could be obtained from a given T and L , as demonstrated by Wong and Guo (2015). Consequently, for these different stress states, the predicted critical strains for macroscopic strain localization are quite distinct, and the same applies to void coalescence, although the stress triaxiality ratio T and the Lode parameter L remain the same. Therefore, with various stress states (β_1, β_2) , one may draw different conclusions regarding the effect of L (see, e.g., Fig. 11 in Wong and Guo, 2015). With the convention for L adopted in our investigation, we obtain trends that are similar to those observed in Zhu et al. (2018).

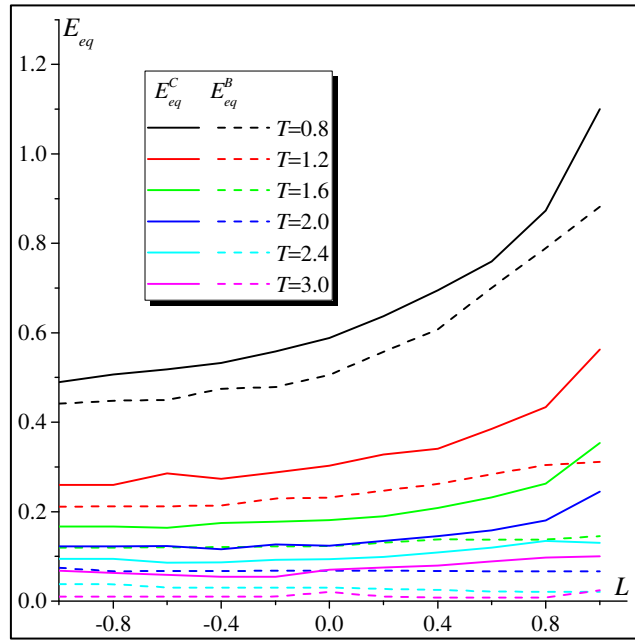


Fig. 3.14. Locus of limit strains E_{eq}^C and E_{eq}^B over the range $-1.0 \leq L \leq 1.0$ and for $T = 0.8; 1.2; 1.6; 2.0; 2.4; 3.0$.

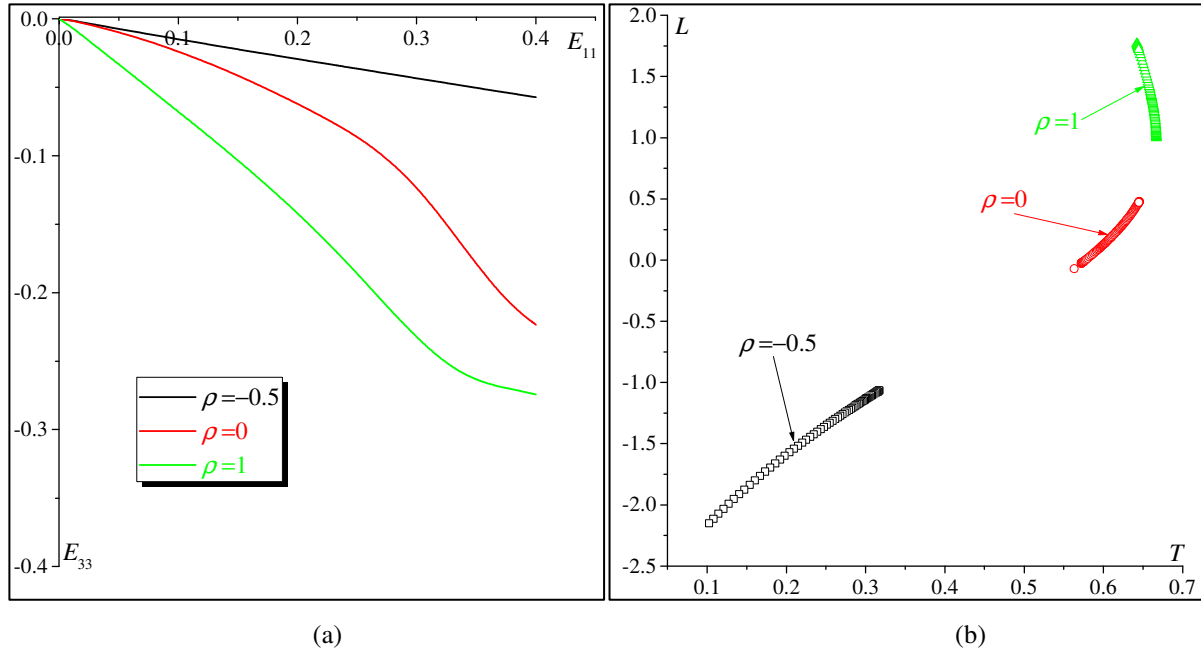
3.5.4. Proportional in-plane strain paths

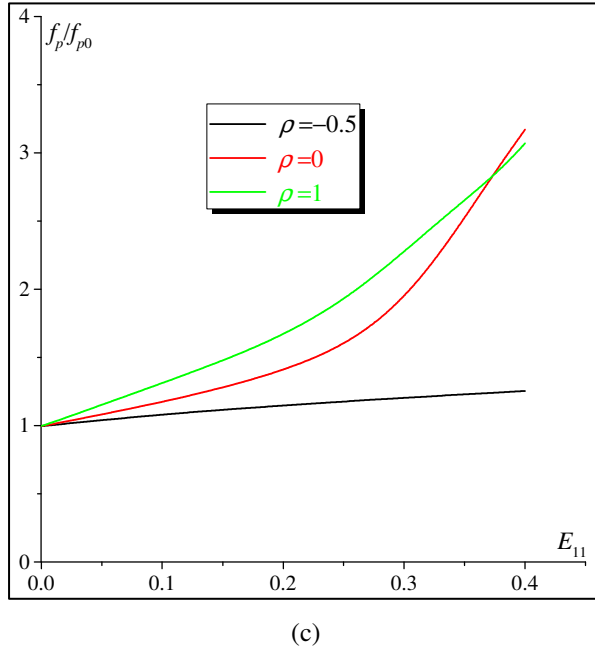
In the current section, the ductility limit of thin metal sheets is predicted and depicted through the conventional representation of forming limit diagrams (FLDs). For this purpose, we consider a unit cell subjected to the boundary conditions shown in Fig. 3.6b. We firstly demonstrate that void coalescence cannot be predicted by the energy-based criterion for this loading configuration (Section 3.5.4.1). The other indicators (namely, the criterion of maximum reaction force on the dummy node and the maximum equivalent stress criterion) are classically considered by the ‘sheet metal forming’ community as diffuse necking criteria and, hence, not relevant to predict forming limit diagrams. Consequently, the Rice bifurcation approach will be the only criterion used for predicting FLDs. It shall be noted that this criterion has been widely used in the literature to predict the onset of localized necking in thin metal sheets (see Chapter 2 and references therein), while this is the first time that it is coupled with 3D unit cell computations. The developed approach is used to investigate the effect of two key factors on the ductility limits of thin metal sheets: the shape of the primary void (Section 3.5.4.2), and the presence of secondary population of voids (Section 3.5.4.3).

3.5.4.1. Prediction of void coalescence by the energy-based criterion

To check whether elastic unloading may occur during the application of proportional strain paths, the evolution of the strain component normal to the thickness direction E_{33} is plotted in Fig. 3.15a versus the major in-plane strain E_{11} for three representative strain-path ratios: $\rho = -0.5; 0.0; 1.0$. The minor in-plane strain E_{22} is equal to ρE_{11} . As one can see in Fig. 3.15a, E_{33} decreases monotonically as the deformation proceeds. Hence, the deformation mode does not switch from elastoplastic loading to elastic

unloading. Consequently, void coalescence is not predicted by the energy-based criterion. This observation is evidently related to, at least, two facts: the range of stress state associated with the applied strain paths, and the nature of the applied macroscopic loading. To thoroughly analyze the first fact, the evolution of the stress state during loading is plotted in the (T, L) -space for some representative strain-path ratios (Fig. 3.15b). It turns out from Fig. 3.15b that the stress triaxiality ratio T does not exceed 0.7 for all the loading cases and, hence, the strain paths corresponding to the FLDs are not covered by the range of stress triaxiality studied in Section 3.5.3 (between 0.7 and 3.0). By making connection between Fig. 3.15b and the curves of Fig. 3.13, it appears immediately evident why the void coalescence, predicted by the energy-based criterion, is not reached for the strain paths considered here. To better illustrate this study, the evolution of the volume fraction of the primary void f_p , normalized by its initial value f_{p0} , is plotted against the major strain E_{11} in Fig. 3.15c. For the strain-path ratio $\rho = -0.5$, ratio f_p / f_{p0} is almost constant during plastic deformation. This result can be explained by the very low stress triaxiality characterizing this particular strain path, as the stress state is near uniaxial tension state (Fig. 3.15b). In this case, only the void shape changes (from spherical to approximately ellipsoidal), without significant void growth. For the strain-path ratios $\rho = 0.0$ and 1.0 , ratio f_p / f_{p0} increases slowly as plastic deformation proceeds. This slight evolution of void growth, without abrupt change, explains the difficulty in reaching void coalescence.





(c)

Fig. 3.15. Study for strain-path ratios $\rho = -0.5; 0.0; 1.0$: (a) evolution of E_{33} versus E_{11} ; (b) distribution of the stress triaxiality ratio T and the Lode parameter L ; (c) evolution of volume fraction of the primary void f_p normalized by f_{p0} .

As to the nature of the applied macroscopic loading, for proportional in-plane strain paths, the strain components E_{11} and E_{22} are prescribed and are assumed to evolve monotonically during the loading. The strain component E_{33} is determined by the plane-stress condition ($\Sigma_{33} = 0$), and this component generally decreases with plastic deformation. Consequently, macroscopic elastic unloading cannot occur in this case. By contrast, for proportional stressing, the stress ratios β_1 and β_2 hold constant and strain components E_{11} , E_{22} and E_{33} adjust to ensure that β_1 and β_2 keep their desired values. During loading, the instant when the sign of at least one of the components \dot{E}_{11} , \dot{E}_{22} and \dot{E}_{33} changes marks the onset of elastic unloading.

In several earlier contributions, void coalescence has been assumed to occur when the growth of the primary void exhibits an abrupt acceleration. As shown in Fig. 3.15c, a clear abrupt change in the void growth is not observed for any of the studied strain paths. This observation is due to the effect of neighboring unit cells on the deceleration of void growth. To elucidate this effect, let us consider two sheet configurations. In the first configuration, the sheet is defined by a 2D arrangement of voided unit cells, identical to the one shown in Fig. 3.6a. As previously stated, void coalescence is not reached under this configuration for all of the applied strain paths. As to the second configuration (see Fig. 3.16), it is defined by a dense sheet crossed by a narrow voided band. The width ratio \tilde{l}_0/l_0 for the current simulations is set to 2.0 (see Fig. 3.16). This second configuration follows the same spirit as the initial imperfection approach introduced by Marciniak and Kuczyński (1967). Under this configuration, the sheet is subjected to the following displacement rate boundary conditions:

$$\begin{cases} \dot{U}_1 = 1; \\ \dot{U}_2 = 0 \text{ (plane strain in direction 2);} \\ U_3 = \text{free (plane stress in direction 3).} \end{cases} \quad (3.50)$$

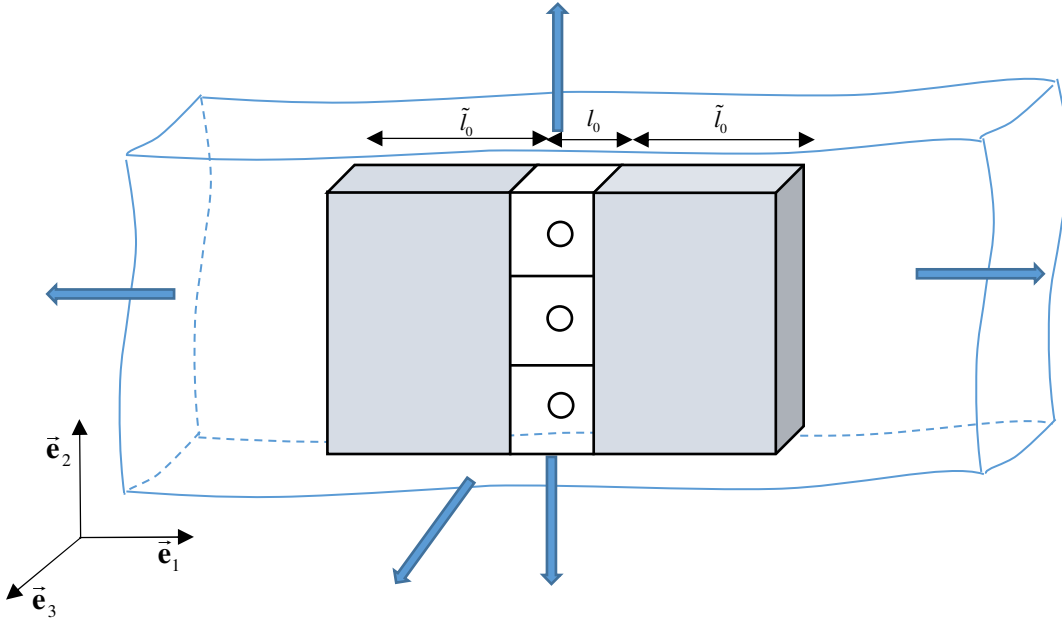


Fig. 3.16. Dense sheet crossed by a narrow voided band.

The application of the classical boundary conditions, given by Eq. (3.50), to the sheet configuration defined in Fig. 3.16 leads to localization of the deformation inside the voided band, along with relatively slight deformation followed by elastic unloading outside the band (called safe zone), as shown in Fig. 3.17a. In this figure, E_{33}^{Band} , E_{33}^{Safe} and $E_{33}^{Classic}$ refer to the 33 component of the macroscopic strain inside the band, in the safe zone and as obtained by classic unit cell computations (configuration 1), respectively. For configuration 2, a rapid void growth can be observed, as displayed in Fig. 3.17b, which may promote the onset of void coalescence. Consequently, void coalescence is dependent on the stress state inside the unit cell and also on the mechanical behavior of regions surrounding this unit cell. The same trends are obtained for the other strain paths, but to be concise, the corresponding results are not presented here. If the width ratio \tilde{l}_0 / l_0 is chosen to be very large (a very small band width), an abrupt change in void growth can be readily obtained, thus characterizing the onset of void coalescence. It shall be noted that the configuration presented in Fig. 3.16 has been widely used in the literature to predict the onset of void coalescence and strain localization in voided solids (Teko\u011f\u011f et al., 2015; Luo and Gao, 2018).

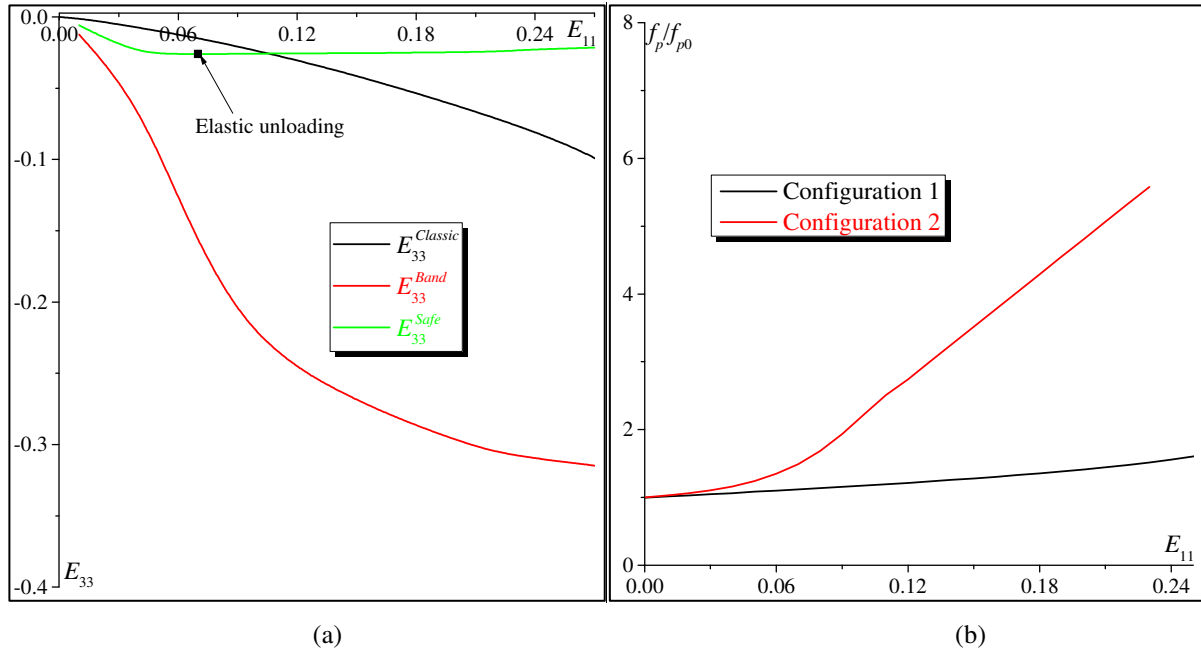


Fig. 3.17. Effect of the neighborhood of the unit cell on: (a) the evolution of the strain component in the thickness direction outside the band; (b) the growth of the primary void.

3.5.4.2. Effect of initial primary void shape on the ductility limits of thin sheets

In the previous sections, the initial shape of the primary void was assumed to be spherical. However, some experimental evidences show that voids are often non-spherical in actual materials, such as rolled plates (Gao and Kim, 2006). And even for materials containing initially spherical voids, the void shape is likely to change as a function of the applied stress state. Voids in real materials may have, for example, the shape of long, prolate ellipsoids, if they nucleate around segregations previously elongated by a rolling process; at the opposite extreme, they may look like wide, oblate ellipsoids if they happen to grow from cleavage cracks generated in the hard phase of a dual-phase structure (see, e.g., Pineau and Joly, 1991). There is thus a need for accurately modeling the effect of void shape on the occurrence of ductile failure. In this aim, the Gurson model has been extended by Gologanu et al. (1993, 1994) to study the growth of non-spherical voids embedded in a ductile dense matrix. In the present chapter, the developed approach is used for the investigation of this effect on the shape and the level of forming limit diagrams. To this end, three shapes are considered for the primary void: oblate, spherical and prolate. Oblate and prolate voids are assumed to be axisymmetric about 2-axis, and their initial aspect ratio is defined as $\mathcal{W}_0 = r_{p2} / r_{p1} = r_{p2} / r_{p3}$. Thus, $\mathcal{W}_0 = 1$ corresponds to a spherical void (Fig. 3.18b), $\mathcal{W}_0 = 1/3$ to oblate void (Fig. 3.18a), and $\mathcal{W}_0 = 3$ to prolate void (Fig. 3.18c). In these three cases, the initial volume fraction of the primary void is taken to be $f_{p0} = 0.04$. The metal matrix is assumed to be fully dense (hence, $f_{s0} = 0.0$).

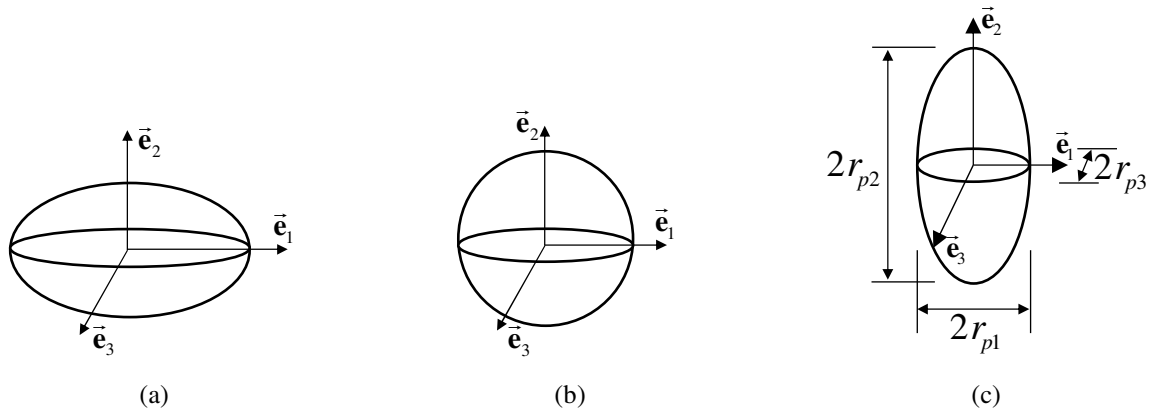


Fig. 3.18. Geometric representation of three void shapes: (a) oblate void ($W'_0 = 1/3$); (b) spherical void; (c) prolate void ($W'_0 = 3$).

The effect of void aspect ratio on the void-induced softening phenomenon has been highlighted in several earlier investigations (Pardoen and Hutchinson, 2000; Keralavarma and Benzerga, 2010). In the present section, attention is focused on the effect of the initial void shape on the ductility limits. As clearly shown in Fig. 3.19a, the initial void shape slightly affects the left-hand side of the FLDs. More interestingly, the ductility limit increases as the aspect ratio W'_0 decreases in the range of positive strain-path ratios. This result is quite expectable considering the fact that the void growth mechanism should be more important for the unit cell with $W'_0 = 3$ and, consequently, the ductility of the unit cell is negatively affected by this void growth. The predictions of Fig. 3.19a are fully consistent with the results published in Pardoen and Hutchinson (2000) and in Keralavarma and Benzerga (2010). To further analyze this effect, the initial macroscopic yield loci corresponding to the different unit cell configurations are plotted in Fig. 3.19b. Focus is confined to the first quadrant of these yield loci ($\Sigma_{11} \geq 0$ and $\Sigma_{22} \geq 0$), as the stress states corresponding to the whole range of strain paths are located in this first quadrant (from uniaxial to equibiaxial tension state). In the case of non-spherical shape (e.g., ellipsoidal) for the primary void, there exists a preferred material orientation and the macroscopic plastic behavior reveals to be anisotropic (even if the metal matrix is elastically and plastically isotropic). Consequently, the change in the initial aspect ratio W'_0 would induce a change in the curvature of the macroscopic yield locus, as shown in Fig. 3.19b. This curvature has an important impact on the predicted ductility limits, especially near the equibiaxial tension state (Barlat, 1987): the sharper the yield surface, the lower the corresponding ductility limit.

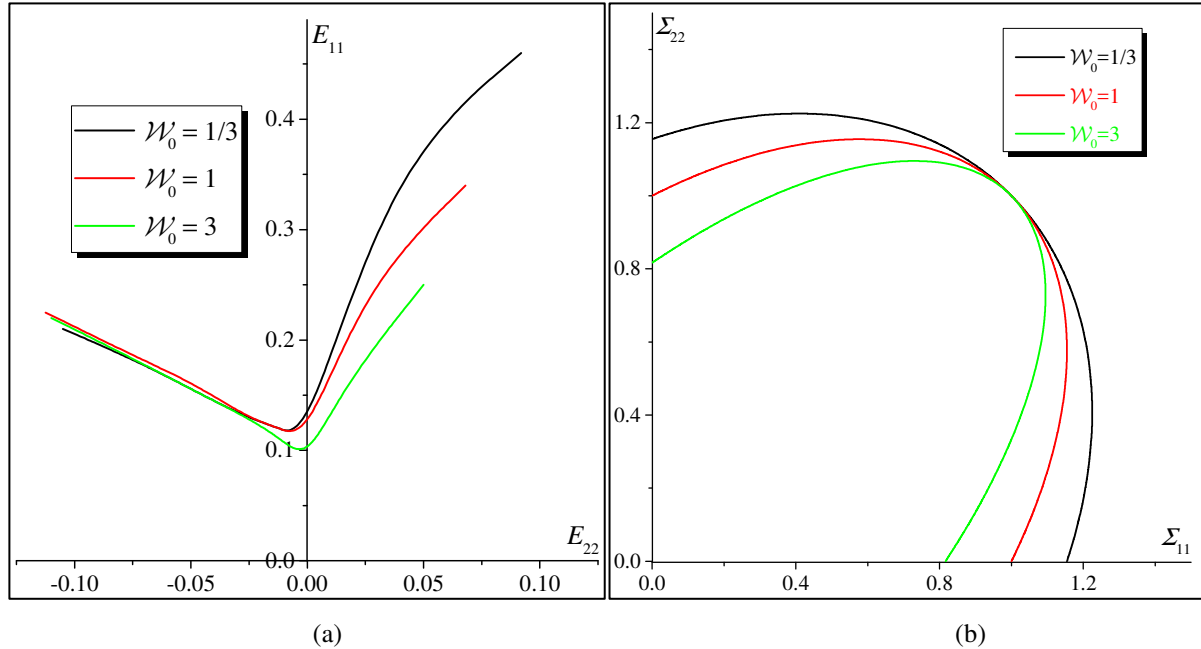


Fig. 3.19. Effect of initial shape of the primary void on: (a) the predicted forming limit diagrams; (b) the shape of the macroscopic yield loci for the quadrant ($\Sigma_{11} \geq 0$ and $\Sigma_{22} \geq 0$).

3.5.4.3. Effect of secondary population of voids on the ductility limits of thin sheets

Just far, we have consistently assumed that the metal matrix is fully dense. However, several experimental observations point out the potential presence of secondary (small) void populations, in addition to the primary void, in most engineering materials. [Gao and Kim \(2006\)](#) and [Fabrègue and Pardoen \(2008\)](#) have developed two extensions of the Gurson model to take into account the impact of secondary void population on the material behavior. It turns out from these investigations that nucleation and growth of secondary voids accelerate the coalescence of the primary void and, thus, lead to a reduction of material ductility. In the present contribution, this effect is investigated by using the Gurson constitutive framework for the modeling of the mechanical behavior of the matrix, as stated in Section 3.2.2. The secondary voids are assumed to be uniformly distributed over the metal matrix and three distinct values for their initial volume fraction f_{s0} are considered: 0.0 (which corresponds to a fully dense matrix), 0.01 and 0.04. The values of f_{s0} adopted here are for the only purpose of demonstrating the effect of secondary voids on void coalescence and macroscopic strain localization. No attempt is made to represent actual physical values. As depicted in Fig. 3.20a, the initial volume fraction of secondary voids f_{s0} affects the limit strains. In the range of positive strain-path ratios, the ductility limits decrease as f_{s0} increases. However, in the range of negative strain-path ratios, the forming limit curves are less sensitive to the value of f_{s0} . This result is quite expectable considering the fact that the growth of primary as well as secondary voids increases with the strain-path ratio. To further investigate the effect of the secondary void population on the mechanical behavior, the evolution of the microscopic equivalent stress σ_{eq} in a finite element near the primary void is plotted for the extreme strain-path ratios

($\rho = -0.5$ and $\rho = 1.0$). As one can see, the stress plots corresponding to $\rho = 1.0$ are more sensitive to the value of f_{s0} . In this case, the microscopic equivalent stress reaches its maximum earlier and decreases more rapidly for the case $f_{s0} = 0.04$. By contrast, for $\rho = -0.5$, the three stress plots are rather similar, and local softening is not observed in this case. This analysis may further explain the effect of f_{s0} on the predicted FLDs.

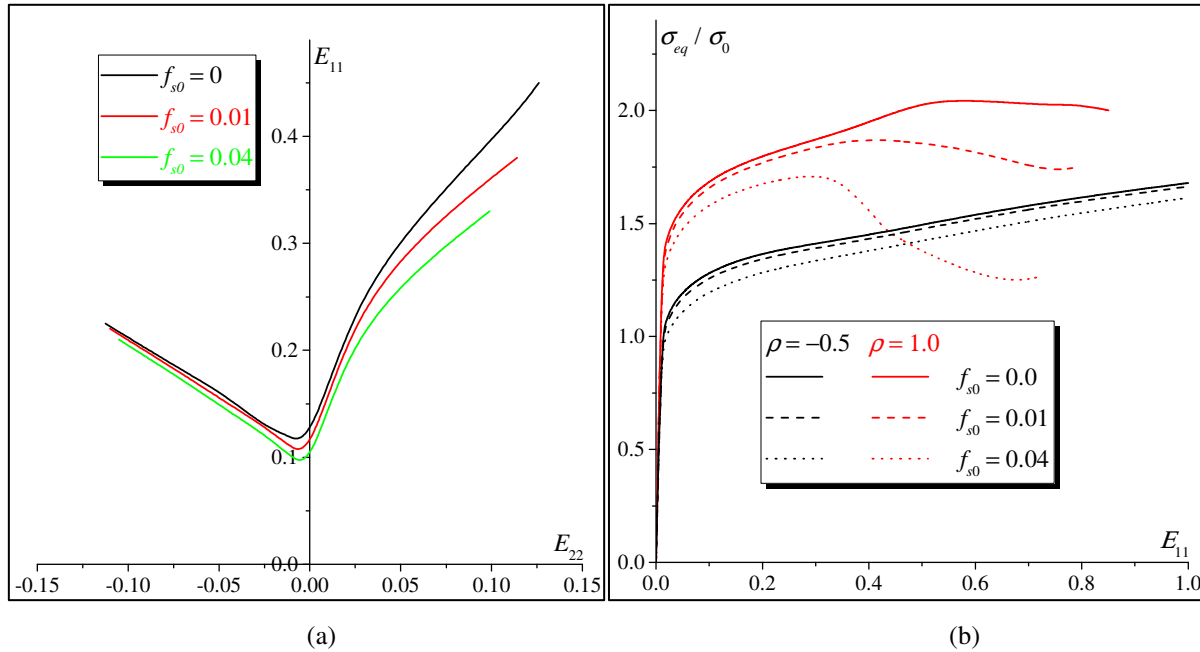


Fig. 3.20. Effect of the initial volume fraction of secondary voids on: (a) the predicted forming limit diagrams; (b) the evolution of the microscopic equivalent stress σ_{eq} normalized by the initial yield stress σ_0 .

3.6. Concluding remarks

In the present chapter, the Rice bifurcation approach has been coupled with the periodic homogenization scheme to predict the onset of macroscopic strain localization in 3D voided materials. For proportional stressing, the predictions given by the Rice bifurcation approach have been compared with those obtained by a void coalescence criterion and other strain localization indicators established in the scientific literature. This comparative study suggests that strain localization predicted by the Rice bifurcation approach acts as a precursor to void coalescence predicted by an elastic unloading criterion, when the stress triaxiality ratio T ranges between 0.7 and 3.0. On the other hand, when $T \leq 2$, the limit strains predicted by the Rice bifurcation theory are much larger than those predicted by other localization criteria defined in the literature (Bomarito and Warner, 2015; Tekoglu et al., 2015 and Guo and Wong, 2018). However, for $T > 2$, the different strain localization criteria predict almost the same limit strains. The effect of the Lode parameter on the limit strains predicted by the different criteria has also been investigated, and we have demonstrated that this effect is more important for low values of T . The developed approach has also been applied to predict the forming limit diagrams of voided thin metal

sheets. We have shown, through numerical investigations, that the ductility of thin metal sheets is only limited by the onset of strain localization, as void coalescence is not observed for the considered range of strain paths. To assess its reliability, the developed approach has been used for examining the effect of two key physical factors on the prediction of forming limit diagrams: the initial shape of primary void, and the presence of secondary void population. It has been pointed out from this analysis that the initial shape of primary void induces initial anisotropy in the macroscopic behavior of the unit cell and, hence, its effect is more pronounced in the range of the positive strain-path ratios. As to the presence of secondary void population, the initial volume fraction of these secondary voids has a negative impact on the ductility limit of the unit cell, especially in the right-hand side of the FLD. This study would be completed by analyzing the competition between microscopic (local) and macroscopic strain localization. This will be one of the objectives of future applications of the developed approach.

Chapter 4

Prediction of the ductility limit of sheet metals based on CPFEM multiscale framework

4.1. Introduction

In the area of material ductility, in general, and more precisely in connection with sheet metal formability, plastic instability phenomena (such as diffuse or localized necking, buckling, wrinkling) have for several decades attracted interest of both metallurgist and computational communities. These phenomena sometimes lead to ultimate material failure. However, in computational analysis, the predictions of instability phenomena are dependent of the mechanical behavior modeling of the materials. Regarding the mechanical behavior modeling, the multiscale schemes based on crystal plasticity have been received widespread attentions. Unlike phenomenological frameworks, crystal plasticity multiscale schemes allow naturally and explicitly linking microstructural phenomena to some relevant in-use properties (ductility, strength ...). In fact, in crystal plasticity multiscale schemes the constitutive relations are established at the single crystal level, thus enabling the accurate description of physical mechanisms and phenomena at this appropriate scale (slip on crystallographic planes, lattice rotation, dislocation motion, grain morphology...). Then, the overall behavior of the polycrystalline medium is obtained from that of the constituent single crystals using relevant multiscale transition rules. Hence, to predict FLDs via multiscale strategies, a scale-transition scheme to derive the overall mechanical behavior from that of the constituent single crystals should be used in conjunction with a strain localization criterion.

- **Modeling at the single crystal scale:** constitutive frameworks developed to model the single crystal behavior for FLD predictions can be broadly classified into two categories: rate-independent modeling (Knockaert et al., 2002; Franz et al., 2009b, 2009a, 2013; Yoshida and

Kuroda, 2012; Akpama et al., 2017) and rate-dependent modeling (Inal et al., 2005; Neil and Agnew, 2009; Signorelli et al., 2009; Lévesque et al., 2010; Kim et al., 2013; Schwindt et al., 2015; Gupta et al., 2018). Considering the low strain-rate sensitivity of the mechanical response during cold forming processes and to avoid some inherent numerical issues due to the use of a rate-dependent approach (e.g., difficulty to integrate the constitutive equations caused by the high value of the rate-sensitivity exponent, and the inadequacy of this modeling approach to be coupled with the bifurcation theory), a rate-independent approach is adopted in this study to model the mechanical behavior of faced centered cubic (FCC) single crystals. The same approach can be readily extended to other crystallographic structures, such as body centered cubic (BCC) or hexagonal close packed (HCP) structures. Compared to rate-independent phenomenological models, single crystal elastoplastic constitutive framework presents two main peculiarities: the plastic deformation is solely activated by the slip on the crystallographic slip systems and the plastic flow is modeled by the classical Schmid criterion (Schmid and Boas, 1950). The evolution of the critical shear stresses, defining the limit of the single crystal yield surface, follows a power-type hardening law, similar to that used in Yoshida and Kuroda (2012). Noting that the resulting constitutive equations can be viewed as a strongly non-linear problem (geometric non-linearities due to the finite strain formulation and material non-linearities caused by the hardening modeling). Hence, the incremental numerical algorithm developed to integrate these equations should be carefully defined to ensure the accuracy of the numerical results and the stability of the time integration scheme. In this chapter, an explicit ultimate algorithm (Borja and Wren, 1993; Akpama et al., 2016) is adopted. This choice is motivated by the comparative study performed in Ben Bettaieb et al. (2012b) where the numerical performance of ultimate algorithms compared to the well-known return-mapping algorithms has been especially emphasized. This performance is crucial when simulating the mechanical behavior of polycrystalline aggregates made of several thousands of single crystals.

- **Multiscale transition schemes:** Various multiscale transition schemes have been set up to predict the overall mechanical behavior of polycrystalline aggregates, assumed to be representative of the studied medium, starting from the mechanical behavior of the constituent single crystals. Among the most commonly-used schemes for the prediction of FLDs, one can quote the mean-field full-constraint Taylor model based on the assumption of strain homogeneity over the polycrystalline aggregate (Knockaert et al., 2002; Inal et al., 2005; Lévesque et al., 2010; Yoshida and Kuroda, 2012). Despite its wide use, the Taylor model present several drawbacks such as the violation of the microscopic equilibrium condition and the lack of accuracy in the description of the interactions between the grains and their surrounding media. To overcome these limitations and hence to better approximate the response of polycrystalline materials, more elaborate mean-field multiscale schemes, such as the self-consistent scheme, have been developed. Compared to the

Taylor model, the self-consistent model allows considering some important aspects not sufficiently accounted for the Taylor model. Thus, within the self-consistent model, the equilibrium condition is fulfilled and the interaction between neighboring grains is correctly considered. Despite its well-recognized advantages, the self-consistent model still presents several conceptual and practical issues. In fact, with this model, each grain is modeled as a separate ellipsoidal inclusion that is embedded within a homogeneous equivalent medium, which has the same mechanical properties as those of the bulk macroscopic medium ([Franz et al., 2013; Akpama et al., 2017](#)). Hence, the description of the grain morphology remains poor. Furthermore, the effect of the spatial location of the grains on the overall mechanical response is disregarded. In addition, some convergence problems may be encountered when solving the self-consistent equations by the fixed-point method especially in the finite strain range ([Akpama et al., 2017](#)). These issues can be naturally avoided when finite elements based crystal plasticity (CPFEM) frameworks are used to model the overall behavior of polycrystalline aggregates ([Tadano et al., 2013](#)). This approach is undoubtedly considered as one of the most efficient and powerful homogenization strategies and is consequently adopted in the current investigation. Considering the spatial quasi-periodicity of the crystallographic structure in polycrystalline media, the periodic homogenization technique turns out to be a relevant scheme to ensure the transition between single crystal and polycrystal scales. As well discussed in the previous chapters, this technique relies on the assumption of periodicity of the mechanical variables (strain and stress fields) over the boundary of representative unit cell of the studied polycrystalline aggregate. Consequently, this technique is adopted to build the CPFEM approach used here to model the mechanical behavior of polycrystalline aggregates and to predict their ductility limits. Contrary to the self-consistent model, the application of CPFEM allows taking into account realistic grain morphologies and not only grains with ellipsoidal shape. Furthermore, the convergence issues encountered in the self-consistent approach are avoided when the CPFEM is used.

- **Strain localization modeling:** The onset of plastic flow localization may occur as a bifurcation from a homogeneous deformation state. Accordingly, the bifurcation analysis is coupled in this chapter with the developed CPFEM to predict the occurrence of localized necking in a representative unit cell of thin metal sheets. Considering the small thickness of the studied sheets, this coupling is performed under the plane-stress condition. The validity of such a condition has been proved in [Hutchinson et al. \(1978\)](#). The bifurcation theory, (see Section 2.3.3 for the theoretical aspects), assumes that localized necking occurs when the macroscopic deformation field becomes discontinuous. However, it is unable to predict localized necking at a realistic strain level in the range of positive in-plane biaxial stretching when the constitutive modeling does not exhibit some destabilizing effects as shown in Section 2.4.1 and [Ben Bettaieb and Abed-Meraiem \(2015\)](#). In the CPFEM developed in the present chapter, the use of the Schmid law (characterized

by the development of vertices on the microscopic yield locus) to model the plastic flow at the single crystal level allows promoting these destabilizing effects. The overall tangent modulus is constructed column by column through the perturbation technique (see Section 1.4.1, also [Temizer and Wriggers, 2008](#) for details) after adapting it to the macroscopic plane-stress state.

The remainder of the chapter is organized as follows:

- ✓ In the second Section, the main lines of the periodic homogenization technique used to derive the overall behavior of the polycrystalline aggregate are presented. Then, the numerical implementation of this technique under the macroscopic plane-stress state is briefly presented.
- ✓ The single crystal constitutive framework is briefly outlined in the third section. This section also includes the associated algorithmic aspects developed to integrate these constitutive equations into ABAQUS/Standard FE code in the form of a user-defined material (UMAT) subroutine.
- ✓ The theoretical framework as well as the numerical implementation of the bifurcation theory are detailed in the fourth section.
- ✓ The fifth section is devoted to the presentation and discussion of the simulation results and ductility predictions obtained by the proposed numerical approach.

4.2. Plane-stress periodic homogenization problem

Considering the spatial quasi-periodicity of the crystallographic structure in polycrystalline media and hence of the various mechanical fields, the periodic homogenization scheme (as applied in Chapter 2 and Chapter 3) turns out to be a good candidate to build this strategy. The first step in the development of this multiscale procedure concerns the selection of a unit cell, which must be sufficiently representative of bulk polycrystalline sheet as depicted in [Fig. 4.1a](#). For the analysis of the ductility limit of thin sheets, a through-thickness 2D unit cell can be considered, implying homogenization with respect to the reference plane of the sheet and direct computation in the thickness direction ([Fig. 4.1b](#)). In this investigation, we have used the Voronoi tessellation technique to generate a thin unit cell occupying an initial volume $\mathcal{V}_0 = [0, \kappa_0] \times [0, \kappa_0] \times [0, 0.1\kappa_0]$ and composed of a large number of grains of various sizes, as schematically depicted in [Fig. 4.1b](#). Within this 2D unit cell, the grain boundaries are projected in the third direction in order to generate a 3D geometry (with one grain through the unit cell thickness). The use of the Voronoi tessellation technique allows realistically representing the grain morphology. The crystal orientation at a point within the microstructure is specified by a local crystal coordinate system whose initial orientation is randomly generated and varies from grain to grain. It is assumed that grains are perfectly bounded together with displacement and traction continuity across the grain-boundary interfaces between adjacent grains. The unit cell is discretized by finite elements and generally each grain is decomposed into several finite elements. Each integration point of each element represents a

single crystal. The constitutive equations at the single crystal scale and the numerical schemes developed to integrate them will be presented in Section 4.3.

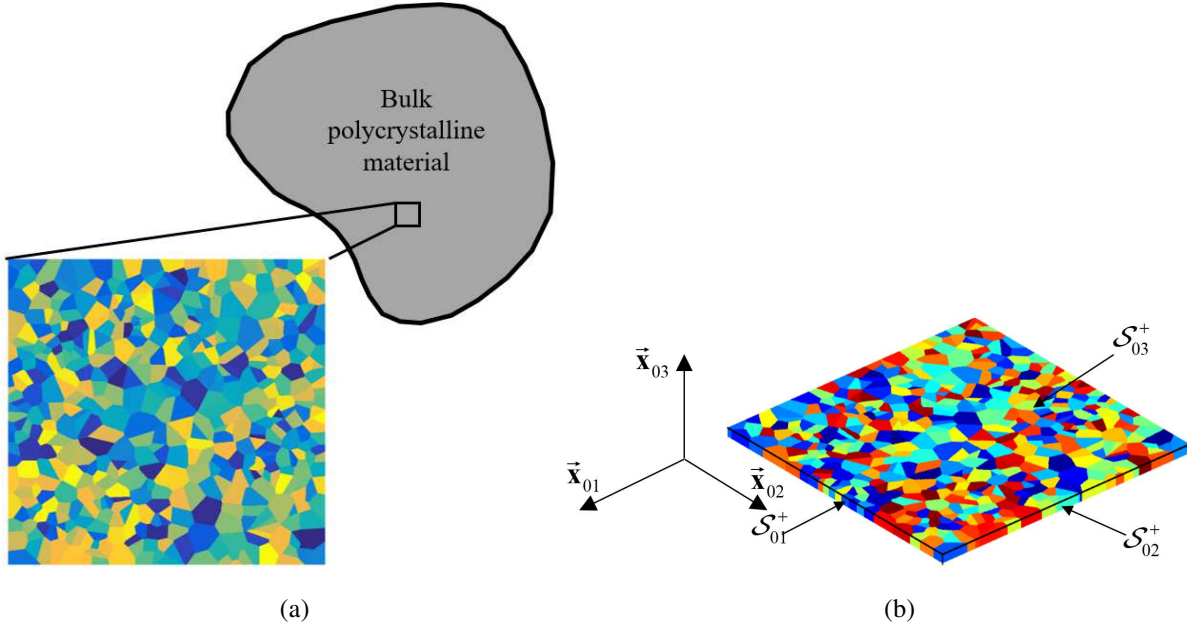


Fig. 4.1. Polycrystalline aggregate: (a) selection of a unit cell from the bulk polycrystalline material; (b) finite element mesh of the unit cell generated by the Voronoi tessellation technique.

The studied unit cell is assumed to undergo finite strains and a total Lagrangian approach is used to formulate the periodic homogenization relationships. Accordingly, the same choice of the strain and stress measures as in the previous chapters, are made: deformation gradient and the first Piola-Kirchhoff stress tensor. Under plane-stress state in the third direction (Fig. 4.1). The macroscopic fields characterizing this in-plane biaxial stretching are defined as:

$$\mathbf{F} = \begin{pmatrix} F_{11} & 0 & ? \\ 0 & F_{22} & ? \\ ? & ? & ? \end{pmatrix} ; \quad \mathbf{P} = \begin{pmatrix} ? & ? & 0 \\ ? & ? & 0 \\ 0 & 0 & 0 \end{pmatrix}, \quad (4.1)$$

where components denoted by ‘?’ are unknowns and need to be determined by finite element computations. Then, the macroscopic loading is applied on the outer orthogonal directions to faces \mathcal{S}_{01}^- , \mathcal{S}_{01}^+ , \mathcal{S}_{02}^- , and \mathcal{S}_{02}^+ . On the other hand, faces \mathcal{S}_{03}^- and \mathcal{S}_{03}^+ are free from any loading. These conditions are the same as those presented in Chapter 2.

The main equations of the periodic homogenization multiscale scheme under plane-stress state are presented in Section 2.2.3, they are not recalled here for brevity. The constitutive relations modeling the microscopic mechanical behavior of the single crystals which will be presented and adequately solved in Section 4.3.

4.3. Single crystal modeling

A single crystal is assigned to each integration point of the unit cell mesh (Fig. 4.1b). To completely solve the periodic homogenization problem presented in Section 4.2, the single crystal constitutive equations need to completely formulated and solved. This is the main task of this section.

4.3.1. Constitutive equations

As a starting point for the presentation of the single crystal constitutive equations, the microscopic velocity gradient \mathbf{g} is expressed in terms of the microscopic deformation gradient \mathbf{f} as:

$$\mathbf{g} = \dot{\mathbf{f}} \cdot \mathbf{f}^{-1}, \quad (4.2)$$

where \mathbf{f} is determined at each integration point by the finite element computation.

As stated earlier, the single crystal behavior is assumed to be elasto-plastic. Hence, \mathbf{f} can be multiplicatively decomposed into elastic and plastic parts which are respectively denoted \mathbf{f}^e and \mathbf{f}^p :

$$\mathbf{f} = \mathbf{f}^e \cdot \mathbf{f}^p. \quad (4.3)$$

The elastic part \mathbf{f}^e may in turn be partitioned into a symmetric stretching tensor \mathbf{v}^e and a rotation $\bar{\mathbf{r}}$, which defines the orientation of the coordinate system associated with the intermediate or relaxed configuration with respect to the current (deformed) configuration:

$$\mathbf{f}^e = \mathbf{v}^e \cdot \bar{\mathbf{r}}. \quad (4.4)$$

The combination of Eqs. (4.2), (4.3), and (4.4) yields:

$$\begin{aligned} \mathbf{g} &= \dot{\mathbf{f}} \cdot \mathbf{f}^{-1} = \dot{\mathbf{f}}^e \cdot \mathbf{f}^{e-1} + \mathbf{f}^e \cdot \dot{\mathbf{f}}^p \cdot \mathbf{f}^{p-1} \cdot \mathbf{f}^{e-1} \\ &= \dot{\mathbf{v}}^e \cdot \mathbf{v}^{e-1} + \mathbf{v}^e \cdot \dot{\bar{\mathbf{r}}} \cdot \bar{\mathbf{r}}^T \cdot \mathbf{v}^{e-1} + \mathbf{v}^e \cdot \bar{\mathbf{r}} \cdot \dot{\mathbf{f}}^p \cdot \mathbf{f}^{p-1} \cdot \bar{\mathbf{r}}^T \cdot \mathbf{v}^{e-1}. \end{aligned} \quad (4.5)$$

As for the majority of metallic materials, elastic deformation remains very small compared to the unity (i.e. $\mathbf{v}^e \approx \mathbf{I}_2$). Accordingly, Eq. (4.5) can be simplified as:

$$\mathbf{g} = \dot{\mathbf{v}}^e + \dot{\bar{\mathbf{r}}} \cdot \bar{\mathbf{r}}^T + \bar{\mathbf{r}} \cdot \dot{\mathbf{f}}^p \cdot \mathbf{f}^{p-1} \cdot \bar{\mathbf{r}}^T. \quad (4.6)$$

The velocity gradient \mathbf{g} can be additively decomposed into its symmetric part \mathbf{d} and skew-symmetric part \mathbf{w} :

$$\mathbf{g} = \mathbf{d} + \mathbf{w} \quad \text{where} \quad \mathbf{d} = \frac{1}{2}(\mathbf{g} + \mathbf{g}^T) \quad \text{and} \quad \mathbf{w} = \frac{1}{2}(\mathbf{g} - \mathbf{g}^T), \quad (4.7)$$

which are themselves decomposed into elastic and plastic parts \mathbf{d}^e , \mathbf{d}^p , \mathbf{w}^e , and \mathbf{w}^p :

$$\begin{aligned}\mathbf{d} &= \mathbf{d}^e + \mathbf{d}^p \quad ; \quad \mathbf{w} = \mathbf{w}^e + \mathbf{w}^p; \\ \mathbf{d}^e &= \dot{\mathbf{v}}^e \quad ; \quad \mathbf{d}^p = \frac{1}{2} \bar{\mathbf{r}} \cdot \left(\dot{\mathbf{f}}^p \cdot \mathbf{f}^{p-1} + (\dot{\mathbf{f}}^p \cdot \mathbf{f}^{p-1})^T \right) \cdot \bar{\mathbf{r}}^T; \\ \mathbf{w}^e &= \dot{\bar{\mathbf{r}}} \cdot \bar{\mathbf{r}}^T \quad ; \quad \mathbf{w}^p = \frac{1}{2} \bar{\mathbf{r}} \cdot \left(\dot{\mathbf{f}}^p \cdot \mathbf{f}^{p-1} - (\dot{\mathbf{f}}^p \cdot \mathbf{f}^{p-1})^T \right) \cdot \bar{\mathbf{r}}^T.\end{aligned}\quad (4.8)$$

By assuming that plastic deformation is exclusively induced by the slip on the crystallographic slip systems, the plastic part $\bar{\mathbf{r}} \cdot \dot{\mathbf{f}}^p \cdot \mathbf{f}^{p-1} \cdot \bar{\mathbf{r}}^T$ of the velocity gradient (see Eq. (4.6)) can be expressed as:

$$\bar{\mathbf{r}} \cdot \dot{\mathbf{f}}^p \cdot \mathbf{f}^{p-1} \cdot \bar{\mathbf{r}}^T = \dot{\gamma}^\alpha \mathbf{M}^\alpha \quad ; \quad \alpha = 1, \dots, N_s, \quad (4.9)$$

where:

- N_s stands for the total number of crystallographic slip systems (equal to 12 for FCC single crystals considered in the present investigation).
- $\dot{\gamma}^\alpha$ denotes the algebraic value of the slip rate corresponding to the slip system α .
- \mathbf{M}^α designates the Schmid tensor of slip system α equal to the tensor product of the slip direction vector $\vec{\mathbf{m}}^\alpha$ and the vector normal to the slip plane $\vec{\mathbf{n}}^\alpha$:

$$\mathbf{M}^\alpha = \vec{\mathbf{m}}^\alpha \otimes \vec{\mathbf{n}}^\alpha. \quad (4.10)$$

For evident practical reasons, and in order to manipulate only positive values of slips rates in the following theoretical and numerical developments, it is more convenient to break each slip system into two opposite pseudo-slip systems $(\vec{\mathbf{m}}^\alpha, \vec{\mathbf{n}}^\alpha)$ and $(-\vec{\mathbf{m}}^\alpha, \vec{\mathbf{n}}^\alpha)$, numbered by α and $\alpha + N_s$, respectively. With this decomposition, Eq. (4.9) is transformed into the following form:

$$\bar{\mathbf{r}} \cdot \dot{\mathbf{f}}^p \cdot \mathbf{f}^{p-1} \cdot \bar{\mathbf{r}}^T = \dot{\gamma}^\alpha \mathbf{M}^\alpha \quad \text{with} \quad \dot{\gamma}^\alpha \geq 0 \quad ; \quad \alpha = 1, \dots, 2N_s. \quad (4.11)$$

Using Eq. (4.11), the plastic strain rate \mathbf{d}^p and plastic spin \mathbf{w}^p , introduced in Eq. (4.8), can be expressed as functions of the symmetric and skew-symmetric parts \mathbf{R}^α and \mathbf{S}^α of the Schmid tensor \mathbf{M}^α :

$$\mathbf{d}^p = \dot{\gamma}^\alpha \mathbf{R}^\alpha \quad ; \quad \mathbf{w}^p = \dot{\gamma}^\alpha \mathbf{S}^\alpha \quad ; \quad \alpha = 1, \dots, 2N_s. \quad (4.12)$$

The rotation $\bar{\mathbf{r}}$ is chosen in such a way that the transport of Schmid tensor \mathbf{M}^α in the intermediate configuration remains constant and equal to $\vec{\mathbf{m}}_0^\alpha \otimes \vec{\mathbf{n}}_0^\alpha$ during the loading (Fig. 4.2):

$$\mathbf{M}_0^\alpha = \bar{\mathbf{r}}^T \cdot \mathbf{M}^\alpha \cdot \bar{\mathbf{r}}. \quad (4.13)$$

The detailed numbering of vectors $\vec{\mathbf{m}}_0^\alpha$ and $\vec{\mathbf{n}}_0^\alpha$ for FCC single crystals is provided in Appendix C.

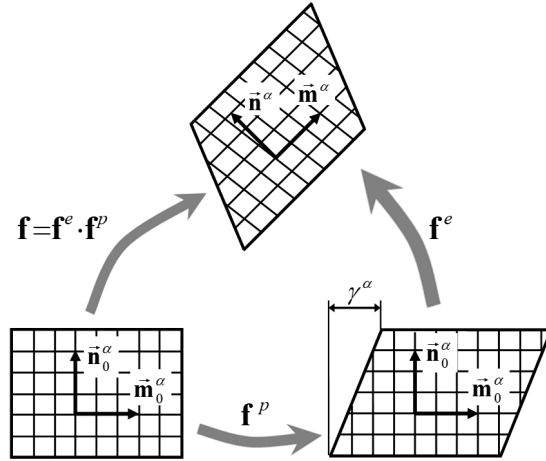


Fig. 4.2. Schematic representation of the multiplicative decomposition of the deformation gradient: plastic slip and rigid rotation along with elastic distortion of the crystallographic lattice.

To fulfill the objectivity principle, the constitutive equations (4.6), (4.8) and (4.9) may be expressed in the lattice frame defined by the rotation $\bar{\mathbf{r}}$. For the sake of clarity, tensors and vectors expressed in this frame are denoted by an overline notation. In this rotated frame, the velocity gradient is expressed as:

$$\bar{\mathbf{g}} = \bar{\mathbf{r}}^T \cdot \mathbf{g} \cdot \bar{\mathbf{r}} = \bar{\mathbf{d}} + \bar{\mathbf{w}}, \quad (4.14)$$

where $\bar{\mathbf{d}}$ and $\bar{\mathbf{w}}$ are obtained from Eqs. (4.8) and (4.9) as:

$$\bar{\mathbf{d}} = \bar{\mathbf{d}}^e + \bar{\mathbf{d}}^p \quad ; \quad \bar{\mathbf{w}} = \bar{\mathbf{r}}^T \cdot \dot{\bar{\mathbf{r}}} + \bar{\mathbf{w}}^p \quad ; \quad \bar{\mathbf{d}}^p = \dot{\gamma}^\alpha \mathbf{R}_0^\alpha \quad ; \quad \bar{\mathbf{w}}^p = \dot{\gamma}^\alpha \mathbf{S}_0^\alpha \quad ; \quad \alpha = 1, \dots, 2N_s. \quad (4.15)$$

Elasticity behavior is assumed to be isotropic and linear, and modeled by the Hooke's law:

$$\dot{\bar{\sigma}} = \bar{\mathbf{c}}^e : \bar{\mathbf{d}}^e, \quad (4.16)$$

where $\bar{\mathbf{c}}^e$ is the fourth-order elastic stiffness tensor expressed in the rotated frame (as elasticity is isotropic, $\bar{\mathbf{c}}^e$ is simply equal to \mathbf{c}^e) and $\dot{\bar{\sigma}}$ is the time derivative of the rotated Cauchy stress tensor $\bar{\sigma}$ ($= \mathbf{r}^T \cdot \sigma \cdot \mathbf{r}$). The use of Eq. (4.16), instead of the classical form of elasticity relation ($\dot{\sigma} = \mathbf{c}^e : \mathbf{d}^e$) enables to ensure the objectivity of the constitutive model.

For rate-independent behavior, the plastic flow is defined by the Schmid law which assumes that the slip arises on a slip systems α (i.e. $\dot{\gamma}^\alpha \geq 0$), only when the absolute value of the resolved shear stress τ^α reaches a critical value τ_c^α :

$$\forall \alpha = 1, \dots, 2N_s : \begin{cases} \tau^\alpha < \tau_c^\alpha \Rightarrow \dot{\gamma}^\alpha = 0; \\ \tau^\alpha = \tau_c^\alpha \Rightarrow \dot{\gamma}^\alpha \geq 0, \end{cases} \quad (4.17)$$

where the resolved shear stress τ^α is the driving force for plastic force on slip system α and is computed in terms of the Cauchy stress tensor σ and the Schmid tensor \mathbf{R}^α according to:

$$\forall \alpha = 1, \dots, 2N_s : \tau^\alpha = \sigma : \mathbf{R}^\alpha = \bar{\sigma} : \mathbf{R}_0^\alpha, \quad (4.18)$$

Equation (4.17) can be equivalently expressed as non-linear complementarity problem (NCP):

$$\forall \alpha = 1, \dots, 2N_s : \chi^\alpha = \tau_c^\alpha - \tau^\alpha \geq 0 ; \dot{\gamma}^\alpha \geq 0 ; \chi^\alpha \dot{\gamma}^\alpha = 0. \quad (4.19)$$

The critical shear stress τ_c^α has as initial value τ_0 , and evolves with the slip on all the crystallographic systems according to the following generic hardening law:

$$\forall \alpha = 1, \dots, N_s : \dot{\tau}_c^\alpha = \dot{\tau}_c^{\alpha+N_s} = H^{\alpha\beta} (\dot{\gamma}^\beta + \dot{\gamma}^{\beta+N_s}) ; \beta = 1, \dots, N_s, \quad (4.20)$$

where $H^{\alpha\beta}$ is the $\alpha\beta$ component of the hardening matrix \mathbf{H} , which is dependent on the accumulated slips of the different slip systems γ^α and some hardening parameters. The explicit expression of the hardening matrix used in the present investigation will be given in Section 4.5.

4.3.2. Incremental integration

The constitutive equations at the single crystal scale are implemented within ABAQUS/Standard FE code through a user-defined material subroutine UMAT. In this implementation, the constitutive equations are integrated over a typical time increment $I^\Delta = [t_0, t_0 + \Delta t]$ using an ultimate integration scheme. The family of ultimate algorithms has been initially introduced by [Borja and Wren \(1993\)](#) for the case of linear single crystal constitutive equations (linear hardening and small strain). More recently, this algorithm has been extended by [Ben Bettaieb et al. \(2012b\)](#) to take into account more general non-linear behavior (non-linear hardening, finite strain and finite rotation). The high performance and the robustness of the ultimate algorithm compared the well-known return-mapping one ([Anand and Kothari, 1996](#)) for the integration of rate-independent single crystal constitutive equations has been emphasized by [Akpama et al. \(2016\)](#) through an extensive comparative study. Moreover, it has been proven in [Akpama et al. \(2016\)](#) that the explicit version of the ultimate algorithm is more efficient than the implicit one, since it yields quite accurate predictions with a reduced computation cost. Consequently, the explicit ultimate algorithm is adopted in the present study to integrate the single crystal constitutive equations. The concept of ultimate algorithm relies on the idea of partition of the time increment I^Δ into several sub-increments $I^{\delta_n} = [t_n, t_{n+1}]$ (where $t_{n=0} = t_0$). The size $\delta t_n = t_{n+1} - t_n$ of sub-increment I^{δ_n} is a priori unknown. It should be determined in such a way that the Schmid criterion (4.17) remains fulfilled over I^{δ_n} . By adopting this partition, the constitutive equations at the single crystal scale must be integrated over each time sub-increment I^{δ_n} and the different mechanical variables updated from one sub-increment to another.

The principal input of the UMAT is the velocity gradient \mathbf{g} which is assumed to be constant over I^Δ (hence, over I^{δ_n}) and is computed from $\mathbf{f}(t_0)$ and $\mathbf{f}(t_0 + \Delta t)$ by the following midpoint approximation:

$$\mathbf{g} = \left(\frac{\mathbf{f}(t_0 + \Delta t) - \mathbf{f}(t_0)}{\Delta t} \right) \cdot \left(\frac{\mathbf{f}(t_0 + \Delta t) + \mathbf{f}(t_0)}{\Delta t} \right)^{-1}. \quad (4.21)$$

To be consistent with the concept of implementation of constitutive equations in ABAQUS/Standard, let us introduce the co-rotational frame described by the rotation $\check{\mathbf{r}}$ ($\neq \bar{\mathbf{r}}$) with respect to the fixed frame. The evolution of this rotation is defined by the following evolution law:

$$\dot{\check{\mathbf{r}}} \cdot \check{\mathbf{r}}^T = \mathbf{w}, \quad (4.22)$$

where \mathbf{w} is the skew-symmetric part of the velocity gradient \mathbf{g} , as determined by Eq. (4.21). Vector and tensor quantities expressed in the co-rotational frame defined by rotation $\check{\mathbf{r}}$ will be highlighted by an arc line (e.g. $\check{\bullet}$).

The other inputs of the UMAT are:

- The elasticity and hardening parameters.
- The rotation of the co-rotational frame $\check{\mathbf{r}}$ and rotation of the crystallographic lattice related to the intermediate configuration $\bar{\mathbf{r}}$ at t_n .
- The Cauchy stress tensor expressed in the co-rotational frame $\check{\sigma}$ at t_n .
- The slips γ^α and the critical shear stresses τ_c^α (for $\alpha=1,\dots,2N_s$) at t_n .

As outputs, the following unknowns need to be determined:

- The rotations $\check{\mathbf{r}}$ and $\bar{\mathbf{r}}$ at t_{n+1} .
- The Cauchy stress tensor expressed in the co-rotational frame $\check{\sigma}$ at t_{n+1} .
- The slips γ^α and the critical shear stresses τ_c^α (for $\alpha=1,\dots,2N_s$) at t_{n+1} .
- The consistent tangent modulus expressed in the co-rotational frame $\check{\mathbf{c}}^{ep}$ (i.e., the **DDSDDE** matrix, using the ABAQUS terminology) defined by the following expression:

$$\check{\mathbf{c}}^{ep} = \frac{\partial \Delta \check{\sigma}}{\partial \Delta \check{\epsilon}}, \quad (4.23)$$

where $\delta\check{\sigma}$ is the variation of $\check{\sigma}$ over the time sub-increment I^{δ_n} , and $\delta\check{\epsilon}$ is the integral of $\check{\mathbf{d}}$ over the same sub-increment.

To clearly highlight the dependence with respect to time of the different quantities in the following algorithmic developments, a variable \bullet evaluated at t_n (resp. t_{n+1}) is denoted by $\bullet(t_n)$ (resp. $\bullet(t_{n+1})$).

The rotation of the co-rotational frame $\check{\mathbf{r}}(t_{n+1})$ can be determined from its counterpart at the beginning of the sub-increment $\check{\mathbf{r}}(t_n)$ and \mathbf{w} by integrating the differential equation (4.22) over I^{δ_n} :

$$\check{\mathbf{r}}(t_{n+1}) = e^{\delta t_n \mathbf{w}} \cdot \check{\mathbf{r}}(t_n). \quad (4.24)$$

A quick analysis of the single crystal constitutive equations reveals that the computation of the slip rates $\dot{\gamma}^\alpha(t_n)$ for the different slip systems is sufficient to determine the evolution of the other single crystal mechanical variables over the current time sub-increment I^{δ_n} and especially their values at t_{n+1} (namely, $\bar{\mathbf{r}}(t_{n+1})$, $\check{\sigma}(t_{n+1})$, $\gamma^\alpha(t_{n+1})$, $\tau_c^\alpha(t_{n+1})$, and $\check{\mathbf{c}}^{ep}$).

To compute $\dot{\gamma}^\alpha(t_n)$ for all slip systems, let us introduce the set of potentially active slip systems \mathcal{P} at t_n defined as:

$$\mathcal{P} = \left\{ \alpha = 1, \dots, 2N_s : \tau^\alpha(t_n) - \tau_c^\alpha(t_n) = \bar{\sigma}(t_n) : \mathbf{R}_0^\alpha(t_n) - \tau_c^\alpha(t_n) = 0 \right\}. \quad (4.25)$$

Considering Eq. (4.25), the Schmid law defined by Eq. (4.17) may be reduced to the set of potentially active slip systems (as the slip rates of the non-potentially active slip systems are obviously equal to zero):

$$\forall \alpha \in \mathcal{P} : \dot{\chi}^\alpha(t_n) = \dot{\tau}_c^\alpha(t_n) - \dot{\tau}^\alpha(t_n) \geq 0 ; \dot{\gamma}^\alpha(t_n) \geq 0 ; \dot{\chi}^\alpha(t_n) \dot{\gamma}^\alpha(t_n) = 0. \quad (4.26)$$

Making use of Eqs. (4.15), (4.16), (4.18), and (4.20), $\dot{\chi}^\alpha(t_n)$ can be expressed as:

$$\begin{aligned} \forall \alpha \in \mathcal{P} : \dot{\chi}^\alpha(t_n) &= \dot{\tau}_c^\alpha(t_n) - \dot{\tau}^\alpha(t_n) = H^{\alpha\beta} \dot{\gamma}^\beta(t_n) - \dot{\bar{\sigma}}(t_n) : \mathbf{R}_0^\alpha \\ &= H^{\alpha\beta}(t_n) \dot{\gamma}^\beta(t_n) - \bar{\mathbf{d}}^e(t_n) : \mathbf{c}^e : \mathbf{R}_0^\alpha \\ &= H^{\alpha\beta}(t_n) \dot{\gamma}^\beta(t_n) - (\bar{\mathbf{d}}(t_n) - \dot{\gamma}^\beta(t_n) \mathbf{R}_0^\beta) : \mathbf{c}^e : \mathbf{R}_0^\alpha \\ &= A^{\alpha\beta}(t_n) \dot{\gamma}^\beta(t_n) - B^\alpha(t_n) ; \beta \in \mathcal{P}. \end{aligned} \quad (4.27)$$

where matrix $\mathbf{A}(t_n)$ and vector $\mathbf{B}(t_n)$ are given by the following index forms:

$$\forall \alpha, \beta \in \mathcal{P} : A^{\alpha\beta}(t_n) = H^{\alpha\beta}(t_n) + \mathbf{R}_0^\alpha : \mathbf{c}^e : \mathbf{R}_0^\beta ; B^\alpha(t_n) = \mathbf{R}_0^\alpha : \mathbf{c}^e : \bar{\mathbf{d}}(t_n). \quad (4.28)$$

Using Eqs. (4.27) and (4.28), the Schmid given by Eq. (4.26) can be expressed in a matrix form more suitable to numerical implementation:

$$\forall \alpha \in \mathcal{P} : \begin{cases} \dot{\chi}^\alpha(t_n) = A^{\alpha\beta}(t_n) \dot{\gamma}^\beta(t_n) - B^\alpha(t_n) \geq 0 ; \\ \dot{\gamma}^\alpha(t_n) \geq 0 ; \\ (A^{\alpha\beta}(t_n) \dot{\gamma}^\beta(t_n) - B^\alpha(t_n)) \dot{\gamma}^\alpha(t_n) = 0. \end{cases} ; \beta \in \mathcal{P}. \quad (4.29)$$

As the components of $\mathbf{A}(t_n)$ and $\mathbf{B}(t_n)$ are determined at the beginning of the sub-increment, the NLCP problem given by Eq. (4.19) is transformed into a linear complementarity problem (LCP) as formulated by Eq. (4.29). This LCP can be easily solved by a combinatorial research procedure, identical to the one presented in Akpama et al. (2016), to compute the slip rates of the potentially active slip systems and thus to distinguish the set of active slip systems \mathcal{A} from the set of potentially active, but inactive slip systems \mathcal{NA} :

$$\begin{aligned} \mathcal{A} \cup \mathcal{NA} &= \mathcal{P} \quad \text{and} \quad \mathcal{A} \cap \mathcal{NA} = \emptyset \\ \forall \alpha \in \mathcal{A} : \dot{\gamma}^\alpha(t_n) &> 0 ; \quad \forall \alpha \in \mathcal{NA} : \dot{\gamma}^\alpha(t_n) = 0. \end{aligned} \quad (4.30)$$

More details about this research procedure can be found in Akpama et al. (2016).

Once the slip rates of the potentially active slip systems are computed, the size of the current sub-increment I^{δ_n} can be determined by satisfying the following conditions: δt_n should be inferior or equal to Δt and the Schmid criterion should be fulfilled for all slip systems over I^{δ_n} . In view of Eq. (4.29), it

is evident that the Schmid criterion is fulfilled for the potentially active slip systems. For the other systems ($\notin \mathcal{P}$), the following condition must be verified:

$$\forall \alpha \notin \mathcal{P} : \tau^\alpha(t_{n+1}) \leq \tau_c^\alpha(t_{n+1}). \quad (4.31)$$

By using the definitions of τ^α and τ_c^α , the following relations can be readily obtained:

$$\forall \alpha \notin \mathcal{P} : \begin{cases} \tau^\alpha(t_{n+1}) = \tau^\alpha(t_n) + \delta t_n \mathbf{R}_0^\alpha : \dot{\bar{\sigma}}(t_n) \\ \quad = \tau^\alpha(t_n) + \delta t_n \mathbf{R}_0^\alpha : \mathbf{c}^e : (\bar{\mathbf{d}}(t_n) - \dot{\gamma}^\beta(t_n) \mathbf{R}_0^\beta), \\ \tau_c^\alpha(t_{n+1}) = \tau_c^\alpha(t_n) + \delta t_n H^{\alpha\beta}(t_n) \dot{\gamma}^\beta(t_n) \quad ; \quad \beta \in \mathcal{P}. \end{cases} \quad (4.32)$$

The combination of Eqs. (4.31) and (4.32) provides the following minimization condition on δt_n :

$$\delta t_n = \min_{\alpha \notin \mathcal{P}} \left\{ \Delta t, \frac{\tau_c^\alpha(t_n) - \tau^\alpha(t_n)}{\mathbf{R}_0^\alpha : \mathbf{c}^e : (\bar{\mathbf{d}}(t_n) - \dot{\gamma}^\beta(t_n) \mathbf{R}_0^\beta) - H^{\alpha\beta}(t_n) \dot{\gamma}^\beta(t_n)} \right\} ; \quad \beta \in \mathcal{P}. \quad (4.33)$$

Once the length δt_n of the current sub-increment I^{δ_n} is determined, the other mechanical variables could be updated at t_{n+1} as:

$$\begin{aligned} \delta \bar{\mathbf{r}}(t_n) &= e^{(\delta t_n (\bar{\mathbf{w}}(t_n) - \dot{\gamma}^\alpha(t_n) \mathbf{s}_0^\alpha))} ; \quad \alpha \in \mathcal{A}; \\ \bar{\mathbf{r}}(t_{n+1}) &= \bar{\mathbf{r}}(t_n) \cdot \delta \bar{\mathbf{r}}(t_n); \\ \dot{\bar{\sigma}}(t_n) &= \mathbf{c}^e : (\bar{\mathbf{d}}(t_n) - \dot{\gamma}^\alpha(t_n) \mathbf{R}_0^\alpha) ; \quad \alpha \in \mathcal{A}; \\ \bar{\sigma}(t_{n+1}) &= \bar{\sigma}(t_n) + \delta t_n \dot{\bar{\sigma}}(t_n); \\ \sigma(t_{n+1}) &= \bar{\mathbf{r}}(t_{n+1}) \cdot \bar{\sigma}(t_{n+1}) \cdot \bar{\mathbf{r}}^T(t_{n+1}); \\ \forall \alpha = 1, \dots, 2N_s : &\begin{cases} \gamma^\alpha(t_{n+1}) = \gamma^\alpha(t_n) + \delta t_n \dot{\gamma}^\alpha(t_n); \\ \tau_c^\alpha(t_{n+1}) = \tau_c^\alpha(t_n) + \delta t_n H^{\alpha\beta}(t_n) \dot{\gamma}^\beta(t_n) \quad ; \quad \beta \in \mathcal{A}. \end{cases} \end{aligned} \quad (4.34)$$

The Cauchy stress tensor $\sigma(t_{n+1})$ is computed by Eq. (4.34)₅. It should be rotated in the co-rotational frame defined by rotation $\bar{\mathbf{r}}(t_{n+1})$ which is updated by Eq. (4.24) to obtain $\check{\sigma}(t_{n+1})$:

$$\check{\sigma}(t_{n+1}) = \check{\mathbf{r}}^T(t_{n+1}) \cdot \sigma(t_{n+1}) \cdot \check{\mathbf{r}}(t_{n+1}). \quad (4.35)$$

Now the consistent tangent modulus $\check{\mathbf{c}}^{ep}$ should be determined. As the integration scheme is explicit, $\check{\mathbf{c}}^{ep}$ can be obtained from the following relation between $\delta \check{\sigma}$ and $\delta \check{\epsilon}$:

$$\delta \check{\sigma} = \check{\mathbf{c}}^{ep} : \delta \check{\epsilon}. \quad (4.36)$$

The stress sub-increment $\delta \check{\sigma}$ can be expressed as:

$$\delta \check{\sigma} = \check{\sigma}(t_{n+1}) - \check{\sigma}(t_n) = \check{\mathbf{r}}^T(t_{n+1}) \cdot \sigma(t_{n+1}) \cdot \check{\mathbf{r}}(t_{n+1}) - \check{\sigma}(t_n) = \hat{\mathbf{r}}(t_{n+1}) \cdot \bar{\sigma}(t_{n+1}) \cdot \hat{\mathbf{r}}^T(t_{n+1}) - \check{\sigma}(t_n), \quad (4.37)$$

where $\hat{\mathbf{r}}$ is the rotation of the intermediate configuration with respect to the co-rotational frame. This rotation is defined by the following evolution rule:

$$\hat{\mathbf{r}}(t_{n+1}) = e^{-\delta t_n \check{\mathbf{w}}^p(t_n)} \cdot \hat{\mathbf{r}}(t_n) = e^{-\delta t_n \dot{\gamma}^\alpha(t_n) \check{\mathbf{s}}^\alpha(t_n)} \cdot \hat{\mathbf{r}}(t_n) ; \quad \alpha \in \mathcal{A}. \quad (4.38)$$

Using Eq. (4.34)₄, $\delta \check{\sigma}$ can be rewritten as:

$$\begin{aligned}\delta\tilde{\sigma} &= \tilde{\sigma}(t_{n+1}) - \tilde{\sigma}(t_n) = \hat{\mathbf{r}}(t_{n+1}) \cdot (\bar{\sigma}(t_n) + \delta t_n \dot{\bar{\sigma}}(t_n)) \cdot \hat{\mathbf{r}}^T(t_{n+1}) - \tilde{\sigma}(t_n) \\ &= [\hat{\mathbf{r}}(t_{n+1}) \cdot \hat{\mathbf{r}}^T(t_n)] \cdot \tilde{\sigma}(t_n) \cdot [\hat{\mathbf{r}}(t_{n+1}) \cdot \hat{\mathbf{r}}(t_n)]^T + \delta t_n \hat{\mathbf{r}}(t_{n+1}) \cdot \dot{\bar{\sigma}}(t_n) \cdot \hat{\mathbf{r}}^T(t_{n+1}) - \tilde{\sigma}(t_n).\end{aligned}\quad (4.39)$$

The expressions of $[\hat{\mathbf{r}}(t_{n+1}) \cdot \hat{\mathbf{r}}^T(t_n)]$ and $[\hat{\mathbf{r}}(t_{n+1}) \cdot \hat{\mathbf{r}}(t_n)]^T$ can be obtained from Eq. (4.38):

$$\hat{\mathbf{r}}(t_{n+1}) \cdot \hat{\mathbf{r}}^T(t_n) = e^{-\delta t_n \dot{\gamma}^\alpha(t_n)} \check{\mathbf{S}}^\alpha(t_n) \quad ; \quad [\hat{\mathbf{r}}(t_{n+1}) \cdot \hat{\mathbf{r}}(t_n)]^T = e^{\delta t_n \dot{\gamma}^\alpha(t_n)} \check{\mathbf{S}}^\alpha(t_n) \quad ; \quad \alpha \in \mathcal{A}. \quad (4.40)$$

The Taylor expansion of tensors $e^{-\delta t_n \dot{\gamma}^\alpha(t_n)} \check{\mathbf{S}}^\alpha(t_n)$ and $e^{\delta t_n \dot{\gamma}^\alpha(t_n)} \check{\mathbf{S}}^\alpha(t_n)$ at the first order yields:

$$e^{-\delta t_n \dot{\gamma}^\alpha(t_n)} \check{\mathbf{S}}^\alpha(t_n) \approx \mathbf{I}_2 - \delta t_n \dot{\gamma}^\alpha(t_n) \check{\mathbf{S}}^\alpha(t_n) \quad ; \quad e^{\delta t_n \dot{\gamma}^\alpha(t_n)} \check{\mathbf{S}}^\alpha(t_n) \approx \mathbf{I}_2 + \delta t_n \dot{\gamma}^\alpha(t_n) \check{\mathbf{S}}^\alpha(t_n) \quad ; \quad \alpha \in \mathcal{A}. \quad (4.41)$$

Considering the approximations (4.41), Eq. (4.39) can be recasted to the following form:

$$\begin{aligned}\delta\tilde{\sigma} &= \tilde{\sigma}(t_{n+1}) - \tilde{\sigma}(t_n) = \hat{\mathbf{r}}(t_{n+1}) \cdot (\bar{\sigma}(t_n) + \delta t_n \dot{\bar{\sigma}}(t_n)) \cdot \hat{\mathbf{r}}^T(t_{n+1}) - \tilde{\sigma}(t_n) \\ &= [\mathbf{I}_2 - \delta t_n \dot{\gamma}^\alpha(t_n) \check{\mathbf{S}}^\alpha(t_n)] \cdot \tilde{\sigma}(t_n) \cdot [\mathbf{I}_2 + \delta t_n \dot{\gamma}^\alpha(t_n) \check{\mathbf{S}}^\alpha(t_n)] \\ &\quad + \delta t_n \hat{\mathbf{r}}(t_{n+1}) \cdot \dot{\bar{\sigma}}(t_n) \cdot \hat{\mathbf{r}}^T(t_{n+1}) - \tilde{\sigma}(t_n) \quad ; \quad \alpha \in \mathcal{A}.\end{aligned}\quad (4.42)$$

Neglecting the second-order terms in δt_n , Eq. (4.42) can be reduced to the following form:

$$\begin{aligned}\delta\tilde{\sigma} &= \tilde{\sigma}(t_{n+1}) - \tilde{\sigma}(t_n) = \hat{\mathbf{r}}(t_{n+1}) \cdot (\bar{\sigma}(t_n) + \delta t_n \dot{\bar{\sigma}}(t_n)) \cdot \hat{\mathbf{r}}^T(t_{n+1}) - \tilde{\sigma}(t_n) \\ &= -\delta t_n \dot{\gamma}^\alpha(t_n) \check{\mathbf{S}}^\alpha(t_n) \cdot \tilde{\sigma}(t_n) + \delta t_n \tilde{\sigma}(t_n) \cdot \dot{\gamma}^\alpha(t_n) \check{\mathbf{S}}^\alpha(t_n) + \delta t_n \hat{\mathbf{r}}(t_{n+1}) \cdot \dot{\bar{\sigma}}(t_n) \cdot \hat{\mathbf{r}}^T(t_{n+1}) \quad ; \quad \alpha \in \mathcal{A}.\end{aligned}\quad (4.43)$$

Tensor $\hat{\mathbf{r}}(t_{n+1}) \cdot \dot{\bar{\sigma}}(t_n) \cdot \hat{\mathbf{r}}^T(t_{n+1})$ can be expressed using Eq. (4.34)₃ as:

$$\hat{\mathbf{r}}(t_{n+1}) \cdot \dot{\bar{\sigma}}(t_n) \cdot \hat{\mathbf{r}}^T(t_{n+1}) = \mathbf{c}^e : (\check{\mathbf{d}}(t_n) - \dot{\gamma}^\alpha(t_n) \check{\mathbf{R}}^\alpha(t_n)) \quad ; \quad \alpha \in \mathcal{A}. \quad (4.44)$$

The analytical expression of the slip rates can be easily obtained from the combination of Eqs. (4.28) and (4.29):

$$\forall \alpha \in \mathcal{A} : \dot{\gamma}^\alpha(t_n) = \Lambda^{\alpha\beta}(t_n) \check{\mathbf{R}}^\beta(t_n) : \mathbf{c}^e : \check{\mathbf{d}}(t_n) \quad ; \quad \beta \in \mathcal{A}, \quad (4.45)$$

where the square matrix $\Lambda(t_n)$ is the inverse of $\mathbf{A}(t_n)$ defined by index form in Eq. (4.28).

Taking into account expression (4.45) for $\dot{\gamma}^\alpha(t_n)$, Eq. (4.44) can be rewritten as:

$$\hat{\mathbf{r}}(t_{n+1}) \cdot \dot{\bar{\sigma}}(t_n) \cdot \hat{\mathbf{r}}^T(t_{n+1}) = [\mathbf{c}^e - \Lambda^{\alpha\beta}(t_n)(\mathbf{c}^e : \check{\mathbf{R}}^\alpha(t_n)) \otimes (\check{\mathbf{R}}^\beta(t_n) : \mathbf{c}^e)] : \check{\mathbf{d}} \quad ; \quad \alpha, \beta \in \mathcal{A}. \quad (4.46)$$

By inserting Eq. (4.46) into Eq. (4.43), and using expression (4.45), one obtains:

$$\begin{aligned}\delta\tilde{\sigma} &= \delta t_n [\mathbf{c}^e - \Lambda^{\alpha\beta}(t_n)(\mathbf{c}^e : \check{\mathbf{R}}^\alpha(t_n) + \check{\mathbf{S}}^\alpha(t_n) \cdot \tilde{\sigma}(t_n) - \tilde{\sigma}(t_n) \cdot \check{\mathbf{S}}^\alpha(t_n)) \otimes (\check{\mathbf{R}}^\beta(t_n) : \mathbf{c}^e)] : \check{\mathbf{d}} \\ &= [\mathbf{c}^e - \Lambda^{\alpha\beta}(t_n)(\mathbf{c}^e : \check{\mathbf{R}}^\alpha(t_n) + \check{\mathbf{S}}^\alpha(t_n) \cdot \tilde{\sigma}(t_n) - \tilde{\sigma}(t_n) \cdot \check{\mathbf{S}}^\alpha(t_n)) \otimes (\check{\mathbf{R}}^\beta(t_n) : \mathbf{c}^e)] : \delta\tilde{\epsilon} \\ &\quad ; \quad \alpha, \beta \in \mathcal{A}.\end{aligned}\quad (4.47)$$

The consistent modulus $\check{\mathbf{c}}^{ep}$ can be thereby identified by comparing Eqs. (4.36) and (4.47):

$$\check{\mathbf{c}}^{ep} = \mathbf{c}^e - \Lambda^{\alpha\beta}(t_n)(\mathbf{c}^e : \check{\mathbf{R}}^\alpha(t_n) + \check{\mathbf{S}}^\alpha(t_n) \cdot \tilde{\sigma}(t_n) - \tilde{\sigma}(t_n) \cdot \check{\mathbf{S}}^\alpha(t_n)) \otimes (\check{\mathbf{R}}^\beta(t_n) : \mathbf{c}^e) \quad ; \quad \alpha, \beta \in \mathcal{A}. \quad (4.48)$$

Once all the mechanical variables are updated at t_{n+1} and the consistent tangent modulus $\check{\mathbf{c}}^{ep}$ are computed, the size of the time increment Δt and the initial time t_n should be also updated:

$$\Delta t \leftarrow \Delta t - \delta t_n ; \quad t_n \leftarrow t_n + \delta t_n. \quad (4.49)$$

After this update procedure, the computation should be restarted with a new sub-increment I^{δ_n} , until reaching the following condition:

$$\Delta t = \delta t_n. \quad (4.50)$$

4.4. Bifurcation analysis

4.4.1. Bifurcation theory

Following the Rice approach (Rudnicki and Rice, 1975; Stören and Rice, 1975; Rice, 1976), the onset of strain localization corresponds to a bifurcation associated with admissible jumps for strain and stress rates through a discontinuity band. In this chapter, the in-plane formulation of this approach will be used, its theoretical aspects can be found in Section 2.3.3. They are not presented again for brevity. The in-plane macroscopic tangent moduli ${}^{IN}\mathbf{C}^{(PK1)}$ needed in this case will be computed in the next section (4.4.2).

4.4.2. Computation of the macroscopic tangent modulus

In this chapter, the in-plane macroscopic tangent modulus ${}^{IN}\mathbf{C}^{(PK1)}$ (its derivative ${}^{IN}\tilde{\mathbf{C}}^{(PK1)}$, is used in the bifurcation theory, see Section 2.3.3 or 3.4.4 for explanation) is computed by adopting the perturbation technique under the plane-stress condition. The details about the perturbation technique can be found in Section 1.4.1. But we outline in the following the main steps for computing ${}^{IN}\mathbf{C}^{(PK1)}$.

The in-plane macroscopic tangent modulus ${}^{IN}\mathbf{C}^{(PK1)}$ allows linking the rate of the in-plane macroscopic deformation gradient ${}^{IN}\dot{\mathbf{F}}$ to the rate of the in-plane macroscopic first Piola–Kirchhoff stress tensor ${}^{IN}\dot{\mathbf{P}}$. Therefore, ${}^{IN}\mathbf{C}^{(PK1)}$ can be determined by differentiation of ${}^{IN}\mathbf{P}$ with respect to ${}^{IN}\mathbf{F}$:

$${}^{IN}\dot{\mathbf{P}} = {}^{IN}\mathbf{C}^{(PK1)} : {}^{IN}\dot{\mathbf{F}} \Leftrightarrow {}^{IN}\Delta\mathbf{P} \approx {}^{IN}\mathbf{C}^{(PK1)} : {}^{IN}\Delta\mathbf{F}, \quad (4.51)$$

where $\Delta \bullet$ is a very small perturbation of field \bullet .

Following the perturbation technique, each column of ${}^{IN}\mathbf{C}^{(PK1)}$ is numerically constructed by perturbing the components of the macroscopic deformation gradient ${}^{IN}\mathbf{F}$ and using the associated perturbed response as:

$$\forall i, j, k, l = 1, 2: \quad {}^{\text{IN}}C_{ijkl}^{(PK1)} \approx \frac{{}^{\text{IN}}\Delta P_{ij}^{(\alpha)}}{{}^{\text{IN}}\Delta F_{kl}^{(\alpha)}} \approx \frac{{}^{\text{IN}}P_{ij}({}^{\text{IN}}\mathbf{F}_{kl}^{(\alpha)}) - {}^{\text{IN}}P_{ij}({}^{\text{IN}}\mathbf{F})}{\alpha} \quad \text{with} \quad {}^{\text{IN}}\mathbf{F}_{kl}^{(\alpha)} = {}^{\text{IN}}\mathbf{F} + {}^{\text{IN}}\Delta\mathbf{F}_{kl}^{(\alpha)}, \quad (4.52)$$

where

$$, \quad (4.53)$$

with α the perturbation magnitude (which typically ranges between 10^{-6} and 10^{-8}). The matrix form of Eq. (1.34) corresponding to the perturbation tensor ${}^{\text{IN}}\Delta\mathbf{F}_{11}^{(\alpha)} = \alpha \bar{\mathbf{x}}_{01} \otimes \bar{\mathbf{x}}_{01}$ can be written as:

$$\begin{bmatrix} {}^{\text{IN}}C_{1111}^{(PK1)} & {}^{\text{IN}}C_{1122}^{(PK1)} & {}^{\text{IN}}C_{1112}^{(PK1)} & {}^{\text{IN}}C_{1121}^{(PK1)} \\ {}^{\text{IN}}C_{2211}^{(PK1)} & {}^{\text{IN}}C_{2222}^{(PK1)} & {}^{\text{IN}}C_{2212}^{(PK1)} & {}^{\text{IN}}C_{2221}^{(PK1)} \\ {}^{\text{IN}}C_{1211}^{(PK1)} & {}^{\text{IN}}C_{1222}^{(PK1)} & {}^{\text{IN}}C_{1212}^{(PK1)} & {}^{\text{IN}}C_{1221}^{(PK1)} \\ {}^{\text{IN}}C_{2111}^{(PK1)} & {}^{\text{IN}}C_{2122}^{(PK1)} & {}^{\text{IN}}C_{2112}^{(PK1)} & {}^{\text{IN}}C_{2121}^{(PK1)} \end{bmatrix} \begin{Bmatrix} \alpha \\ 0 \\ 0 \\ 0 \end{Bmatrix} = \begin{Bmatrix} {}^{\text{IN}}\Delta P_{11}^{(\alpha)} \\ {}^{\text{IN}}\Delta P_{22}^{(\alpha)} \\ {}^{\text{IN}}\Delta P_{12}^{(\alpha)} \\ {}^{\text{IN}}\Delta P_{21}^{(\alpha)} \end{Bmatrix}. \quad (4.54)$$

Thus, the first column of modulus ${}^{\text{IN}}\mathbf{C}^{(PK1)}$ is computed as:

$${}^{\text{IN}}C_{ij11}^{(PK1)} \approx \frac{{}^{\text{IN}}P_{ij}({}^{\text{IN}}\mathbf{F}_{11}^{(\alpha)}) - {}^{\text{IN}}P_{ij}({}^{\text{IN}}\mathbf{F})}{\alpha}. \quad (4.55)$$

The three other columns are obtained in the same way as the first column.

To determine the macroscopic tangent modulus ${}^{\text{IN}}\mathbf{C}^{(PK1)}$ by the perturbation technique, five FE computational steps are performed: one general computation step to compute the unperturbed tensor ${}^{\text{IN}}\mathbf{P}({}^{\text{IN}}\mathbf{F})$ followed by four perturbation steps to compute the perturbed tensors ${}^{\text{IN}}\mathbf{P}({}^{\text{IN}}\mathbf{F}_{kl}^{(\alpha)})$ for $k, l = 1, 2$. The perturbation steps are achieved using the ABAQUS/Standard restart technique. The algorithmic steps of the perturbation technique under plane-stress condition are illustrated in Fig. 4.3.

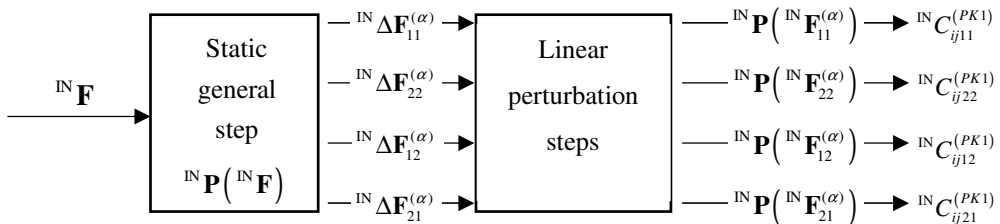


Fig. 4.3. Basic algorithmic steps of the perturbation technique under plane-stress condition.

4.5. Numerical results

To perform the various FE computations with reasonable CPU time, the studied unit cells are meshed with 5000 eight-node brick elements C3D8 (50 elements in both of the plane directions, and 2 elements in the thickness direction). The ABAQUS job corresponding to each strain path requires around 20 to 24 hours to complete the computation. Earlier contributions reveal that a unit cell composed of a hundred grains is sufficient to ensure good representativeness of the bulk polycrystalline media (Barbe et al.,

2001; Kanit et al., 2003). Consequently, four aggregates made of 50, 200, 500, and 1000 grains are generated using the Voronoi tessellation technique as shown in Fig. 4.4. These aggregates are marked hereafter as UC50, UC200, UC500, UC1000, respectively. The initial crystal orientations of the different unit cell configurations are randomly and uniformly distributed as revealed by the (100) pole figures plotted in Fig. 4.5. For the predictions presented hereafter, the unit cell made of 200 grains is exclusively used. The effect of the number of grains on the predicted FLDs is investigated in Fig. 4.13b.

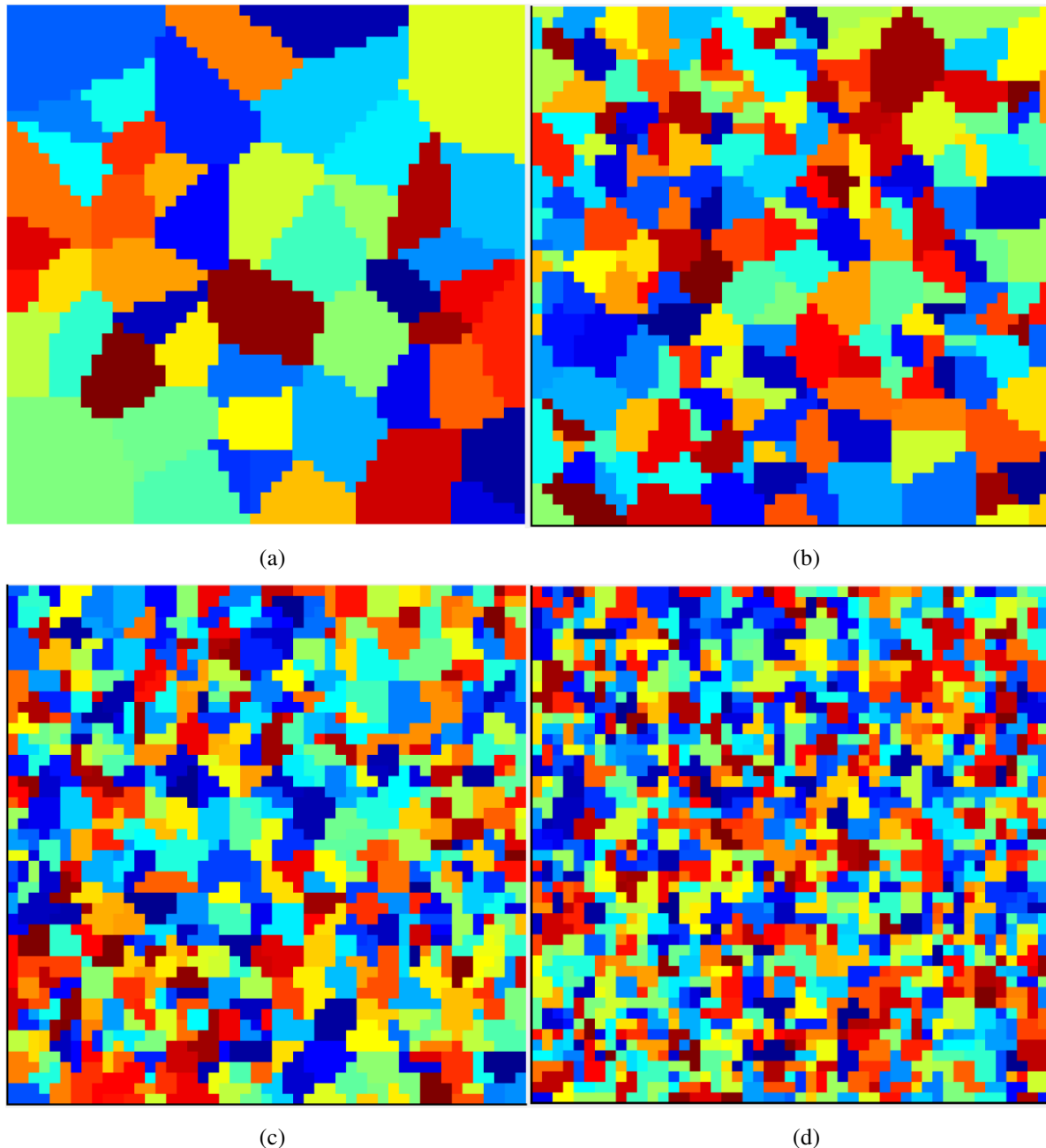


Fig. 4.4. Microstructure of the different unit cell configurations: (a) UC50; (b) UC200; (c) UC500; (d) UC1000.

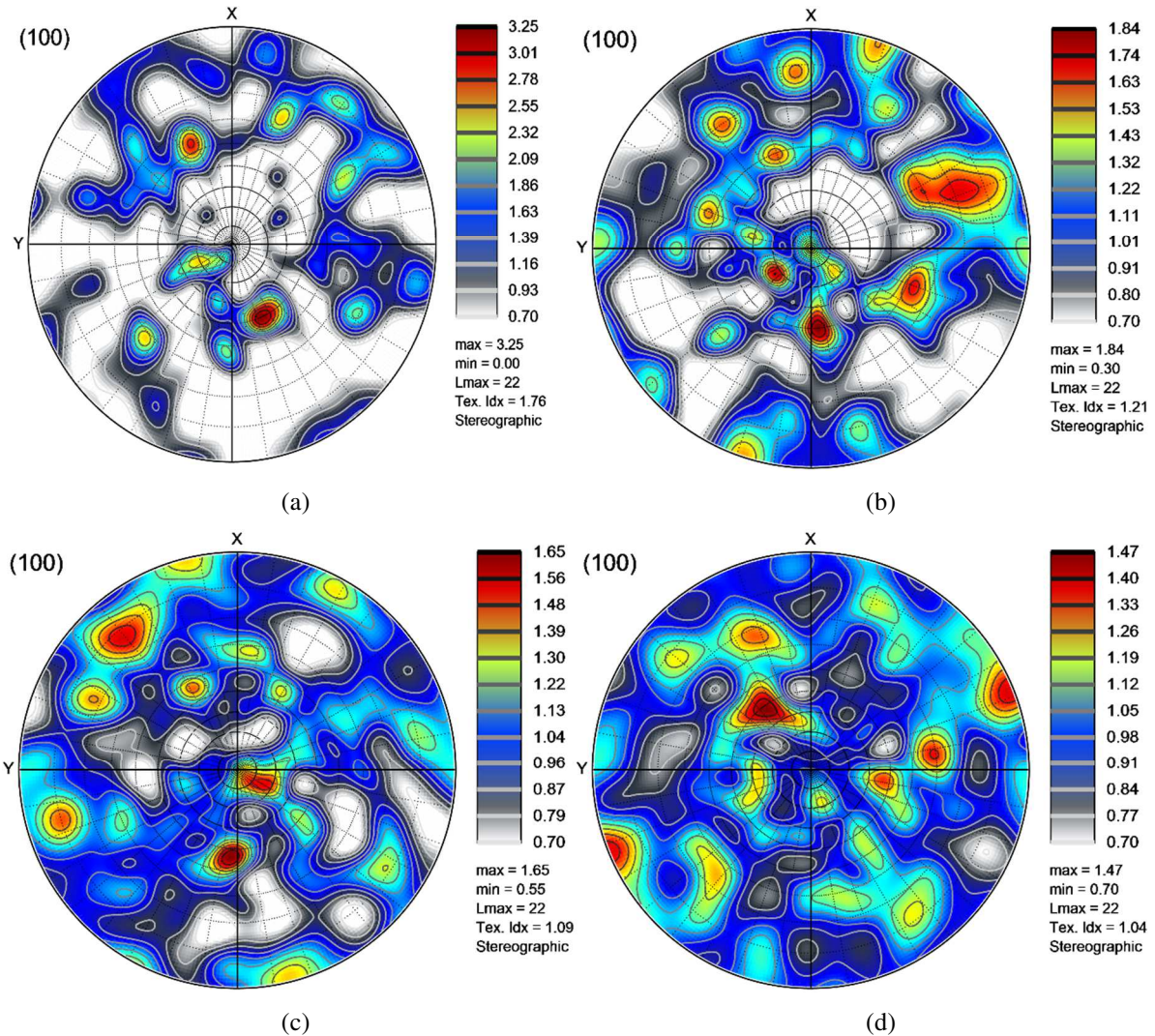


Fig. 4.5. Initial textures of the different unit cell configurations: (a) UC50; (b) UC200; (c) UC500; (d) UC1000.

The initial critical shear stress is assumed to be the same for all the crystallographic slip systems, and it is taken equal to τ_0 . The evolution of the critical shear stresses is described by an isotropic nonlinear hardening model, for which the components of the interaction-hardening matrix \mathbf{H} are given as follows (similar to the hardening matrix used in [Yoshida and Kuroda, 2012](#)):

$$\forall \alpha, \beta = 1, \dots, N_s : H^{\alpha\beta} = h_0 \left(1 + \frac{h_0 \hbar}{\tau_0 n} \right)^{n-1} ; \quad \hbar = \sum_{\alpha=1}^{2N_s} \gamma^\alpha, \quad (4.56)$$

where h_0 and n are hardening parameters, and \hbar is the accumulated slips on all the crystallographic slip systems, equal to $\sum_{k=1}^{2N_s} \gamma^k$. The material parameters used in the different simulations are reported in [Table 4.1](#).

Table 4.1. Elastic and hardening parameters.

Elasticity		Hardening		
E (GPa)	ν	τ^0 (MPa)	h_0 (MPa/s)	n
200	0.3	40	390	0.184

4.5.1. Mechanical response

Before investigating the ductility limits of polycrystalline aggregates, the mechanical responses at both macroscopic and microscopic levels will be presented and carefully analyzed.

4.5.1.1. Macroscopic predictions

The evolutions of the components 11 and 12 of the macroscopic first Piola-Kirchhoff stress tensor \mathbf{P} versus $F_{11} - 1$ are plotted in Fig. 4.6 for three particular strain paths: $\rho = -0.5$, $\rho = 0.$, and $\rho = 0.5$. It must be recalled that the studied unit cell is made of 200 grains (Fig. 4.4b). The curves plotted in Fig. 4.6 show that the macroscopic stress components are mainly dependent on the applied strain path. Furthermore, Fig. 4.6a demonstrates that component P_{11} increases monotonically until reaching a maximum value and decreases after this maximum value. This maximum value is reached almost at the same strain level for strain paths $\rho = 0.$, and $\rho = 0.5$, which is lower than the strain level corresponding to the maximum of P_{11} for $\rho = -0.5$. The evolution of the shear stress component P_{12} is plotted in Fig. 4.6b. The evolution of this component is less smooth than the evolution of P_{11} for the different strain paths. This component remains relatively small compared to component P_{11} , but not equal to zero (despite the fact that $F_{12} = 0$).

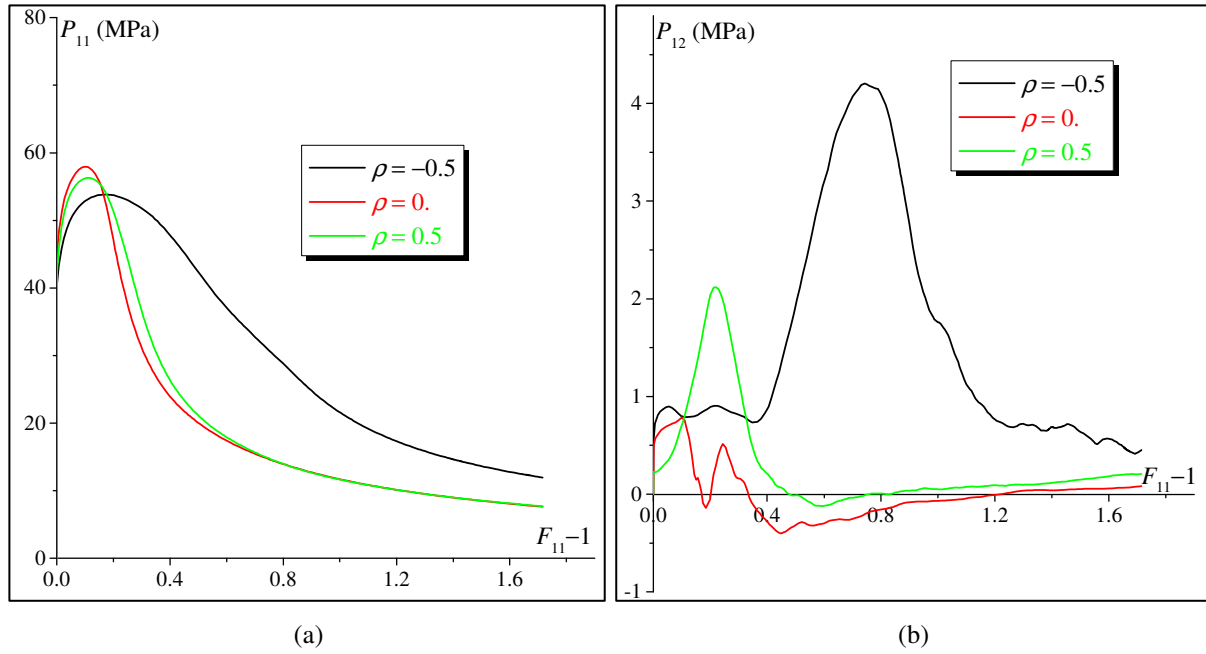


Fig. 4.6. Evolutions of some components of the macroscopic first Piola-Kirchhoff stress tensor versus $F_{11}-1$: (a) Component P_{11} ; (b) Component P_{12} .

To further investigate the polycrystalline mechanical response, we have plotted in Fig. 4.7, Fig. 4.8, and Fig. 4.9 the isovales of some relevant microscopic variables (namely, the von Mises equivalent stress, the Cauchy stress component σ_{33} , and the maximum logarithmic strain le_{max}) for three strain paths: $\rho = -0.5$, $\rho = 0.$, and $\rho = 0.5$. The different isovales are plotted at the moment when the major strain $E_{11} = \ln(F_{11})$ reaches the value 0.2. As demonstrated in the different figures, the distributions of these microscopic fields are obviously heterogeneous. This heterogeneity is mainly due to the difference between the initial crystallographic orientations of the different constituent grains. As revealed in Fig. 4.7, the microscopic equivalent stress is heterogeneously distributed. This distribution is expected considering the fact that both crystallographic orientation and plastic strain are heterogeneous (the activity of the slip systems and the magnitude of the accumulated slips change from one grain to another and from one integration point to another of the same grain). Despite the satisfaction of the macroscopic plane-stress condition (see Eq. (4.1)), the microscopic plane-stress condition is not strictly fulfilled as shown in Fig. 4.8. In this figure, one can observe that the component σ_{33} is around zero in all of the integration points of the mesh. The heterogeneity of the strain distribution is illustrated by the isovales of le_{max} plotted in Fig. 4.9. One can easily observe especially in Fig. 4.9b and c the beginning of formation of localized deformation zones (or bands) in the right side of the unit cell. By carefully checking the boundaries of the different unit cells, one can confirm from these figures that the periodic boundary conditions are respected.

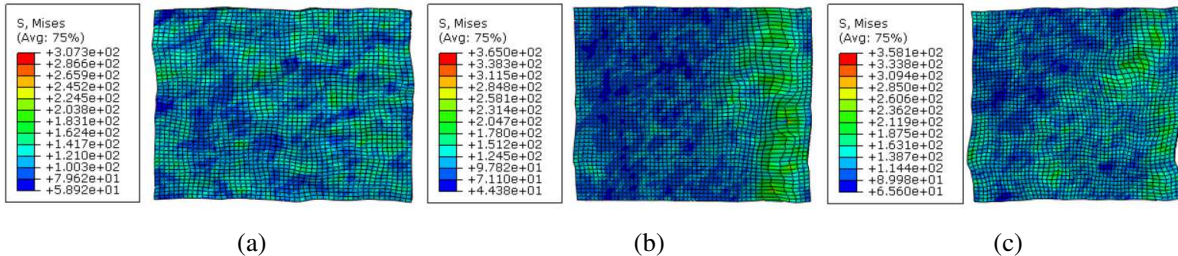


Fig. 4.7. Contour plot of the von Mises microscopic stress: (a) $\rho = -0.5$; (b) $\rho = 0.$; (c) $\rho = 0.5$.

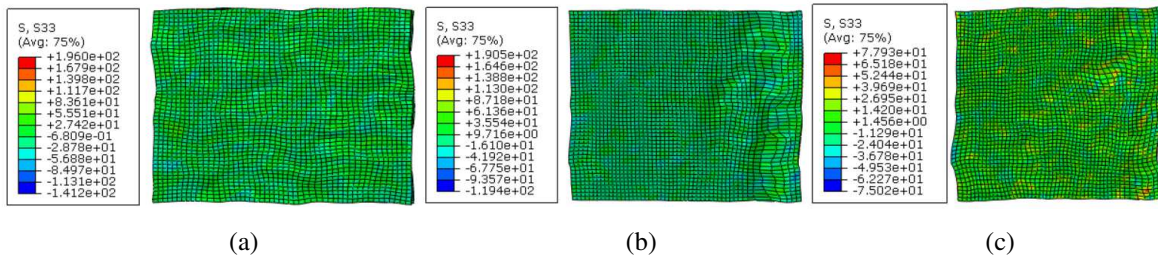


Fig. 4.8. Contour plot of the component 33 of the microscopic stress: (a) $\rho = -0.5$; (b) $\rho = 0.$; (c) $\rho = 0.5$.

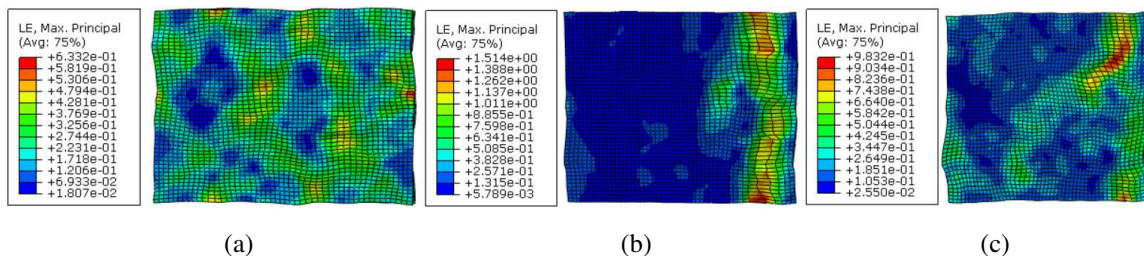


Fig. 4.9. Contour plot of the maximum microscopic logarithmic strain le_{max} : (a) $\rho = -0.5$; (b) $\rho = 0.$; (c) $\rho = 0.5$.

4.5.1.2. Microscopic predictions

To better analyze the heterogeneity of the mechanical responses, we study in this section the evolution of some mechanical variables associated with two different single crystals belonging to the same grain (hence, these two single crystals have the same initial crystallographic orientation). In this aim, attention is focused on a large grain from the UC200 which is loaded under uniaxial tension state ($\rho = -0.5$). The evolution of some components of the microscopic stress tensor corresponding to these single crystals are plotted in Fig. 4.10. From this figure, three conclusions can be drawn:

- Despite the fact that the initial orientation is the same for both single crystals, the evolutions of the components differ from one single crystal to another. This result is expected when taking into account the interactions between the grains and the assumption of continuity of displacement and traction fields across the grain-boundary interfaces between adjacent grains.
- The macroscopic stress state significantly differs from the microscopic states. Indeed, as clearly shown in Fig. 4.10, the microscopic plane-stress condition is not fulfilled since the component σ_{33} evolves during the loading. On the other hand, the macroscopic plane-stress condition is obviously respected as the average of σ_{33} is around 0.

- Unlike the macroscopic stress components plotted in Fig. 4.6, which exhibit relatively smooth evolutions (especially component P_{11}), the evolution of the microscopic stress components are not quite smooth. This lack of smoothness is probably due to the evolution of the crystallographic texture and the evolution of the accumulated slips of active slip systems.

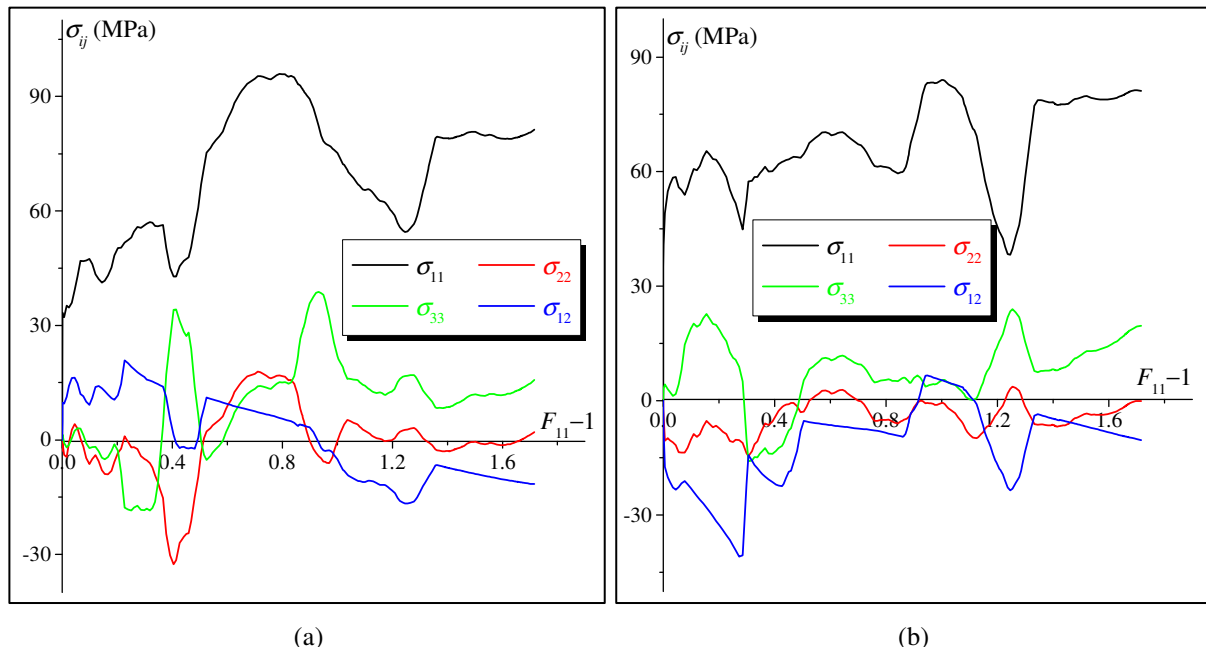


Fig. 4.10. Evolution of some components of the microscopic stress tensor versus $F_{11} - 1$: (a) first single crystal; (b) second single crystal.

The evolution of the slips of the active slip systems of both single crystals are plotted in Fig. 4.11. As clearly shown in this figure, the set of active slip systems as well as the evolution of the corresponding slips differ from one integration point to another. This result better explains the differences observed in the evolution of the components of the microscopic stress tensor, as shown in Fig. 4.10.

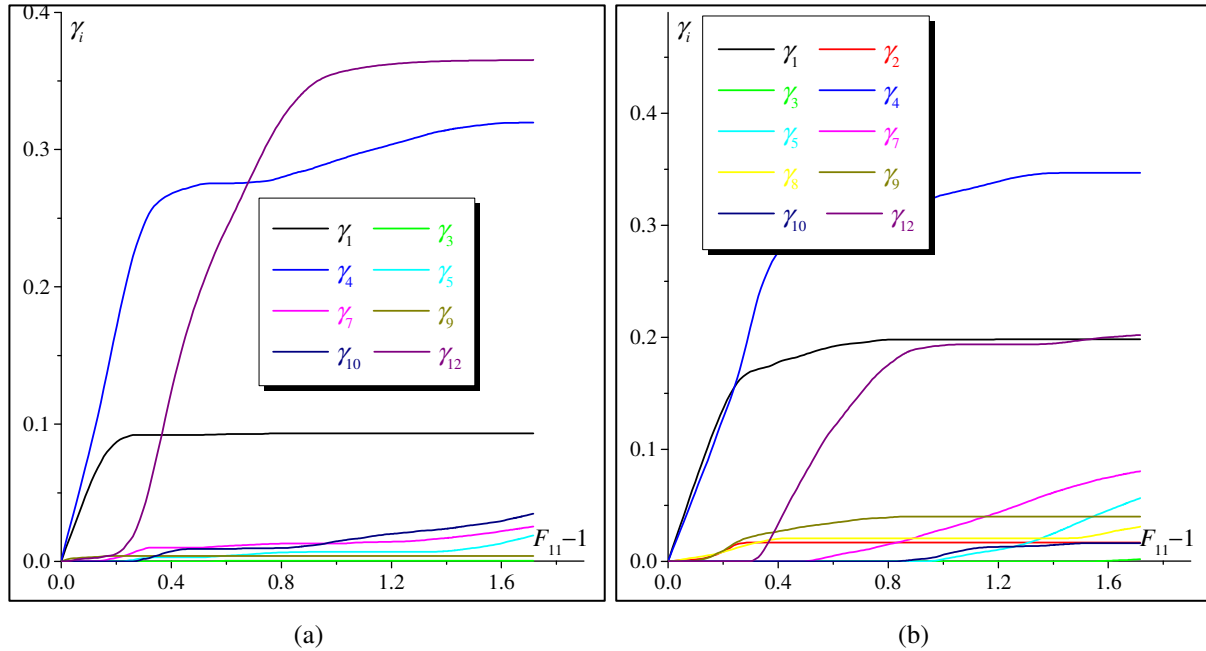


Fig. 4.11. Evolution of the slips of the active slip systems: (a) first single crystal; (b) second single crystal.

4.5.2. Ductility limit predictions

Before analyzing the ductility limits predicted by the coupling of the CPFEM approach with the bifurcation theory, let us firstly examine the evolution of the components ${}^{IN}\tilde{C}_{1111}^{(PK1)}$ and ${}^{IN}\tilde{C}_{1212}^{(PK1)}$ of the macroscopic tangent modulus. To this end, the two components are plotted in Fig. 4.12 as functions of the macroscopic strain component $E_{11} = \ln(F_{11})$, for three representative strain paths ($\rho = -0.5$, $\rho = 0$, and $\rho = 0.5$). Moreover, the shearing component ${}^{IN}\tilde{C}_{1212}^{(PK1)}$ is significantly reduced during the deformation and becomes very low. This observation is a natural outcome of the multi-slip character of crystal plasticity, which leads to the formation of vertices at the current points of the Schmid yield surfaces of single crystals. The reduction of this shearing component is the main destabilizing factor responsible for bifurcation, thus promoting early plastic strain localization. It is worth noting that, when a smooth yield function is used, the shearing component ${}^{IN}\tilde{C}_{1212}^{(PK1)}$ keeps the same magnitude as its elastic counterpart. It is also observed from the different curves in Fig. 4.12 (especially the curves corresponding to the evolution of the shearing component ${}^{IN}\tilde{C}_{1212}^{(PK1)}$), that the evolutions of the components of the tangent modulus are not quite smooth.

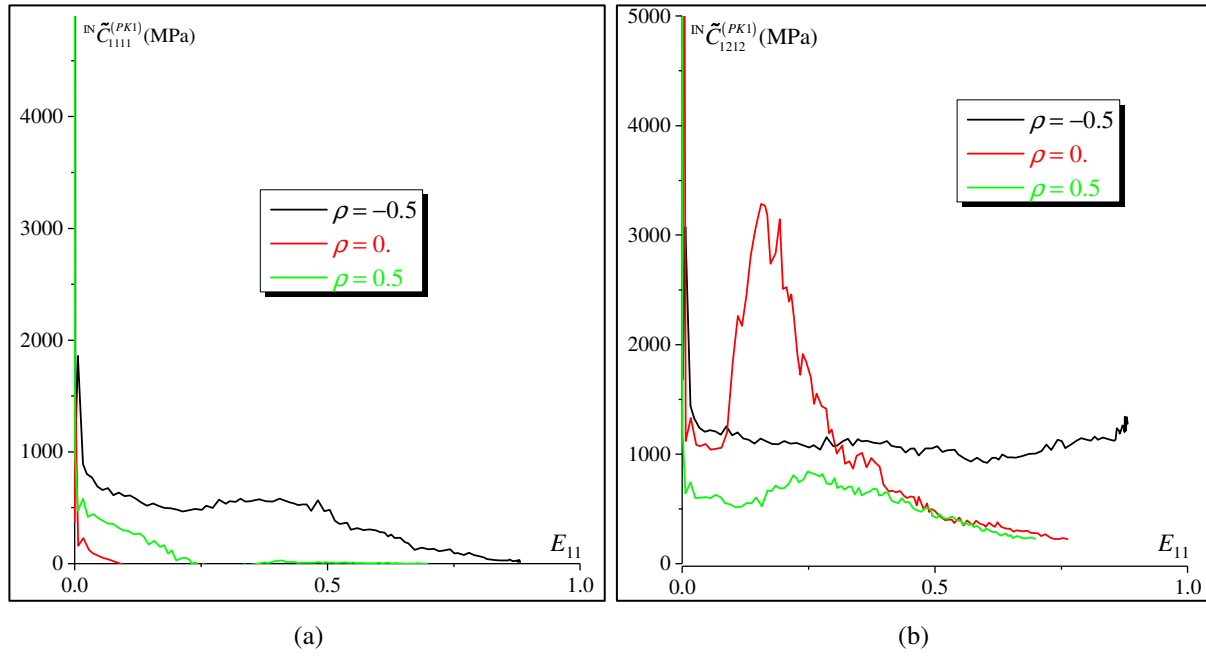


Fig. 4.12. Evolution of some components of the in-plane tangent modulus versus $E_{11} = \ln(F_{11})$: (a) Component ${}^{\text{IN}}\tilde{C}_{1111}^{(PK1)}$; (b) Component ${}^{\text{IN}}\tilde{C}_{1212}^{(PK1)}$.

The evolution of the determinant of the macroscopic in-plane acoustic tensor $\vec{\mathcal{N}} \cdot {}^{\text{IN}}\tilde{\mathbf{C}}^{(PK1)} \cdot \vec{\mathcal{N}}$ is plotted in Fig. 4.13a. As the acoustic tensor is definitely positive in the deformation range that precedes the occurrence of localized necking, the unit normal vector $\vec{\mathcal{N}}$, corresponding to the vanishing of its determinant at the onset of strain localization, is the same as the one minimizing this determinant. It can be seen that, regardless of the selected strain path, the minimum of the determinant abruptly decreases during the transition between the elastic and plastic regimes, which occurs at small strains. By contrast, in the plastic regime, the decrease is much slower and, accordingly, the minimum of the determinant reaches zero at large strain. The FLDs predicted by the bifurcation criterion, in conjunction with CPFEM approach, are shown in Fig. 4.13b for the four considered unit cells (namely UC50, UC200, UC500, and UC1000). This figure clearly emphasizes the effect of the number of grains on the predicted ductility limits. Indeed, the predicted limit strains increase with the number of grains. This result is likely attributable to the crystallographic and morphologic texture evolution in crystal plasticity descriptions. Indeed, plastic anisotropy is obviously more pronounced when the number of grains is small. Complementary simulations will be performed very soon to deeply and better investigate all these aspects (to be prepared for the thesis defense).

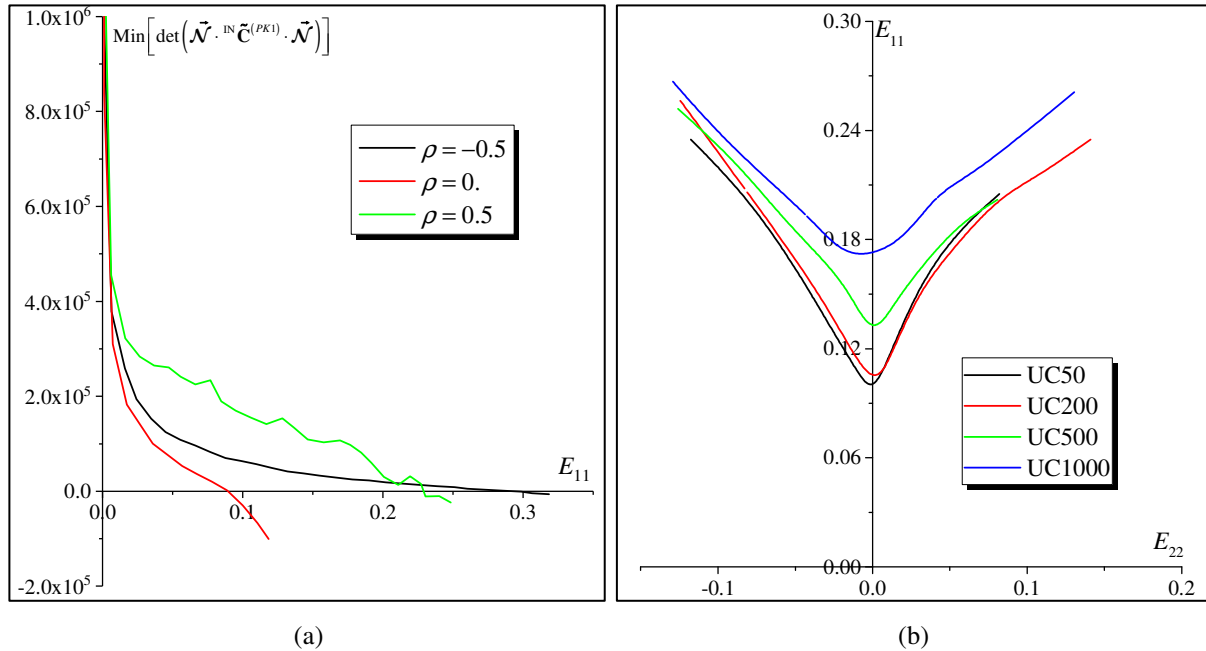


Fig. 4.13. Prediction of the ductility limits: (a) evolution of the minimum of the determinant of the acoustic tensor $\vec{\mathcal{N}} \cdot {}^{\text{IN}}\tilde{\mathbf{C}}^{(PK1)} \cdot \vec{\mathcal{N}}$ as a function of $E_{11} = \ln(F_{11})$ for three different strain paths ($\rho = -0.5$, $\rho = 0$, and $\rho = 0.5$); (b) effect of the number of grains on the predicted FLDs.

4.6. Summary and conclusions

In this chapter, a new multiscale constitutive modeling framework based on a crystal plasticity finite element homogenization method has been developed to accurately predict the mechanical behavior of thin metal sheets. This framework, which belongs to the family of CPFEM approaches, is based on the periodic homogenization scheme. This approach has been implemented into ABAQUS/Standard to predict the mechanical behavior of 2D polycrystalline aggregates, assumed to be statistically representative of thin metal sheets, from that of the constituent single crystals. To ensure the efficient implementation of the developed framework, a set of robust numerical techniques have been developed. This framework has been coupled with the bifurcation theory to predict the ductility limits using 2D unit cell computation. Several numerical predictions have been performed to study the mechanical response as well as the ductility limits of polycrystalline aggregates. Further results and explorations will be performed in the future to better illustrate the relevance and usefulness of the developed numerical framework.

Conclusions and perspectives

Summary and conclusions

The proposed numerical strategy

In this work, a finite element based multiscale numerical strategy has been proposed to predict the ductility limits of heterogeneous media, such as voided materials and polycrystalline aggregates.... To build this strategy, the periodic homogenization method has been used as the multiscale transition scheme to determine the macroscopic mechanical behavior of the heterogeneous medium from that of their microscopic constituents. The proposed strategy is based on the coupling of mechanical behavior modeling and plastic instability criteria. Thus, this strategy is concerning two levels of modeling: plastic instability and mechanical behavior.

Modeling of plastic instability

The Rice bifurcation approach has been mainly used to predict the occurrence of plastic instability. This criterion corresponds to the singularity of the macroscopic acoustic tensor, in which the evolution of macroscopic tangent moduli is essential to be determined during the deformation. To ensure the accurate and efficient implementation of this criterion, a comparative study of three techniques (namely, the perturbation technique, the fluctuation technique and the condensation technique) has been conducted for computing the macroscopic tangent moduli by periodic homogenization scheme. In this comparative study, these three techniques have been implemented by developing a set of Python scripts. The reliability, accuracy and ease of implementation have been evaluated through some typical numerical examples.

Modeling of the mechanical behavior

✓ Phenomenological modeling

In this context, the phenomenological modeling has been coupled with some plastic instability criteria. On the one hand, this strategy has been adopted to predict the ductility limits of perforated sheets, where the plastic response of the matrix material is characterized by a finite strain J_2 flow theory with isotropic hardening. The prediction of plastic instability is based on three necking criteria: the maximum force criterion (diffuse necking), the general bifurcation criterion (diffuse necking), and the Rice bifurcation criterion (localized necking). The results obtained by these necking criteria have been thoroughly analyzed and compared. A sensitivity study has also been conducted to numerically investigate the influence on the prediction of necking of the design parameters (dimension, aspect-ratio, orientation, and shape of the holes), the macroscopic boundary conditions and the metal matrix material parameters (plastic

anisotropy, hardening). On the other hand, this strategy has been adopted to investigate the competition between the occurrence of two typical failure mechanisms in voided solids: void coalescence and macroscopic strain localization, where the mechanical behavior of the metal matrix is modeled by the initial porous Gurson model. This study is based on the coupling of the periodic homogenization approach and several criteria (the Rice bifurcation and an energy-based coalescence criterion, among others). The occurrence of failure has been examined under two loading configurations: loadings under proportional stressing (classically used in unit cell computations to study the effect of stress state on void growth and coalescence), and loadings under proportional in-plane strain paths (traditionally used for predicting forming limit diagrams). It turns out from the numerical investigation that macroscopic strain localization acts as a precursor to void coalescence when the unit cells are proportionally stressed. However, for loadings under constant in-plane strain paths, only macroscopic strain localization can occur, while void coalescence is not possible. Meanwhile, the relations between the two configurations of loading have been carefully explained within these two failure mechanisms. The effect of primary void shape and the presence of secondary voids on the occurrence of macroscopic strain localization have been also investigated.

✓ Crystal plasticity modeling

In this context, the CPFEM model has been coupled with the Rice bifurcation theory to predict the ductility limit of FCC polycrystals. The CPFEM model is, in essence, a multiscale approach that allows linking physical mechanisms and microstructure-induced properties to the macroscopic (or homogenized) mechanical behavior. In this model, the plastic deformation is solely activated by the slip on the crystallographic slip systems and the plastic flow is modeled by the classical Schmid criterion. Using this strategy, the mechanical response at both single crystal and polycrystalline scales has been highlighted through several simulations. Moreover, the crystal texture and hardening evolutions at the microscale as well as the formability of sheet metals at the macroscale have been investigated. The effect of the number of grains on formability has been also investigated.

Perspectives

In our investigations, the ductility limit is predicted on the basis of unit cell computations by the Rice bifurcation approach at the macroscopic scale. So that, the predictions are expected to be compared with those from other instability criteria, such as the well-known imperfection approach ([Signorelli et al., 2019](#)). It is worth mentioning that microscopic plastic instability can be an important driver of void growth, coalescence and ultimate ductile failure. To this end, attention is also needed to the plastic instability at microscopic scale. Meanwhile, the competition between the plastic instability at the microscopic scale and the macroscopic scale can be pursued in future works.

In the failure predictions of the voided solids, a Gurson model was used to consider the effect of secondary voids on strain localization. However, the nucleation and coalescence in the secondary voids were not taken into account. These predictions can be firstly improved by using the advanced Gurson-type models (GTN, GLD) to consider the combined effects of secondary void nucleation and coalescence on the macroscopic behavior and strain localization. Secondly, our analysis was conducted by assuming that the materials were undergoing quasi-static deformation. Namely, the effect of strain rate on ductile failure was neglected in our modeling. The rate-dependent models should be developed to investigate the influence of strain rate sensitivity on macroscopic strain localization and void coalescence (see, e.g., [Reboul et al., 2020](#)). Thirdly, it would be more attractive to substitute the phenomenological model by the CPFEM model in the prediction of ductile failure in porous polycrystals (see, e.g., [Hure, 2019](#)).

In the ductility prediction of polycrystalline aggregates, our attention has been paid only to FCC polycrystals, in which the plastic deformation is exclusively induced by the slip on the crystallographic slip systems. In the near future, attention will be paid to BCC and HCP polycrystals or some dual phase materials (such as BCC plus FCC). The plastic deformation mechanisms involving twinning in polycrystals also deserves to be considered in the constitutive description. It is worth noting that the size effects in accordance with physical facts sometimes present prominent influence on the mechanical response, especially in micromechanical analysis. Although, the microscopic and macroscopic mechanical response of the studied polycrystals, as well as the effect of grain number on ductility has been already investigated in this work. However, the size effect is not considered in this study. To remedy this limitation, the use of strain gradient crystal plasticity models may provide more insights in understanding some practical analysis results (grain orientation, grain size...) ([Niordson and Tvergaard, 2019](#); [Guo et al., 2020](#)).

Part II: Résumé étendu en Français

Introduction générale

Contexte de la thèse

Ce travail a été réalisé au sein de l'axe de recherche « Méthodes Numériques, Instabilités et Vibrations » du Laboratoire d'Étude des Microstructures et de Mécanique des Matériaux (LEM3) rattaché au Campus ENSAM de Metz. L'objectif essentiel de cette thèse est de développer un outil numérique, basé sur la technique d'homogénéisation périodique, pour la prédiction de la ductilité des matériaux métalliques hétérogènes (composites, agrégats polycristallins, milieux poreux...).

Cadre général de l'étude

Les matériaux métalliques sont largement utilisés, souvent sous forme de structures minces, dans de nombreux secteurs industriels et technologiques (automobile, ferroviaire, aéronautique, électroménager, électronique...). Sous l'impulsion d'accords européens et internationaux (protocole de Kyoto, COP21...), portant sur la réduction des émissions de gaz à effet de serre, ainsi qu'en raison de l'augmentation des prix des matières premières, les producteurs et les transformateurs de tôles métalliques (sidérurgistes, industrie automobile...) doivent optimiser leurs méthodes et technologies de production pour pouvoir satisfaire les nouvelles normes environnementales. L'une des solutions pratiques, suivies pour atteindre les objectifs fixés par ces accords, consiste à alléger considérablement les pièces métalliques et les produits finis. Cet effort d'allègement nécessite la conception de nouveaux matériaux métalliques ayant des propriétés physiques et mécaniques optimales (faible densité massique, haute résistance mécanique, ductilité élevée, haute résistance à la corrosion...). Le développement de ces nouvelles générations de matériaux métalliques n'est généralement pas possible sans une maîtrise approfondie des mécanismes physiques mis en jeux lors des opérations de formage par déformation plastique. En effet, l'application des procédés de mise en forme, tel que l'emboutissage, peut souvent engendrer l'apparition d'instabilités plastiques (ex., des zones à forte localisation de déformations plastiques) dans les pièces, ce qui peut conduire à la défaillance de séries de pièces et nécessiter de coûteuses modifications des procédés d'industrialisation (traitement thermomécanique, outillage...). Ces instabilités peuvent être classées en deux familles : les instabilités de type structure (flambement, plissement, retour élastique...) et les instabilités de type matériau (striction diffuse, striction localisée, endommagement...). Dans ce travail, notre attention se porte sur l'étude des instabilités matérielles et en particulier la striction localisée. La déformation au moment de l'apparition de la striction localisée représente la déformation ultime qu'une pièce peut atteindre lors de sa mise en forme ou sa mise en service, puisque ce phénomène est souvent précurseur de la rupture de la pièce. La ductilité (ou formabilité) d'un matériau peut donc être quantifiée par sa capacité à subir des déformations irréversibles sans l'apparition de striction localisée. Afin de déterminer la limite de ductilité, le concept de courbe

limite de formage (CLF) est communément utilisé par les acteurs industriels et académiques. Ce concept, initialement introduit par des approches expérimentales dans [Keeler et Backofen \(1964\)](#) et [Goodwin \(1968\)](#), permet de représenter la limite de formabilité dans l'espace des déformations principales dans le plan de la tôle. L'utilisation des méthodes expérimentales pour déterminer les CLF est confrontée à plusieurs difficultés pratiques, tel que le coût élevé de la mise en œuvre de ces méthodes et le manque de noms standardisées, entraînant une forte variabilité des résultats d'un laboratoire à un autre. Ces difficultés pratiques ont poussé les chercheurs à développer des méthodes alternatives basées sur des approches théoriques (analytiques et/ou numériques). Ces approches théoriques sont généralement basées sur le couplage entre un critère de striction localisé et un modèle qui décrit l'évolution du comportement mécanique du matériau étudié. Parmi les critères théoriques de striction localisée utilisés dans la littérature, nous pouvons citer la théorie de bifurcation de Rice ([Rudnicki et Rice, 1975](#) ; [Stören et Rice, 1975](#) ; [Rice, 1976](#)), l'approche par imperfection initiale de Marciniack–Kuczynski ([Marciniak et Kuczynski, 1967](#) ; [Hutchinson et al., 1978b](#)) et la méthode de perturbation ([Dudzinski et Morinari, 1991](#) ; [Toth et al., 1996](#)). Les approches utilisées pour modéliser le comportement mécanique des matériaux peuvent être classées en deux familles : les approches phénoménologiques et les approches multi-échelles.

Objectifs de la thèse

Le travail actuel a pour objectif de concevoir et développer un outil numérique pour une prédiction fiable et robuste de la ductilité des matériaux métalliques hétérogènes. Pour développer cet outil numérique, la modélisation multi-échelles est privilégiée par rapport aux approches phénoménologiques. Ce choix est motivé par la capacité des approches multi-échelles à prendre en compte explicitement l'effet de paramètres microstructuraux essentiels, tels que les textures cristallographique et morphologique (initiales et induites) ou la présence de cavités, sur le comportement macroscopique du matériau étudié et par conséquent sur sa ductilité. Ce travail est limité aux structures métalliques minces présentant une distribution périodique ou quasi-périodique d'hétérogénéités. Par conséquent, la technique d'homogénéisation périodique est retenue pour développer cette approche multi-échelles. Cette modélisation multi-échelles est couplée au critère de bifurcation de Rice pour prédire l'apparition de la localisation des déformations plastiques. Ce travail s'inscrit dans la continuité logique de travaux précédents réalisés au sein de l'axe de recherche « Méthodes Numériques, Instabilités et Vibrations ». En effet, les approches multi-échelles ont été utilisées pour modéliser le comportement d'agrégats polycristallins dans les thèses de [Lorrain \(2005\)](#), [Franz \(2008\)](#) et [Akpama \(2017\)](#). Dans ces derniers travaux, l'approche multi-échelles auto-cohérente a été couplée au critère de bifurcation de Rice ou à l'approche par imperfection initiale pour prédire les limites de ductilité des matériaux polycristallins. La contribution actuelle a permis d'étendre les investigations précédentes ([Lorrain, 2005](#) ; [Franz, 2008](#) ; [Akpama, 2017](#)) à l'homogénéisation périodique et à d'autres structures métalliques hétérogènes (tôles

métalliques trouées, matériaux poreux). Par rapport aux travaux antérieurs de la littérature, la contribution actuelle peut être vue comme une avancée importante, car elle permet de coupler, pour la première fois, la technique d'homogénéisation périodique à l'approche de bifurcation de Rice pour prédire l'apparition de striction localisée dans les tôles minces.

Plan du résumé

Ce résumé étendu en français sera articulé autour de deux chapitres qui suivent cette introduction :

- Le premier chapitre sera dédié à la présentation de la technique d'homogénéisation périodique, d'un point de vue théorique et pratique. Les méthodes implantées pour déterminer le module tangent macroscopique relatif à la technique d'homogénéisation périodique seront détaillées dans ce chapitre (la méthode de perturbation, la méthode de condensation et la méthode de fluctuation).
- Le second chapitre présentera deux applications du couplage entre la technique homogénéisation périodique et l'approche de bifurcation de Rice pour la prédiction de la limite de ductilité : les milieux poreux et les agrégats polycristallins élastoplastiques. Les autres applications sont bien détaillées dans la version anglaise de ce manuscrit.

Afin d'assurer une certaine auto-cohérence de ce résumé (et ainsi son indépendance par rapport à la version anglaise), nous avons choisi de bien détailler les développements théoriques et numériques là où cela nous a semblé nécessaire.

Chapitre 1

Étude comparative de trois techniques pour le calcul du module tangent macroscopique par l'approche d'homogénéisation périodique

1.1. Introduction

Dans le cadre de cette thèse, nous avons étudié et implanté trois techniques numériques pour le calcul du module tangent macroscopique obtenu par la méthode d'homogénéisation périodique : la technique de perturbation (TP), la technique de condensation (TC) et la technique de fluctuation (TF). Compte tenu de son importance dans l'analyse de perte de ductilité par l'approche de bifurcation de Rice, la détermination robuste et précise de ce module tangent est d'un intérêt majeur dans ces travaux de thèse. Ce chapitre a pour objectif de présenter le concept numérique sur lequel reposent ces techniques et leurs implantations sous la forme de scripts Python en relation avec le code de calcul par élément finis ABAQUS.

Le reste du chapitre est organisé comme suit :

- La formulation du problème d'homogénéisation périodique dans le cadre des grandes déformations et les aspects pratiques liés à sa résolution par la méthode des éléments finis sont discutés dans la Section 1.2.
- Les aspects numériques et les détails opérationnels liés à la mise en œuvre des trois techniques de calcul du module tangent macroscopique sont détaillés dans la Section 1.3.

- La mise en œuvre des trois techniques est validée dans la Section 1.4 en comparant nos prédictions à celles publiées dans [Miehe et al. \(2002b\)](#). Les performances de ces techniques sont discutées et comparées à travers quelques cas tests.

1.2. Problème d'homogénéisation périodique

La technique d'homogénéisation périodique est utilisée pour assurer la transition entre les échelles microscopique et macroscopique. Sans perte de généralité, nous supposons que la configuration initiale \mathcal{V}_0 de la cellule de base (le volume élémentaire représentatif au sens de l'homogénéisation périodique) occupe le domaine $[-\lambda_0/2, \lambda_0/2] \times [-\lambda_0/2, \lambda_0/2] \times [-\lambda_0/2, \lambda_0/2]$. La cellule de base étudiée est sollicitée en grandes déformations et une formulation lagrangienne totale est adoptée pour exprimer les équations relatives à cette approche multi-échelles. Par conséquent, le gradient de transformation et le premier tenseur de contraintes de Piola–Kirchhoff sont retenus comme mesures de déformation et de contrainte conjuguées appropriées. Dans un souci de clarté, les quantités microscopiques (resp. macroscopiques) seront désignées par des caractères et symboles minuscules (resp. majuscules).

Les principales équations régissant le problème d'homogénéisation périodique sont décrites ci-dessous :

- Le gradient de transformation microscopique \mathbf{f} est décomposé additivement en une partie macroscopique \mathbf{F} et un gradient \mathcal{V}_0 -périodique \mathbf{f}_{per} qui reflète le degré d'hétérogénéité entre les différentes phases constitutives :

$$\mathbf{f} = \mathbf{F} + \mathbf{f}_{per}. \quad (1.1)$$

La position courante \mathbf{x} d'un point matériel peut être obtenue par intégration spatiale de l'équation (1.18) :

$$\mathbf{x} = \mathbf{F} \cdot \mathbf{x}_0 + \mathbf{u}_{per}, \quad (1.2)$$

où \mathbf{x}_0 est la position initiale du même point matériel et \mathbf{u}_{per} un déplacement \mathcal{V}_0 -périodique. La vitesse \mathbf{v} est obtenue par dérivation temporelle de l'équation (1.2) :

$$\mathbf{v} = \dot{\mathbf{F}} \cdot \mathbf{x}_0 + \dot{\mathbf{u}}_{per}. \quad (1.3)$$

- Les relations de moyenne reliant le gradient de transformation microscopique \mathbf{f} et le premier tenseur de contraintes de Piola–Kirchhoff microscopique \mathbf{p} à leurs homologues macroscopiques \mathbf{F} et \mathbf{P} :

$$\mathbf{F} = \frac{1}{|\mathcal{V}_0|} \int_{\mathcal{V}_0} \mathbf{f} d\mathcal{V}_0 ; \quad \mathbf{P} = \frac{1}{|\mathcal{V}_0|} \int_{\mathcal{V}_0} \mathbf{p} d\mathcal{V}_0, \quad (1.4)$$

où $|\mathcal{V}_0|$ est le volume initial de la cellule de base égal à $(\lambda_0)^3$.

L'équation (1.4) peut être exprimée de manière équivalente sous la forme dérivée suivante :

$$\dot{\mathbf{F}} = \frac{1}{|\mathcal{V}_0|} \int_{\mathcal{V}_0} \dot{\mathbf{f}} d\mathcal{V}_0 ; \quad \dot{\mathbf{P}} = \frac{1}{|\mathcal{V}_0|} \int_{\mathcal{V}_0} \dot{\mathbf{p}} d\mathcal{V}_0. \quad (1.5)$$

- L'équation d'équilibre microscopique statique (en l'absence de forces volumiques) :

$$\operatorname{div}_{x_0}(\dot{\mathbf{p}}) = \mathbf{0}. \quad (1.6)$$

- Les équations constitutives décrivant le comportement mécanique microscopique et macroscopique et qui peuvent être formulées sous les formes génériques suivantes :

$$\dot{\mathbf{p}} = \mathbf{c}^{(PK1)} : \dot{\mathbf{f}} ; \quad \dot{\mathbf{P}} = \mathbf{C}^{(PK1)} : \dot{\mathbf{F}}, \quad (1.7)$$

où $\mathbf{c}^{(PK1)}$ et $\mathbf{C}^{(PK1)}$ désignent les modules tangents microscopique et macroscopique.

Comparé aux problèmes classiques traités par la méthode des éléments finis, le problème d'homogénéisation périodique, défini par les équations (1.18)–(1.7), présente deux spécificités particulières : la nature du chargement auquel la cellule de base est soumise et les conditions aux limites appliquées sur les surfaces extérieures de cette cellule. Ces aspects pratiques seront clarifiés dans les développements suivants. Comme point de départ de ces développements, le principe des travaux virtuels est exprimé en l'absence de forces volumiques sous la forme intégrale suivante :

$$\int_{\mathcal{V}_0} \left[\frac{\partial \delta \mathbf{v}}{\partial \mathbf{x}_0} : \dot{\mathbf{p}} \right] d\mathcal{V}_0 = \int_{\mathcal{S}_0} \delta \mathbf{v} \cdot \dot{\mathbf{t}}_0 d\mathcal{S}_0. \quad (1.8)$$

Tenant compte des équations (1.3) et (1.6), le membre de gauche de l'équation (1.8) peut s'écrire sous la forme suivante :

$$\begin{aligned} \int_{\mathcal{V}_0} \left(\frac{\partial \delta \mathbf{v}}{\partial \mathbf{x}_0} : \dot{\mathbf{p}} \right) d\mathcal{V}_0 &= \int_{\mathcal{V}_0} \left(\left(\delta \dot{\mathbf{F}} + \frac{\partial \delta \mathbf{v}_{per}}{\partial \mathbf{x}_0} \right) : \dot{\mathbf{p}} \right) d\mathcal{V}_0 \\ &= \int_{\mathcal{V}_0} (\delta \dot{\mathbf{F}} : \dot{\mathbf{p}}) d\mathcal{V}_0 + \int_{\mathcal{S}_0} ((\delta \mathbf{v}_{per} \otimes \vec{\mathbf{n}}_0) : \dot{\mathbf{p}}) d\mathcal{S}_0. \end{aligned} \quad (1.9)$$

Compte tenu de l'anti-périodicité du tenseur $\delta \mathbf{v}_{per} \otimes \vec{\mathbf{n}}_0$ et de la périodicité du tenseur $\dot{\mathbf{p}}^T$ sur \mathcal{V}_0 , on peut aisément démontrer que :

$$\int_{\mathcal{S}_0} ((\delta \mathbf{v}_{per} \otimes \vec{\mathbf{n}}_0) : \dot{\mathbf{p}}) d\mathcal{S}_0 = 0. \quad (1.10)$$

Considérant l'équation (1.10), l'équation (1.9) peut être réduite à la condition de Hill–Mandel (Ben Bettaieb et al., 2012) :

$$\int_{\mathcal{V}_0} \left(\frac{\partial \delta \mathbf{v}}{\partial \mathbf{x}_0} : \dot{\mathbf{p}} \right) d\mathcal{V}_0 = |\mathcal{V}_0| \delta \dot{\mathbf{F}} : \dot{\mathbf{P}}. \quad (1.11)$$

Comme précédemment établi par Débordes (1986), Miehe et Bayreuther (2006), Temizer et Wriggers

(2008), la formulation (1.11) permet de traiter $\dot{\mathbf{F}}$ comme des degrés de liberté (ddl) macroscopiques associés aux forces macroscopiques nodales $|\mathcal{V}_0| \dot{\mathbf{P}}$. En pratique, l'application du chargement macroscopique en combinaison avec les conditions aux limites périodiques dans ABAQUS est assurée par l'utilisation de la technique de point (ou nœud) de référence (Lejeunes et Bourgeois, 2011). Nous détaillerons dans les développements qui suivent comment cette technique permet de gérer ces aspects dans une seule direction de l'espace (direction 1). La même logique peut être similairement appliquée aux autres directions spatiales.

Si nous considérons deux nœuds M^- et M^+ appartenant aux faces \mathcal{S}_{01}^- et \mathcal{S}_{01}^+ et ayant des coordonnées identiques dans les directions 2 et 3 (Fig. 1.1), la position de ces deux nœuds peut être déterminée à partir de l'équation (1.2) :

$$\mathbf{x}_{M^-} = \mathbf{F} \cdot \mathbf{x}_{0M^-} + \mathbf{u}_{M^-}^{per} ; \quad \mathbf{x}_{M^+} = \mathbf{F} \cdot \mathbf{x}_{0M^+} + \mathbf{u}_{M^+}^{per}. \quad (1.12)$$

Les conditions de périodicité exigent que $\mathbf{u}_{M^-}^{per} = \mathbf{u}_{M^+}^{per}$. Par conséquent, les équations (1.12)₁ et (1.12)₂ peuvent être combinées pour obtenir :

$$\mathbf{x}_{M^+} - \mathbf{x}_{M^-} = \mathbf{F} \cdot (\mathbf{x}_{0M^+} - \mathbf{x}_{0M^-}). \quad (1.13)$$

Par ailleurs, la différence $\mathbf{x}_{M^+} - \mathbf{x}_{M^-}$ peut être définie comme :

$$\mathbf{x}_{M^+} - \mathbf{x}_{M^-} = (\mathbf{u}_{M^+} - \mathbf{u}_{M^-}) + (\mathbf{x}_{0M^+} - \mathbf{x}_{0M^-}), \quad (1.14)$$

où \mathbf{u}_{M^+} et \mathbf{u}_{M^-} sont les déplacements des nœuds M^+ et M^- , respectivement. En considérant les coordonnées initiales des nœuds M^+ et M^- , la substitution de l'équation (1.14) dans l'équation (1.13) conduit à la relation suivante entre les déplacements \mathbf{u}_{M^+} et \mathbf{u}_{M^-} :

$$\mathbf{u}_{M^+} - \mathbf{u}_{M^-} = (\mathbf{F} - \mathbf{I}_2) \cdot (\mathbf{x}_{0M^+} - \mathbf{x}_{0M^-}) = (\mathbf{F} - \mathbf{I}_2) \cdot \begin{bmatrix} \lambda_0 \\ 0 \\ 0 \end{bmatrix}. \quad (1.15)$$

Pratiquement, les conditions aux limites périodiques sur les faces opposées \mathcal{S}_{01}^- et \mathcal{S}_{01}^+ et le chargement macroscopique \mathbf{F} , résumés par l'équation (1.15), sont appliqués en utilisant l'option de contrainte cinématique ‘MPC’ d'ABAQUS pour chaque paire de nœuds (M^-, M^+) . La boîte à outils *Homotools* (Lejeunes et Bourgeois, 2011) nous a servi pour pouvoir identifier automatiquement toutes les paires de nœuds appartenant aux faces \mathcal{S}_{01}^- et \mathcal{S}_{01}^+ et d'appliquer ainsi la contrainte ‘MPC’ entre les nœuds de la même paire. Pour gérer facilement l'application du chargement macroscopique et pour automatiser le calcul de la réponse mécanique macroscopique, un point de référence, désigné RP_1 , doit être créé. Le chargement macroscopique est appliqué en imposant le déplacement suivant sur RP_1 : $(U_1 = (F_{11} - 1)\lambda_0; U_2 = 0; U_3 = 0)$. Ce point de référence est connecté à chaque paire de nœuds pour appliquer la contrainte ‘MPC’ représentée par l'équation (1.15). Les composantes de la réaction nodale

induite par les déplacements appliqués sur RP_1 sont égales aux composantes 11, 12 et 13 du tenseur des contraintes macroscopiques de Piola–Kirchhoff \mathbf{P} multipliées par le volume initial $|\mathcal{V}_0|$ de la cellule de base (Lejeunes et Bourgeois, 2011). Des développements similaires peuvent être réalisés pour appliquer le chargement macroscopique et les conditions de périodicité sur les autres faces.

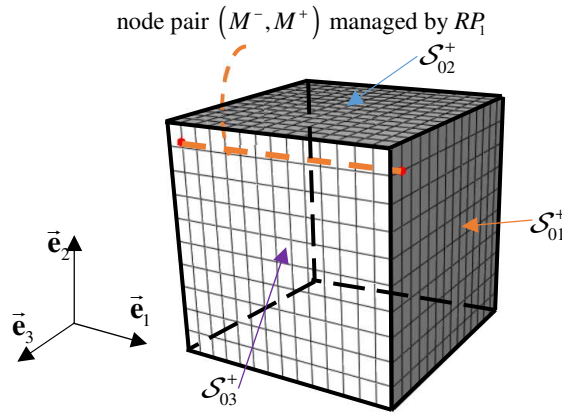


Fig. 1.1. Illustration des conditions de périodicité appliquées entre sur les nœuds M^- et M^+ .

1.3. Calcul du module tangent macroscopique

Les aspects pratiques liés à la résolution du problème d'homogénéisation périodique par la méthode des éléments finis ont été détaillés dans la Section 1.2. Cette résolution se base sur l'utilisation de la boîte à outils *Homotools* capable de gérer automatiquement l'application des conditions aux limites périodiques, du chargement macroscopique ainsi que la détermination de la réponse macroscopique. Pour compléter cet effort technique, nous avons développé un ensemble de scripts Python pour déterminer automatiquement l'évolution du module tangent macroscopique en utilisant trois techniques basées sur la méthode des éléments finis (MEF). C'est l'objectif principal de la présente section, où les concepts théoriques derrière les trois techniques sont brièvement passés en revue et les implémentations pratiques de ces techniques en relation avec le code EF ABAQUS / Standard sont discutées.

1.3.1. Technique de perturbation

1.3.1.1. Concept numérique

Le module tangent macroscopique, noté $\mathbf{C}^{(PK1)}$, relie le taux du gradient de transformation macroscopique $\dot{\mathbf{F}}$ au taux du premier tenseur de contraintes de Piola–Kirchhoff macroscopique $\dot{\mathbf{P}}$. On peut donc déduire $\mathbf{C}^{(PK1)}$ par différentiation du premier tenseur de contraintes de Piola–Kirchhoff par rapport au gradient de transformation :

$$\dot{\mathbf{P}} = \mathbf{C}^{(PK1)} : \dot{\mathbf{F}} \Leftrightarrow \Delta \mathbf{P} \approx \mathbf{C}^{(PK1)} : \Delta \mathbf{F}, \quad (1.16)$$

où $\Delta \bullet$ est une petite perturbation appliquée au champ \bullet .

En appliquant la technique de perturbation, chaque colonne de $\mathbf{C}^{(PK1)}$ est construite numériquement en perturbant les composantes du gradient de transformation macroscopique \mathbf{F} et en utilisant la réponse perturbée associée :

$$\forall i, j, k, l = 1, 2, 3: \quad C_{ijkl}^{(PK1)} \approx \frac{\Delta P_{ij}^{(\alpha)}}{\Delta F_{kl}^{(\alpha)}} \approx \frac{P_{ij}(\mathbf{F}_{kl}^{(\alpha)}) - P_{ij}(\mathbf{F})}{\alpha} \quad \text{avec} \quad \mathbf{F}_{kl}^{(\alpha)} = \mathbf{F} + \Delta \mathbf{F}_{kl}^{(\alpha)} = \mathbf{F} + \alpha \vec{\mathbf{e}}_k \otimes \vec{\mathbf{e}}_l, \quad (1.17)$$

où $\vec{\mathbf{e}}_k$ et $\vec{\mathbf{e}}_l$ sont respectivement le k -ème et le l -ème vecteur unitaire, et α est l'amplitude de la perturbation (comprise généralement entre 10^{-6} et 10^{-8}). Pour illustrer ce concept, la forme matricielle de l'équation (1.17) correspondant au tenseur de perturbation $\Delta \mathbf{F}_{11}^{(\alpha)} = \alpha \vec{\mathbf{e}}_1 \otimes \vec{\mathbf{e}}_1$ peut s'écrire sous la forme suivante :

$$\begin{bmatrix} C_{1111}^{(PK1)} & C_{1122}^{(PK1)} & C_{1133}^{(PK1)} & C_{1112}^{(PK1)} & C_{1123}^{(PK1)} & C_{1113}^{(PK1)} & C_{1121}^{(PK1)} & C_{1132}^{(PK1)} & C_{1131}^{(PK1)} \\ C_{2211}^{(PK1)} & C_{2222}^{(PK1)} & C_{2233}^{(PK1)} & C_{2212}^{(PK1)} & C_{2223}^{(PK1)} & C_{2213}^{(PK1)} & C_{2221}^{(PK1)} & C_{2232}^{(PK1)} & C_{2232}^{(PK1)} \\ C_{3311}^{(PK1)} & C_{3322}^{(PK1)} & C_{3333}^{(PK1)} & C_{3312}^{(PK1)} & C_{3323}^{(PK1)} & C_{3313}^{(PK1)} & C_{3321}^{(PK1)} & C_{3332}^{(PK1)} & C_{3331}^{(PK1)} \\ C_{1211}^{(PK1)} & C_{1222}^{(PK1)} & C_{1233}^{(PK1)} & C_{1212}^{(PK1)} & C_{1223}^{(PK1)} & C_{1213}^{(PK1)} & C_{1221}^{(PK1)} & C_{1232}^{(PK1)} & C_{1231}^{(PK1)} \\ C_{2311}^{(PK1)} & C_{2322}^{(PK1)} & C_{2333}^{(PK1)} & C_{2312}^{(PK1)} & C_{2323}^{(PK1)} & C_{2313}^{(PK1)} & C_{2321}^{(PK1)} & C_{2332}^{(PK1)} & C_{2331}^{(PK1)} \\ C_{1311}^{(PK1)} & C_{1322}^{(PK1)} & C_{1333}^{(PK1)} & C_{1312}^{(PK1)} & C_{1323}^{(PK1)} & C_{1313}^{(PK1)} & C_{1321}^{(PK1)} & C_{1332}^{(PK1)} & C_{1331}^{(PK1)} \\ C_{2111}^{(PK1)} & C_{2122}^{(PK1)} & C_{2133}^{(PK1)} & C_{2112}^{(PK1)} & C_{2123}^{(PK1)} & C_{2113}^{(PK1)} & C_{2121}^{(PK1)} & C_{2132}^{(PK1)} & C_{2131}^{(PK1)} \\ C_{3211}^{(PK1)} & C_{3222}^{(PK1)} & C_{3233}^{(PK1)} & C_{3212}^{(PK1)} & C_{3223}^{(PK1)} & C_{3213}^{(PK1)} & C_{3221}^{(PK1)} & C_{3232}^{(PK1)} & C_{3231}^{(PK1)} \end{bmatrix} \begin{Bmatrix} \alpha \\ 0 \\ 0 \\ 0 \\ 0 \\ 0 \\ 0 \\ 0 \end{Bmatrix} = \begin{Bmatrix} \Delta P_{11}^{(\alpha)} \\ \Delta P_{22}^{(\alpha)} \\ \Delta P_{33}^{(\alpha)} \\ \Delta P_{12}^{(\alpha)} \\ \Delta P_{23}^{(\alpha)} \\ \Delta P_{13}^{(\alpha)} \\ \Delta P_{21}^{(\alpha)} \\ \Delta P_{32}^{(\alpha)} \\ \Delta P_{31}^{(\alpha)} \end{Bmatrix}. \quad (1.18)$$

Ainsi, la première colonne du module $\mathbf{C}^{(PK1)}$ est calculée par l'expression :

$$\forall i, j = 1, 2, 3: \quad C_{ij11}^{(PK1)} \approx \frac{P_{ij}(\mathbf{F}_{11}^{(\alpha)}) - P_{ij}(\mathbf{F})}{\alpha}. \quad (1.19)$$

Les huit autres colonnes sont obtenues de la même manière que la première colonne.

1.3.1.2. Implantation pratique

Pour déterminer le module tangent macroscopique $\mathbf{C}^{(PK1)}$ par la technique de perturbation, dix étapes de calcul EF sont nécessaires : une étape générale de calcul pour déterminer le tenseur non perturbé $\mathbf{P}(\mathbf{F})$, suivie de neuf étapes pour calculer les tenseurs perturbés $\mathbf{P}(\mathbf{F}_{kl}^{(\alpha)})$ pour $k, l = 1, 2, 3$. Les étapes de perturbation sont réalisées en utilisant l'option de redémarrage (communément connue sous le nom 'Restart') d'ABAQUS / Standard. Dans l'étape générale de calcul, il est nécessaire de spécifier les fichiers de redémarrage ('Restart') demandés dans le fichier d'entrée ('input') de l'étape générale. Dans ABAQUS / Standard, ces fichiers incluent les fichiers de redémarrage (.res), de base de données d'analyse (.mdl et .stt), de pièce (.prt), de base de données de sortie (.odb) et de base de données de sous-structure (.sim). Par conséquent, à chaque instant de redémarrage spécifique, les neuf étapes de perturbation relanceront l'analyse avec le gradient de transformation macroscopique perturbé. Il

convient de noter que l'étape générale de calcul peut être linéaire ou non-linéaire, modélisée via un modèle de comportement standard intégré dans Abaqus ou via une routine matériau utilisateur (UMAT). Quant aux étapes de calcul des perturbations, elles sont effectuées en utilisant l'option d'analyse de perturbation statique linéaire d'ABAQUS/Standard. Les étapes algorithmiques de la technique de perturbation sont illustrées par la Fig. 1.2.

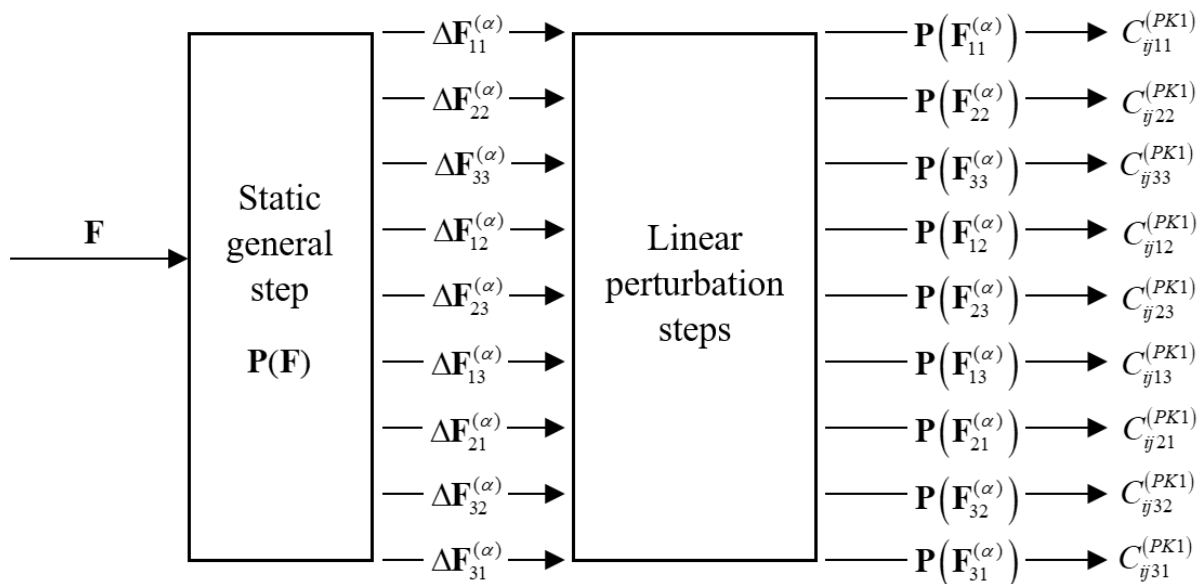


Fig. 1.2. Étapes algorithmiques de base de la technique de perturbation.

1.3.2. Technique de condensation

1.3.2.1. Concept numérique

Cette technique est basée sur une procédure de condensation de la matrice de rigidité globale \mathbf{K} calculée par la MEF. Nous avons constaté que lorsque des modèles de comportement standards existants dans ABAQUS (pas ceux utilisant une UMAT) sont utilisés pour intégrer le comportement microscopique, la partie matérielle de la matrice de rigidité \mathbf{K}_M est construite à partir du module tangente élastique. Dans ce cas, et même si le comportement est inélastique, la technique de condensation ne permet d'obtenir que le module tangent macroscopique élastique (donc la partie inélastique du comportement n'est pas prise en compte). Pour éviter ce problème, une subroutine UMAT doit être utilisée pour implanter les équations constitutives à l'échelle microscopique.

Pour appliquer la technique de condensation, les nœuds du maillage de la cellule de base doivent être partitionnés en deux ensembles : l'ensemble \mathcal{A} composé des nœuds situés à l'intérieur strictement de la cellule de base et l'ensemble \mathcal{B} composé des nœuds situés à la surface (ou sur la frontière) de la même cellule. Notons par N_A et N_B les nombres de nœuds des ensembles \mathcal{A} et \mathcal{B} , respectivement.

En se basant sur cette décomposition, introduisons les trois matrices topologiques $\mathbb{D}_q \in \mathcal{R}^9 \times \mathcal{R}^3$, $\mathbb{Q}_q \in \mathcal{R}^9 \times \mathcal{R}^3$ et $\mathbb{H}_q \in \mathcal{R}^3 \times \mathcal{R}^{3N_B}$ qui seront définies dans les développements qui vont suivre. Ces

matrices sont introduites afin de simplifier le traitement algorithmique et la mise en œuvre de la technique de condensation. La matrice topologique \mathbb{D}_q , associée au nœud q qui appartient à la frontière de la cellule de base, est définie par les composantes x_{q01} , x_{q02} et x_{q03} du vecteur de coordonnées initiales du nœud q :

$$\forall q = 1, \dots, N_B : \quad \mathbb{D}_q = \begin{bmatrix} x_{q01} & 0 & 0 \\ 0 & x_{q02} & 0 \\ 0 & 0 & x_{q03} \\ x_{q02} & 0 & 0 \\ 0 & x_{q03} & 0 \\ x_{q03} & 0 & 0 \\ 0 & x_{q01} & 0 \\ 0 & 0 & x_{q02} \\ 0 & 0 & x_{q01} \end{bmatrix}. \quad (1.20)$$

La matrice \mathbb{D}_q est introduite afin d'exprimer l'équation (1.13) sous une forme matricielle plus adaptée à la mise en œuvre algorithmique :

$$\forall q = 1, \dots, N_p : \quad \mathbf{x}_{q^+} - \mathbf{x}_{q^-} = (\mathbb{D}_{q^+}^T - \mathbb{D}_{q^-}^T) \cdot \mathbf{F} := \mathbb{Q}_q^T \cdot \mathbf{F}, \quad (1.21)$$

avec N_p le nombre total de paires de nœuds.

Quant à la matrice \mathbb{H}_q , elle est conçue pour relier le vecteur de coordonnées courantes des nœuds sur la frontière de la cellule de base \mathbf{x}_b au vecteur de coordonnées courantes $\mathbf{x}_q = \mathbf{x}_{q^+} - \mathbf{x}_{q^-}$ de la paire de nœuds q :

$$\forall q = 1, \dots, N_p : \quad \mathbf{x}_q = \mathbb{H}_q \cdot \mathbf{x}_b. \quad (1.22)$$

De toute évidence, les composantes de la matrice \mathbb{H}_q prennent l'une des valeurs suivantes : 0, -1 ou 1.

En utilisant les matrices \mathbb{H}_q et \mathbb{Q}_q , l'équation (1.21) peut être ré-exprimée sous une forme plus compacte :

$$\forall q = 1, \dots, N_p : \quad \mathbb{H}_q \cdot \mathbf{x}_b = \mathbb{Q}_q^T \cdot \mathbf{F}. \quad (1.23)$$

Ainsi, toutes les conditions de périodicité appliquées sur la cellule de base peuvent être assemblées sous la forme matricielle globale :

$$\mathbb{H} \cdot \mathbf{x}_b = \mathbb{Q}^T \cdot \mathbf{F}, \quad (1.24)$$

où les matrices globales \mathbb{H} et \mathbb{Q} sont construites par concaténation de leurs homologues nodaux \mathbb{H}_q et \mathbb{Q}_q ($1 \leq q \leq N_p$) :

$$\mathbb{H} := \begin{bmatrix} \mathbb{H}_1 \\ \vdots \\ \mathbb{H}_q \\ \vdots \\ \mathbb{H}_{N_p} \end{bmatrix}; \quad \mathbb{Q}^T := \begin{bmatrix} \mathbb{Q}_1^T \\ \vdots \\ \mathbb{Q}_q^T \\ \vdots \\ \mathbb{Q}_{N_p}^T \end{bmatrix}. \quad (1.25)$$

D'autre part, suite à la partition de l'ensemble des noeuds en sous-ensembles \mathcal{A} et \mathcal{B} , la forme matricielle faible du principe des travaux virtuels peut être reformulée (après permutation des lignes et des colonnes de la matrice de rigidité globale \mathbf{K} et des composantes correspondantes des vecteurs de vitesses et de réactions nodales $\dot{\mathbf{q}}$ et $\dot{\mathbf{r}}$) sous la forme :

$$\begin{bmatrix} \mathbf{K}_{\mathcal{A}\mathcal{A}} & \mathbf{K}_{\mathcal{A}\mathcal{B}} \\ \mathbf{K}_{\mathcal{B}\mathcal{A}} & \mathbf{K}_{\mathcal{B}\mathcal{B}} \end{bmatrix} \cdot \begin{bmatrix} \dot{\mathbf{q}}_{\mathcal{A}} \\ \dot{\mathbf{q}}_{\mathcal{B}} \end{bmatrix} = \begin{bmatrix} \dot{\mathbf{r}}_{\mathcal{A}} \\ \dot{\mathbf{r}}_{\mathcal{B}} \end{bmatrix}. \quad (1.26)$$

Tenant compte de l'équation d'équilibre microscopique (1.6), le vecteur $\dot{\mathbf{r}}_{\mathcal{A}}$ s'annule à la convergence des calculs EF. Par conséquent, à l'équilibre, l'équation (1.26) devient :

$$\begin{bmatrix} \mathbf{K}_{\mathcal{A}\mathcal{A}} & \mathbf{K}_{\mathcal{A}\mathcal{B}} \\ \mathbf{K}_{\mathcal{B}\mathcal{A}} & \mathbf{K}_{\mathcal{B}\mathcal{B}} \end{bmatrix} \cdot \begin{bmatrix} \dot{\mathbf{q}}_{\mathcal{A}} \\ \dot{\mathbf{q}}_{\mathcal{B}} \end{bmatrix} = \begin{bmatrix} \mathbf{0} \\ \dot{\mathbf{r}}_{\mathcal{B}} \end{bmatrix}. \quad (1.27)$$

L'élimination du vecteur $\dot{\mathbf{q}}_{\mathcal{A}}$ de l'équation (1.27) permet de déduire la matrice de rigidité condensée (ou réduite) $\tilde{\mathbf{K}}_{\mathcal{B}\mathcal{B}}$ reliant $\dot{\mathbf{q}}_{\mathcal{B}}$ à $\dot{\mathbf{r}}_{\mathcal{B}}$:

$$\tilde{\mathbf{K}}_{\mathcal{B}\mathcal{B}} \cdot \dot{\mathbf{q}}_{\mathcal{B}} = \dot{\mathbf{r}}_{\mathcal{B}} \quad \text{avec} \quad \tilde{\mathbf{K}}_{\mathcal{B}\mathcal{B}} = \mathbf{K}_{\mathcal{B}\mathcal{B}} - \mathbf{K}_{\mathcal{B}\mathcal{A}} \cdot \mathbf{K}_{\mathcal{A}\mathcal{A}}^{-1} \cdot \mathbf{K}_{\mathcal{A}\mathcal{B}}. \quad (1.28)$$

À la convergence du calcul incrémental, le module tangent macroscopique $\mathbf{C}^{(PK1)}$ est déterminé en termes des matrices $\tilde{\mathbf{K}}_{\mathcal{B}\mathcal{B}}$, \mathbb{H} et \mathbb{Q} comme (Miehe, 2003 ; Geers et al., 2017) :

$$\mathbf{C}^{(PK1)} = \frac{1}{|\mathcal{V}_0|} \mathbb{Q} \cdot \left[\mathbb{H} \cdot \tilde{\mathbf{K}}_{\mathcal{B}\mathcal{B}}^{-1} \cdot \mathbb{H}^T \right]^{-1} \cdot \mathbb{Q}^T. \quad (1.29)$$

Tenant compte de l'expression (1.28) de $\tilde{\mathbf{K}}_{\mathcal{B}\mathcal{B}}$, le module tangent macroscopique $\mathbf{C}^{(PK1)}$ peut être exprimé sous la forme :

$$\mathbf{C}^{(PK1)} = \frac{1}{|\mathcal{V}_0|} \mathbb{Q} \cdot \left[\mathbb{H} \cdot \left(\mathbf{K}_{\mathcal{B}\mathcal{B}} - \mathbf{K}_{\mathcal{B}\mathcal{A}} \cdot \mathbf{K}_{\mathcal{A}\mathcal{A}}^{-1} \cdot \mathbf{K}_{\mathcal{A}\mathcal{B}} \right)^{-1} \cdot \mathbb{H}^T \right]^{-1} \cdot \mathbb{Q}^T. \quad (1.30)$$

Pour être concis, seul le résultat final de la technique de condensation est fourni par l'équation (1.30). Les lecteurs intéressés peuvent se référer aux références Miehe (2003) et Geers et al. (2017) pour plus de détails sur la façon dont l'équation (1.30) est obtenue.

1.3.2.2. Implantation pratique

Comme présenté dans la Section 1.3.2.1, le module tangent macroscopique $\mathbf{C}^{(PK1)}$ est obtenu par une procédure de condensation de la matrice de rigidité globale \mathbf{K} , qui est assemblée à partir des matrices

de rigidité élémentaires \mathbf{K}_{el} . Après avoir réalisé le calcul par éléments finis, les matrices de rigidités élémentaires seront stockées dans un fichier externe portant l'extension '.mtx'. Ce fichier représente l'entrée des codes Python que nous avons développés pour assembler et gérer la matrice de rigidité globale \mathbf{K} . Rappelons que tous les nœuds du maillage de la cellule de base sont regroupés dans deux ensembles \mathcal{A} et \mathcal{B} . Par conséquent, un nœud q fait partie de l'ensemble \mathcal{B} si au moins une des conditions suivantes est remplie :

$$x_{q01} = -\lambda_0 / 2 \text{ ou } \lambda_0 / 2 ; \quad x_{q02} = -\lambda_0 / 2 \text{ ou } \lambda_0 / 2 ; \quad x_{q03} = -\lambda_0 / 2 \text{ ou } \lambda_0 / 2, \quad (1.31)$$

sinon, ce nœud appartient à l'ensemble \mathcal{A} .

Afin de construire les matrices topologiques \mathbb{Q} et \mathbb{H} , l'ensemble des paires de nœuds ainsi que les coordonnées initiales correspondantes doivent être identifiés. Comme illustré par la Fig. 1.3, les nœuds i et j constituent une paire de nœuds dans la direction Z.

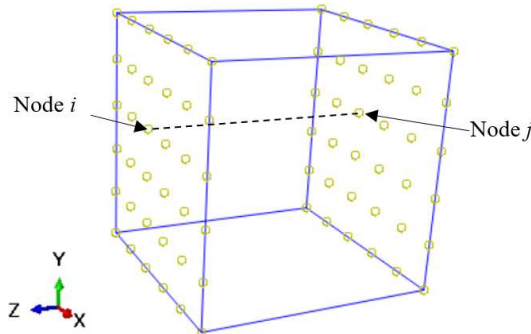


Fig. 1.3. Paires de nœuds dans la direction Z.

Pour identifier toutes les paires de nœuds appartenant à l'ensemble \mathcal{B} , l'algorithme suivant est développé et implanté dans une subroutine Python :

Les nœuds i et j forment une paire de nœuds dans la direction X, si :

$$x_{i01} - x_{j01} = \pm \lambda_0 \text{ et } x_{i02} = x_{j02} \text{ et } x_{i03} = x_{j03}.$$

Les nœuds i et j forment une paire de nœuds dans la direction Y, si :

$$x_{i02} - x_{j02} = \pm \lambda_0 \text{ et } x_{i01} = x_{j01} \text{ et } x_{i03} = x_{j03}.$$

Les nœuds i et j forment une paire de nœuds dans la direction Z, si :

$$x_{i03} - x_{j03} = \pm \lambda_0 \text{ et } x_{i01} = x_{j01} \text{ et } x_{i02} = x_{j02}.$$

Les composantes de la matrice $\mathbb{H} \in \mathcal{R}^{3N_p} \times \mathcal{R}^{3N_B}$ sont égales à l'une des trois valeurs suivantes : 0, $-\lambda_0$ ou 1. Une fois toutes les paires de nœuds détectées, ces composantes peuvent être déterminées selon l'algorithme :

Si les nœuds i et j forment une paire de nœuds (avec $i < j$), la distribution des valeurs 1 et $-\lambda_0$ dans la matrice \mathbb{H} peut être résumée comme :

$$\begin{aligned}\mathbb{H}_{3i-2,3j-2} &= 1 \quad ; \quad \mathbb{H}_{3i-2,3j-2} = -1, \\ \mathbb{H}_{3i-1,3j-1} &= 1 \quad ; \quad \mathbb{H}_{3i-1,3j-1} = -1, \\ \mathbb{H}_{3i,3j} &= 1 \quad ; \quad \mathbb{H}_{3i,3j} = -1.\end{aligned}\tag{1.32}$$

Les autres composantes de la matrice \mathbb{H} , non définies par l'équation (1.32), sont naturellement nulles.

La matrice $\mathbb{D} \in \mathcal{R}^9 \times \mathcal{R}^{3N_B}$ est assemblée à partir des matrices $\mathbb{D}_q \in \mathcal{R}^9 \times \mathcal{R}^3$, définies par l'équation (1.20), comme :

$$\mathbb{D} = \begin{bmatrix} & \mathbb{D}_i & & \mathbb{D}_j & & \\ \cdots & x_{i01} & 0 & 0 & \cdots & x_{j01} & 0 & 0 & \cdots \\ \cdots & 0 & x_{i02} & 0 & \cdots & 0 & x_{j02} & 0 & \cdots \\ \cdots & 0 & 0 & x_{i03} & \cdots & 0 & 0 & x_{i03} & \cdots \\ \cdots & x_{i02} & 0 & 0 & \cdots & x_{j02} & 0 & 0 & \cdots \\ \cdots & 0 & x_{i03} & 0 & \cdots & 0 & x_{j03} & 0 & \cdots \\ \cdots & x_{i03} & 0 & 0 & \cdots & x_{j03} & 0 & 0 & \cdots \\ \cdots & 0 & x_{i01} & 0 & \cdots & 0 & x_{j01} & 0 & \cdots \\ \cdots & 0 & 0 & x_{i02} & \cdots & 0 & 0 & x_{j02} & \cdots \\ \cdots & 0 & 0 & x_{i01} & \cdots & 0 & 0 & x_{j01} & \cdots \end{bmatrix}.\tag{1.33}$$

Une fois la matrice \mathbb{D} construite, la matrice \mathbb{Q} peut être déterminée par la multiplication matricielle suivante :

$$\mathbb{Q} = \mathbb{D} \cdot \mathbb{H}^T.\tag{1.34}$$

En utilisant les labels (numéros) des nœuds appartenant aux ensembles \mathcal{A} et \mathcal{B} , on peut facilement extraire les quatre sous-matrices $\mathbf{K}_{\mathcal{A}\mathcal{A}}$, $\mathbf{K}_{\mathcal{A}\mathcal{B}}$, $\mathbf{K}_{\mathcal{B}\mathcal{A}}$ et $\mathbf{K}_{\mathcal{B}\mathcal{B}}$ de la matrice de rigidité globale \mathbf{K} , comme indiqué par l'équation (1.26), et ensuite déterminer le module tangent macroscopique $\mathbf{C}^{(PK1)}$ par l'équation (1.30).

1.3.3. Technique de fluctuation

1.3.3.1. Concept numérique

Compte tenu des équations (1.9) et (1.10), la condition suivante doit être remplie à la convergence du calcul itératif par éléments finis :

$$G := \int_{\mathcal{V}_0} \left[\frac{\partial \delta \mathbf{v}_{per}}{\partial \mathbf{x}_0} : \hat{\mathbf{p}} \right] d\mathcal{V}_0 = 0.\tag{1.35}$$

La linéarisation de l'équation (1.35), classiquement adoptée dans les calculs par éléments finis, conduit à :

$$G + \mathcal{D}G = 0,\tag{1.36}$$

où $\mathcal{D}\bullet$ est l'itération du champ \bullet (au sens des éléments finis). Les termes d'ordre supérieur sont négligés dans la forme linéarisée (1.36). Cette forme linéarisée nécessite que $G \rightarrow 0$ et $\mathcal{D}G \rightarrow 0$ à la convergence du calcul par éléments finis. Par conséquent, la forme itérative suivante peut être déduite de l'équation (1.35) :

$$\mathcal{D}G = \int_{\mathcal{V}_0} \left[\frac{\partial \delta \mathbf{v}_{per}}{\partial \mathbf{x}_0} : \mathbf{c}^{(PK1)} : \left(\mathcal{D}\dot{\mathbf{F}} + \mathcal{D} \frac{\partial \mathbf{v}_{per}}{\partial \mathbf{x}_0} \right) \right] d\mathcal{V}_0 = 0. \quad (1.37)$$

Après discréétisation par éléments finis, la vitesse périodique \mathbf{v}_{per} peut être obtenue par interpolation du vecteur des vitesses périodiques nodales $\dot{\mathbf{q}}_{per}$:

$$\mathbf{v}_{per} = \mathbf{N} \cdot \dot{\mathbf{q}}_{per}, \quad (1.38)$$

où \mathbf{N} est la fonction de forme correspondante.

La substitution de l'équation (1.38) dans (1.37) conduit au système algébrique linéaire :

$$\mathbf{K} \cdot \mathcal{D}\dot{\mathbf{q}}_{per} = -\hat{\mathbf{K}} \cdot \mathcal{D}\dot{\mathbf{F}}, \quad (1.39)$$

où la matrice de rigidité globale \mathbf{K} et la matrice de fluctuation $\hat{\mathbf{K}}$ sont définies comme :

$$\mathbf{K} = \bigcup_{el=1}^n \int_{\mathcal{V}_0^{el}} \mathbf{B}^T \cdot \mathbf{c}^{(PK1)} \cdot \mathbf{B} d\mathcal{V}_0^{el} ; \quad \hat{\mathbf{K}} = \bigcup_{el=1}^n \int_{\mathcal{V}_0^{el}} \mathbf{B}^T \cdot \mathbf{c}^{(PK1)} d\mathcal{V}_0^{el}, \quad (1.40)$$

où $\bigcup_{el=1}^n$ désigne l'opérateur d'assemblage classiquement utilisé dans la méthode des éléments finis.

Le vecteur $\mathcal{D}\dot{\mathbf{q}}_{per}$ peut être obtenu par la résolution de l'équation linéarisée (1.39) :

$$\mathcal{D}\dot{\mathbf{q}}_{per} = -\mathbf{K}^{-1} \cdot \hat{\mathbf{K}} \cdot \mathcal{D}\dot{\mathbf{F}}, \quad (1.41)$$

puis l'itération $\mathcal{D}\dot{\mathbf{f}}_{per}$ peut être déterminée à partir de l'équation (1.41) :

$$\mathcal{D}\dot{\mathbf{f}}_{per} = \mathbf{B} \cdot \mathcal{D}\dot{\mathbf{q}}_{per} = -\mathbf{B} \cdot \mathbf{K}^{-1} \cdot \hat{\mathbf{K}} \cdot \mathcal{D}\dot{\mathbf{F}}. \quad (1.42)$$

D'un autre côté, nous disposons de la relation suivante :

$$\mathcal{D}\dot{\mathbf{P}} = \frac{1}{|\mathcal{V}_0|} \int_{\mathcal{V}_0} \mathcal{D}\dot{\mathbf{p}} d\mathcal{V}_0 = \frac{1}{|\mathcal{V}_0|} \int_{\mathcal{V}_0} \mathbf{c}^{(PK1)} : (\mathcal{D}\dot{\mathbf{F}} + \mathcal{D}\dot{\mathbf{f}}_{per}) d\mathcal{V}_0. \quad (1.43)$$

La combinaison des équations (1.42) et (1.43) permet d'exprimer $\mathcal{D}\dot{\mathbf{P}}$ sous la forme :

$$\mathcal{D}\dot{\mathbf{P}} = \frac{1}{|\mathcal{V}_0|} \int_{\mathcal{V}_0} \mathcal{D}\dot{\mathbf{p}} d\mathcal{V}_0 = \frac{1}{|\mathcal{V}_0|} \int_{\mathcal{V}_0} \mathbf{c}^{(PK1)} : (\mathcal{D}\dot{\mathbf{F}} - \mathbf{B} \cdot \mathbf{K}^{-1} \cdot \hat{\mathbf{K}} \cdot \mathcal{D}\dot{\mathbf{F}}) d\mathcal{V}_0. \quad (1.44)$$

L'itération $\mathcal{D}\dot{\mathbf{F}}$ étant homogène sur le volume initial \mathcal{V}_0 de la cellule de base ; par conséquent, l'équation (1.44) peut être reformulée comme :

$$\mathcal{D}\dot{\mathbf{P}} = \frac{1}{|\mathcal{V}_0|} \int_{\mathcal{V}_0} \mathcal{D}\dot{\mathbf{p}} d\mathcal{V}_0 = \frac{1}{|\mathcal{V}_0|} \left(\int_{\mathcal{V}_0} \mathbf{c}^{(PK1)} d\mathcal{V}_0 - \hat{\mathbf{K}}^T \cdot \mathbf{K}^{-1} \cdot \hat{\mathbf{K}} \right) : \mathcal{D}\dot{\mathbf{F}}. \quad (1.45)$$

En comparant les équations (1.16) et (1.45), on peut facilement déduire que :

$$\mathbf{C}^{(PK1)} = \frac{1}{|\mathcal{V}_0|} \left(\int_{\mathcal{V}_0} \mathbf{c}^{(PK1)} d\mathcal{V}_0 - \hat{\mathbf{K}}^T \cdot \mathbf{K}^{-1} \cdot \hat{\mathbf{K}} \right). \quad (1.46)$$

1.3.3.2. Implantation pratique

Comme indiqué par l'équation (1.46), le module tangent macroscopique $\mathbf{C}^{(PK1)}$ se compose de deux parties principales : la moyenne volumique des modules microscopiques $\mathbf{c}^{(PK1)}$ et une partie fluctuante dépendant de la matrice de rigidité globale \mathbf{K} et d'une matrice de fluctuation globale $\hat{\mathbf{K}}$. Les matrices globales \mathbf{K} et $\hat{\mathbf{K}}$ sont obtenues à partir de leurs homologues élémentaires \mathbf{K}_{el} et $\hat{\mathbf{K}}_{el}$ par la procédure d'assemblage décrite par l'équation (1.40). Les matrices élémentaires \mathbf{K}_{el} et $\hat{\mathbf{K}}_{el}$ dépendent de $\mathbf{c}^{(PK1)}$. Ainsi, pour assurer le calcul précis du module tangent macroscopique, les modules tangents microscopiques doivent être correctement définis et implantés. En plus, pour déterminer les différents ingrédients requis pour le calcul par la technique de fluctuation, une subroutine d'élément utilisateur (UEL) doit être utilisée. Pour réaliser cette tâche, nous avons utilisé l'UEL développée par [Salahouelhadj et al. \(2012\)](#), après quelques modifications et améliorations. En effet, le principe des travaux virtuels a été légèrement modifié pour considérer la dérivée de Jaumann des contraintes de Kirchhoff au lieu de la dérivée de Truesdell utilisée dans la version initiale. Après ces modifications, la matrice de rigidité élémentaire \mathbf{K}_{el} a été correctement calculée dans l'UEL en ajoutant la contribution des non-linéarités géométriques $\mathbf{K}_{GNL el}$ à la contribution due au comportement du matériau $\mathbf{K}_{M el}$. Quant au tenseur $\mathbf{c}^{(PK1)}$ associé à chaque point d'intégration, il est déterminé à partir de la matrice jacobienne **DDSDDE** (une sortie de l'UMAT correspondante). Une fois les matrices calculées pour tous les points d'intégration de l'élément, la contribution élémentaire à la moyenne volumique des modules microscopiques $\int_{\mathcal{V}_0^{el}} \mathbf{c}^{(PK1)} d\mathcal{V}_0^{el}$ peut être déterminée par une opération d'intégration simple, et la matrice de rigidité élémentaire \mathbf{K}_{el} ainsi que la matrice de fluctuation $\hat{\mathbf{K}}_{el}$ peuvent être déduites par les relations suivantes :

$$\mathbf{K}_{el} = \int_{\mathcal{V}_0^{el}} \mathbf{B}^T \cdot \mathbf{c}^{(PK1)} \cdot \mathbf{B} d\mathcal{V}_0^{el} \quad ; \quad \hat{\mathbf{K}}_{el} = \int_{\mathcal{V}_0^{el}} \mathbf{B}^T \cdot \mathbf{c}^{(PK1)} d\mathcal{V}_0^{el}. \quad (1.47)$$

Les différentes contributions élémentaires doivent être éditées et stockées dans des fichiers séparés.

1.4. Validation de l'implantation des trois techniques

1.4.1. Validation basique

Pour valider l'implantation des trois techniques (à savoir TC, TF et TP), les prédictions numériques obtenues par ces techniques sont comparées à celles publiées dans [Miehe et al. \(2002b\)](#). Pour cela, une microstructure composite plane est considérée (largeur/longueur = 1/1). Cette microstructure est

constituée d'une matrice souple renforcée par une inclusion rigide. Le comportement de chaque phase est supposé élastique, linéaire et isotrope avec les paramètres d'élasticité suivants :

- Matrice : $E_m = 2081.06 \text{ MPa}$; $\nu_m = 0.3007$.
- Inclusion : $E_i = 10 E_m$; $\nu_i = \nu_m$.

L'inclusion a la forme d'une fibre cylindrique centrée dans la matrice et sa fraction volumique est égale à 12,56% (Fig. 1.4). La cellule de base est discrétisée par 700 éléments finis. Pour calculer le module tangent macroscopique par les différentes techniques, un chargement biaxial, le même que celui défini dans [Miehe et al. \(2002b\)](#), a été appliqué à la cellule de base. Dans ce cas, nous rapportons et comparons les composantes planes de $\mathbf{C}^{(PK1)}$ stockées dans la matrice \mathbf{Z} :

$$\mathbf{Z} = \begin{bmatrix} C_{1111}^{(PK1)} & C_{1122}^{(PK1)} & 0 \\ C_{2211}^{(PK1)} & C_{2222}^{(PK1)} & 0 \\ 0 & 0 & C_{1212}^{(PK1)} \end{bmatrix}. \quad (1.48)$$

La différence entre les résultats de [Miehe et al. \(2002b\)](#) et nos prédictions obtenues par les trois techniques est quantifiée par un indicateur scalaire m défini comme :

$$m = \|\mathbf{Z}\| / \|\mathbf{Z}^{Ref}\| = \left(\sum_{i=1}^3 \sum_{j=1}^3 (Z_{ij})^2 \right)^{1/2} / \left(\sum_{i=1}^3 \sum_{j=1}^3 (Z_{ij}^{Ref})^2 \right)^{1/2}, \quad (1.49)$$

où \mathbf{Z}^{Ref} et \mathbf{Z} désignent le module tangent macroscopique déterminé dans [Miehe et al. \(2002b\)](#) et celui calculé par nos prédictions, respectivement.

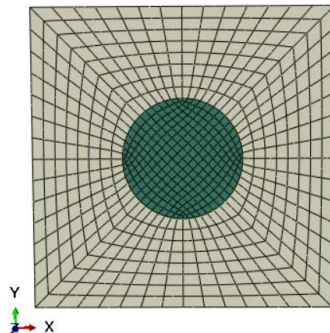


Fig. 1.4. Discrétisation par éléments finis de la cellule de base étudiée.

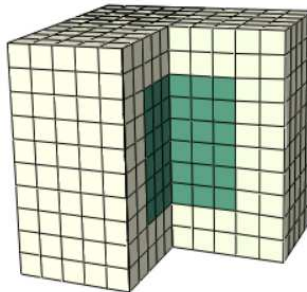
Comme indiqué dans le [Tab. 1.1](#), les résultats obtenus par la TC, TF et TP sont presque identiques et très proches des valeurs de référence. Ces résultats fournissent une première validation de nos implémentations.

Tab. 1.1. Composantes de la matrice \mathbf{Z} relative à la cellule de base étudiée.

Reference (Miehe et al., 2002b)	TC	TF	TP
Z_{11}	3413.1	3400.7	3400.7
Z_{22}	3413.1	3400.8	3400.8
Z_{12}	1415.1	1407.2	1407.2
Z_{33}	960.1	958.8	958.8
m	1.000	0.996	0.996

1.4.2. Validation avancée

Dans la Section 1.4.1, les implantations des trois techniques ont été validées en comparant favorablement nos prédictions aux résultats présentés dans Miehe et al. (2002b). Il ressort de cette étude préliminaire que les trois techniques prédisent avec précision le module tangent macroscopique. Ainsi, la précision et la fiabilité de la mise en œuvre des trois techniques sont partiellement validées. Dans cette section, notre attention sera focalisée sur l'évaluation des performances des trois techniques, en considérant un nouvel exemple : une inclusion cubique centrée dans une matrice cubique. L'inclusion occupe 20% du volume total de la cellule de base (Fig. 1.5). Cette microstructure est discrétisée par 1000 éléments finis 3D.


Fig. 1.5. Microstructure cubique avec une inclusion cubique.

- Le comportement mécanique de la matrice est supposé élastoplastique et il est défini par les paramètres d'élasticité et d'écrouissage suivants :

$$E_m = 210 \text{ GPa} \quad ; \quad \nu_m = 0.3 \quad ; \quad \text{écrouissage isotrope : } \sigma_y = 362.99 \left(0.008 + \varepsilon_{eq}^p \right)^{0.184}.$$

- Le comportement mécanique de l'inclusion est supposé élastique, linéaire et isotrope et il est défini par les paramètres d'élasticité suivants :

$$E_i = 10 E_m \quad ; \quad \nu_i = \nu_m.$$

La cellule de base est soumise au chargement macroscopique suivant :

$$\text{état initial: } \mathbf{F}(0) = \begin{bmatrix} 1 & 0 & 0 \\ 0 & 1 & 0 \\ 0 & 0 & 1 \end{bmatrix} \rightarrow \text{état final: } \mathbf{F}(t_f) = \begin{bmatrix} 1.2 & 0 & 0 \\ 0 & 0.91287 & 0 \\ 0 & 0 & 0.91287 \end{bmatrix}, \quad (1.50)$$

où t_f correspond à la fin de l'histoire du chargement et le gradient de transformation \mathbf{F} est supposé évoluer linéairement entre $\mathbf{F}(0)$ et $\mathbf{F}(t_f)$.

Les évolutions des composantes planes $C_{1111}^{(PKI)}$, $C_{2222}^{(PKI)}$, $C_{1122}^{(PKI)}$ et $C_{1212}^{(PKI)}$ obtenues par la TC, la TF et la TP sont reportées sur la Fig. 1.6. Il apparaît de cette figure que les trois techniques permettent d'obtenir des résultats identiques, apportant ainsi une validation supplémentaire à notre implémentation.

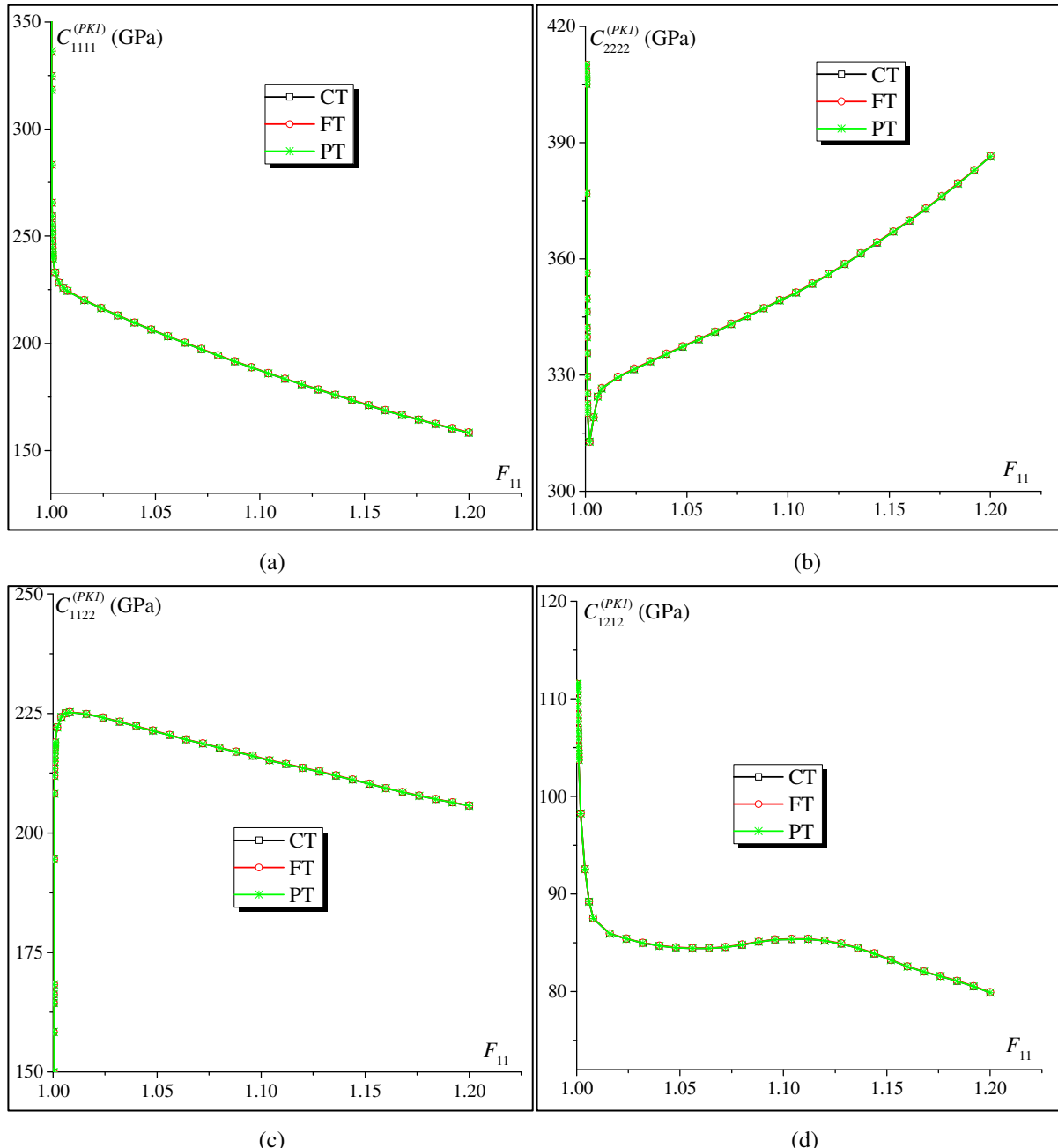


Fig. 1.6. Évolution des composantes planes de $\mathbf{C}^{(PKI)}$ obtenues par la TC, la TF et la TP : (a) $C_{1111}^{(PKI)}$; (b) $C_{2222}^{(PKI)}$; (c) $C_{1122}^{(PKI)}$; (d) $C_{1212}^{(PKI)}$.

Le module tangent macroscopique est évalué à chaque $\Delta t = 0.01t_f$ (voir l'équation (1.50)). Ainsi, $\mathbf{C}^{(PK1)}$ est calculé 100 fois au cours de l'histoire du chargement. Comme le montre le Tab. 1.2, la technique de perturbation consomme plus d'espace disque et de temps CPU que la technique de condensation et celle de fluctuation. Ce résultat est prévisible compte tenu du fait que dix calculs par éléments finis sont nécessaires lorsque la TP est utilisée, contre un seul calcul pour les autres techniques. Malgré le fait que les neuf étapes de calcul par éléments finis nécessaires pour construire numériquement le module tangent global par la TP soient linéaires (donc relativement rapides à exécuter), le temps CPU consommé par les calculs dans ce cas reste relativement élevé. Même s'il n'y a pas beaucoup de différence entre les temps CPU consommés par la TC et la TF, la taille des fichiers externes requis par la TF est presque le double de celle des fichiers requis par la TC. Ce résultat est également prévisible compte tenu de la quantité de données à stocker lorsque la TF est appliquée.

Tab. 1.2. Performance des trois techniques de calcul du module tangent macroscopique en termes d'allocation d'espace disque et temps CPU.

	TC	TF	TP
Fichiers externes (GB)	3.979	7.654	11.087
Temps CPU (Minutes)	82	85.1	111.64

1.5. Conclusions

Dans ce chapitre, trois techniques numériques utilisées pour calculer le module tangent macroscopique par la méthode d'homogénéisation périodique ont été brièvement présentées et mises en œuvre dans ABAQUS / Standard en développant un ensemble de scripts Python. Plusieurs conclusions peuvent être tirées sur la base de l'étude menée pour comparer ces différentes techniques :

- La technique de perturbation peut être mise en œuvre en utilisant uniquement la boîte à outils *Homtools* (pour l'application des conditions aux limites périodiques et le chargement macroscopique) et les scripts Python que nous avons développés. Par conséquent, des sous-programmes ou outils supplémentaires (tels que UMAT ou UEL) ne sont pas indispensables pour le calcul du module tangent par cette technique. Les prédictions numériques révèlent que la TP est la plus coûteuse en termes de temps CPU et de stockage de fichiers externes. Le temps CPU élevé est attribuable à la nécessité d'effectuer dix étapes de calcul par éléments finis (1 étape générale et 9 étapes de perturbation) pour chaque calcul du module tangent.
- Pour implémenter et exécuter la technique de fluctuation, une subroutine UEL doit être utilisée. Cela limite l'utilisation potentielle de cette méthode par la communauté des utilisateurs d'ABAQUS. De plus, même si cette technique ne consomme pas trop de temps CPU, l'espace disque occupé par les fichiers externes générés par cette méthode reste relativement important par rapport au cas de la méthode de condensation.

- Par rapport à ces dernières techniques, la technique de condensation semble être la plus simple à utiliser et permet un gain de temps considérable. Pour utiliser cette technique conjointement à un comportement inélastique, une subroutine utilisateur UMAT doit être utilisée.

Ainsi, ce chapitre fournit de précieuses directives de référence aux utilisateurs d'ABAQUS / Standard pour la détermination des modules tangents homogénéisés de matériaux hétérogènes linéaires ou non-linéaires, tels que des composites, des agrégats polycristallins et des solides poreux. Les techniques et outils développés dans ce chapitre pourraient être utilisés, après quelques adaptations, en relation avec d'autres progiciels EF commerciaux.

Chapitre 2

Prédiction des limites de ductilité de matériaux hétérogènes par la technique d'homogénéisation périodique

2.1. Introduction

Dans ce chapitre, nous utiliserons la technique d'homogénéisation périodique pour déterminer le comportement macroscopique de deux types de matériaux métalliques : des matériaux poreux ([Section 2.2](#)) et des milieux polycristallins ([Section 2.3](#)). Cette technique sera couplée à un ou plusieurs critères de ductilité pour prédire la limite de ductilité de ces structures.

2.2. Prédiction de la limite de ductilité des matériaux poreux

Cette section est dédiée à l'étude de la compétition entre le phénomène de la coalescence de cavités et celui de la localisation des déformations plastiques dans les milieux poreux. Dans ce cas, la perte de ductilité est due à la croissance des cavités primaires et secondaires. Cette section est organisée comme suit :

- La Section [2.2.1](#) détaille l'approche micromécanique mise en place pour modéliser le comportement mécanique de la cellule de base poreuse.
- La Section [2.2.2](#) détaille les conditions aux limites et le chargement macroscopique appliqués à la cellule de base.
- Les critères de localisation et de coalescence adoptés sont décrits dans la Section [2.2.3](#).
- Les résultats numériques de la présente étude sont présentés et discutés dans la Section [2.2.4](#).

- La Section 2.2.5 clôture cette première étude en résumant quelques conclusions.

2.2.1. Modélisation micromécanique du comportement de la cellule de base

Nous considérons un milieu tridimensionnel défini comme un cluster de cellules de base cubiques contenant une cavité primaire en leur centre, comme le montre la Fig. 2.1a. Chaque cellule de base peut être considérée comme un milieu hétérogène composé de deux phases principales : la cavité primaire et la matrice métallique, qui est elle-même supposée être poreuse pour tenir compte du possible effet d'une seconde population de cavités (Fig. 2.1b). La forme initiale de la cavité primaire est supposée sphérique ou ellipsoïdale, tandis que toutes les cavités secondaires sont supposées sphériques. Un repère cartésien ($\vec{e}_1, \vec{e}_2, \vec{e}_3$) est introduit pour définir la position de chaque point de la cellule de base, où les vecteurs \vec{e}_1, \vec{e}_2 et \vec{e}_3 sont normaux aux faces de la cellule dans sa configuration initiale. L'origine de ce système de coordonnées est située au centre de la cellule. Par conséquent, cette cellule occupe initialement le domaine $\mathcal{V}_0 = [-l_0 / 2, l_0 / 2] \times [-l_0 / 2, l_0 / 2] \times [-l_0 / 2, l_0 / 2]$, comme le montre la Fig. 2.1b (avec $l_0 = 1\text{mm}$).

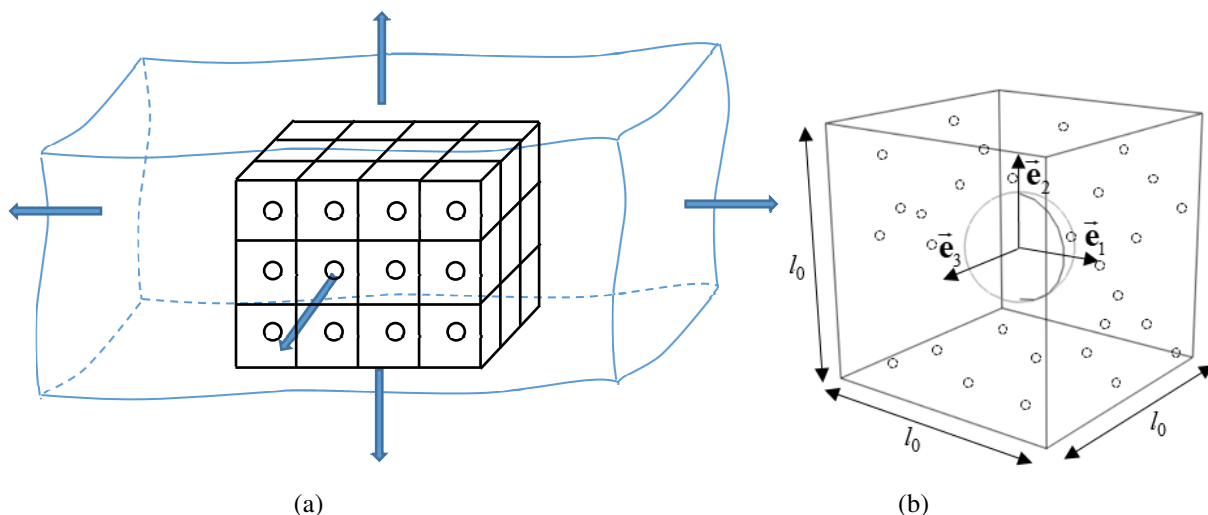


Fig. 2.1. (a) Modèle micromécanique d'un cluster de matériau composé d'un agencement de cellules de base cubiques ; (b) une cellule de base contenant une cavité sphérique entourée d'une matrice poreuse.

Compte tenu de la périodicité de l'arrangement des cavités (Fig. 2.1a), la technique d'homogénéisation périodique semble être le schéma multi-échelles le plus approprié pour déterminer le comportement homogénéisé de la cellule de base (Miehe, 2003 ; Zhu et al., 2020). L'utilisation de cette technique permet de substituer la cellule de base hétérogène par un milieu homogène équivalent ayant les mêmes propriétés mécaniques effectives (Fig. 2.2).

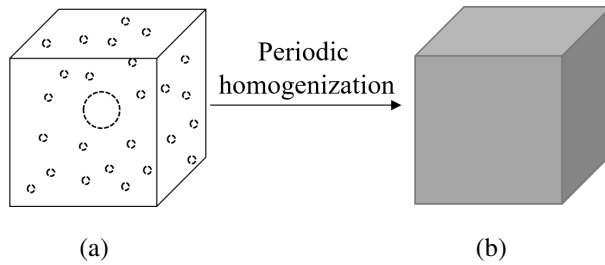


Fig. 2.2. Illustration du concept d'homogénéisation périodique : (a) cellule de base contenant des cavités primaires et secondaires ; (b) milieu homogénéisé équivalent.

Les équations gouvernant le schéma d'homogénéisation périodique sont présentées dans le chapitre précédent et dans la version anglaise de ce manuscrit. Par souci de brièveté, ces équations ne sont pas rappelées ici. De plus amples détails sur les aspects pratiques liés à l'application des conditions de périodicité sur les surfaces extérieures de la cellule de base sont également fournis dans le chapitre précédent.

Pour tenir compte de l'effet d'une seconde population de cavités, le comportement mécanique de la matrice métallique est modélisé par le modèle poreux de Gurson (Gurson, 1977). La même méthodologie peut être appliquée à tout autre cadre constitutif (par exemple, le modèle GTN pour inclure la germination et la coalescence des cavités). Un maillage par éléments finis typique de la cellule de base est présenté sur la Fig. 2.3.

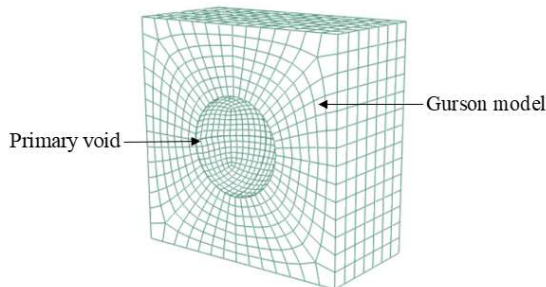


Fig. 2.3. Maillage par éléments finis d'une demi cellule de base.

Les relations constitutives décrivant le comportement mécanique de la matrice métallique peuvent être résumées par la relation générique suivante :

$$\dot{\mathbf{p}} = \mathbf{c}^{(PK1)} : \dot{\mathbf{f}}. \quad (2.1)$$

L'expression du module tangent microscopique $\mathbf{c}^{(PK1)}$ sera déterminée par les développements suivants. Comme point de départ de ces développements, le taux de déformation \mathbf{d} est exprimé comme la partie symétrique du gradient de vitesse microscopique \mathbf{g} :

$$\mathbf{d} = \frac{1}{2} (\mathbf{g} + \mathbf{g}^T). \quad (2.2)$$

Le taux de déformation \mathbf{d} peut être lui-même décomposé en une partie élastique \mathbf{d}^e et une partie plastique \mathbf{d}^p :

$$\mathbf{d} = \mathbf{d}^e + \mathbf{d}^p. \quad (2.3)$$

Pour respecter le principe d'objectivité, le taux de contraintes de Cauchy $\dot{\boldsymbol{\sigma}}$ est relié à \mathbf{d}^e par la loi élastique exprimée dans le repère co-rotationnel :

$$\dot{\boldsymbol{\sigma}} = \mathbf{c}^e : \mathbf{d}^e, \quad (2.4)$$

avec \mathbf{c}^e le tenseur d'élasticité d'ordre 4.

Le taux de déformation plastique \mathbf{d}^p est déterminé par la règle de normalité :

$$\mathbf{d}^p = \dot{\lambda} \frac{\partial \Phi}{\partial \boldsymbol{\sigma}}, \quad (2.5)$$

où $\dot{\lambda}$ est le multiplicateur plastique et Φ la fonction de charge de Gurson définie comme :

$$\Phi = \left(\frac{\sigma_{eq}}{\sigma_y} \right)^2 + 2f_s \cosh \left(\frac{3\sigma_h}{2\sigma_y} \right) - (1 + f_s^2) \leq 0, \quad (2.6)$$

avec :

- σ_{eq} la contrainte équivalente de von Mises égale à $(3\boldsymbol{\sigma}_{dev} : \boldsymbol{\sigma}_{dev} / 2)^{1/2}$.
- $\boldsymbol{\sigma}_{dev}$ et $\sigma_h = \text{tr}(\boldsymbol{\sigma}) / 3$ les parties déviatorique et hydrostatique de la contrainte de Cauchy $\boldsymbol{\sigma}$, respectivement.
- σ_y la contrainte limite de la partie dense de la matrice. Elle est définie par la loi d'écrouissage de Swift :

$$\sigma_y = K (\varepsilon_0 + \bar{\varepsilon}^p)^n, \quad (2.7)$$

où K , ε_0 et n sont les paramètres d'écrouissage et $\bar{\varepsilon}^p$ la déformation plastique équivalente relative à la partie dense de la matrice.

Lorsque la matrice est complètement dense, le modèle de Gurson se réduit naturellement à la loi d'écoulement plastique classique de type J_2 .

Dans le présent chapitre, seule la croissance des cavités secondaires est prise en compte (c'est-à-dire que les effets de la germination de nouvelles cavités secondaires et de la coalescence entre les cavités existantes sont négligés). En négligeant le changement de volume dû à la déformation élastique, le taux de croissance de la fraction volumique de cavités secondaires peut s'exprimer sous la forme suivante :

$$\dot{f}_s = (1 - f_s) \text{tr}(\mathbf{d}^p). \quad (2.8)$$

L'expression du taux de déformation plastique équivalente $\dot{\bar{\varepsilon}}^p$ peut être déduite à partir du principe d'équivalence entre les taux de travail plastique de la matrice métallique et sa partie dense :

$$(1 - f_s) \sigma_y \dot{\bar{\varepsilon}}^p = \boldsymbol{\sigma} : \mathbf{d}^p \Leftrightarrow \dot{\bar{\varepsilon}}^p = \frac{\boldsymbol{\sigma} : \mathbf{d}^p}{(1 - f_s) \sigma_y}. \quad (2.9)$$

L'activation de l'écoulement plastique est gouvernée par les conditions de Kuhn–Tucker :

$$\begin{aligned} \text{chargement / déchargement élastique : } & \Phi \leq 0 ; \quad \dot{\Phi} < 0 ; \quad \dot{\lambda} = 0 ; \\ \text{chargement élastoplastique : } & \Phi = 0 ; \quad \dot{\Phi} = 0 ; \quad \dot{\lambda} > 0 . \end{aligned} \quad (2.10)$$

Pour le cas d'un chargement élastoplastique, la condition $\dot{\Phi} = 0$ peut être développée comme :

$$\dot{\Phi} = \mathbf{V}_\sigma : \dot{\boldsymbol{\sigma}} + V_{\sigma_y} \dot{\sigma}_y + V_{f_s} \dot{f}_s = 0 , \quad (2.11)$$

avec :

$$\begin{aligned} \mathbf{V}_\sigma &= \frac{\partial \Phi}{\partial \boldsymbol{\sigma}} = \frac{1}{\sigma_y} \left[3 \frac{\sigma_{dev}}{\sigma_y} + f_s \cosh \left(\frac{3\sigma_h}{2\sigma_y} \right) \mathbf{I}_2 \right] ; \\ V_{\sigma_y} &= \frac{\partial \Phi}{\partial \sigma_y} = -\frac{1}{\sigma_y} \left[2 \left(\frac{\sigma_{eq}}{\sigma_y} \right)^2 + 3 f_s \sinh \left(\frac{3\sigma_h}{2\sigma_y} \right) \right] ; \\ V_{f_s} &= \frac{\partial \Phi}{\partial f_s} = 2 \cosh \left(\frac{3\sigma_h}{2\sigma_y} \right) - 2 f_s . \end{aligned} \quad (2.12)$$

La substitution des équations (2.3), (2.5) et (2.12)₁ dans l'équation (2.4) conduit à l'expression de $\dot{\boldsymbol{\sigma}}$:

$$\dot{\boldsymbol{\sigma}} = \mathbf{c}^e : (\mathbf{d} - \mathbf{d}^p) = \mathbf{c}^e : (\mathbf{d} - \dot{\lambda} \mathbf{V}_\sigma) = \mathbf{c}^{ep} : \mathbf{d} . \quad (2.13)$$

La combinaison des équations ci-dessus permet d'obtenir l'expression du multiplicateur plastique $\dot{\lambda}$:

$$\dot{\lambda} = \frac{\mathbf{V}_\sigma : \mathbf{c}^e : \mathbf{d}}{H_\lambda} \quad \text{avec} \quad H_\lambda = \mathbf{V}_\sigma : \mathbf{c}^e : \mathbf{V}_\sigma - \frac{V_{\sigma_y}}{(1-f_s)} \frac{(\boldsymbol{\sigma} : \mathbf{V}_\sigma) \partial \sigma_y}{\partial \epsilon^p} . \quad (2.14)$$

L'expression du module tangent élastoplastique microscopique \mathbf{c}^{ep} peut être déduite en combinant les équations (2.13) et (2.14) :

$$\mathbf{c}^{ep} = \mathbf{c}^e - \alpha \frac{(\mathbf{c}^e : \mathbf{V}_\sigma) \otimes (\mathbf{V}_\sigma : \mathbf{c}^e)}{H_\lambda} , \quad (2.15)$$

où $\alpha = 0$ pour un chargement ou déchargement élastique et $\alpha = 1$ pour un chargement élastoplastique.

Comme Mansouri et al. (2014) l'ont démontré, le module tangent microscopique $\mathbf{c}^{(PKI)}$ est relié au module tangent élastoplastique \mathbf{c}^{ep} par les relations :

$$\forall i, j, k, l = 1, 2, 3 : \quad c_{ijkl}^{(PKI)} = c_{ijkl}^{ep} + \ell_{ijkl}^1 - \ell_{ijkl}^2 - \ell_{ijkl}^3 , \quad (2.16)$$

où ℓ_{ijkl}^1 , ℓ_{ijkl}^2 , ℓ_{ijkl}^3 sont les formes indicielles des tenseurs d'ordre 4 ℓ^1 , ℓ^2 et ℓ^3 qui reflètent les contributions des termes convectifs dans l'expression du module tangent $\mathbf{c}^{(PKI)}$:

$$\forall i, j, k, l = 1, 2, 3: \begin{cases} \ell_{ijkl}^1 = \sigma_{ij} \delta_{kl} & ; \\ \ell_{ijkl}^2 = \frac{1}{2} (\sigma_{jl} \delta_{ik} + \sigma_{jk} \delta_{il}) & ; \\ \ell_{ijkl}^3 = \frac{1}{2} (\sigma_{ik} \delta_{jl} - \sigma_{il} \delta_{jk}). \end{cases} \quad (2.17)$$

2.2.2. Conditions aux limites et chargement macroscopique

Afin d'étudier l'effet du taux de triaxialité T et du paramètre de Lode L sur la compétition entre les phénomènes de coalescence des cavités et de localisation des déformations plastiques macroscopiques, la cellule de base est soumise à des chargements tridimensionnels proportionnels dans l'espace des contraintes macroscopiques. La Fig. 2.4 illustre le chargement macroscopique triaxial appliqué à la cellule de base.

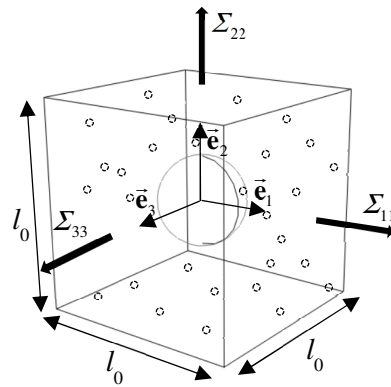


Fig. 2.4. Cellule de base soumise à un chargement macroscopique triaxial (sans cisaillement).

L'application d'un chargement proportionnel dans l'espace des contraintes nécessite que les rapports β_1 et β_2 définis par les relations :

$$\beta_1 = \frac{\Sigma_{11}}{\Sigma_{33}}, \quad \beta_2 = \frac{\Sigma_{22}}{\Sigma_{33}}, \quad (2.18)$$

restent constants durant l'histoire de chargement. Dans l'équation (2.18), Σ_{11} , Σ_{22} et Σ_{33} désignent les composantes diagonales du tenseur des contraintes macroscopiques de Cauchy Σ qui est relié à son homologue microscopique σ par la relation de moyenne :

$$\Sigma = \frac{1}{|\mathcal{V}|} \int_{\mathcal{V}} \sigma(x) d\mathcal{V}, \quad (2.19)$$

où \mathcal{V} est le volume occupé par la cellule de base dans la configuration courante.

La contrainte hydrostatique macroscopique Σ_h et la contrainte équivalente, au sens de von Mises, macroscopique Σ_{eq} sont obtenues à partir des composantes Σ_{11} , Σ_{22} et Σ_{33} :

$$\Sigma_h = \frac{\Sigma_{11} + \Sigma_{22} + \Sigma_{33}}{3} ; \quad \Sigma_{eq} = \frac{1}{\sqrt{2}} \sqrt{(\Sigma_{11} - \Sigma_{22})^2 + (\Sigma_{11} - \Sigma_{33})^2 + (\Sigma_{22} - \Sigma_{33})^2}. \quad (2.20)$$

En supposant que $\Sigma_{11} \geq \Sigma_{22} \geq \Sigma_{33}$, le taux de triaxialité macroscopique T et le paramètre de Lode L peuvent être exprimés en termes des rapports β_1 et β_2 (Liu et al., 2016) :

$$\begin{cases} T = \frac{\Sigma_h}{\Sigma_{eq}} = \frac{\sqrt{2}(1+\beta_1+\beta_2)}{3\sqrt{(1-\beta_1)^2+(1-\beta_2)^2+(\beta_1-\beta_2)^2}} \operatorname{sgn}(\Sigma_{33}); \\ L = \frac{(2\beta_2 - \beta_1 - 1)}{\beta_1 - 1}, \quad -1 \leq L \leq 1. \end{cases} \quad (2.21)$$

Le taux de triaxialité macroscopique T et le paramètre de Lode L caractérisent la partie sphérique et déviatorique du tenseur Σ , respectivement. En inversant l'équation (2.21), on peut exprimer les rapports β_1 et β_2 en fonction de T et L :

$$\beta_1 = \frac{3T\sqrt{3+L^2} + 3 - L}{3T\sqrt{3+L^2} - 3 - L} ; \quad \beta_2 = \frac{3T\sqrt{3+L^2} + 2L}{3T\sqrt{3+L^2} - 3 - L}. \quad (2.22)$$

Pour appliquer un chargement triaxial proportionnel dans l'espace des contraintes, des conditions aux limites périodiques tridimensionnelles doivent être imposées sur les six faces extérieures de la cellule de base (deux par deux faces), conformément au concept présenté dans le chapitre précédent. Dans ce cas, trois points de référence RP_1 , RP_2 et RP_3 sont créés en utilisant la boîte à outils *Homtools* pour gérer ces conditions aux limites et le chargement macroscopique. Ces points de référence sont définis par les déplacements suivants :

$$\begin{aligned} RP_1 : U_{11} &= (F_{11} - 1)l_0 ; U_{12} = 0 ; U_{13} = 0 ; \\ RP_2 : U_{21} &= 0 ; U_{22} = (F_{22} - 1)l_0 ; U_{23} = 0 ; \\ RP_3 : U_{31} &= 0 ; U_{32} = 0 ; U_{33} = (F_{33} - 1)l_0. \end{aligned} \quad (2.23)$$

Les composantes F_{11} , F_{22} et F_{33} du gradient de transformation macroscopique \mathbf{F} sont définies de telle sorte que le taux de triaxialité T et le paramètre de Lode L restent constants durant le chargement. Il n'est pas possible d'imposer une telle condition en définissant directement les composantes de déplacement des points de référence RP_1 , RP_2 et RP_3 . Pour surmonter cette difficulté, un nœud muet (ou nœud fantôme) supplémentaire est introduit dans le modèle éléments finis. Les ddl de ce nœud muet et les forces de réaction associées sont notées (U_1^*, U_2^*, U_3^*) et $(\alpha_1, \alpha_2, \alpha_3)$, respectivement. Une subroutine MPC (Abaqus, 2014) a été développée pour connecter le nœud muet aux trois points de référence RP_1 , RP_2 et RP_3 . Dans cette subroutine, les points de référence servent de nœuds esclaves, tandis que le nœud muet sert de nœud maître sur lequel le chargement macroscopique est imposé. Le nœud maître transmet le chargement à travers les contraintes multipoints aux points de référence comme indiqué par l'équation suivante :

$$\begin{bmatrix} U_{11} \\ U_{22} \\ U_{33} \end{bmatrix} = \mathcal{T} \begin{bmatrix} U_1^* \\ U_2^* \\ U_3^* \end{bmatrix}. \quad (2.24)$$

où \mathcal{T} est une fonction à déterminer afin de s'assurer que les déplacements U_{11} , U_{22} et U_{33} appliqués sur les points de référence permettent d'obtenir les rapports β_1 et β_2 entre les différentes composantes du tenseur Σ . Une illustration simplifiée du fonctionnement de cette subroutine est présentée sur la Fig. 2.5.

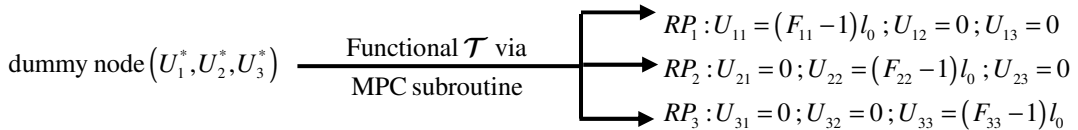


Fig. 2.5. Illustration schématique de la subroutine MPC utilisée pour définir les relations entre les déplacements du nœud maître et ceux des points de référence (RP_1, RP_2, RP_3).

Pour déterminer l'expression de la fonction \mathcal{T} , la relation suivante exprimant l'équivalence entre le taux de travail mécanique correspondant au nœud muet et sa contrepartie relative à la cellule de base peut être utilisée (Liu et al., 2016) :

$$\boldsymbol{\alpha}^T \cdot \dot{\mathbf{U}}^* = |V| \tilde{\boldsymbol{\Sigma}}^T \cdot \tilde{\mathbf{G}}, \quad (2.25)$$

où \mathbf{U}^* et $\boldsymbol{\alpha}$ sont respectivement les vecteurs des déplacements et les forces de réaction associés au nœud muet. Quant à $\tilde{\boldsymbol{\Sigma}}$ et $\tilde{\mathbf{G}}$, ils représentent respectivement les vecteurs de stockage des composantes diagonales de la contrainte macroscopique de Cauchy et du gradient de vitesse macroscopique associé à la cellule de base :

$$\boldsymbol{\alpha} = \begin{bmatrix} \alpha_1 \\ \alpha_2 \\ \alpha_3 \end{bmatrix} ; \quad \mathbf{U}^* = \begin{bmatrix} U_1^* \\ U_2^* \\ U_3^* \end{bmatrix} ; \quad \tilde{\boldsymbol{\Sigma}} = \begin{bmatrix} \Sigma_{11} \\ \Sigma_{22} \\ \Sigma_{33} \end{bmatrix} ; \quad \tilde{\mathbf{G}} = \begin{bmatrix} G_{11} \\ G_{22} \\ G_{33} \end{bmatrix}. \quad (2.26)$$

Les vecteurs $\dot{\mathbf{U}}^*$ et $\tilde{\mathbf{G}}$ peuvent être reliés par la matrice de transformation \mathcal{R} appartenant à l'espace $\mathcal{SO}(3)$ ³ (Wong et Guo, 2015) :

$$\begin{bmatrix} G_{11} \\ G_{22} \\ G_{33} \end{bmatrix} = \mathcal{R} \cdot \begin{bmatrix} \dot{U}_1^* \\ \dot{U}_2^* \\ \dot{U}_3^* \end{bmatrix}. \quad (2.27)$$

Dans ce travail, nous avons adopté la forme de \mathcal{R} fournie par Liu et al. (2016) :

³ La matrice \mathcal{R} appartient à $\mathcal{SO}(3)$ si \mathcal{R} est orthogonale (i.e., $\mathcal{R}^{-1} = \mathcal{R}^T$) et $\det(\mathcal{R}) = 1$.

$$\mathcal{R} = \begin{bmatrix} \sin^2 \varphi_1 + \cos \varphi_2 \cos^2 \varphi_1 & \cos \varphi_2 \cos \varphi_1 \sin \varphi_1 - \cos \varphi_1 \sin \varphi_1 & \cos \varphi_1 \sin \varphi_2 \\ \cos \varphi_2 \cos \varphi_1 \sin \varphi_1 - \cos \varphi_1 \sin \varphi_1 & \cos \varphi_2 \sin^2 \varphi_1 + \cos^2 \varphi_1 & \sin \varphi_2 \sin \varphi_1 \\ -\cos \varphi_1 \sin \varphi_2 & -\sin \varphi_1 \sin \varphi_2 & \cos \varphi_2 \end{bmatrix}. \quad (2.28)$$

L'expression (2.28) de la matrice de transformation \mathcal{R} est valable lorsque $\Sigma_{33} > 0$ (c'est-à-dire $\text{sgn}(\Sigma_{33}) = 1$). Cette condition est évidemment assurée pour les chargements étudiés dans la Section 2.2.4, où $0.7 \leq T \leq 3$ et $-1 \leq L \leq 1$, ce qui correspond à des valeurs positives des rapports β_1 et β_2 . Les expressions des angles de rotation φ_1 et φ_2 utilisées pour paramétriser la matrice \mathcal{R} seront établies dans les développements suivants.

Le chargement externe est appliqué sur le nœud muet et la matrice de transformation \mathcal{R} est utilisée pour transférer adéquatement ce chargement aux différents points de référence. Nous appliquons un déplacement linéaire uniquement sur le troisième ddl du nœud muet avec $\dot{U}_3^* = 1$. Les deux premiers ddl sont laissés libres. Par conséquent, les forces de réaction correspondantes sont égales à zéro (à savoir, $\alpha_1 = \alpha_2 = 0$). Avec ce chargement particulier, l'équation (2.25) sera réduite à la forme suivante :

$$\alpha_3 \dot{U}_3^* = |\mathcal{V}| (\Sigma_{11} G_{11} + \Sigma_{22} G_{22} + \Sigma_{33} G_{33}). \quad (2.29)$$

Sans détailler davantage les développements mathématiques associés, l'expression de α_3 peut-être déduite en fonction de $|\mathcal{V}|$ et des composantes Σ_{11} , Σ_{22} et Σ_{33} comme :

$$\alpha_3 = |\mathcal{V}| \sqrt{(\Sigma_{11})^2 + (\Sigma_{22})^2 + (\Sigma_{33})^2}. \quad (2.30)$$

En utilisant les expressions (2.18) de β_1 et β_2 , l'équation (2.30) peut être formulée comme :

$$\alpha_3 = |\mathcal{V}| \sqrt{(\Sigma_{11})^2 + (\Sigma_{22})^2 + (\Sigma_{33})^2} = |\mathcal{V}| \left(\sqrt{(\beta_1)^2 + (\beta_2)^2 + 1} \right) \Sigma_{33}. \quad (2.31)$$

Considérant le fait que $\alpha_1 = \alpha_2 = 0$, les expressions des angles de rotation φ_1 et φ_2 peuvent être exprimées comme (Liu et al., 2016) :

$$\varphi_1 = \tan^{-1} \left(\frac{\beta_2}{\beta_1} \right) \quad ; \quad \varphi_2 = \tan^{-1} \left(\sqrt{(\beta_1)^2 + (\beta_2)^2} \right). \quad (2.32)$$

La substitution des équations (2.32) dans l'équation (2.28) permet d'obtenir l'expression de la matrice de transformation \mathcal{R} :

$$\mathcal{R} = \begin{bmatrix} \frac{(\beta_1)^2 \mu + (\beta_2)^2}{(\beta_1)^2 + (\beta_2)^2} & \frac{\beta_1 \beta_2 (\mu - 1)}{(\beta_1)^2 + (\beta_2)^2} & \beta_1 \mu \\ \frac{\beta_1 \beta_2 (\mu - 1)}{(\beta_1)^2 + (\beta_2)^2} & \frac{(\beta_1)^2 + (\beta_2)^2 \mu}{(\beta_1)^2 + (\beta_2)^2} & \beta_2 \mu \\ -\beta_1 \mu & -\beta_2 \mu & \mu \end{bmatrix} \quad \text{avec} \quad \mu = \frac{1}{\sqrt{(\beta_1)^2 + (\beta_2)^2 + 1}}. \quad (2.33)$$

Pour un chargement triaxial proportionnel dans l'espace des contraintes, la matrice de transformation \mathcal{R} reste constante durant le chargement. Par conséquent, l'intégration de l'équation (2.27) conduit à :

$$\begin{bmatrix} E_{11} \\ E_{22} \\ E_{33} \end{bmatrix} = \mathcal{R} \cdot \begin{bmatrix} U_1^* \\ U_2^* \\ U_3^* \end{bmatrix}, \quad (2.34)$$

où \mathbf{E} est le tenseur de déformation logarithmique macroscopique défini comme :

$$\mathbf{E} = \int_0^t \mathbf{G} dt = \ln(\mathbf{F}). \quad (2.35)$$

La combinaison des équations (2.23), (2.34) et (2.35) conduit à :

$$\begin{cases} F_{11} = (U_{11} / l_0) + 1 = e^{(\mathcal{R}_{11} U_1^* + \mathcal{R}_{12} U_2^* + \mathcal{R}_{13} U_3^*)}; \\ F_{22} = (U_{22} / l_0) + 1 = e^{(\mathcal{R}_{21} U_1^* + \mathcal{R}_{22} U_2^* + \mathcal{R}_{23} U_3^*)}; \\ F_{33} = (U_{33} / l_0) + 1 = e^{(\mathcal{R}_{31} U_1^* + \mathcal{R}_{32} U_2^* + \mathcal{R}_{33} U_3^*)}. \end{cases} \quad (2.36)$$

L'expression de la fonction \mathcal{T} peut être facilement identifiée à partir des équations (2.36). Ainsi, les relations entre les ddl du nœud muet et ceux des trois points de référence à planter dans la subroutine MPC sont résumées par les équations (2.36). Les conditions aux limites périodiques ainsi que les équations (2.36) résument le problème aux valeurs aux limites à résoudre sur la cellule de base.

2.2.3. Critères de coalescence et de localisation de la déformation plastique

Dans la présente application, notre attention est focalisée sur la prédition de la rupture ductile des matériaux poreux en utilisant les quatre indicateurs présentés ci-après : les trois premiers ont été utilisés dans des contributions précédentes (mais sans le couplage rigoureux avec la technique d'homogénéisation périodique), tandis que le dernier est appliqué pour la première fois ici.

2.2.3.1. Critère de force maximum

Cet indicateur a été adopté par [Guo et Wong \(2018\)](#) pour prédire le début de la localisation des déformations plastiques. Avec ce critère, la localisation des déformations est atteinte lorsque la composante de la force de réaction α_3 appliquée sur le nœud muet et définie par l'équation (2.31) atteint sa valeur maximale, ou de manière équivalente :

$$\dot{\alpha}_3 = 0. \quad (2.37)$$

La déformation équivalente critique prédite au moment où ce critère est vérifié sera notée E_{eq}^R .

2.2.3.2. Critère de contrainte équivalente maximum

Cet indicateur, initié par [Tvergaard \(2012\)](#), indique que la rupture du matériau se produit lorsque la contrainte macroscopique équivalente Σ_{eq} atteint sa valeur maximale. Pour un chargement

proportionnel dans l'espace des contraintes, la contrainte macroscopique Σ prend la forme générale suivante :

$$\Sigma = \begin{bmatrix} \Sigma_{11} & 0 & 0 \\ 0 & \Sigma_{22} & 0 \\ 0 & 0 & \Sigma_{33} \end{bmatrix} = \Sigma_{33} \begin{bmatrix} \beta_1 & 0 & 0 \\ 0 & \beta_2 & 0 \\ 0 & 0 & 1 \end{bmatrix}. \quad (2.38)$$

Dans ce cas, la contrainte macroscopique équivalente Σ_{eq} peut être exprimée comme :

$$\Sigma_{eq} = \sqrt{\frac{(\Sigma_{11} - \Sigma_{22})^2 + (\Sigma_{11} - \Sigma_{33})^2 + (\Sigma_{22} - \Sigma_{33})^2}{2}} = \sqrt{(\beta_1)^2 + (\beta_2)^2 - \beta_1\beta_2 - \beta_1 - \beta_2 + 1} |\Sigma_{33}|. \quad (2.39)$$

La déformation équivalente critique prédite au moment où ce critère est vérifié sera notée E_{eq}^s .

2.2.3.3. Critère énergétique

Le critère énergétique a été proposé par Wong et Guo (2015). Il est basé sur l'hypothèse stipulant l'équivalence entre la coalescence des cavités et le début de la localisation des déformations plastiques entre les cavités voisines. Au moment de l'apparition de cette coalescence, le matériau en dehors de la bande de localisation subit une décharge élastique (Pardoen et Hutchinson, 2000). Pour appliquer ce critère, le taux de travail élastique et plastique doivent être calculés :

$$\dot{W}^e = \int_{\mathcal{V}} \boldsymbol{\sigma} : \mathbf{d}^e \, d\mathcal{V} \quad ; \quad \dot{W}^p = \int_{\mathcal{V}} \boldsymbol{\sigma} : \mathbf{d}^p \, d\mathcal{V}, \quad (2.40)$$

où $\boldsymbol{\sigma}$ est la contrainte microscopique de Cauchy, \mathbf{d}^e et \mathbf{d}^p sont respectivement les parties élastique et plastique du tenseur taux de déformation \mathbf{d} . Le signe du rapport \dot{W}^e / \dot{W}^p définit trois états de chargement différents : $\dot{W}^e / \dot{W}^p > 0$ pour un état de chargement élastoplastique, $\dot{W}^e / \dot{W}^p < 0$ pour un état de décharge élastique, $\dot{W}^e / \dot{W}^p = 0$ pour un état de charge neutre. Selon Wong et Guo (2015), le début de coalescence des cavités se produit lorsque le rapport \dot{W}^e / \dot{W}^p atteint une valeur minimale négative.

La déformation équivalente critique prédite au moment où ce critère est vérifié sera notée E_{eq}^c .

2.2.3.4. Critère de bifurcation de Rice

Suivant l'approche de Rice (Rudnicki et Rice, 1975 ; Rice, 1976), le début de la localisation des déformations plastiques peut être mathématiquement interprété par la perte d'ellipticité des équations constitutives macroscopiques. Ce critère peut être traduit mathématiquement par la singularité du tenseur acoustique macroscopique $\vec{\mathcal{N}} \cdot \tilde{\mathbf{C}}^{(PK1)} \cdot \vec{\mathcal{N}}$:

$$\det(\vec{\mathcal{N}} \cdot \tilde{\mathbf{C}}^{(PK1)} \cdot \vec{\mathcal{N}}) = 0, \quad (2.41)$$

où \vec{N} est le vecteur unitaire normal à la bande de localisation et $\tilde{\mathbf{C}}^{(PK1)}$ est le transposé du module tangent macroscopique $\mathbf{C}^{(PK1)}$ introduit dans l'équation (1.7)₂. Par conséquent, le module tangent $\tilde{\mathbf{C}}^{(PK1)}$ est obtenu à partir de $\mathbf{C}^{(PK1)}$ par permutation des deux premiers indices (Zhu et al., 2020) :

$$\forall i, j, k, l = 1, 2, 3: \quad \tilde{C}_{ijkl}^{(PK1)} = C_{jikl}^{(PK1)}. \quad (2.42)$$

Les détails pratiques relatifs à la mise en œuvre de la technique de condensation pour le calcul de $\mathbf{C}^{(PK1)}$ peuvent être trouvés dans le chapitre précédent.

La déformation équivalente critique prédictive au moment où ce critère est vérifié sera notée E_{eq}^B .

2.2.4. Prédictions numériques

Bien que l'approche numérique soit conçue pour des matériaux présentant deux populations de cavités (une cavité primaire et plusieurs cavités secondaires), comme nous l'avons détaillé dans la Section 2.2.1, dans ce résumé notre attention sera focalisée sur une cellule de base contenant juste une cavité primaire. Par conséquent, la matrice métallique sera supposée dense. L'effet d'une seconde population de cavités sur la limite de ductilité est bien décrit dans la version anglaise de ce manuscrit.

La fraction volumique initiale de la cavité primaire f_{p0} est fixée à 0.04 dans toutes les simulations présentées ci-après. Le comportement mécanique de la partie dense de la matrice métallique est supposé être isotrope élastiquement et plastiquement. Pour des comparaisons cohérentes avec Liu et al. (2016), les paramètres d'élasticité et d'écrouissage fournis dans le Tab. 2.1 sont utilisés dans les différentes simulations.

Tab. 2.1. Propriétés élastoplastiques de la matrice métallique.

Élasticité		Écrouissage		
E (GPa)	ν	K (MPa)	ε_0	n
210	0.3	958.8	0.0025	0.1058

La limite d'élasticité initiale de la matrice dense peut être déduite des paramètres donnés dans le Tab. 2.1 :

$$\sigma_0 = K (\varepsilon_0)^n. \quad (2.43)$$

2.2.4.1. Comparaison avec les résultats de Liu et al. (2016)

Pour valider l'approche développée, nos prédictions numériques seront comparées à celles publiées dans Liu et al. (2016). Dans cet objectif, des conditions cinématiques seront appliquées à la place des conditions de périodicité sur les bords de la cellule de base ($\mathbf{f} = \mathbf{F}$ sur $\partial\mathcal{V}_0$). Cette cellule de base est soumise à un chargement triaxial proportionnel dans l'espace des contraintes, où l'état de contrainte est défini par $T = 1.0$ et $L = 0.0$. Le début de la coalescence des cavités est prédict par le critère énergétique

présenté dans la Section 2.2.3.3. Les évolutions du rapport \dot{W}^e / \dot{W}^p , des composantes de la déformation macroscopique logarithmique (E_{11} , E_{22} , E_{33}) et de la contrainte macroscopique équivalente Σ_{eq} sont tracées en fonction de la déformation macroscopique équivalente E_{eq} dans les Fig. 2.6a, b et c, respectivement. Sur ces figures, nos prédictions numériques sont indiquées par des courbes rouges et celles publiées dans Liu et al. (2016) par des courbes grises. Les évolutions des déformations logarithmiques principales et la réponse contrainte–déformation équivalente sont en très bon accord avec celles rapportées par Liu et al. (2016). C'est également le cas pour la valeur de la déformation critique E_{eq}^C prédite au moment du début de coalescence des cavités ($E_{eq}^C = 0.597$ dans Liu et al., 2016, par rapport à $E_{eq}^C = 0.605$ prédite par le modèle actuel). Cependant, l'amplitude du rapport \dot{W}^e / \dot{W}^p au moment où la coalescence des cavités se produit n'est pas en parfait accord. Cette différence est probablement attribuable au type d'élément fini utilisé dans les simulations. En effet, l'élément C3D8R (élément solide à intégration réduite à huit noeuds) est utilisé dans Liu et al. (2016), alors que dans la présente étude, la cellule de base est discrétisée en utilisant l'élément solide C3D8 (avec intégration complète). On peut observer à partir des courbes de la Fig. 2.6a que, lorsque la cellule de base se déforme plastiquement, le rapport \dot{W}^e / \dot{W}^p décroît jusqu'à devenir nul. Cela signifie que l'état de chargement appliqué sur la cellule de base passe d'un chargement élastoplastique à une décharge élastique. Au fur et à mesure que la déformation augmente, le rapport \dot{W}^e / \dot{W}^p décroît vers une valeur minimale, là où la décharge élastique maximale se produit. Ce point est identifié comme le début de la coalescence des cavités. Au-delà de ce point, le rapport \dot{W}^e / \dot{W}^p passera de négatif à positif. Ce changement signifie que l'état mécanique dans la cellule de base revient à un état de chargement élastoplastique. Avec la Fig. 2.6a, la Fig. 2.6b montre une modification claire des déformations logarithmiques principales au moment de la coalescence des cavités. En effet, on observe que le mode de déformation cellulaire passe de l'état de déformation triaxiale à uniaxiale avec $\dot{E}_{22} = \dot{E}_{33} = 0$ (Koplik et Needleman, 1988). Il est à noter que ce changement de mode de déformation se produit au moment où le rapport \dot{W}^e / \dot{W}^p atteint sa valeur minimale (ce qui correspond au début de la coalescence des cavités).

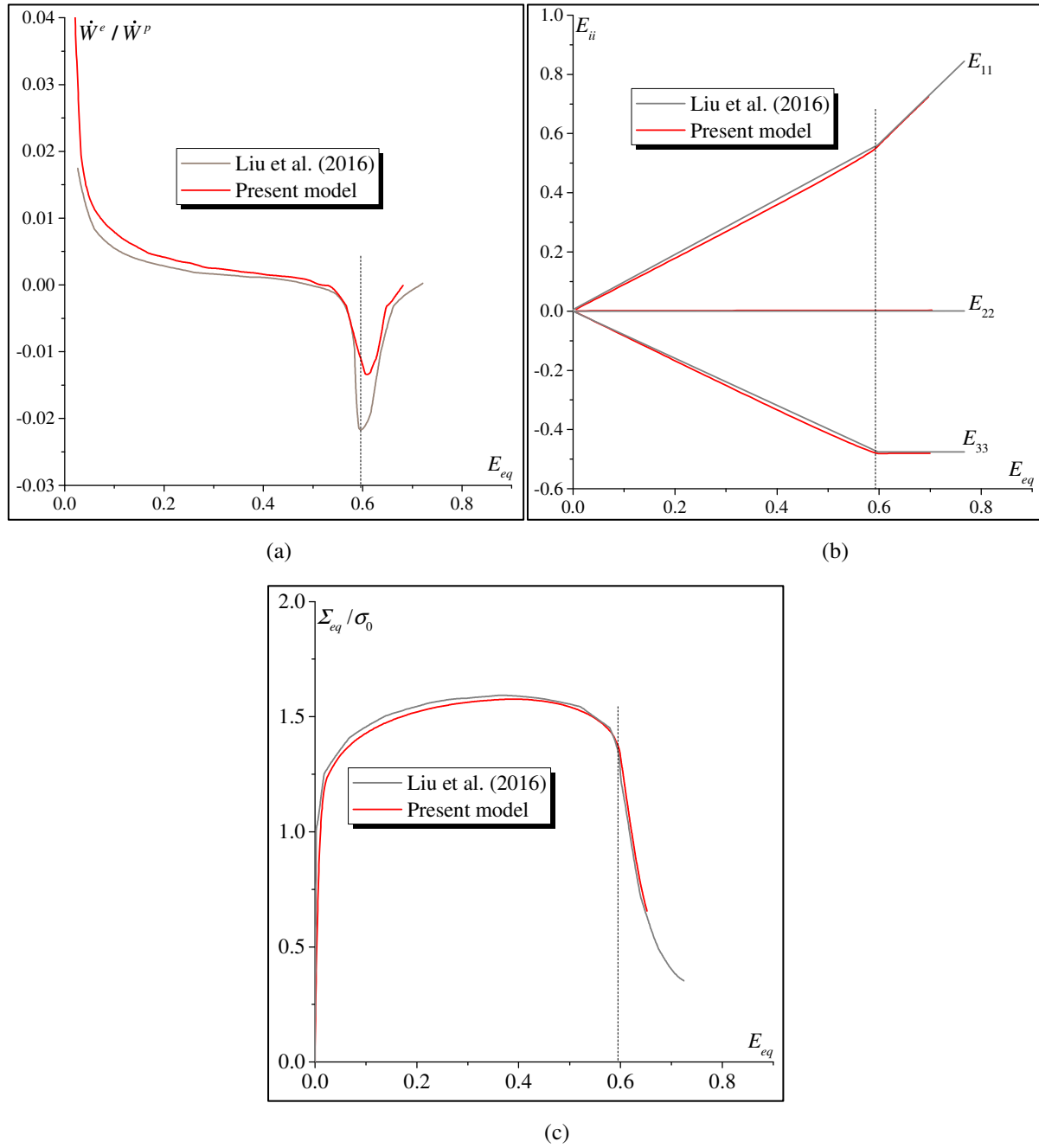


Fig. 2.6. Validation de l’implantation numérique en comparant nos prédictions aux résultats publiés dans Liu et al. (2016) : (a) évolution du rapport \dot{W}^e / \dot{W}^p ; (b) évolution des composantes de la déformation macroscopique logarithmique E_{11} , E_{22} et E_{33} ; (c) évolution de la contrainte macroscopique équivalente Σ_{eq} normalisée par la contrainte initiale σ_0 .

2.2.4.2. Compétition entre le phénomène de coalescence des cavités et le phénomène de localisation de la déformation plastique

Pour démarrer l’analyse de la compétition entre la coalescence des cavités et la localisation des déformations plastiques macroscopiques, trois sollicitations dans l’espace des contraintes proportionnelles sont considérées. Pour ces chargements, le paramètre de Lode L est fixé à 1.0 et trois valeurs du taux de triaxialité T sont considérées : 0,8 ; 1,0 et 2,0. Nous rappelons que la matrice de la

cellule de base est supposée être entièrement dense et que la fraction volumique initiale de la cavité primaire f_{p0} est fixée à 0.04. Les évolutions de certaines variables macroscopiques, pertinentes pour étudier la compétition entre la coalescence des cavités et la localisation des déformations plastiques macroscopiques, sont tracées sur la Fig. 2.7. Dans les différents résultats, la déformation équivalente E_{eq} est souvent utilisée pour mesurer la limite de ductilité de la cellule de base. Par conséquent, une déformation équivalente critique, prédite par chaque indicateur, a également été utilisée pour indiquer la rupture du matériau. À des fins de comparaisons, quatre symboles sont marqués sur chaque courbe de la Fig. 2.7 pour désigner le niveau de la déformation macroscopique équivalente correspondant à chaque critère :

- Un carré (\square) pour désigner E_{eq}^R (lorsque la composante α_3 appliquée sur le nœud muet atteint sa valeur maximale).
- Un cercle (\circlearrowright) pour désigner E_{eq}^S (lorsque la contrainte macroscopique équivalente Σ_{eq} atteint sa valeur maximale).
- Une étoile ($*$) pour désigner E_{eq}^B (lorsque le déterminant du tenseur acoustique $\vec{\mathcal{N}} \cdot \tilde{\mathbf{C}}^{(PK1)} \cdot \vec{\mathcal{N}}$ s'annule).
- Un triangle haut (\triangle) pour désigner E_{eq}^C (lorsque le rapport \dot{W}^e / \dot{W}^p atteint une valeur minimale négative).

En analysant les courbes de la Fig. 2.7, quelques conclusions peuvent être tirées :

- Pour tous les taux de triaxialité étudiés, les déformations équivalentes critiques prédites par les différents critères sont classées dans cet ordre :

$$E_{eq}^S < E_{eq}^R < E_{eq}^B < E_{eq}^C. \quad (2.44)$$

- Comme prévu, les différentes déformations équivalentes critiques (à savoir, E_{eq}^S , E_{eq}^R , E_{eq}^B et E_{eq}^C) diminuent avec l'augmentation du taux de triaxialité T , reflétant la perte de ductilité. De plus, la dépendance des différentes déformations critiques équivalentes est plus prononcée dans la plage de faibles taux de triaxialité T .
- La différence entre les différentes déformations équivalentes critiques diminue lorsque le taux de triaxialité augmente. Par exemple, la différence entre E_{eq}^S et E_{eq}^C diminue de 0.73 pour $T = 0.8$ à 0.20 pour $T = 2.0$.

L'effet du taux de triaxialité T sur le début de la rupture ductile sera étudié avec plus de détails dans la Section 2.2.4.3, où une large gamme de T sera considérée et pas seulement trois valeurs particulières comme c'est le cas dans cette section.

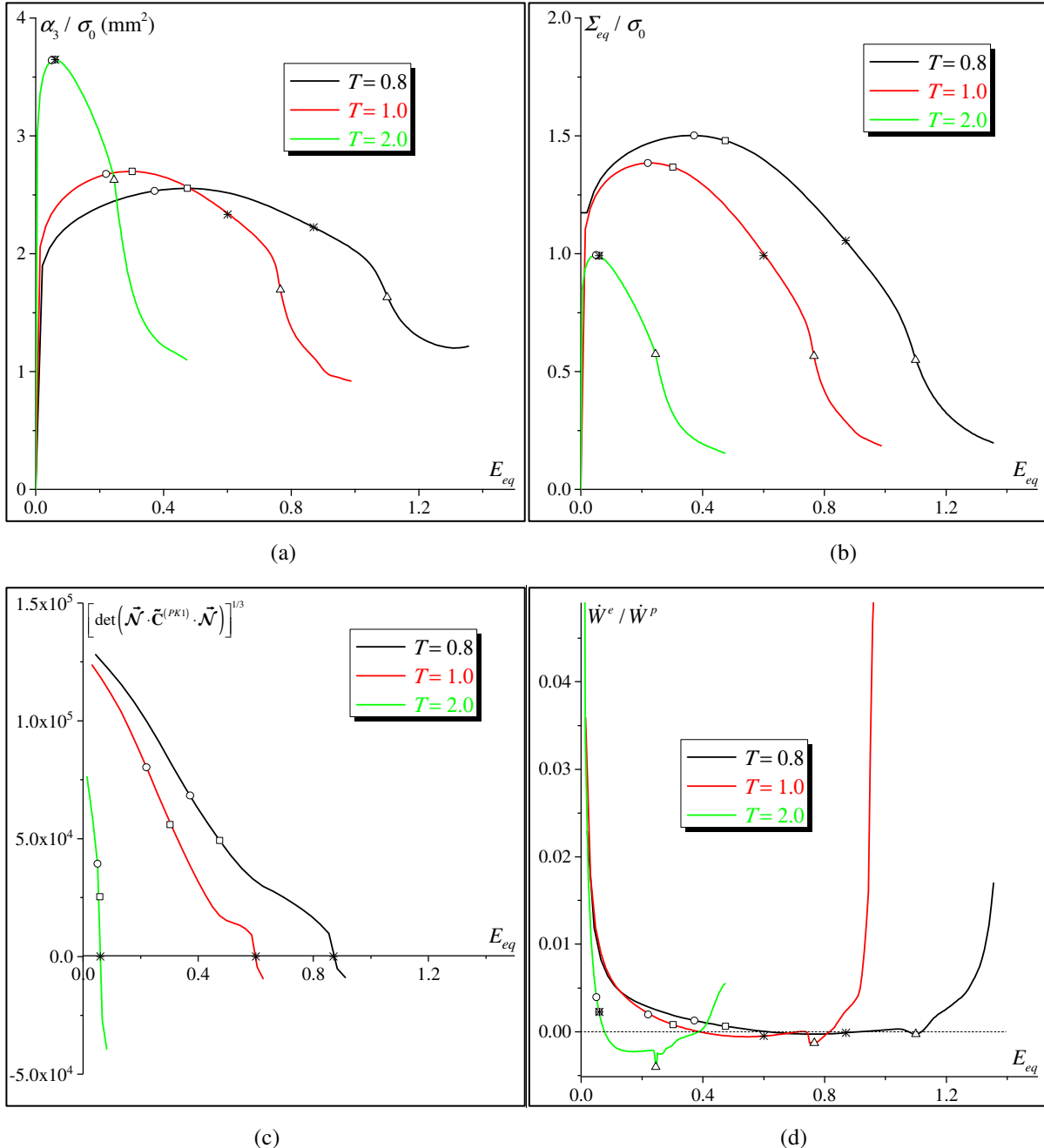


Fig. 2.7. Compétition entre la coalescence des cavités et la localisation des déformations macroscopiques pour les trois sollicitations dans l'espace des contraintes proportionnelles définies par $T = 0.8, 1 \text{ et } 2$ avec $L = 1$: (a) évolution de la composante α_3 de la force de réaction appliquée au nœud muet normalisée par la contrainte initiale σ_0 ; (b) évolution de la contrainte équivalente Σ_{eq} normalisée par la contrainte initiale σ_0 ; (c) évolution de la racine cubique du déterminant du tenseur acoustique $\vec{\mathcal{N}} \cdot \tilde{\mathbf{C}}^{(PK1)} \cdot \vec{\mathcal{N}}$; (d) évolution du rapport \dot{W}^e / \dot{W}^p .

2.2.4.3. Effet du taux de triaxialité sur la rupture ductile

Un aperçu de la compétition entre la coalescence des cavités et le début de la localisation de la déformation plastique est donné au travers de la Fig. 2.8, où les évolutions des déformations équivalentes critiques E_{eq}^S , E_{eq}^R , E_{eq}^B et E_{eq}^C sont tracées en fonction de T pour la plage ($0.7 \leq T \leq 3.0$) et pour trois valeurs de L (-1 ; 0 et 1.0). Comme on peut le constater sur cette figure, les quatre déformations limites

décroissent au fur et à mesure que le taux de triaxialité T augmente (indépendamment de la valeur de L). En examinant l'évolution de E_{eq}^B et pour une gamme donnée de T , on peut confirmer que E_{eq}^B est toujours inférieure à E_{eq}^C indépendamment de la valeur de L . Par conséquent, la localisation de la déformation plastique prédicta par l'approche de bifurcation de Rice se produit avant le début de la coalescence des cavités, prédict par le critère énergétique, pour la gamme complète de T . Pour $T < 2.0$, les déformations limites E_{eq}^B , E_{eq}^R et E_{eq}^S sont atteintes avec $E_{eq}^S < E_{eq}^R < E_{eq}^B$ et la différence entre ces déformations limites diminue au fur et à mesure que le taux de triaxialité T augmente pour les différentes valeurs de L . Pour des valeurs plus élevées de T , notamment $T > 2.0$, les courbes correspondant aux déformations E_{eq}^B , E_{eq}^R et E_{eq}^S sont presque indiscernables. Ce résultat signifie que pour des niveaux élevés de T , le maximum de la force de réaction appliquée sur le nœud muet, la contrainte équivalente maximale et la bifurcation sont atteints approximativement au même moment. Cette dernière conclusion est parfaitement cohérente avec les prédictions obtenues par [Guo et Wong \(2018\)](#), où il a été démontré que la force de réaction maximale appliquée sur le nœud muet (utilisé comme critère de localisation des déformations dans [Guo et Wong, 2018](#)) et la contrainte équivalente maximale sont simultanément atteintes pour des valeurs élevées de T (généralement supérieures à 1.5). En revanche, le critère de bifurcation (utilisé dans la présente contribution comme critère rigoureux de localisation des déformations macroscopiques) semble être moins conservatif que le critère de force de réaction maximum appliquée sur le nœud muet (utilisé comme critère de localisation des déformations dans [Guo et Wong, 2018](#)) pour des taux de triaxialité faibles ($T < 2.0$), ce qui est encore plus remarquable pour $L = 1.0$. Quel que soit le critère de localisation des déformations macroscopiques adopté, défini comme la contrainte équivalente maximale dans [Bomarito et Warner \(2015\)](#) et [Tekoglu et al. \(2015\)](#) ou comme la force de réaction maximale dans [Guo et Wong \(2018\)](#), le critère de bifurcation présenté ici conduit à des déformations limites relativement plus élevées pour $T < 2.0$. Pour un taux de triaxialité plus élevée ($2.0 < T < 3.0$), ces trois critères de localisation des déformations prédisent presque les mêmes résultats.

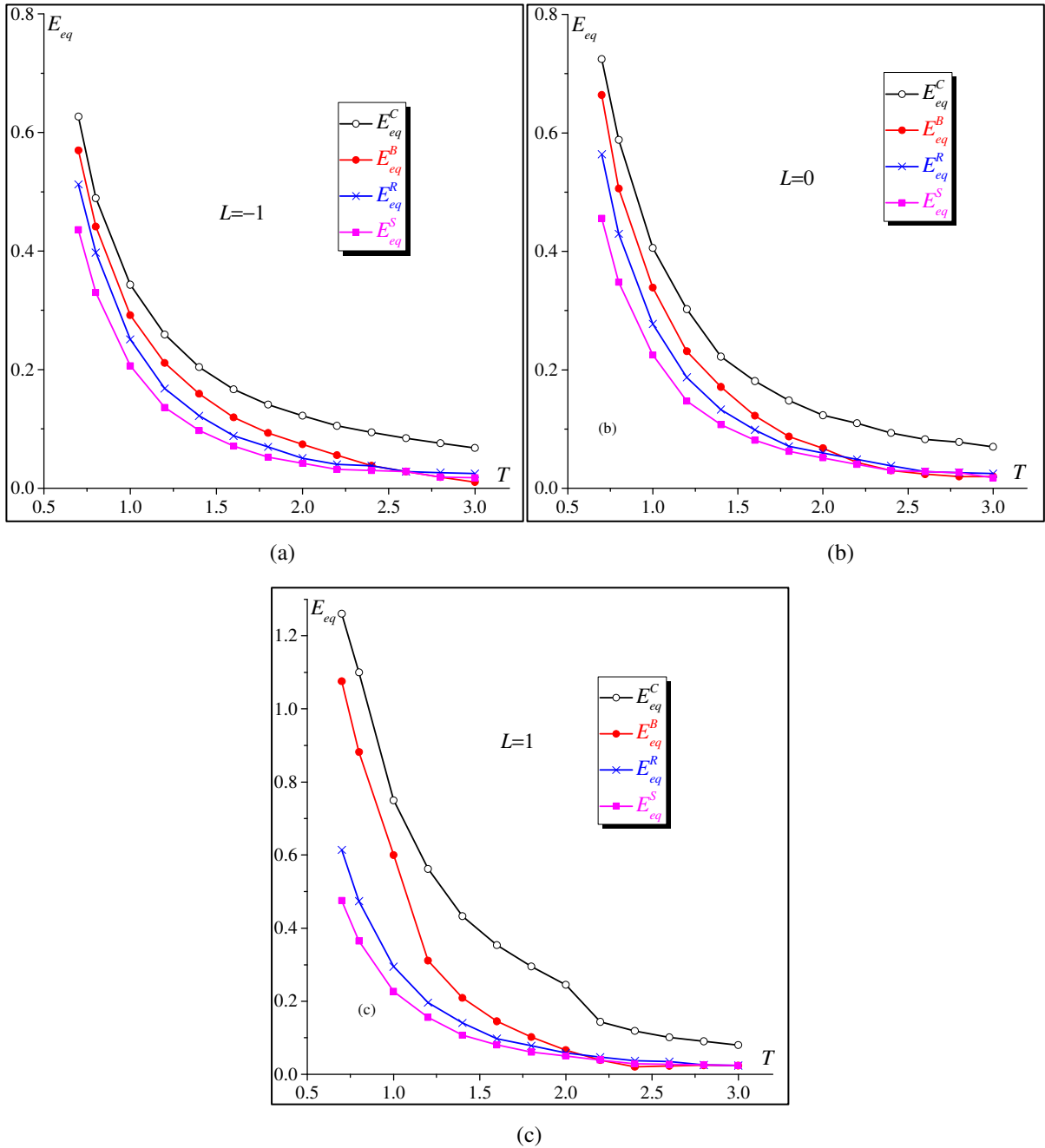


Fig. 2.8. Évolution des déformations équivalentes critiques E_{eq}^S , E_{eq}^R , E_{eq}^B et E_{eq}^C sur la plage $0.7 \leq T \leq 3.0$ et pour : (a) $L = -1$; (b) $L = 0$; (c) $L = 1$.

2.2.4.4. Effet du paramètre de Lode sur la rupture ductile

Une attention particulière est désormais portée dans cette section à l'analyse de l'effet du paramètre de Lode L sur la localisation des déformations macroscopiques et la coalescence des cavités. Les évolutions des déformations équivalentes critiques E_{eq}^C et E_{eq}^B sont tracées sur la Fig. 2.9 pour la gamme $-1.0 \leq L \leq 1.0$ et pour certaines valeurs particulières de T (0.8 ; 1.2 ; 1.6 ; 2.0 ; 2.4 et 3.0). Les évolutions de E_{eq}^C et E_{eq}^B sont désignées respectivement par des lignes pleines et des tirets. À première

vue, il est clair que la déformation E_{eq}^C est plus élevée que E_{eq}^B pour la gamme d'étude de L . Pour des niveaux faibles à modérés de T , les déformations limites E_{eq}^C et E_{eq}^B augmentent avec L , en particulier pour $0 \leq L \leq 1.0$, avec différentes vitesses d'augmentation. De plus, la différence entre E_{eq}^C et E_{eq}^B augmente avec L dans la gamme $0 \leq L \leq 1.0$ pour des niveaux de triaxialité relativement faibles. Pour des niveaux élevés de triaxialité (par exemple $T = 2.4$ et $T = 3.0$), les déformations critiques E_{eq}^C et E_{eq}^B ont une évolution quasi-linéaire sur tout le domaine de variation de L . En d'autres termes, l'effet du paramètre de Lode est plus prononcé lorsque le taux de triaxialité est faible. Concernant l'effet de L , [Barsoum et Faleskog \(2011\)](#) et [Dunand et Mohr \(2014\)](#) ont constaté que l'évolution de E_{eq}^C en fonction de L suit une allure convexe et non symétrique pour $-1.0 < L < 1.0$ en suivant le critère de coalescence développé par [Needleman et Tvergaard \(1992\)](#).

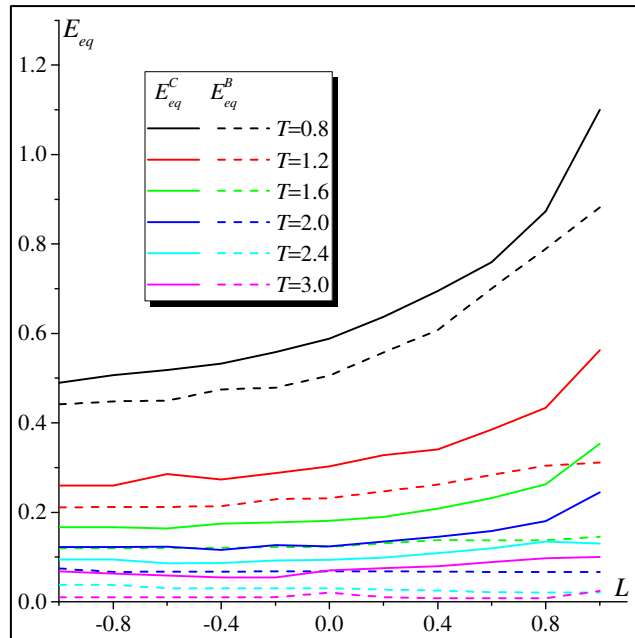


Fig. 2.9. Évolution des déformations critiques E_{eq}^C et E_{eq}^B sur la plage $-1.0 \leq L \leq 1.0$ et pour $T = 0.8 ; 1.2 ; 1.6 ; 2.0 ; 2.4 ; 3.0$.

2.2.5. Bilan de l'étude

Dans cette première étude, l'approche de bifurcation de Rice a été couplée à la technique d'homogénéisation périodique pour prédire le début de la localisation des déformations plastiques macroscopiques dans les matériaux poreux à structure tridimensionnelle. Dans cette étude, les sollicitations sont appliquées dans l'espace des contraintes proportionnelles permettant ainsi d'étudier l'effet du taux de triaxialité macroscopique T et du paramètre de Lode L sur la compétition entre les phénomènes de coalescence des cavités et de localisation des déformations plastiques macroscopiques. Pour cela, plusieurs indicateurs (ou critères) ont été couplés à la technique d'homogénéisation périodique. Cette étude comparative révèle que la localisation des déformations plastiques prédicta par

l'approche de bifurcation de Rice agit comme un précurseur de la coalescence des cavités prédictes par le critère de décharge élastique, lorsque le taux de triaxialité T se situe entre 0,7 et 3,0. D'un autre côté, lorsque $T \leq 2$, les déformations limites prédictes par la théorie de bifurcation de Rice sont beaucoup plus élevées que celles prédictes par d'autres critères de localisation définis dans la littérature (Bomarito et Warner, 2015 ; Tekoğlu et al., 2015 et Guo et Wong, 2018). Cependant, pour $T > 2$, les différents critères de localisation prédisent presque les mêmes déformations critiques. L'effet du paramètre de Lode L sur les déformations limites prédictes par les différents critères a également été étudié. Nous avons montré que cet effet est plus important pour les faibles valeurs de T .

2.3. Prédiction de la limite de ductilité des matériaux polycristallins

Dans cette deuxième étude, la limite de ductilité dans les agrégats polycristallins sera prédictée par le couplage de la technique d'homogénéisation périodique à l'approche de bifurcation de Rice. Dans ce cas, l'effet désstabilisant induisant la perte de ductilité est lié à l'utilisation de critère classique de Schmid. Ce dernier induit la formation de vertex sur la surface de plasticité associée.

Cette section est organisée comme suit :

- La Section 2.3.1 détaille l'adaptation de la technique d'homogénéisation périodique pour un état plan de contrainte macroscopique.
- La Section 2.3.2 présente brièvement les équations constitutives du monocristal et les techniques numériques adoptées pour résoudre ces équations.
- Les résultats numériques de la présente étude sont présentés et discutés dans la Section 2.3.3.
- La Section 2.3.4 clôture cette deuxième étude par quelques conclusions.

2.3.1. Adaptation de la technique d'homogénéisation périodique à un chargement en état plan de contraintes

L'objectif principal de la présente étude est de prédire l'apparition de la localisation de la déformation plastique dans les tôles métalliques minces en utilisant une stratégie multi-échelles basée sur la plasticité cristalline couplée à la méthode des éléments finis (communément connue sous le nom CPFEM). Compte tenu de la quasi-périodicité spatiale de la structure cristallographique dans les milieux polycristallins et par conséquent des différents champs mécaniques, le schéma d'homogénéisation périodique s'avère être un bon candidat pour construire cette stratégie. La première étape dans l'application de ce processus multi-échelles concerne la sélection d'une cellule de base qui doit assurer la représentativité de la tôle étudiée, comme illustré par la Fig. 2.10a. Pour l'analyse de la ductilité des tôles minces, une cellule de base 2D à travers l'épaisseur peut être sélectionnée, impliquant une homogénéisation par rapport au plan de référence de la tôle et un calcul classique dans le sens de l'épaisseur (Fig. 2.10a). Dans cette analyse, nous avons utilisé la technique de diagramme de Voronoï

pour générer la cellule de base occupant un volume initial $\mathcal{V}_0 = [0, l_0] \times [0, l_0] \times [0, 0.1l_0]$ et composée d'un grand nombre de grains de taille variable, comme schématisé sur la Fig. 2.10b. Dans cette cellule de base 2D, les joints de grains sont projetés dans la troisième direction afin de générer une géométrie 3D (avec un grain à travers l'épaisseur de la cellule de base). L'utilisation de la technique de diagramme de Voronoï permet de représenter de manière réaliste la morphologie des grains. L'orientation des cristaux en un point de la microstructure est spécifiée par un système de coordonnées cristallines locales dont l'orientation initiale est générée de manière aléatoire et varie d'un grain à l'autre. On suppose que les grains sont parfaitement délimités avec une continuité du déplacement et de la force à travers les interfaces entre les grains adjacents. La cellule de base est discrétisée par des éléments finis et, généralement, chaque grain est constitué de plusieurs éléments finis. Chaque point d'intégration de chaque élément fini représente un monocristal. Les équations constitutives à l'échelle monocrystalline et les schémas numériques développés pour les intégrer seront présentés dans la Section 2.3.2.

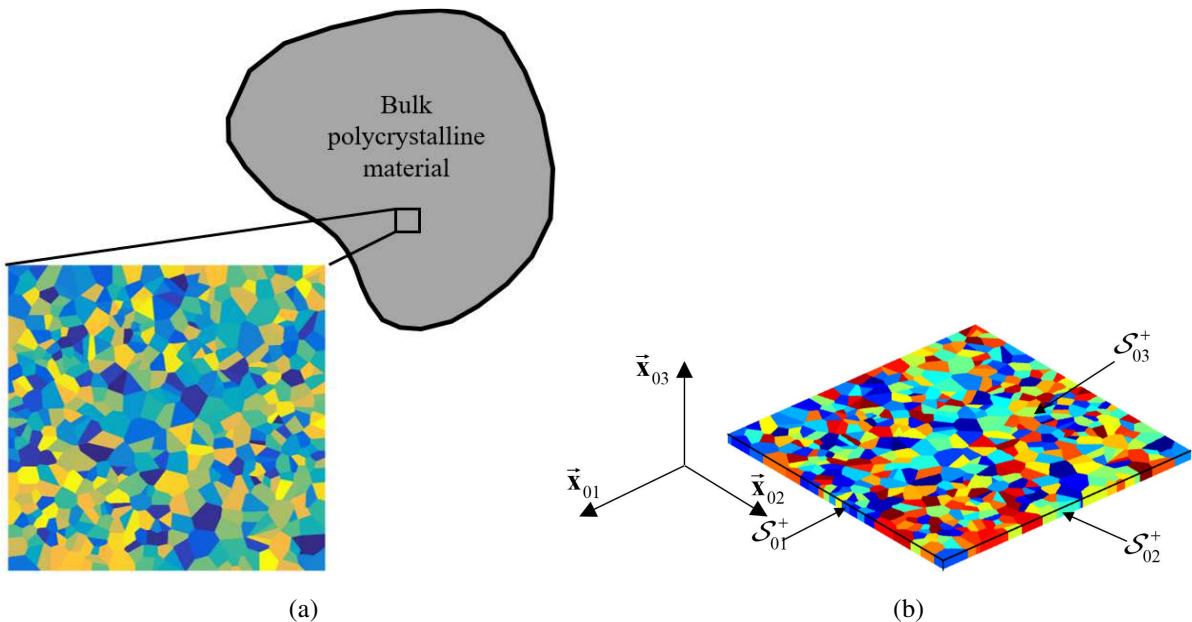


Fig. 2.10. Agrégat polycristallin : (a) sélection d'une cellule de base à partir d'une structure polycristalline ; (b) maillage par éléments finis de la cellule de base par la technique de diagramme de Voronoï.

La cellule de base étudiée est supposée être sollicitée en grandes déformations et une approche lagrangienne totale est utilisée pour formuler les relations d'homogénéisation périodique. En conséquence, le gradient de transformation et le premier tenseur des contraintes de Piola–Kirchhoff sont utilisés de manière appropriée comme mesures de déformation et de contrainte conjuguées. Pour prédire l'apparition de la localisation des déformations plastiques sous la forme de courbes limites de formage (CLF), la cellule de base est soumise à un chargement biaxial le long des directions 1 et 2, tout en restant sous un état plan de contrainte dans la troisième direction (Fig. 2.10). Les champs macroscopiques définissant ce chargement biaxial sont définis comme :

$$\mathbf{F} = \begin{pmatrix} F_{11} & 0 & ? \\ 0 & F_{22} & ? \\ ? & ? & ? \end{pmatrix} ; \quad \mathbf{P} = \begin{pmatrix} ? & ? & 0 \\ ? & ? & 0 \\ 0 & 0 & 0 \end{pmatrix}, \quad (2.45)$$

où les composantes notées « ? » sont inconnues et doivent être déterminées par les calculs par éléments finis. Ensuite, le chargement macroscopique est appliqué sur les directions orthogonales externes aux faces \mathcal{S}_{01}^- , \mathcal{S}_{01}^+ , \mathcal{S}_{02}^- et \mathcal{S}_{02}^+ . En revanche, les faces \mathcal{S}_{03}^- et \mathcal{S}_{03}^+ sont libres de tout chargement. Nous rappelons que ces faces sont définies par les composantes suivantes de coordonnées, comme le montre la Fig. 2.10b :

$$\begin{aligned} \mathcal{S}_{01}^- : x_{01} &= 0 & \mathcal{S}_{01}^+ : x_{01} &= l_0; \\ \mathcal{S}_{02}^- : x_{02} &= 0 & \mathcal{S}_{02}^+ : x_{02} &= l_0; \\ \mathcal{S}_{03}^- : x_{03} &= 0 & \mathcal{S}_{03}^+ : x_{03} &= 0.1l_0. \end{aligned} \quad (2.46)$$

Comme classiquement suivi dans la prédition de courbes limites de formage, les composantes F_{11} et F_{22} du gradient de transformation macroscopique \mathbf{F} sont définies en fonction du trajet de déformation ρ (compris entre $-1/2$ et 1) et la déformation principale majeure E_{11} :

$$F_{11} = e^{E_{11}} \quad ; \quad F_{22} = e^{E_{22}} \quad \text{avec} \quad E_{22} = \rho E_{11}. \quad (2.47)$$

Les principales équations du schéma multi-échelles d'homogénéisation périodique, décrites dans le Chapitre 1, seront adaptées ici pour la cinématique imposée pour prédire les CLF (chargement biaxial et état plan de contrainte). Pour cela, la relation cinématique (1.18) est remplacée par la forme plane suivante :

- Le gradient de transformation microscopique dans le plan ${}^{IN}\mathbf{f}$ est décomposé additivement en une partie macroscopique ${}^{IN}\mathbf{F}$ et un gradient de fluctuation périodique ${}^{IN}\mathbf{f}_{per}$, reflétant l'hétérogénéité du comportement mécanique induite par la différence d'orientation cristallographique entre les grains constitutifs (texture cristallographique) :

$${}^{IN}\mathbf{f} = {}^{IN}\mathbf{F} + {}^{IN}\mathbf{f}_{per}. \quad (2.48)$$

Les coordonnées courantes dans le plan ${}^{IN}\mathbf{x}$ (dans les directions 1 et 2) d'un point matériel sont ainsi déterminées par intégration spatiale de Eq. (2.48) :

$${}^{IN}\mathbf{x} = {}^{IN}\mathbf{F} \cdot {}^{IN}\mathbf{x}_0 + {}^{IN}\mathbf{u}_{per}, \quad (2.49)$$

où ${}^{IN}\mathbf{x}_0$ est le vecteur de coordonnées initiales du point matériel dans le plan, et ${}^{IN}\mathbf{u}_{per}$ est un déplacement périodique dans les directions 1 et 2 de la configuration initiale (non déformée) de la cellule élémentaire.

La dérivée temporelle de l'équation (2.49) permet d'obtenir l'expression de la vitesse dans le plan ${}^{IN}\mathbf{v}$:

$${}^{IN} \mathbf{v} = {}^{IN} \dot{\mathbf{F}} \cdot {}^{IN} \mathbf{x}_0 + {}^{IN} \dot{\mathbf{u}}_{per} := {}^{IN} \dot{\mathbf{F}} \cdot {}^{IN} \mathbf{x}_0 + {}^{IN} \mathbf{v}_{per}. \quad (2.50)$$

Les autres relations définissant le problème d'homogénéisation périodique sont les mêmes que celles présentées dans le premier chapitre (par souci de brièveté, ces relations ne seront pas rappelées dans ce chapitre).

Pour compléter l'approche numérique proposée dans le premier chapitre, nous démontrons ici uniquement l'adaptation de la condition de Hill–Mandel à un état plan de contrainte. Cette adaptation est nécessaire pour justifier la résolution des équations de l'homogénéisation périodique par la méthode des éléments finis. La condition de Hill–Mandel stipule l'équivalence énergétique incrémentale entre les échelles microscopique et macroscopique :

$$\int_{\mathcal{V}_0} \left[\frac{\partial \delta \mathbf{v}}{\partial \mathbf{x}_0} : \dot{\mathbf{p}} \right] d\mathcal{V}_0 - |\mathcal{V}_0| \delta \dot{\mathbf{F}} : \dot{\mathbf{P}} = 0. \quad (2.51)$$

Pour démontrer la validité de l'égalité (2.51), le membre de gauche de cette dernière équation peut être reformulé comme :

$$\int_{\mathcal{V}_0} \left[\frac{\partial \delta \mathbf{v}}{\partial \mathbf{x}_0} : \dot{\mathbf{p}} \right] d\mathcal{V}_0 - |\mathcal{V}_0| \delta \dot{\mathbf{F}} : \dot{\mathbf{P}} = \int_{\mathcal{S}_0} [\delta \mathbf{v} - \delta \dot{\mathbf{F}} \cdot \mathbf{x}_0] \cdot [\dot{\mathbf{t}}_0 - \dot{\mathbf{P}} \cdot \bar{\mathbf{n}}_0] d\mathcal{S}_0. \quad (2.52)$$

Après décomposition de la frontière totale de la cellule de base en six faces, le membre de droite de l'équation (2.52) peut être développé comme :

$$\begin{aligned} \int_{\mathcal{S}_0} [\delta \mathbf{v} - \delta \dot{\mathbf{F}} \cdot \mathbf{x}_0] \cdot [\dot{\mathbf{t}}_0 - \dot{\mathbf{P}} \cdot \bar{\mathbf{n}}_0] d\mathcal{S}_0 &= \int_{\mathcal{S}_{01}^- \cup \mathcal{S}_{01}^+ \cup \mathcal{S}_{02}^- \cup \mathcal{S}_{02}^+} [\delta \mathbf{v} - \delta \dot{\mathbf{F}} \cdot \mathbf{x}_0] \cdot [\dot{\mathbf{t}}_0 - \dot{\mathbf{P}} \cdot \bar{\mathbf{n}}_0] d\mathcal{S}_0 \\ &\quad + \int_{\mathcal{S}_{03}^- \cup \mathcal{S}_{03}^+} [\delta \mathbf{v} - \delta \dot{\mathbf{F}} \cdot \mathbf{x}_0] \cdot [\dot{\mathbf{t}}_0 - \dot{\mathbf{P}} \cdot \bar{\mathbf{n}}_0] d\mathcal{S}_0. \end{aligned} \quad (2.53)$$

En utilisant la relation cinématique (2.48), la première partie du membre de droite de l'équation (2.53) peut être transformé comme :

$$\begin{aligned} &\int_{\mathcal{S}_{01}^- \cup \mathcal{S}_{01}^+ \cup \mathcal{S}_{02}^- \cup \mathcal{S}_{02}^+} [\delta \mathbf{v} - \delta \dot{\mathbf{F}} \cdot \mathbf{x}_0] \cdot [\dot{\mathbf{t}}_0 - \dot{\mathbf{P}} \cdot \bar{\mathbf{n}}_0] d\mathcal{S}_0 \\ &= \int_{\mathcal{S}_{01}^- \cup \mathcal{S}_{01}^+ \cup \mathcal{S}_{02}^- \cup \mathcal{S}_{02}^+} [{}^{IN} \delta \mathbf{v} - {}^{IN} \delta \dot{\mathbf{F}} \cdot {}^{IN} \mathbf{x}_0] \cdot [{}^{IN} \dot{\mathbf{t}}_0 - {}^{IN} \dot{\mathbf{P}} \cdot {}^{IN} \bar{\mathbf{n}}_0] d\mathcal{S}_0 \\ &= \int_{\mathcal{S}_{01}^- \cup \mathcal{S}_{01}^+ \cup \mathcal{S}_{02}^- \cup \mathcal{S}_{02}^+} {}^{IN} \delta \mathbf{v}_{per} \cdot [{}^{IN} \dot{\mathbf{t}}_0 - {}^{IN} \dot{\mathbf{P}} \cdot {}^{IN} \bar{\mathbf{n}}_0] d\mathcal{S}_0, \end{aligned} \quad (2.54)$$

où ${}^{IN} \delta \mathbf{v}$, ${}^{IN} \mathbf{x}_0$, ${}^{IN} \dot{\mathbf{t}}_0$, ${}^{IN} \bar{\mathbf{n}}_0$, ${}^{IN} \delta \mathbf{v}_{per}$, ${}^{IN} \delta \dot{\mathbf{F}}$ et ${}^{IN} \dot{\mathbf{P}}$ sont les formes planes des champs vectoriels et tensoriels $\delta \mathbf{v}$, \mathbf{x}_0 , $\dot{\mathbf{t}}_0$, $\bar{\mathbf{n}}_0$, $\delta \mathbf{v}_{per}$, $\delta \dot{\mathbf{F}}$ et $\dot{\mathbf{P}}$, respectivement. La périodicité du vecteur ${}^{IN} \delta \mathbf{v}_{per}$ et l'anti-périodicité du vecteur $[{}^{IN} \dot{\mathbf{t}}_0 - {}^{IN} \dot{\mathbf{P}} \cdot {}^{IN} \bar{\mathbf{n}}_0]$ sur l'ensemble des faces $\mathcal{S}_{01}^- \cup \mathcal{S}_{01}^+ \cup \mathcal{S}_{02}^- \cup \mathcal{S}_{02}^+$ conduisent à l'égalité intégrale suivante :

$$\int_{\mathcal{S}_{01}^- \cup \mathcal{S}_{01}^+ \cup \mathcal{S}_{02}^- \cup \mathcal{S}_{02}^+} {}^{IN} \delta \mathbf{v}_{per} \cdot [{}^{IN} \dot{\mathbf{t}}_0 - {}^{IN} \dot{\mathbf{P}} \cdot {}^{IN} \bar{\mathbf{n}}_0] d\mathcal{S}_0 = 0. \quad (2.55)$$

En tenant compte des équations (2.54) et (2.55), la condition Hill–Mandel donnée par l'équation (2.51) est validée pour un état plan de contrainte.

2.3.2. Modélisation du comportement d'un monocristal élastoplastique

Un monocristal est affecté à chaque point d'intégration du maillage de la cellule de base (Fig. 2.10b). Pour résoudre complètement le problème d'homogénéisation périodique, les équations constitutives du monocristal doivent être entièrement formulées et résolues. C'est la tâche principale de la section courante.

2.3.2.1. Équations constitutives

Comme point de départ pour la présentation des équations constitutives du monocristal, le gradient de vitesse microscopique \mathbf{g} est exprimé en fonction du gradient de transformation microscopique \mathbf{f} par la relation classique :

$$\mathbf{g} = \dot{\mathbf{f}} \cdot \mathbf{f}^{-1}, \quad (2.56)$$

où \mathbf{f} est déterminé à chaque point d'intégration par le calcul par éléments finis.

Comme indiqué précédemment, le comportement monocrystallin est supposé être élastoplastique. Par conséquent, \mathbf{f} peut être décomposé de manière multiplicative en partie élastique \mathbf{f}^e et partie plastique \mathbf{f}^p :

$$\mathbf{f} = \mathbf{f}^e \cdot \mathbf{f}^p. \quad (2.57)$$

La partie élastique \mathbf{f}^e peut, à son tour, être décomposée en un tenseur de déformation symétrique \mathbf{v}^e et une rotation $\bar{\mathbf{r}}$ définissant l'orientation du système de coordonnées associé à la configuration intermédiaire ou relâchée par rapport à la configuration actuelle (déformée) :

$$\mathbf{f}^e = \mathbf{v}^e \cdot \bar{\mathbf{r}}. \quad (2.58)$$

La combinaison des équations (2.56), (2.57) et (2.58) permet d'obtenir l'expression du tenseur \mathbf{g} :

$$\begin{aligned} \mathbf{g} &= \dot{\mathbf{f}} \cdot \mathbf{f}^{-1} = \dot{\mathbf{f}}^e \cdot \mathbf{f}^{e-1} + \mathbf{f}^e \cdot \dot{\mathbf{f}}^p \cdot \mathbf{f}^{p-1} \cdot \mathbf{f}^{e-1} \\ &= \dot{\mathbf{v}}^e \cdot \mathbf{v}^{e-1} + \mathbf{v}^e \cdot \dot{\bar{\mathbf{r}}} \cdot \bar{\mathbf{r}}^T \cdot \mathbf{v}^{e-1} + \mathbf{v}^e \cdot \bar{\mathbf{r}} \cdot \dot{\mathbf{f}}^p \cdot \mathbf{f}^{p-1} \cdot \bar{\mathbf{r}}^T \cdot \mathbf{v}^{e-1}. \end{aligned} \quad (2.59)$$

Comme pour la majorité des matériaux métalliques, la déformation élastique reste très faible par rapport à l'unité (c'est-à-dire, $\mathbf{v}^e \approx \mathbf{I}_2$). En conséquence, l'équation (2.59) peut être simplifiée comme :

$$\mathbf{g} = \dot{\mathbf{v}}^e + \dot{\bar{\mathbf{r}}} \cdot \bar{\mathbf{r}}^T + \bar{\mathbf{r}} \cdot \dot{\mathbf{f}}^p \cdot \mathbf{f}^{p-1} \cdot \bar{\mathbf{r}}^T. \quad (2.60)$$

Le gradient de vitesse \mathbf{g} peut être décomposé additivement en ses parties symétrique \mathbf{d} et anti-symétrique \mathbf{w} :

$$\mathbf{g} = \mathbf{d} + \mathbf{w} \quad \text{avec} \quad \mathbf{d} = \frac{1}{2}(\mathbf{g} + \mathbf{g}^T) \quad \text{et} \quad \mathbf{w} = \frac{1}{2}(\mathbf{g} - \mathbf{g}^T). \quad (2.61)$$

Les tenseurs \mathbf{d} et \mathbf{w} sont eux-mêmes décomposés en parties élastiques et plastiques \mathbf{d}^e , \mathbf{d}^p , \mathbf{w}^e et \mathbf{w}^p :

$$\begin{aligned}\mathbf{d} &= \mathbf{d}^e + \mathbf{d}^p \quad ; \quad \mathbf{w} = \mathbf{w}^e + \mathbf{w}^p; \\ \mathbf{d}^e &= \dot{\mathbf{v}}^e \quad ; \quad \mathbf{d}^p = \frac{1}{2} \bar{\mathbf{r}} \cdot (\dot{\mathbf{f}}^p \cdot \mathbf{f}^{p-1} + (\dot{\mathbf{f}}^p \cdot \mathbf{f}^{p-1})^T) \cdot \bar{\mathbf{r}}^T; \\ \mathbf{w}^e &= \dot{\bar{\mathbf{r}}} \cdot \bar{\mathbf{r}}^T \quad ; \quad \mathbf{w}^p = \frac{1}{2} \bar{\mathbf{r}} \cdot (\dot{\mathbf{f}}^p \cdot \mathbf{f}^{p-1} - (\dot{\mathbf{f}}^p \cdot \mathbf{f}^{p-1})^T) \cdot \bar{\mathbf{r}}^T.\end{aligned}\quad (2.62)$$

En supposant que la déformation plastique est exclusivement due au glissement sur les systèmes cristallographiques, la partie plastique $\bar{\mathbf{r}} \cdot \dot{\mathbf{f}}^p \cdot \mathbf{f}^{p-1} \cdot \bar{\mathbf{r}}^T$ du gradient de vitesse peut être exprimée sous la forme :

$$\bar{\mathbf{r}} \cdot \dot{\mathbf{f}}^p \cdot \mathbf{f}^{p-1} \cdot \bar{\mathbf{r}}^T = \dot{\gamma}^\alpha \mathbf{M}^\alpha \quad ; \quad \alpha = 1, \dots, N_s, \quad (2.63)$$

Où :

- N_s représente le nombre total de systèmes de glissement (égal à 12 pour les monocristaux CFC considérés dans la présente étude).
- $\dot{\gamma}^\alpha$ désigne la valeur algébrique de la vitesse de glissement relative au système cristallographique α .
- \mathbf{M}^α désigne le tenseur d'orientation de Schmid relatif au système α , égal au produit tensoriel du vecteur de direction de glissement $\vec{\mathbf{m}}^\alpha$ et du vecteur normal au plan de glissement $\vec{\mathbf{n}}^\alpha$:

$$\mathbf{M}^\alpha = \vec{\mathbf{m}}^\alpha \otimes \vec{\mathbf{n}}^\alpha. \quad (2.64)$$

Pour des raisons pratiques évidentes et afin de ne manipuler que des valeurs positives de vitesses de glissement dans les développements théoriques et numériques suivants, il est plus pratique de décomposer chaque système de glissement en deux pseudo-systèmes opposés $(\vec{\mathbf{m}}^\alpha, \vec{\mathbf{n}}^\alpha)$ et $(-\vec{\mathbf{m}}^\alpha, \vec{\mathbf{n}}^\alpha)$, numérotés α et $\alpha + N_s$, respectivement. Avec cette décomposition, l'équation (2.63) sera exprimée sous la forme suivante :

$$\bar{\mathbf{r}} \cdot \dot{\mathbf{f}}^p \cdot \mathbf{f}^{p-1} \cdot \bar{\mathbf{r}}^T = \dot{\gamma}^\alpha \mathbf{M}^\alpha \quad \text{avec} \quad \dot{\gamma}^\alpha \geq 0 \quad ; \quad \alpha = 1, \dots, 2N_s. \quad (2.65)$$

En utilisant l'équation (2.65), le taux de déformation plastique \mathbf{d}^p et le taux de rotation plastique \mathbf{w}^p , introduits dans l'équation (2.62), peuvent être exprimés en fonction des parties symétrique et anti-symétrique \mathbf{R}^α et \mathbf{S}^α du tenseur de Schmid \mathbf{M}^α :

$$\mathbf{d}^p = \dot{\gamma}^\alpha \mathbf{R}^\alpha \quad ; \quad \mathbf{w}^p = \dot{\gamma}^\alpha \mathbf{S}^\alpha \quad ; \quad \alpha = 1, \dots, 2N_s. \quad (2.66)$$

La rotation $\bar{\mathbf{r}}$ est choisie de telle sorte que le transport du tenseur de Schmid \mathbf{M}^α dans la configuration intermédiaire relâchée reste constant et égal à $\vec{\mathbf{m}}_0^\alpha \otimes \vec{\mathbf{n}}_0^\alpha$ durant le chargement (Fig. 2.11) :

$$\mathbf{M}_0^\alpha = \bar{\mathbf{r}}^T \cdot \mathbf{M}^\alpha \cdot \bar{\mathbf{r}}. \quad (2.67)$$

La numérotation détaillée des vecteurs $\vec{\mathbf{m}}_0^\alpha$ et $\vec{\mathbf{n}}_0^\alpha$ des monocristaux CFC est fournie dans l'Annexe C.

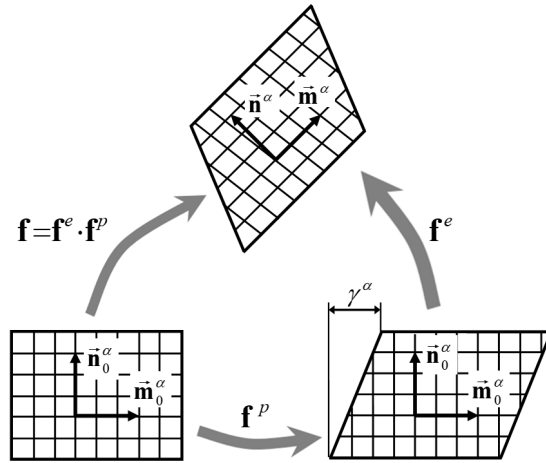


Fig. 2.11. Illustration schématique de la décomposition multiplicative du gradient de transformation \mathbf{f} : glissement plastique et rotation rigide avec distorsion élastique du réseau cristallographique.

Pour satisfaire le principe d'objectivité, les équations constitutives (2.60), (2.62) et (2.65) peuvent être exprimées dans le repère du réseau cristallin défini par la rotation $\bar{\mathbf{r}}$. Par souci de clarté, les tenseurs et vecteurs exprimés dans ce repère seront surlignés dans les développements suivants. Dans ce repère, le gradient de vitesse \mathbf{g} a la forme suivante :

$$\bar{\mathbf{g}} = \bar{\mathbf{r}}^T \cdot \mathbf{g} \cdot \bar{\mathbf{r}} = \bar{\mathbf{d}} + \bar{\mathbf{w}}, \quad (2.68)$$

où $\bar{\mathbf{d}}$ et $\bar{\mathbf{w}}$ sont déduits des équations (2.62) et (2.65) par :

$$\bar{\mathbf{d}} = \bar{\mathbf{d}}^e + \bar{\mathbf{d}}^p \quad ; \quad \bar{\mathbf{w}} = \bar{\mathbf{r}}^T \cdot \dot{\bar{\mathbf{r}}} + \bar{\mathbf{w}}^p \quad ; \quad \bar{\mathbf{d}}^p = \dot{\gamma}^\alpha \mathbf{R}_0^\alpha \quad ; \quad \bar{\mathbf{w}}^p = \dot{\gamma}^\alpha \mathbf{S}_0^\alpha \quad ; \quad \alpha = 1, \dots, 2N_s. \quad (2.69)$$

L'élasticité est supposée être isotrope et linéaire et elle est modélisée par la loi de Hooke :

$$\dot{\bar{\sigma}} = \bar{\mathbf{c}}^e : \bar{\mathbf{d}}^e, \quad (2.70)$$

où $\bar{\mathbf{c}}^e$ est le tenseur d'élasticité du quatrième ordre exprimé dans le repère du réseau cristallin (comme l'élasticité est isotrope, $\bar{\mathbf{c}}^e$ est identique à \mathbf{c}^e) et $\dot{\bar{\sigma}}$ est la dérivée temporelle du tenseur des contraintes de Cauchy tourné dans le repère du réseau cristallin $\bar{\sigma}$ ($= \bar{\mathbf{r}}^T \cdot \sigma \cdot \bar{\mathbf{r}}$). L'utilisation de l'équation (2.70) au lieu de la forme classique de la relation d'élasticité ($\dot{\sigma} = \mathbf{c}^e : \mathbf{d}^e$) permet d'assurer l'objectivité du modèle de comportement.

Pour un comportement élastoplastique, l'écoulement plastique est défini par la loi de Schmid qui suppose que le glissement se produit sur un système de glissement α (c'est-à-dire $\dot{\gamma}^\alpha \geq 0$), uniquement lorsque la cission résolue τ^α atteint une valeur critique τ_c^α :

$$\forall \alpha = 1, \dots, 2N_s : \begin{cases} \tau^\alpha < \tau_c^\alpha \Rightarrow \dot{\gamma}^\alpha = 0; \\ \tau^\alpha = \tau_c^\alpha \Rightarrow \dot{\gamma}^\alpha \geq 0, \end{cases} \quad (2.71)$$

où la cission résolue τ^α est calculée à partir du tenseur des contraintes de Cauchy σ et du tenseur de Schmid \mathbf{R}^α selon l'expression :

$$\forall \alpha = 1, \dots, 2N_s : \tau^\alpha = \sigma : \mathbf{R}^\alpha = \bar{\sigma} : \mathbf{R}_0^\alpha. \quad (2.72)$$

L'équation (2.71) peut être exprimée de manière équivalente sous la forme d'un problème de complémentarité non-linéaire (NLCP) :

$$\forall \alpha = 1, \dots, 2N_s : \chi^\alpha = \tau_c^\alpha - \tau^\alpha \geq 0 ; \quad \dot{\gamma}^\alpha \geq 0 ; \quad \chi^\alpha \dot{\gamma}^\alpha = 0. \quad (2.73)$$

Les cissions critiques τ_c^α ont une valeur initiale τ_0 et évoluent en fonction des vitesses de glissement sur les différents systèmes cristallographiques selon la loi d'écrouissage générique suivante :

$$\forall \alpha = 1, \dots, N_s : \dot{\tau}_c^\alpha = \dot{\tau}_c^{\alpha+N_s} = H^{\alpha\beta} (\dot{\gamma}^\beta + \dot{\gamma}^{\beta+N_s}) ; \quad \beta = 1, \dots, N_s, \quad (2.74)$$

où $H^{\alpha\beta}$ est la composante $\alpha\beta$ de la matrice d'écrouissage \mathbf{H} qui dépend des glissements cumulés sur les différents systèmes de glissement et de certains paramètres d'écrouissage. L'expression explicite de la matrice d'écrouissage utilisée dans la présente étude sera donnée dans la Section 2.3.3.

2.3.2.2. Intégration numérique

Les équations constitutives du monocristal sont implantées dans le code EF ABAQUS / Standard via une routine matériau utilisateur (UMAT). Dans cette implantation, les équations constitutives sont intégrées sur un incrément de temps typique $I^\Delta = [t_0, t_0 + \Delta t]$, en utilisant un schéma d'intégration évolutif (communément connu en anglais sous le nom ‘ultimate algorithm’). La famille des algorithmes évolutifs a été initialement introduite par [Borja et Wren \(1993\)](#) pour le cas d'un modèle linéaire (écrouissage linéaire et petites déformations élastoplastiques). Par la suite, cet algorithme a été étendu par [Ben Bettaieb et al. \(2012\)](#) aux modèles non-linéaires (écrouissage non-linéaire, grandes déformations et rotations). La haute performance et la robustesse de l'algorithme évolutif, comparé à l'algorithme de type retour radial ([Anand et Kothari, 1996](#)) pour l'intégration des équations constitutives des monocristaux élastoplastiques, ont été mises en évidence par [Akpama et al. \(2016\)](#) en se basant sur une étude comparative approfondie. De plus, il a été prouvé dans [Akpama et al. \(2016\)](#) que la version explicite de l'algorithme évolutif est plus efficace que la version implicite, car elle permet d'obtenir des prédictions assez précises avec un coût de calcul réduit. Par conséquent, l'algorithme évolutif explicite est adopté dans la présente étude pour intégrer les équations constitutives du monocristal. Le concept d'algorithme évolutif repose sur l'idée de partition de l'incrément de temps en plusieurs sous-incréments $I^{\delta_n} = [t_n, t_{n+1}]$ (où $t_{n=0} = t_0$). La taille $\delta t_n = t_{n+1} - t_n$ du sous-incrément I^{δ_n} est *a priori* inconnue. Elle doit être déterminée de manière à ce que le critère de Schmid (2.71) reste vérifié sur I^{δ_n} . En adoptant cette partition, les équations constitutives à l'échelle du monocristal doivent être intégrées sur chaque sous-incrément de temps I^{δ_n} et les différentes variables mécaniques mises à jour d'un sous-incrément à l'autre.

L'entrée principale de l'UMAT est le gradient de vitesse \mathbf{g} qui est supposé être constant sur I^Δ (donc, sur I^{δ_n}) et est calculé à partir de $\mathbf{f}(t_0)$ et $\mathbf{f}(t_0 + \Delta t)$ par l'approximation :

$$\mathbf{g} = \left(\frac{\mathbf{f}(t_0 + \Delta t) - \mathbf{f}(t_0)}{\Delta t} \right) \cdot \left(\frac{\mathbf{f}(t_0 + \Delta t) + \mathbf{f}(t_0)}{\Delta t} \right)^{-1}. \quad (2.75)$$

Pour être cohérent avec le concept de mise en œuvre des équations constitutives dans le code EF ABAQUS / standard, introduisons le repère co-rotationnel défini par la rotation $\check{\mathbf{r}}$ ($\neq \bar{\mathbf{r}}$) par rapport au repère fixe. La rotation $\check{\mathbf{r}}$ évolue selon la loi :

$$\dot{\check{\mathbf{r}}} \cdot \check{\mathbf{r}}^T = \mathbf{w}, \quad (2.76)$$

où \mathbf{w} est la partie anti-symétrique du gradient de vitesse \mathbf{g} déterminé par l'équation (2.75). Les quantités vectorielles et tensorielles exprimées dans le repère co-rotationnel défini par la rotation $\check{\mathbf{r}}$ seront surlignées par une ligne ondulée.

Les autres entrées de l'UMAT sont :

- Les paramètres d'élasticité et d'écrouissage.
- La rotation du repère co-rotationnel $\check{\mathbf{r}}$ et la rotation du réseau cristallographique liées à la configuration intermédiaire $\bar{\mathbf{r}}$ à t_n .
- Le tenseur des contraintes de Cauchy exprimé dans le repère co-rotationnel $\check{\sigma}$ à t_n .
- Les glissements γ^α et les cissions critiques τ_c^α (pour $\alpha=1,\dots,2N_s$) à t_n .

En tant que sorties, les inconnues suivantes doivent être déterminées :

- Les rotations $\check{\mathbf{r}}$ et $\bar{\mathbf{r}}$ à t_{n+1} .
- Le tenseur des contraintes de Cauchy exprimé dans le repère co-rotationnel $\check{\sigma}$ à t_{n+1} .
- Les glissements γ^α et les cissions critiques τ_c^α (pour $\alpha=1,\dots,2N_s$) à t_{n+1} .
- Le module tangent cohérent exprimé dans le repère co-rotationnel $\check{\mathbf{c}}^{ep}$ (c.à.d., la matrice **DDSDDE**, en utilisant la terminologie d'ABAQUS) défini par l'expression suivante :

$$\check{\mathbf{c}}^{ep} = \frac{\partial \delta \check{\sigma}}{\partial \delta \check{\epsilon}}, \quad (2.77)$$

où $\delta \check{\sigma}$ est la variation du tenseur $\check{\sigma}$ sur le sous-incrément de temps I^{δ_n} et $\delta \check{\epsilon}$ est l'intégrale de $\check{\mathbf{d}}$ sur le même sous-incrément.

Pour mettre clairement en évidence la dépendance des différentes quantités par rapport au temps, une variable \bullet évaluée à t_n (resp. t_{n+1}) sera notée $\bullet(t_n)$ (resp. $\bullet(t_{n+1})$).

La rotation du repère co-rotationnel $\check{\mathbf{r}}(t_{n+1})$ peut être déterminée à partir de son homologue au début du sous-incrément $\check{\mathbf{r}}(t_n)$ et \mathbf{w} en intégrant l'équation différentielle (2.76) sur I^{δ_n} :

$$\check{\mathbf{r}}(t_{n+1}) = e^{\delta_n \mathbf{w}} \cdot \check{\mathbf{r}}(t_n). \quad (2.78)$$

Une analyse rapide des équations constitutives du monocristal permet de conclure que le calcul des vitesses de glissement $\dot{\gamma}^\alpha(t_n)$ pour les différents systèmes de glissement est suffisant pour déterminer

l'évolution des autres variables mécaniques sur le sous-incrément de temps courant I^{δ_n} et en particulier leurs valeurs à t_{n+1} (à savoir $\bar{\mathbf{r}}(t_{n+1})$, $\bar{\boldsymbol{\sigma}}(t_{n+1})$, $\gamma^\alpha(t_{n+1})$, $\tau_c^\alpha(t_{n+1})$ et $\bar{\mathbf{c}}^{ep}$).

Pour calculer ces vitesses de glissement, introduisons l'ensemble des systèmes de glissement potentiellement actifs \mathcal{P} à l'instant t_n défini comme suit :

$$\mathcal{P} = \left\{ \alpha = 1, \dots, 2N_s : \tau^\alpha(t_n) - \tau_c^\alpha(t_n) = \bar{\boldsymbol{\sigma}}(t_n) : \mathbf{R}_0^\alpha(t_n) - \tau_c^\alpha(t_n) = 0 \right\}. \quad (2.79)$$

Considérant la définition (2.79), la loi de Schmid définie par l'équation (2.71) peut être réduite à l'ensemble des systèmes de glissement potentiellement actifs \mathcal{P} (car les vitesses de glissement des systèmes cristallographiques n'appartenant pas à \mathcal{P} sont évidemment égales à zéro) :

$$\forall \alpha \in \mathcal{P} : \dot{\chi}^\alpha(t_n) = \dot{\tau}_c^\alpha(t_n) - \dot{\tau}^\alpha(t_n) \geq 0 ; \dot{\gamma}^\alpha(t_n) \geq 0 ; \dot{\chi}^\alpha(t_n) \dot{\gamma}^\alpha(t_n) = 0. \quad (2.80)$$

En utilisant les égalités (2.69), (2.70), (2.72) et (2.73), les composantes $\dot{\chi}^\alpha(t_n)$ peuvent s'exprimer comme :

$$\begin{aligned} \forall \alpha \in \mathcal{P} : \dot{\chi}^\alpha(t_n) &= \dot{\tau}_c^\alpha(t_n) - \dot{\tau}^\alpha(t_n) = H^{\alpha\beta} \dot{\gamma}^\beta(t_n) - \dot{\bar{\boldsymbol{\sigma}}}(t_n) : \mathbf{R}_0^\alpha \\ &= H^{\alpha\beta}(t_n) \dot{\gamma}^\beta(t_n) - \bar{\mathbf{d}}^e(t_n) : \mathbf{c}^e : \mathbf{R}_0^\alpha \\ &= H^{\alpha\beta}(t_n) \dot{\gamma}^\beta(t_n) - (\bar{\mathbf{d}}(t_n) - \dot{\gamma}^\beta(t_n) \mathbf{R}_0^\beta) : \mathbf{c}^e : \mathbf{R}_0^\alpha \\ &= A^{\alpha\beta}(t_n) \dot{\gamma}^\beta(t_n) - B^\alpha(t_n) ; \beta \in \mathcal{P}, \end{aligned} \quad (2.81)$$

où la matrice $\mathbf{A}(t_n)$ et le vecteur $\mathbf{B}(t_n)$ sont donnés par les formes indicielles suivantes :

$$\forall \alpha, \beta \in \mathcal{P} : A^{\alpha\beta}(t_n) = H^{\alpha\beta}(t_n) + \mathbf{R}_0^\alpha : \mathbf{c}^e : \mathbf{R}_0^\beta ; B^\alpha(t_n) = \mathbf{R}_0^\alpha : \mathbf{c}^e : \bar{\mathbf{d}}(t_n). \quad (2.82)$$

La substitution des équations (2.81) et (2.82) dans la loi de Schmid (2.80) conduit à la forme matricielle suivante qui est plus adaptée à une mise en œuvre numérique :

$$\forall \alpha \in \mathcal{P} : \begin{cases} \dot{\chi}^\alpha(t_n) = A^{\alpha\beta}(t_n) \dot{\gamma}^\beta(t_n) - B^\alpha(t_n) \geq 0 ; \\ \dot{\gamma}^\alpha(t_n) \geq 0 ; \\ (A^{\alpha\beta}(t_n) \dot{\gamma}^\beta(t_n) - B^\alpha(t_n)) \dot{\gamma}^\alpha(t_n) = 0. \end{cases} ; \beta \in \mathcal{P}. \quad (2.83)$$

Comme les composantes de $\mathbf{A}(t_n)$ et $\mathbf{B}(t_n)$ sont déterminées au début du sous-incrément I^{δ_n} (donc constantes sur I^{δ_n}), le problème NLCP donné par l'équation (2.73) est transformé en un problème de complémentarité linéaire (LCP), tel que formulé par l'équation (2.83). Ce problème LCP peut être facilement résolu par une procédure de recherche combinatoire, identique à celle présentée dans Akpama et al. (2016), pour calculer les vitesses de glissement des systèmes potentiellement actifs et par conséquent pour distinguer l'ensemble des systèmes de glissement actifs \mathcal{A} de l'ensemble des systèmes de glissement potentiels, mais inactifs \mathcal{NA} :

$$\begin{aligned} \mathcal{A} \cup \mathcal{NA} &= \mathcal{P} \text{ et } \mathcal{A} \cap \mathcal{NA} = \emptyset \\ \forall \alpha \in \mathcal{A} : \dot{\gamma}^\alpha(t_n) &> 0 ; \forall \alpha \in \mathcal{NA} : \dot{\gamma}^\alpha(t_n) = 0. \end{aligned} \quad (2.84)$$

Plus de détails concernant la technique de recherche combinatoire peuvent être consultés dans Akpama et al. (2016).

Une fois les vitesses de glissement des systèmes potentiellement actifs calculés, la taille I^{δ_n} du sous-incrément courant peut être déterminée en respectant les conditions suivantes : δt_n doit être inférieure ou égale à Δt et le critère Schmid doit être respecté pour tous les systèmes de glissement sur I^{δ_n} . Au vu de l'équation (2.83), il est évident que ce critère est rempli pour les systèmes de glissement potentiellement actifs. Pour les autres systèmes ($\notin \mathcal{P}$), la condition suivante doit être vérifiée :

$$\forall \alpha \notin \mathcal{P} : \tau^\alpha(t_{n+1}) \leq \tau_c^\alpha(t_{n+1}). \quad (2.85)$$

En utilisant les définitions de τ^α et τ_c^α , les relations suivantes peuvent être facilement établies :

$$\forall \alpha \notin \mathcal{P} : \begin{cases} \tau^\alpha(t_{n+1}) = \tau^\alpha(t_n) + \delta t_n \mathbf{R}_0^\alpha : \dot{\bar{\sigma}}(t_n) \\ \quad = \tau^\alpha(t_n) + \delta t_n \mathbf{R}_0^\alpha : \mathbf{c}^e : (\bar{\mathbf{d}}(t_n) - \dot{\gamma}^\beta(t_n) \mathbf{R}_0^\beta), \\ \tau_c^\alpha(t_{n+1}) = \tau_c^\alpha(t_n) + \delta t_n H^{\alpha\beta}(t_n) \dot{\gamma}^\beta(t_n) ; \beta \in \mathcal{P}. \end{cases} \quad (2.86)$$

La combinaison des équations (2.85) et (2.86) permet d'exprimer le problème de détermination de δt_n sous la forme du problème de minimisation suivant :

$$\delta t_n = \min_{\alpha \in \mathcal{P}} \left\{ \Delta t, \frac{\tau_c^\alpha(t_n) - \tau^\alpha(t_n)}{\mathbf{R}_0^\alpha : \mathbf{c}^e : (\bar{\mathbf{d}}(t_n) - \dot{\gamma}^\beta(t_n) \mathbf{R}_0^\beta) - H^{\alpha\beta}(t_n) \dot{\gamma}^\beta(t_n)} \right\} ; \beta \in \mathcal{P}. \quad (2.87)$$

Une fois que la longueur δt_n du sous-incrément courant I^{δ_n} est déterminée, les autres variables mécaniques peuvent être actualisées comme :

$$\begin{aligned} \bar{\mathbf{r}}(t_n) &= e^{(\delta t_n (\bar{\mathbf{w}}(t_n) - \dot{\gamma}^\alpha(t_n) \mathbf{s}_0^\alpha))} ; \alpha \in \mathcal{A}; \\ \bar{\mathbf{r}}(t_{n+1}) &= \bar{\mathbf{r}}(t_n) \cdot \delta \bar{\mathbf{r}}(t_n); \\ \dot{\bar{\sigma}}(t_n) &= \mathbf{c}^e : (\bar{\mathbf{d}}(t_n) - \dot{\gamma}^\alpha(t_n) \mathbf{R}_0^\alpha) ; \alpha \in \mathcal{A}; \\ \bar{\sigma}(t_{n+1}) &= \bar{\sigma}(t_n) + \delta t_n \dot{\bar{\sigma}}(t_n); \\ \sigma(t_{n+1}) &= \bar{\mathbf{r}}(t_{n+1}) \cdot \bar{\sigma}(t_{n+1}) \cdot \bar{\mathbf{r}}^T(t_{n+1}); \\ \forall \alpha = 1, \dots, 2N_s : & \begin{cases} \gamma^\alpha(t_{n+1}) = \gamma^\alpha(t_n) + \delta t_n \dot{\gamma}^\alpha(t_n); \\ \tau_c^\alpha(t_{n+1}) = \tau_c^\alpha(t_n) + \delta t_n H^{\alpha\beta}(t_n) \dot{\gamma}^\beta(t_n) ; \beta \in \mathcal{A}. \end{cases} \end{aligned} \quad (2.88)$$

Le tenseur des contraintes de Cauchy $\sigma(t_{n+1})$ est calculé par l'équation (2.88)₅. Il doit être tourné dans le repère co-rotationnel défini par la rotation $\check{\mathbf{r}}(t_{n+1})$ qui est mise à jour par l'équation (2.78) pour obtenir :

$$\check{\sigma}(t_{n+1}) = \check{\mathbf{r}}^T(t_{n+1}) \cdot \sigma(t_{n+1}) \cdot \check{\mathbf{r}}(t_{n+1}). \quad (2.89)$$

Pour compléter le développement de ce schéma d'intégration, il faut déterminer le module tangent cohérent $\check{\mathbf{c}}^{ep}$. Le schéma d'intégration étant explicite, ce module tangent peut être déduit de la relation suivante entre $\delta \check{\sigma}$ et $\delta \check{\epsilon}$:

$$\delta \check{\sigma} = \check{\mathbf{c}}^{ep} : \delta \check{\epsilon}. \quad (2.90)$$

Le sous-incrément de contrainte $\delta \check{\sigma}$ peut être exprimé comme :

$$\delta \check{\sigma} = \check{\sigma}(t_{n+1}) - \check{\sigma}(t_n) = \check{\mathbf{r}}^T(t_{n+1}) \cdot \sigma(t_{n+1}) \cdot \check{\mathbf{r}}(t_{n+1}) - \check{\sigma}(t_n) = \hat{\mathbf{r}}(t_{n+1}) \cdot \bar{\sigma}(t_{n+1}) \cdot \hat{\mathbf{r}}^T(t_{n+1}) - \check{\sigma}(t_n), \quad (2.91)$$

où $\hat{\mathbf{r}}$ est la rotation de la configuration intermédiaire par rapport au repère co-rotationnel. Cette rotation est définie par la règle d'évolution suivante :

$$\hat{\mathbf{r}}(t_{n+1}) = e^{-\delta t_n \tilde{\mathbf{w}}^P(t_n)} \cdot \hat{\mathbf{r}}(t_n) = e^{-\delta t_n \dot{\gamma}^\alpha(t_n)} \tilde{\mathbf{s}}^\alpha(t_n) \cdot \hat{\mathbf{r}}(t_n) ; \quad \alpha \in \mathcal{A}. \quad (2.92)$$

En utilisant l'équation (2.88)₄, $\delta\tilde{\sigma}$ peut être réécrit comme :

$$\begin{aligned} \delta\tilde{\sigma} &= \tilde{\sigma}(t_{n+1}) - \tilde{\sigma}(t_n) = \hat{\mathbf{r}}(t_{n+1}) \cdot (\bar{\sigma}(t_n) + \delta t_n \dot{\bar{\sigma}}(t_n)) \cdot \hat{\mathbf{r}}^T(t_{n+1}) - \tilde{\sigma}(t_n) \\ &= [\hat{\mathbf{r}}(t_{n+1}) \cdot \hat{\mathbf{r}}^T(t_n)] \cdot \tilde{\sigma}(t_n) \cdot [\hat{\mathbf{r}}(t_{n+1}) \cdot \hat{\mathbf{r}}^T(t_n)]^T + \delta t_n \hat{\mathbf{r}}(t_{n+1}) \cdot \dot{\bar{\sigma}}(t_n) \cdot \hat{\mathbf{r}}^T(t_{n+1}) - \tilde{\sigma}(t_n). \end{aligned} \quad (2.93)$$

Les expressions de $[\hat{\mathbf{r}}(t_{n+1}) \cdot \hat{\mathbf{r}}^T(t_n)]$ et $[\hat{\mathbf{r}}(t_{n+1}) \cdot \hat{\mathbf{r}}^T(t_n)]^T$ peuvent être obtenues à partir de l'équation (2.92) :

$$\hat{\mathbf{r}}(t_{n+1}) \cdot \hat{\mathbf{r}}^T(t_n) = e^{-\delta t_n \dot{\gamma}^\alpha(t_n)} \tilde{\mathbf{s}}^\alpha(t_n) ; \quad [\hat{\mathbf{r}}(t_{n+1}) \cdot \hat{\mathbf{r}}^T(t_n)]^T = e^{\delta t_n \dot{\gamma}^\alpha(t_n)} \tilde{\mathbf{s}}^\alpha(t_n) ; \quad \alpha \in \mathcal{A}. \quad (2.94)$$

Le développement de Taylor des tenseurs $e^{-\delta t_n \dot{\gamma}^\alpha(t_n)} \tilde{\mathbf{s}}^\alpha(t_n)$ et $e^{\delta t_n \dot{\gamma}^\alpha(t_n)} \tilde{\mathbf{s}}^\alpha(t_n)$ au premier ordre donne :

$$e^{-\delta t_n \dot{\gamma}^\alpha(t_n)} \tilde{\mathbf{s}}^\alpha(t_n) \approx \mathbf{I}_2 - \delta t_n \dot{\gamma}^\alpha(t_n) \tilde{\mathbf{s}}^\alpha(t_n) ; \quad e^{\delta t_n \dot{\gamma}^\alpha(t_n)} \tilde{\mathbf{s}}^\alpha(t_n) \approx \mathbf{I}_2 + \delta t_n \dot{\gamma}^\alpha(t_n) \tilde{\mathbf{s}}^\alpha(t_n) ; \quad \alpha \in \mathcal{A}. \quad (2.95)$$

En considérant les approximations (2.95), l'équation (2.93) peut être remaniée sous la forme :

$$\begin{aligned} \delta\tilde{\sigma} &= \tilde{\sigma}(t_{n+1}) - \tilde{\sigma}(t_n) = \hat{\mathbf{r}}(t_{n+1}) \cdot (\bar{\sigma}(t_n) + \delta t_n \dot{\bar{\sigma}}(t_n)) \cdot \hat{\mathbf{r}}^T(t_{n+1}) - \tilde{\sigma}(t_n) \\ &= [\mathbf{I}_2 - \delta t_n \dot{\gamma}^\alpha(t_n) \tilde{\mathbf{s}}^\alpha(t_n)] \cdot \tilde{\sigma}(t_n) \cdot [\mathbf{I}_2 + \delta t_n \dot{\gamma}^\alpha(t_n) \tilde{\mathbf{s}}^\alpha(t_n)] \\ &\quad + \delta t_n \hat{\mathbf{r}}(t_{n+1}) \cdot \dot{\bar{\sigma}}(t_n) \cdot \hat{\mathbf{r}}^T(t_{n+1}) - \tilde{\sigma}(t_n) ; \quad \alpha \in \mathcal{A}. \end{aligned} \quad (2.96)$$

En négligeant les termes de second ordre en δt_n , l'équation (2.96) peut être réduite à la forme :

$$\begin{aligned} \delta\tilde{\sigma} &= \tilde{\sigma}(t_{n+1}) - \tilde{\sigma}(t_n) = \hat{\mathbf{r}}(t_{n+1}) \cdot (\bar{\sigma}(t_n) + \delta t_n \dot{\bar{\sigma}}(t_n)) \cdot \hat{\mathbf{r}}^T(t_{n+1}) - \tilde{\sigma}(t_n) \\ &= -\delta t_n \dot{\gamma}^\alpha(t_n) \tilde{\mathbf{s}}^\alpha(t_n) \cdot \tilde{\sigma}(t_n) + \delta t_n \dot{\gamma}^\alpha(t_n) \tilde{\sigma}(t_n) \cdot \tilde{\mathbf{s}}^\alpha(t_n) + \delta t_n \hat{\mathbf{r}}(t_{n+1}) \cdot \dot{\bar{\sigma}}(t_n) \cdot \hat{\mathbf{r}}^T(t_{n+1}) ; \quad \alpha \in \mathcal{A}. \end{aligned} \quad (2.97)$$

Le tenseur $\hat{\mathbf{r}}(t_{n+1}) \cdot \dot{\bar{\sigma}}(t_n) \cdot \hat{\mathbf{r}}^T(t_{n+1})$ peut être exprimé à l'aide de l'équation (2.88)₃ comme :

$$\hat{\mathbf{r}}(t_{n+1}) \cdot \dot{\bar{\sigma}}(t_n) \cdot \hat{\mathbf{r}}^T(t_{n+1}) = \mathbf{c}^e : (\check{\mathbf{d}}(t_n) - \dot{\gamma}^\alpha(t_n) \check{\mathbf{R}}^\alpha(t_n)) ; \quad \alpha \in \mathcal{A}. \quad (2.98)$$

L'expression analytique des vitesses de glissement peut être facilement obtenue à partir de la combinaison des équations (2.82) et (2.83) :

$$\forall \alpha \in \mathcal{A} : \quad \dot{\gamma}^\alpha(t_n) = \Lambda^{\alpha\beta}(t_n) \check{\mathbf{R}}^\beta(t_n) : \mathbf{c}^e : \check{\mathbf{d}}(t_n) ; \quad \beta \in \mathcal{A}, \quad (2.99)$$

où la matrice carrée $\Lambda(t_n)$ est l'inverse de $\mathbf{A}(t_n)$ définie par la forme indicielle donnée par l'équation (2.82).

En tenant compte de l'expression (2.99) de $\dot{\gamma}^\alpha(t_n)$, l'équation (2.98) peut être réécrite comme :

$$\hat{\mathbf{r}}(t_{n+1}) \cdot \dot{\bar{\sigma}}(t_n) \cdot \hat{\mathbf{r}}^T(t_{n+1}) = [\mathbf{c}^e - \Lambda^{\alpha\beta}(t_n)(\mathbf{c}^e : \check{\mathbf{R}}^\alpha(t_n)) \otimes (\check{\mathbf{R}}^\beta(t_n) : \mathbf{c}^e)] : \check{\mathbf{d}} ; \quad \alpha, \beta \in \mathcal{A}. \quad (2.100)$$

En insérant l'équation (2.100) dans l'équation (2.97) et en utilisant l'expression (2.98), on obtient :

$$\begin{aligned}\delta\tilde{\sigma} &= \delta t_n \left[\mathbf{c}^e - A^{\alpha\beta}(t_n) (\mathbf{c}^e : \check{\mathbf{R}}^\alpha(t_n) + \check{\mathbf{S}}^\alpha(t_n) \cdot \check{\sigma}(t_n) - \check{\sigma}(t_n) \cdot \check{\mathbf{S}}^\alpha(t_n)) \otimes (\check{\mathbf{R}}^\beta(t_n) : \mathbf{c}^e) \right] : \check{\mathbf{d}} \\ &= \left[\mathbf{c}^e - A^{\alpha\beta}(t_n) (\mathbf{c}^e : \check{\mathbf{R}}^\alpha(t_n) + \check{\mathbf{S}}^\alpha(t_n) \cdot \check{\sigma}(t_n) - \check{\sigma}(t_n) \cdot \check{\mathbf{S}}^\alpha(t_n)) \otimes (\check{\mathbf{R}}^\beta(t_n) : \mathbf{c}^e) \right] : \delta\tilde{\epsilon} \quad (2.101)\end{aligned}$$

; $\alpha, \beta \in \mathcal{A}$.

Le module tangent cohérent peut ainsi être identifié en comparant les équations (2.90) et (2.101) :

$$\check{\mathbf{c}}^{ep} = \mathbf{c}^e - A^{\alpha\beta}(t_n) (\mathbf{c}^e : \check{\mathbf{R}}^\alpha(t_n) + \check{\mathbf{S}}^\alpha(t_n) \cdot \check{\sigma}(t_n) - \check{\sigma}(t_n) \cdot \check{\mathbf{S}}^\alpha(t_n)) \otimes (\check{\mathbf{R}}^\beta(t_n) : \mathbf{c}^e) ; \quad \alpha, \beta \in \mathcal{A}. \quad (2.102)$$

Une fois que toutes les variables mécaniques sont mises à jour à t_{n+1} et le module tangent cohérent $\check{\mathbf{c}}^{ep}$ calculé, la taille de l'incrément de temps Δt et le temps initial t_n doivent également être mis à jour :

$$\Delta t \leftarrow \Delta t - \delta t_n ; \quad t_n \leftarrow t_n + \delta t_n. \quad (2.103)$$

Après cette procédure de mise à jour, le calcul doit être redémarré avec un nouveau sous-incrément I^{δ_n} , jusqu'à atteindre la condition suivante :

$$\Delta t = \delta t_n. \quad (2.104)$$

2.3.3. Résultats numériques

Pour maintenir un temps CPU raisonnable, les différentes cellules de base étudiées sont maillées par 5000 éléments finis C3D8 (50 éléments finis dans les deux directions du plan de la cellule et 2 éléments finis dans la direction de l'épaisseur). Le temps CPU nécessaire pour détecter la localisation pour chaque trajet de chargement varie entre 20 et 24 heures. Des investigations précédentes révèlent qu'une cellule de base constituée d'une centaine de grains est suffisante pour assurer une bonne représentativité des milieux polycristallins étudiés (Barbe et al., 2001 ; Kanit et al., 2003). Par conséquent, quatre agrégats composés de 50, 200, 500 et 1000 grains sont générés en utilisant la technique de diagramme de Voronoï, comme indiqué sur la Fig. 2.12. Ces agrégats sont désignés ci-après respectivement comme UC50, UC200, UC500, UC1000. Les orientations cristallines initiales des différentes configurations de cellules de base sont distribuées de manière aléatoire et uniforme, comme le révèlent les (100) figures de pôles représentées sur la Fig. 2.13. Pour les prédictions présentées ci-après, la cellule de base composée de 200 grains est exclusivement utilisée. L'effet du nombre de grains sur la prédition des CLF sera analysé au travers de la Fig. 2.19b.

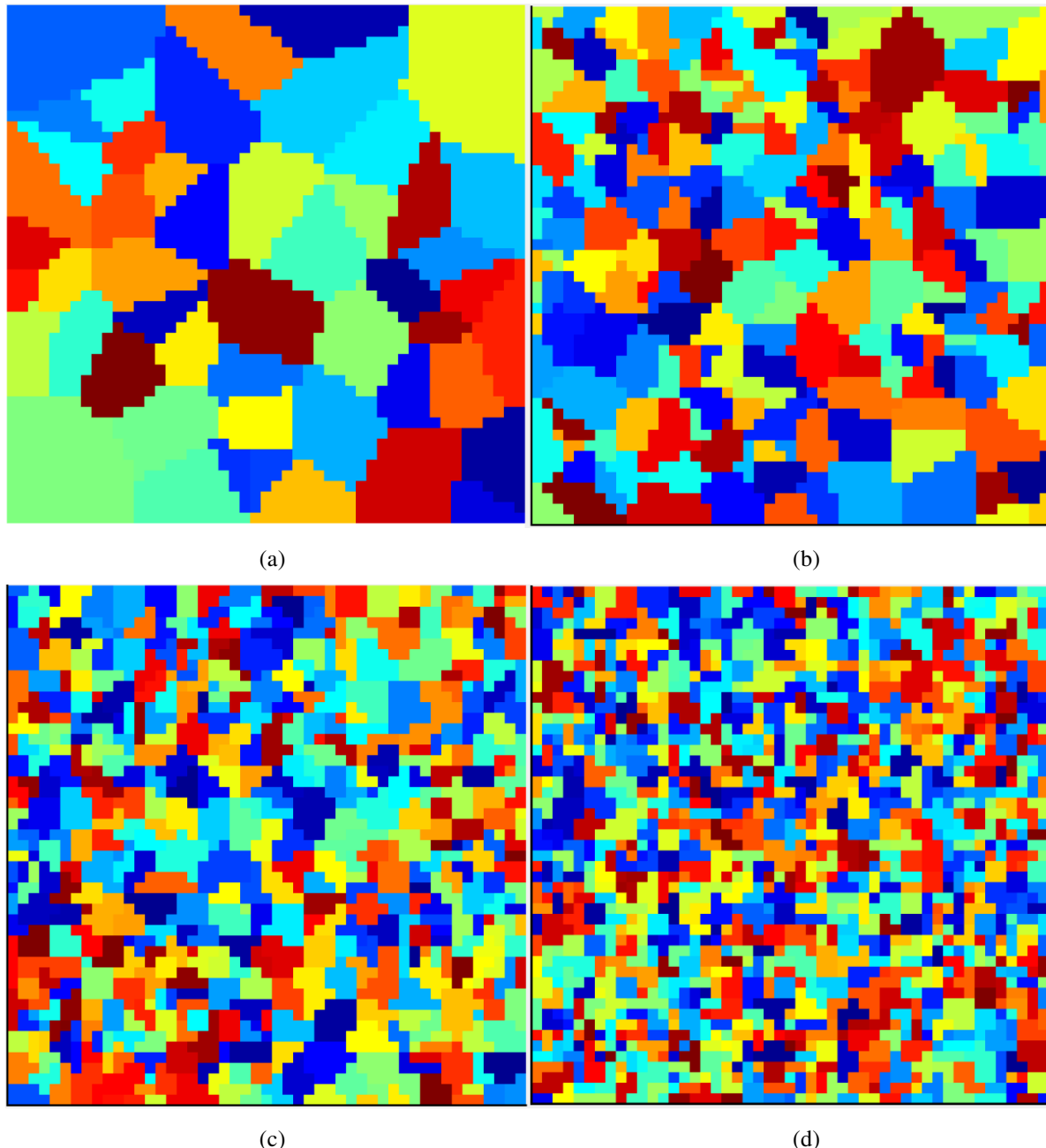


Fig. 2.12. Microstructures des différentes configurations de cellule de base : (a) UC50 ; (b) UC200 ; (c) UC500 ; (d) UC1000.

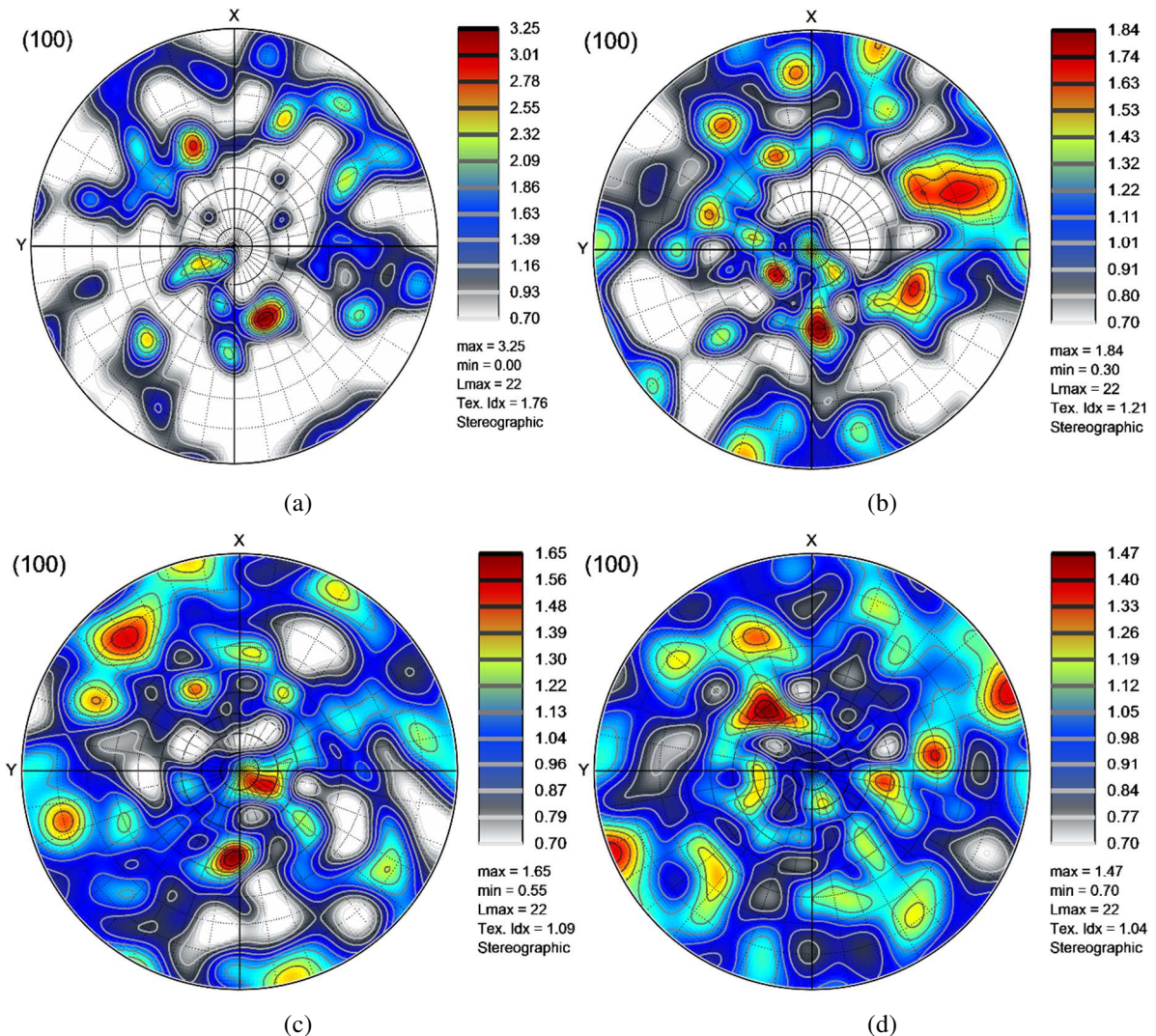


Fig. 2.13. Textures initiales des différentes configurations de cellule de base : (a) UC50 ; (b) UC200 ; (c) UC500 ; (d) UC1000.

La cission critique initiale est supposée identique pour tous les systèmes de glissement cristallographique et égale à τ_0 . L'évolution des cissions critiques est décrite par un modèle d'écrouissage non linéaire et isotrope, pour lequel les composantes de la matrice d'écrouissage \mathbf{H} sont données par l'expression suivante (similaire à la matrice d'écrouissage utilisée dans [Yoshida et Kuroda, 2012](#)) :

$$\forall \alpha, \beta = 1, \dots, N_s : H^{\alpha\beta} = h_0 \left(1 + \frac{h_0 \hbar}{\tau_0 n} \right)^{n-1} ; \quad \hbar = \sum_{\alpha=1}^{2N_s} \gamma^\alpha, \quad (2.105)$$

où h_0 et n sont des paramètres d'écrouissage et \hbar est le glissement total cumulé sur tous les systèmes de glissement cristallographique ($= \sum_{k=1}^{2N_s} \gamma^k$). Les paramètres d'élasticité et d'écrouissage utilisés dans les différentes simulations sont reportés dans le [Tab. 2.2](#).

Tab. 2.2. Paramètres d'élasticité d'écrouissage.

Élasticité		Écrouissage		
E (GPa)	ν	τ^0 (MPa)	h_0 (MPa/s)	n
200	0.3	40	390	0.184

2.3.3.1. Réponse mécanique

Les évolutions des composantes 11 et 12 du premier tenseur des contraintes macroscopiques de Piola–Kirchhoff \mathbf{P} sont tracées en fonction de $F_{11}-1$ sur la Fig. 2.14 pour trois trajets particuliers de déformation: $\rho = -0.5$, $\rho = 0$. et $\rho = 0.5$. Il faut rappeler que la cellule de base étudiée est constituée de 200 grains (Fig. 2.12b). Les courbes tracées sur la Fig. 2.14 montrent que les composantes de \mathbf{P} dépendent principalement du chemin de déformation appliqué. En outre, la Fig. 2.14a montre que la composante P_{11} augmente de façon monotone jusqu'à atteindre une valeur maximale et diminue après cette valeur maximale. Cette valeur maximale est atteinte presque au même niveau de déformation pour les trajets de déformation $\rho = 0$. et $\rho = 0.5$ qui est inférieure au niveau de déformation correspondant au maximum de P_{11} pour $\rho = -0.5$. L'évolution de la composante de cisaillement P_{12} est représentée sur la Fig. 2.14b. L'évolution de cette composante est moins lisse que l'évolution de P_{11} pour les différents trajets de déformation. Cette composante reste relativement faible par rapport à la composante P_{11} mais pas égale à zéro (malgré le fait que $F_{12} = 0$).

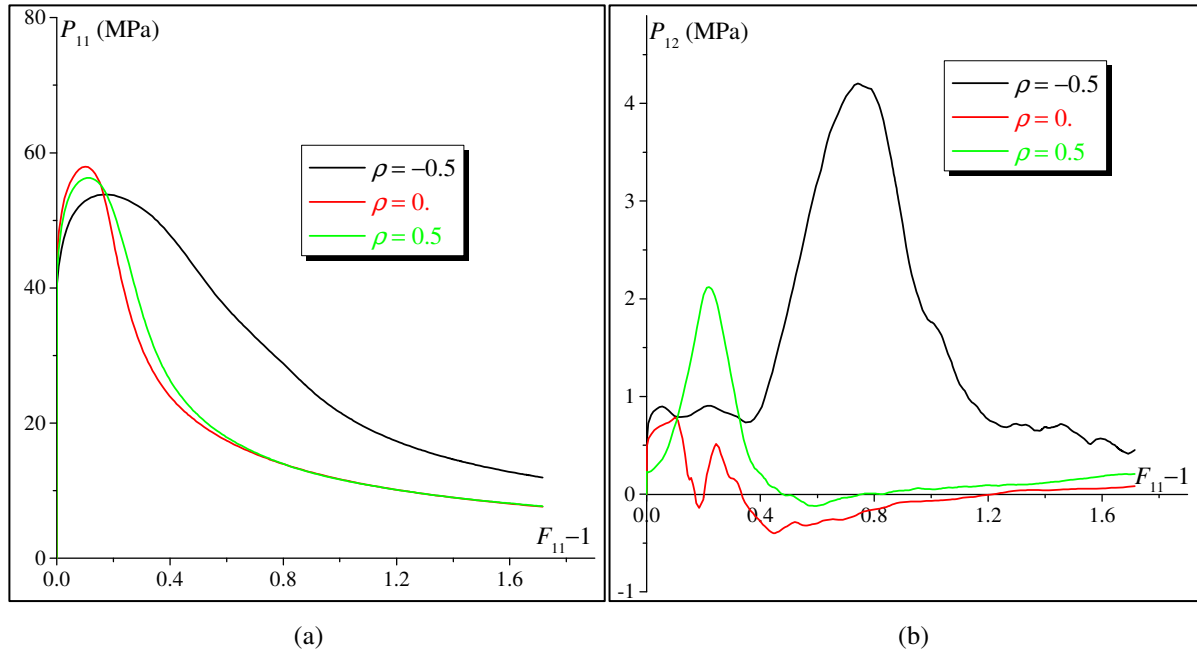


Fig. 2.14. Évolution de quelques composantes du premier tenseur de contrainte macroscopique de Piola–Kirchhoff en fonction de $F_{11}-1$: (a) composante P_{11} ; (b) composante P_{12} .

Pour approfondir l'analyse de la réponse mécanique polycristalline, nous avons tracé sur la Fig. 2.15, la Fig. 2.16 et la Fig. 2.17 les isovaleurs de certaines variables microscopiques pertinentes (à savoir, la

contrainte équivalente de von Mises, la composante σ_{33} des contraintes de Cauchy et la déformation logarithmique maximale (le_{max}) pour trois chemins de déformation : $\rho = -0.5$, $\rho = 0$. et $\rho = 0.5$. Les différentes isovaleurs sont tracées au moment où la déformation majeure atteint la valeur 0,2. Comme le montrent les différentes figures, les distributions des différents champs microscopiques sont évidemment hétérogènes. Cette hétérogénéité est principalement due à la différence entre les orientations cristallographiques initiales des différents grains constitutifs. Comme indiqué sur la Fig. 2.15, la contrainte microscopique équivalente est répartie de façon hétérogène. Cette distribution est prévisible compte tenu du fait que les orientations cristallographiques et la déformation plastique sont hétérogènes (l'activité des systèmes de glissement et l'amplitude des glissements cumulés changent d'un grain à l'autre et d'un point d'intégration à un autre du même grain). Malgré la satisfaction de la condition de contrainte plane macroscopique, la condition de contrainte plane microscopique n'est pas remplie comme le montre la Fig. 2.16. Sur cette figure, on peut observer que la composante σ_{33} est autour de zéro dans tout le maillage. L'hétérogénéité de la distribution de la composante le_{max} de la déformation est illustrée par les isovaleurs de la Fig. 2.17. On peut facilement observer en particulier sur la Fig. 2.17b et c le début de la formation de zones (ou bandes) de déformations localisées du côté droit de la cellule de base. En vérifiant soigneusement les limites des différentes cellules unitaires, on peut confirmer que les conditions aux limites périodiques sont bien respectées.

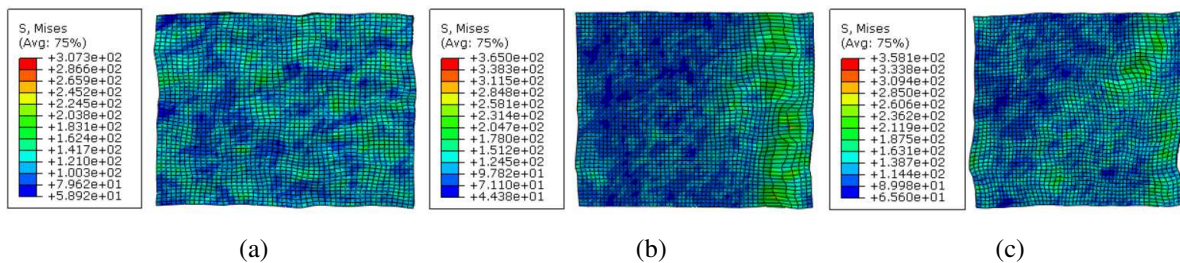


Fig. 2.15. Distribution de la contrainte équivalente de von Mises microscopique : (a) $\rho = -0.5$; (b) $\rho = 0$. ; (c) $\rho = 0.5$.

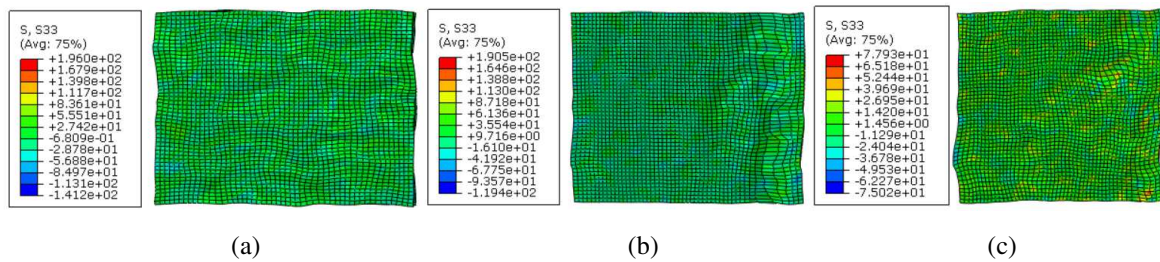


Fig. 2.16. Distribution de la composante 33 de la contrainte microscopique : (a) $\rho = -0.5$; (b) $\rho = 0$. ; (c) $\rho = 0.5$

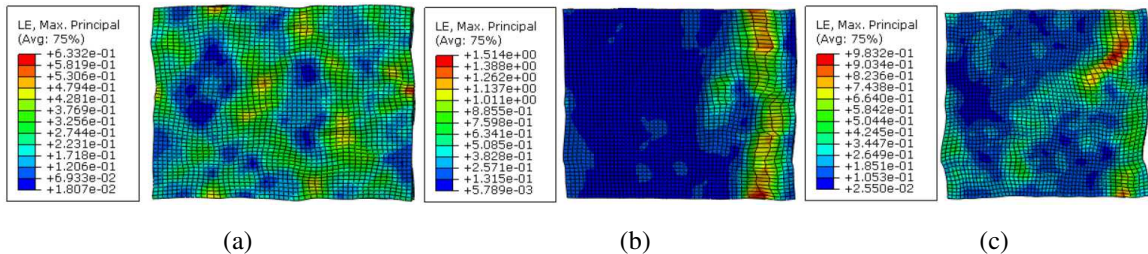


Fig. 2.17. Distribution de la déformation logarithmique maximale microscopique le_{max} : (a) $\rho = -0.5$; (b) $\rho = 0$; (c) $\rho = 0.5$.

2.3.3.2. Prédiction de la limite de ductilité

Avant d'analyser les limites de ductilité prédictes par le couplage de l'approche CPFEM à la théorie de bifurcation, examinons d'abord l'évolution des composantes ${}^{IN}\tilde{C}_{1111}^{(PK1)}$ et ${}^{IN}\tilde{C}_{1212}^{(PK1)}$ du module tangent macroscopique plan. Dans cet objectif, les composantes ci-dessus sont tracés sur la Fig. 2.18 en fonction de la composante $E_{11} = \ln(F_{11} - 1)$ de la déformation macroscopique, pour trois trajets de déformation représentatifs ($\rho = -0.5$, $\rho = 0$. et $\rho = 0.5$). Comme cela est clairement montré sur cette figure, la composante ${}^{IN}\tilde{C}_{1111}^{(PK1)}$ diminue rapidement dès le début de chargement. De plus, la composante de cisaillement ${}^{IN}\tilde{C}_{1212}^{(PK1)}$ est considérablement réduite lors de la déformation et devient très faible. Cette observation est le résultat naturel du caractère multi-glissement de la plasticité cristalline, qui conduit à la formation de sommets ('vertex') sur la surface de plasticité de Schmid. La réduction de cette composante de cisaillement est le principal facteur de déstabilisation responsable de la bifurcation, favorisant ainsi une localisation précoce des déformations plastiques. Il convient de noter que, lorsqu'une surface de plasticité lisse est utilisée, la composante de cisaillement ${}^{IN}\tilde{C}_{1212}^{(PK1)}$ conserve la même amplitude que sa contrepartie élastique. On observe également à partir des différentes courbes de la Fig. 2.18 (notamment les courbes correspondant à l'évolution de la composante de cisaillement ${}^{IN}\tilde{C}_{1212}^{(PK1)}$), que les évolutions des composantes du module tangent ne sont pas très lisses.

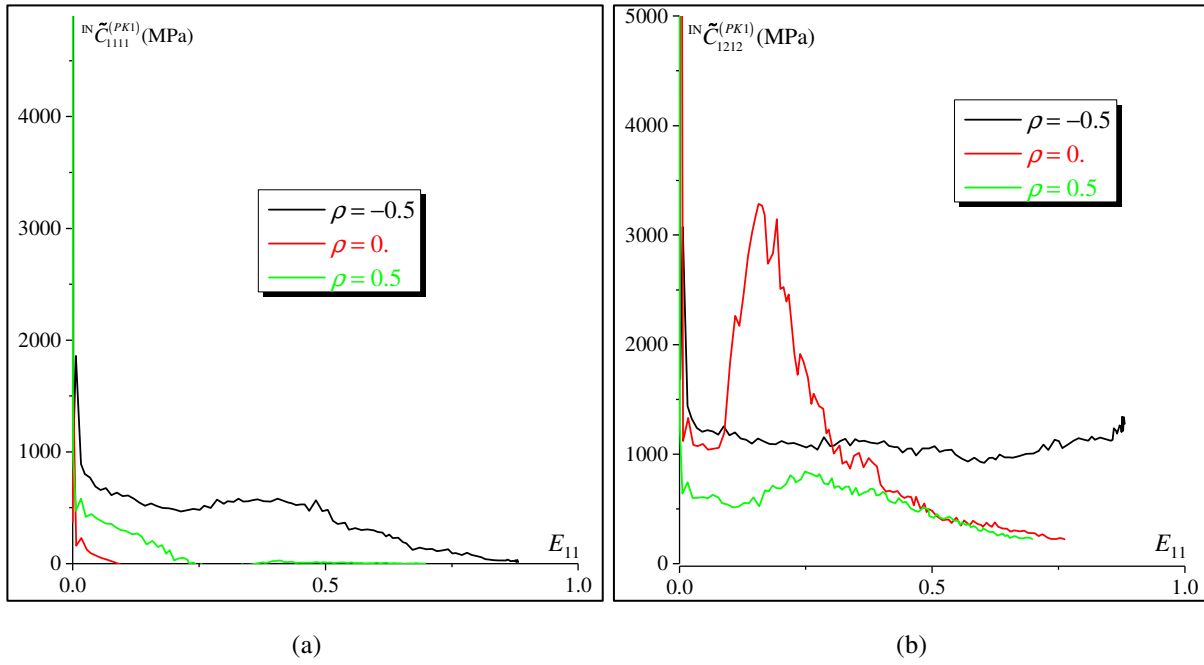


Fig. 2.18. Évolution de quelques composantes du module tangent plan ${}^{\text{IN}}\tilde{C}^{(\text{PK1})}$ en fonction de $E_{11} = \ln(F_{11} - 1)$:
 (a) ${}^{\text{IN}}\tilde{C}_{1111}^{(\text{PK1})}$; (b) ${}^{\text{IN}}\tilde{C}_{1212}^{(\text{PK1})}$.

L'évolution du déterminant du tenseur acoustique macroscopique plan $\vec{\mathcal{N}} \cdot {}^{\text{IN}}\tilde{C}^{(\text{PK1})} \cdot \vec{\mathcal{N}}$ est représentée sur la Fig. 2.19a. Comme nous pouvons aisément le constater, quel que soit le trajet de déformation étudié, le minimum de ce déterminant diminue brusquement pendant la transition entre régimes élastique et plastique, qui se produit à de petites déformations. En revanche, dans le régime plastique, la diminution est beaucoup plus lente et, par conséquent, le minimum du déterminant atteint zéro en grandes déformations. Les CLF prédictées par le critère de bifurcation, conjointement avec l'approche CPFEM, sont montrées sur la Fig. 2.19b pour les quatre cellules de base considérées (à savoir, UC50, UC200, UC500 et UC1000). Cette figure souligne clairement l'effet du nombre de grains sur les limites de ductilité prédictes. Globalement, les déformations limites augmentent avec le nombre de grains. Ce résultat est probablement attribuable à l'évolution de la texture cristallographique et morphologique. En effet, l'anisotropie plastique est évidemment plus prononcée lorsque le nombre de grains est faible. Des simulations complémentaires seront exécutées très prochainement pour approfondir et mieux étudier tous ces aspects (en vue de préparer la soutenance de thèse).

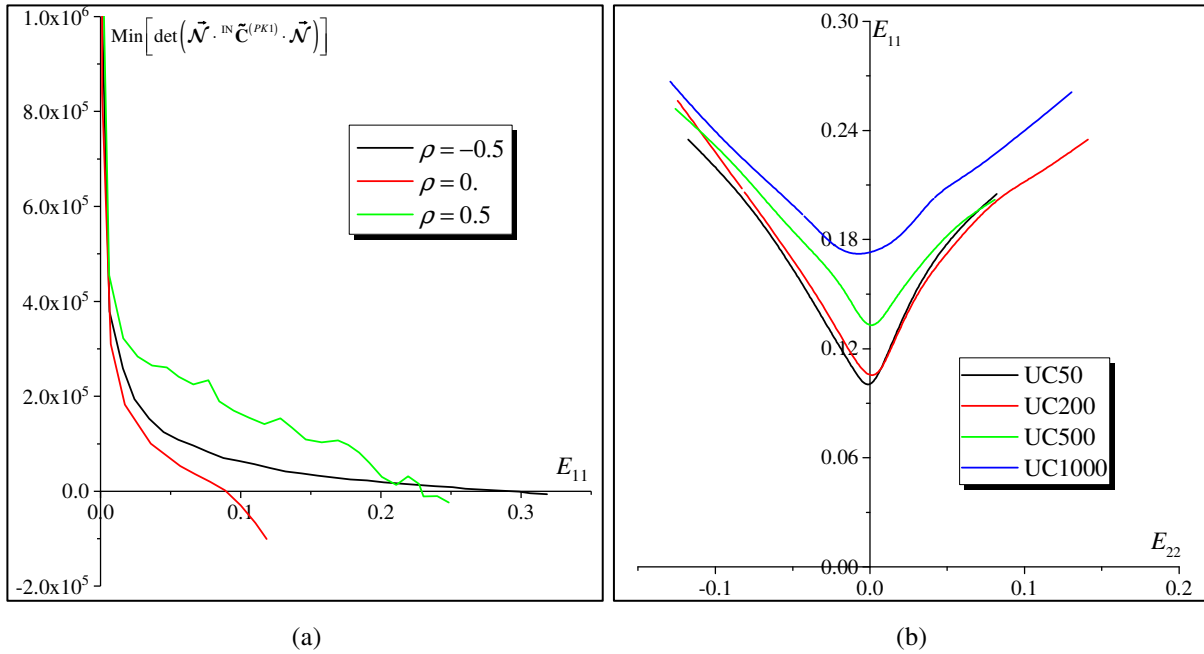


Fig. 2.19. Prédiction des limites de ductilité: (a) évolution du minium du déterminant du tenseur acoustique $\vec{\mathcal{N}} \cdot {}^{\text{IN}}\tilde{\mathbf{C}}^{(PK)} \cdot \vec{\mathcal{N}}$ en fonction de $E_{11} = \ln(F_{11}-1)$ pour trois trajets de déformation différents ($\rho = -0.5$, $\rho = 0$, et $\rho = 0.5$) ; (b) effet du nombre de grains sur la prédiction des CLF.

2.3.4. Bilan de l'étude

Dans cette deuxième application, l'approche d'homogénéisation périodique a été couplée à un modèle de plasticité cristalline pour prédire avec précision le comportement mécanique des agrégats polycristallins 2D, supposés être statistiquement représentatifs de tôles minces, à partir de celui des monocristaux constitutifs. Pour assurer la mise en œuvre efficace de l'approche numérique résultante, un ensemble de techniques numériques robustes a été mis en place. Cette approche a été couplée à la théorie de bifurcation pour prédire les limites de ductilité des cellules de base planes qui sont supposées être représentatives des tôles minces étudiées. Plusieurs prédictions numériques ont été réalisées pour étudier la réponse mécanique ainsi que les limites de ductilité d'agrégats polycristallins. D'autres simulations et investigations seront effectuées très prochainement pour mieux illustrer l'utilité et la pertinence de l'approche numérique développée.

Appendix A. Typical input file to output elementary stiffness matrices

In this example, the statements in red are required to be added to the input file. In this additional part, ‘Nel’ and ‘Frequency=n’ denote the total number of elements and the frequency of record of the elementary stiffness matrices (each ‘n’ increments).

```
...
** ASSEMBLY
**
*Assembly, name=Assembly
...
*Elset, elset=Set-1, internal, instance=Part-1-1, Generated
1, Nel, 1
*End Assembly
...
** STEP: Step-1
**
*Step, name=Step-1, nlgeom=YES, inc=50000
...
*Element Matrix Output, Elset=Set-1, File Name=myMatrix, Frequency=n, Output File=User Defined,
Stiffness=Yes
*End Ste
```


Appendix B. Some sections of Python scripts

B.1. The perturbation technique

```
#=====
# A restart file with perturbation (magnitude 10-7) for component 11 of F, restart from increment 400 of step 1
#=====

*Heading
*RESTART, READ, STEP=1, INC=400, END STEP
** -----
**
** STEP: Step-2
**
*STEP, PERTURBATION
*Static
**
**
** BOUNDARY CONDITIONS
**
** Name: BC-1 Type: Displacement/Rotation
*Boundary
Set-1806, 1, 1, 1e-07
Set-1806, 2, 2
Set-1806, 3, 3
** Name: BC-2 Type: Displacement/Rotation
*Boundary
Set-1807, 1, 1
Set-1807, 2, 2
Set-1807, 3, 3
** Name: BC-3 Type: Displacement/Rotation
*Boundary
Set-1808, 1, 1
Set-1808, 2, 2
Set-1808, 3, 3
**
** OUTPUT REQUESTS
**
*Restart, write, frequency=0
**
** FIELD OUTPUT: F-Output-1
**
*Output, field, variable=PRESELECT
**
```

```
** HISTORY OUTPUT: H-Output-1
**
*Output, history, variable=PRESELECT
*End Step
```

B.2. The condensation technique

```
#=====
# This function is capable of computing macro moduli at increment i
#=====

def macro_tangent(labelA,i,dictionary): # labelA is an array used to store the labels of nodes in interior
    initial_Ki=np.asarray(initial_Ki)
    Kab=np.delete(Kaa_Kab,aaindex,axis=1)
    Kba=Kab.transpose()
    Kbb=np.delete(initial_Ki,aaindex,axis=0)
    Kbb=np.delete(Kbb,aaindex,axis=1)
    inv_KaaKab=np.linalg.solve(Kaa,Kab)
    bb=np.dot(Kba,inv_KaaKab)
    condense_Kbb=Kbb-bb
    inv_condense_Kbb=linalg.pinvh(condense_Kbb)
    effective_K_temp=np.dot(dot(P,inv_condense_Kbb),PT)
    effective_K=linalg.pinvh(effective_K_temp)

#=====
# Compute C
#=====

    C=(1/V)*(np.dot(dot(Q,effective_K),QT))
    dictionary[i]=[C]

#=====
num_proc=15 # specify the number of processor
manager = multiprocessing.Manager()
dictionaryP=manager.dict()
#=====

# Parallel for the calculation
#=====

for ii in range (0,incnum,num_proc):
    currentUpLimit=ii+num_proc
    if (currentUpLimit>incnum):
        currentUpLimit=incnum
    processes = [multiprocessing.Process(target= macro_tangent,args=(labelA,kk,dictionaryP))]
    for kk in range(ii,currentUpLimit)]
        [process.start() for process in processes]
        [process.join() for process in processes]
#=====

# Write C into a ".txt" file
#=====
```

```

fo = open("C-con.txt", "w")
for jj in range (incnum):
    L=dictionaryP[jj]
    fo.write('inc=')
    fo.write('%d\n'%incnum_sav[jj])
    for kk in range(9):
        fo.write('%10.3f\t%10.3f\t%10.3f\t%10.3f\t%10.3f\t%10.3f\t%10.3f\t%10.3f\n'%
(L[0][kk][0],L[0][kk][1],
L[0][kk][2],L[0][kk][3],L[0][kk][4],L[0][kk][5],L[0][kk][6],L[0][kk][7],L[0][kk][8]))
fo.close()

```

B.3. The fluctuation technique

```

#=====
# This function is capable of computing the softening part and macro moduli, at increment j
#=====

def softeningpart(j,dictionary):
    C=np.zeros((9,9))
    initial_Kj=np.asarray(initial_Kj)
    initial_Lj=np.asarray(initial_Lj)
    #=====

    # Compute C
    #=====

    inv_initial_Kj=linalg.pinvh(initial_Kj)
    softeningpart=np.dot(dot(initial_LjT,inv_initial_Kj),initial_Lj)
    for i in range(elenum):
        C=C+C_ele[i]
    C=C/V-softeningpart/V
    dictionary[j]=[C]
    #=====

    num_proc=15 # specify the number of processor
    manager = multiprocessing.Manager()
    dictionaryP=manager.dict()
    #=====

    # Parallel for the calculation
    #=====

    for ii in range (0,incnum,num_proc):
        currentUpLimit=ii+num_proc
        if (currentUpLimit>incnum):
            currentUpLimit=incnum
        processes = [multiprocessing.Process(target= softeningpart,args=(kk,dictionaryP)) for kk in
range(ii,currentUpLimit)]
        [process.start() for process in processes]
        [process.join() for process in processes]
    #=====

    # Write C into a ".txt" file

```

```
#=====
fo = open("C-flu.txt", "w")
for jj in range (incnum):
    L=DictionaryP[jj]
    fo.write('inc=')
    fo.write('%d\n'%incnum_total[jj])
    for kk in range(9):
        fo.write('%10.3f%10.3f%10.3f%10.3f%10.3f%10.3f%10.3f%10.3f\n'%
(L[0][kk][0],L[0][kk][1],L[0][kk][2],L[0][kk][3],L[0][kk][4],L[0][kk][5],L[0][kk][6],L[0][kk][7],L[0][kk][8]))
fo.close()
```

Appendix C. The numbering of the slip systems for FCC single crystals

For the different simulations, single crystals with face-centered cubic (FCC) crystallographic structure are considered. Nevertheless, the proposed numerical methodology remains quite general to be applied to any other crystallographic structure. In FCC single crystals, plastic deformation results from crystallographic slip along four slip planes $\{111\}$ and three slip directions $\langle 1\bar{1}0 \rangle$, thus leading to twelve CSSs (i.e., $N_s = 12$). The numbering of vectors $\vec{\mathbf{m}}_0^\alpha$ and $\vec{\mathbf{n}}_0^\alpha$, measured in the intermediate configuration related to the crystallographic lattice, is enumerated in [Table C.1](#).

Table C.1. The numbering of the crystallographic slip systems for FCC single crystal.

k	1	2	3	4	5	6	7	8	9	10	11	12
$\sqrt{3}\vec{\mathbf{n}}_0^\alpha$	$\begin{Bmatrix} 1 \\ 1 \\ 1 \end{Bmatrix}$			$\begin{Bmatrix} -1 \\ 1 \\ 1 \end{Bmatrix}$			$\begin{Bmatrix} 1 \\ -1 \\ 1 \end{Bmatrix}$			$\begin{Bmatrix} 1 \\ 1 \\ -1 \end{Bmatrix}$		
$\sqrt{2}\vec{\mathbf{m}}_0^\alpha$	$\begin{Bmatrix} 1 \\ -1 \\ 0 \end{Bmatrix}$	$\begin{Bmatrix} 1 \\ 0 \\ -1 \end{Bmatrix}$	$\begin{Bmatrix} 0 \\ 1 \\ -1 \end{Bmatrix}$	$\begin{Bmatrix} 1 \\ 1 \\ 0 \end{Bmatrix}$	$\begin{Bmatrix} 1 \\ 0 \\ 1 \end{Bmatrix}$	$\begin{Bmatrix} 0 \\ 1 \\ -1 \end{Bmatrix}$	$\begin{Bmatrix} 1 \\ 1 \\ 0 \end{Bmatrix}$	$\begin{Bmatrix} 1 \\ 0 \\ -1 \end{Bmatrix}$	$\begin{Bmatrix} 0 \\ 1 \\ 1 \end{Bmatrix}$	$\begin{Bmatrix} 1 \\ -1 \\ 0 \end{Bmatrix}$	$\begin{Bmatrix} 1 \\ 0 \\ 1 \end{Bmatrix}$	$\begin{Bmatrix} 0 \\ 1 \\ 1 \end{Bmatrix}$

References

- Abaqus, 2014. ABAQUS Version 6.14. Dassault Systèmes Simulia Corp., Provid. RI.
- Abed-Meraim, F., Peerlings, R.H.J., Geers, M.G.D., 2014. Bifurcation analysis versus maximum force criteria in formability limit assessment of stretched metal sheets. *Int. J. Appl. Mech.* 6.
- Akpama, H.K., 2016. Approche multi-échelles pour une prédition fiable de la ductilité des matériaux métalliques. Arts et Métiers ParisTech, Metz, France.
- Akpama, H.K., Ben Bettaieb, M., Abed-Meraim, F., 2017. Localized necking predictions based on rate-independent self-consistent polycrystal plasticity: Bifurcation analysis versus imperfection approach. *Int. J. Plast.* 91, 205–237.
- Akpama, H.K., Ben Bettaieb, M., Abed-Meraim, F., 2016. Numerical integration of rate-independent BCC single crystal plasticity models: comparative study of two classes of numerical algorithms. *Int. J. Numer. Methods Eng.* 108, 363–422.
- Anand, L., Kothari, M., 1996. A computational procedure for rate-independent crystal plasticity. *J. Mech. Phys. Solids* 44, 525–558.
- Andrianov, I. V., Danishevskyy, V. V., Kalamkarov, A.L., 2012a. Asymptotic analysis of perforated plates and membranes. Part 1: Static problems for small holes. *Int. J. Solids Struct.* 49, 298–310.
- Andrianov, I. V., Danishevskyy, V. V., Kalamkarov, A.L., 2012b. Asymptotic analysis of perforated plates and membranes. Part 2: Static and dynamic problems for large holes. *Int. J. Solids Struct.* 49, 311–317.
- Asada, T., Ohno, N., 2007. Fully implicit formulation of elastoplastic homogenization problem for two-scale analysis. *Int. J. Solids Struct.* 44, 7261–7275.
- Baik, S.C., Han, H.N., Lee, S.H., Oh, K.H., Lee, D.N., 1997. Plastic behaviour of perforated sheets under biaxial stress state. *Int. J. Mech. Sci.* 39, 781–793.
- Bao, Y.B., Wierzbicki, T., 2004. On fracture locus in the equivalent strain and stress triaxiality space. *Int. J. Mech. Sci.* 46, 81–98.
- Barbe, F., Forest, S., Cailletaud, G., 2001. Intergranular and intragranular behavior of polycrystalline aggregates. Part 2: Results. *Int. J. Plast.* 17, 537–563.
- Barlat, F., 1987. Crystallographic texture, anisotropic yield surfaces and forming limits of sheet metals. *Mater. Sci. Eng.* 91, 55–72.
- Barsoum, I., Faleskog, J., 2011. Micromechanical analysis on the influence of the Lode parameter on void growth and coalescence. *Int. J. Solids Struct.* 48, 925–938.
- Barsoum, I., Faleskog, J., 2007. Rupture mechanisms in combined tension and shear-Experiments. *Int. J. Solids Struct.* 44, 1768–1786.
- Ben Bettaieb, M., Abed-Meraim, F., 2015. Investigation of localized necking in substrate-supported metal layers: Comparison of bifurcation and imperfection analyses. *Int. J. Plast.* 65, 168–190.

- Ben Bettaieb, M., Débordes, O., Dogui, A., D'Uchene, L., 2012a. Averaging properties for periodic homogenization and large deformation. *Int. J. Multiscale Comput. Eng.* 10, 281–293.
- Ben Bettaieb, M., Débordes, O., Dogui, A., Duchêne, L., Keller, C., 2012b. On the numerical integration of rate independent single crystal behavior at large strain. *Int. J. Plast.* 32–33, 184–217.
- Ben Bettaieb, M., Lemoine, X., Duchêne, L., Habraken, A.M., 2011. On the numerical integration of an advanced Gurson model. *Int. J. Numer. Methods Eng.* 85, 1049–1072.
- Bomarito, G.F., Warner, D.H., 2015. Micromechanical investigation of ductile failure in Al 5083-H116 via 3D unit cell modeling. *J. Mech. Phys. Solids.*
- Borja, R.I., Wren, J.R., 1993. Discrete micromechanics of elastoplastic crystals. *Int. J. Numer. Methods Eng.* 36, 3815–3840.
- Bouktir, Y., Chalal, H., Abed-Meraim, F., 2018. Prediction of necking in thin sheet metals using an elastic–plastic model coupled with ductile damage and bifurcation criteria. *Int. J. Damage Mech.* 27, 801–839.
- Bruno, D., Greco, F., Lonetti, P., Blasi, P.N., Sgambitterra, G., 2010. An investigation on microscopic and macroscopic stability phenomena of composite solids with periodic microstructure. *Int. J. Solids Struct.* 47, 2806–2824.
- Castaneda, P.P., Willis, J.R., 1988. On the overall properties of nonlinearly viscous composites., in: *Proceedings of The Royal Society of London, Series A: Mathematical and Physical Sciences*. pp. 217–244.
- Chalal, H., Abed-Meraim, F., 2015. Hardening effects on strain localization predictions in porous ductile materials using the bifurcation approach. *Mech. Mater.* 91, 152–166.
- Chen, F.K., 1993. Analysis of plastic deformation for sheet metals with circular perforations. *J. Mater. Process. Tech.* 37, 175–188.
- Chiba, R., Takeuchi, H., Nakamura, R., 2015. Forming-limit prediction of perforated aluminium sheets with square holes. *J. Strain Anal. Eng. Des.* 50, 391–404.
- Considère, 1885. *Mémoire sur l'emploi du fer et de l'acier dans les constructions*. Ch. Dunod, Editeur.
- Dæhli, L.E.B., Morin, D., Børvik, T., Hopperstad, O.S., 2017. Influence of yield surface curvature on the macroscopic yielding and ductile failure of isotropic porous plastic materials. *J. Mech. Phys. Solids* 107, 253–283.
- Debordes, O., 1986. Homogenization computations in the elastic or plastic collapse range applications to unidirectional composites and perforated sheets, in: *Proceedings of the 4th International Symposium Innovative Numerical Methods in Engineering, Computational Mechanics Publications*. pp. 453–458.
- Driemeier, L., Brünig, M., Micheli, G., Alves, M., 2010. Experiments on stress-triaxiality dependence of material behavior of aluminum alloys. *Mech. Mater.* 42, 207–217.
- Drucker, D.C., 1956. On uniqueness in the theory of plasticity. *Q. Appl. Math.* 14, 35–42.
- Drucker, D.C., 1950. Some implications of work-hardening and ideal plasticity. *Q. Appl. Math.* 7, 411–418.
- Dudzinski, D., Molinari, A., 1991. Perturbation analysis of thermoviscoplastic instabilities in biaxial loading. *Int.*

- J. Solids Struct. 27, 601–628.
- Dunand, M., Mohr, D., 2014. Effect of Lode parameter on plastic flow localization after proportional loading at low stress triaxialities. *J. Mech. Phys. Solids* 66, 133–153.
- Fabrègue, D., Pardoen, T., 2008. A constitutive model for elastoplastic solids containing primary and secondary voids. *J. Mech. Phys. Solids* 56, 719–741.
- Feyel, F., 1999. Multiscale FE2 elastoviscoplastic analysis of composite structures. *Comput. Mater. Sci.* 16, 344–354.
- Franz, G., 2008. Prédiction de la limite de formabilité des aciers multiphasés par une approche micromécanique. Arts et Métiers ParisTech, Metz, France.
- Franz, G., Abed-Meraim, F., Berveiller, M., 2013. Strain localization analysis for single crystals and polycrystals: Towards microstructure-ductility linkage. *Int. J. Plast.* 48, 1–33.
- Franz, G., Abed-Meraim, F., Lorrain, J.P., Ben Zineb, T., Lemoine, X., Berveiller, M., 2009a. Ellipticity loss analysis for tangent moduli deduced from a large strain elastic–plastic self-consistent model. *Int. J. Plast.* 25, 205–238.
- Franz, G., Abed-Meraim, F., Zineb, T.B., Lemoine, X., Berveiller, M., 2009b. Strain localization analysis using a multiscale model. *Comput. Mater. Sci.* 45, 768–773.
- Gao, X.S., Kim, J., 2006. Modeling of ductile fracture: Significance of void coalescence. *Int. J. Solids Struct.* 43, 6277–6293.
- Geers, M.G.D., Kouznetsova, V.G., Matouš, K., Yvonnet, J., 2017. Homogenization Methods and Multiscale Modeling: Nonlinear Problems, in: Encyclopedia of Computational Mechanics Second Edition. pp. 1–34.
- Ghossein, E., Lévesque, M., 2014. A comprehensive validation of analytical homogenization models: The case of ellipsoidal particles reinforced composites. *Mech. Mater.* 75, 135–150.
- Gologanu, M., Leblond, J.B., Devaux, J., 1994. Approximate Models for Ductile Metals Containing Nonspherical Voids—Case of Axisymmetric Oblate Ellipsoidal Cavities. *J. Eng. Mater. Technol.* 116, 290–297.
- Gologanu, M., Leblond, J.B., Devaux, J., 1993. Approximate models for ductile metals containing non-spherical voids—Case of axisymmetric prolate ellipsoidal cavities. *J. Mech. Phys. Solids* 41, 1723–1754.
- Goodwin, G.M., 1968. Application of Strain Analysis to Sheet Metal Forming Problems in the Press Shop, in: SAE Technical Papers. SAE International.
- Guo, N., Wang, J., Sun, C.Y., Zhang, Y.F., Fu, M.W., 2020. Analysis of size dependent earing evolution in micro deep drawing of TWIP steel by using crystal plasticity modeling. *Int. J. Mech. Sci.* 165, 105200.
- Guo, T.F., Wong, W.H., 2018. Void-sheet analysis on macroscopic strain localization and void coalescence. *J. Mech. Phys. Solids* 118, 172–203.
- Gupta, A., Ben Bettaieb, M., Abed-Meraim, F., Kalidindi, S.R., 2018. Computationally efficient predictions of crystal plasticity based forming limit diagrams using a spectral database. *Int. J. Plast.*
- Gurson, A.L., 1977. Continuum theory of ductile rupture by void nucleation and growth: Part 1 - yield criteria and

- flow rules for porous ductile media. *J. Eng. Mater. Technol. Trans. ASME* 99, 2–15.
- Habbar, M., 1994. Instabilités plastiques en élasto-plasticité anisotrope et grandes déformations. École Centrale de Lyon, Lyon, France.
- Haddag, B., Balan, T., Abed-Meraim, F., 2007. Investigation of advanced strain-path dependent material models for sheet metal forming simulations. *Int. J. Plast.* 23, 951–979.
- Hashin, Z., Shtrikman, S., 1962. On some variational principles in anisotropic and nonhomogeneous elasticity. *J. Mech. Phys. Solids* 10, 335–342.
- Henyš, P., Čapek, L., Březina, J., 2019. Comparison of current methods for implementing periodic boundary conditions in multi-scale homogenisation. *Eur. J. Mech. - A/Solids* 78, 103825.
- Hill, R., 1963. Elastic properties of reinforced solids: Some theoretical principles. *J. Mech. Phys. Solids* 11, 357–372.
- Hill, R., 1958. A general theory of uniqueness and stability in elastic-plastic solids. *J. Mech. Phys. Solids* 6, 236–249.
- Hill, R., 1952. On discontinuous plastic states, with special reference to localized necking in thin sheets. *J. Mech. Phys. Solids* 1, 19–30.
- Hill, R., 1948. A theory of the yielding and plastic flow of anisotropic metals, in: Proceedings of the Royal Society of London. Series A. Mathematical and Physical Sciences. pp. 281–297.
- Hure, J., 2019. A coalescence criterion for porous single crystals. *J. Mech. Phys. Solids* 124, 505–525.
- Hutchinson, J.W., Neale, K.W., 1978. Sheet Necking-II. Time-Independent Behavior, in: Koistinen, D.P., Wang, H.M. (Eds.), *Mechanics of Sheet Metal Forming*. Springer, Boston, MA, pp. 127–153.
- Hutchinson, J.W., Neale, K.W., Needleman, A., 1978. Sheet Necking—I. Validity of Plane Stress Assumptions of the Long-Wavelength Approximation, in: *Mechanics of Sheet Metal Forming*. Springer US, Boston, MA, pp. 111–126.
- Inal, K., Neale, K.W., Aboutajeddine, A., 2005. Forming limit comparisons for FCC and BCC sheets, in: *International Journal of Plasticity*. pp. 1255–1266.
- IPA., 2015. Designers, specifiers and buyers handbook for perforated metals. The Industrial Perforators Association, Washington.
- Iseki, H., Murota, T., Kato, K., 1989. on the forming limit diagram of perforated sheet metals under biaxial tension. *Trans Jpn Soc Mech Eng* 33, 1660–1668.
- Ji, W., Waas, A.M., Bazant, Z.P., 2013. On the Importance of Work-Conjugacy and Objective Stress Rates in Finite Deformation Incremental Finite Element Analysis. *J. Appl. Mech.* 80, 041024.
- Jia, S., Raiser, G.F., Povirk, G.L., 2002. Modeling the effects of hole distribution in perforated aluminum sheets I: Representative unit cells. *Int. J. Solids Struct.* 39, 2517–2532.
- Kalamkarov, A.L., 2014. Asymptotic Homogenization Method and Micromechanical Models for Composite Materials and Thin-Walled Composite Structures., in: *Mathematical Methods and Models in Composites*.

- Imperial College Press, London, pp. 1–60.
- Kalamkarov, A.L., 1992. Composite and reinforced elements of construction. New York: Wiley, Chichester.
- Kalamkarov, A.L., Andrianov, I. V., Weichert, D., 2012. Asymptotic analysis of perforated shallow shells. *Int. J. Eng. Sci.* 53, 1–18.
- Kalamkarov, A.L., Kolpakov, A.G., 1997. Analysis, design, and optimization of composite structures. New York: J. Wiley & Sons, Chichester.
- Kanit, T., Forest, S., Galliet, I., Mounoury, V., Jeulin, D., 2003. Determination of the size of the representative volume element for random composites: Statistical and numerical approach. *Int. J. Solids Struct.* 40, 3647–3679.
- Keeler, S., Backofen, W., 1964. Plastic instability and fracture in sheets stretched over rigid punches. *ASM Trans. Quart.* 56, 25–48.
- Keralavarma, S.M., Benzerga, A.A., 2010. A constitutive model for plastically anisotropic solids with non-spherical voids. *J. Mech. Phys. Solids.*
- Khatam, H., Pindera, M.J., 2011. Plastic deformation modes in perforated sheets and their relation to yield and limit surfaces. *Int. J. Plast.* 27, 1537–1559.
- Kim, J.H., Lee, M.G., Kim, D., Barlat, F., 2013. Numerical procedures for predicting localization in sheet metals using crystal plasticity. *Comput. Mater. Sci.* 72, 107–115.
- Kiran, R., Khandelwal, K., 2014. Complex step derivative approximation for numerical evaluation of tangent moduli. *Comput. Struct.* 140, 1–13.
- Knockaert, R., Chastel, Y., Massoni, E., 2002. Forming limits prediction using rate-independent polycrystalline plasticity. *Int. J. Plast.* 18, 231–247.
- Koplik, J., Needleman, A., 1988. Void growth and coalescence in porous plastic solids. *Int. J. Solids Struct.* 24, 835–853.
- Krajcinovic, D., Mallick, K., Basista, M., Sumarac, D., 1992. Elastic moduli of perforated plates in the neighborhood of critical state. *Int. J. Solids Struct.* 29, 1837–1847.
- Ladevèze, P., Loiseau, O., Dureisseix, D., 2001. A micro–macro and parallel computational strategy for highly heterogeneous structures. *Int. J. Numer. Methods Eng.* 52, 121–138.
- Lejeunes, S., Bourgeois, S., 2011. Une Toolbox Abaqus pour le calcul de propriétés effectives de milieux hétérogènes, in: 10ème Colloque National En Calcul Des Structures. pp. 1–9.
- Léné, F., 1984. Contribution à l'étude des matériaux composites et de leur endommagement. Université Paris VI, Paris, France.
- Lévesque, J., Inal, K., Neale, K.W., Mishra, R.K., 2010. Numerical modeling of formability of extruded magnesium alloy tubes. *Int. J. Plast.*
- Liu, Z.G., Wong, W.H., Guo, T.F., 2016. Void behaviors from low to high triaxialities: Transition from void collapse to void coalescence. *Int. J. Plast.* 84, 183–202.

- Lorrain, J.P., 2005. Critère de ductilité basé sur la perte d'ellipticité du module tangent élastoplastique déduit d'un modèle autocohérent. Arts et Métiers ParisTech, Metz, France.
- Luo, T., Gao, X.S., 2018. On the prediction of ductile fracture by void coalescence and strain localization. *J. Mech. Phys. Solids* 113, 82–104.
- Mansouri, L.Z., Chalal, H., Abed-Meraim, F., 2014. Ductility limit prediction using a GTN damage model coupled with localization bifurcation analysis. *Mech. Mater.* 76, 64–92.
- Marciniak, Z., Kuczyński, K., 1967. Limit strains in the processes of stretch-forming sheet metal. *Int. J. Mech. Sci.* 9, 609–620.
- Matsui, K., Terada, K., Yuge, K., 2004. Two-scale finite element analysis of heterogeneous solids with periodic microstructures. *Comput. Struct.* 82, 593–606.
- Mercier, S., Molinari, A., Berbenni, S., Berveiller, M., 2012. Comparison of different homogenization approaches for elasticviscoplastic materials. *Model. Simul. Mater. Sci. Eng.* 20.
- Michel, J.C., Lopez-Pamies, O., Ponte Castañeda, P., Triantafyllidis, N., 2007. Microscopic and macroscopic instabilities in finitely strained porous elastomers. *J. Mech. Phys. Solids* 55, 900–938.
- Michel, J.C., Moulinec, H., Suquet, P., 1999. Effective properties of composite materials with periodic microstructure: a computational approach. *Comput. Methods Appl. Mech. Eng.* 172, 109–143.
- Miehe, C., 2003. Computational micro-to-macro transitions for discretized micro-structures of heterogeneous materials at finite strains based on the minimization of averaged incremental energy. *Comput. Methods Appl. Mech. Eng.* 192, 559–591.
- Miehe, C., 2002. Strain-driven homogenization of inelastic microstructures and composites based on an incremental variational formulation. *Int. J. Numer. Methods Eng.* 55, 1285–1322.
- Miehe, C., Bayreuther, C.G., 2007. On multiscale FE analyses of heterogeneous structures: From homogenization to multigrid solvers. *Int. J. Numer. Methods Eng.* 71, 1135–1180.
- Miehe, C., Bayreuther, C.G., 2006. Multilevel FEM for heterogeneous structures: From homogenization to multigrid solvers. *Lect. Notes Appl. Comput. Mech.*
- Miehe, C., Koch, A., 2002. Computational micro-to-macro transitions of discretized microstructures undergoing small strains. *Arch. Appl. Mech.* 72, 300–317.
- Miehe, C., Schotte, J., Lambrecht, M., 2002a. Homogenization of inelastic solid materials at finite strains based on incremental minimization principles. Application to the texture analysis of polycrystals. *J. Mech. Phys. Solids* 50, 2123–2167.
- Miehe, C., Schröder, J., Bayreuther, C.G., 2002b. On the homogenization analysis of composite materials based on discretized fluctuations on the micro-structure. *Acta Mech.* 155, 1–16.
- Miehe, C., Schröder, J., Becker, M., 2002c. Computational homogenization analysis in finite elasticity: Material and structural instabilities on the micro- and macro-scales of periodic composites and their interaction. *Comput. Methods Appl. Mech. Eng.* 191, 4971–5005.

- Moulinec, H., Silva, F., 2014. Comparison of three accelerated FFT-based schemes for computing the mechanical response of composite materials. *Int. J. Numer. Methods Eng.* 97, 960–985.
- Moulinec, H., Suquet, P., 2003. Comparison of FFT-based methods for computing the response of composites with highly contrasted mechanical properties, in: *Physica B: Condensed Matter*. pp. 58–60.
- Moulinec, H., Suquet, P., 1995. A FFT-Based Numerical Method for Computing the Mechanical Properties of Composites from Images of their Microstructures, in: *Solid Mechanics and Its Applications*. pp. 235–246.
- Moulinec, H., Suquet, P., 1994. A fast numerical method for computing the linear and nonlinear mechanical properties of composites. *Comptes rendus l'Académie des Sci. Série II, Mécanique, Phys. Chim. Astron.* 318, 1417–1423.
- Mura, T., Shodja, H.M., Hirose, Y., 1988. Inclusion problems. *Appl. Mech. Rev.* 41, 118–127.
- Needleman, A., Tvergaard, V., 1992. Analyses of plastic flow localization in metals. *Appl. Mech. Rev.* 45, S3–S18.
- Neil, C.J., Agnew, S.R., 2009. Crystal plasticity-based forming limit prediction for non-cubic metals: Application to Mg alloy AZ31B. *Int. J. Plast.* 25, 379–398.
- Nemat-Nasser, S., Lori, M., Datta, S.K., 1996. Micromechanics: Overall Properties of Heterogeneous Materials. *J. Appl. Mech.* 63, 561.
- Niordson, C.F., Tvergaard, V., 2019. A homogenized model for size-effects in porous metals. *J. Mech. Phys. Solids* 123, 222–233.
- O'Donnell, W.J., Langer, B.F., 1962. Design of perforated plates. *J. Eng. Ind.* 84, 307–319.
- Omairey, S.L., Dunning, P.D., Sriramula, S., 2019. Development of an ABAQUS plugin tool for periodic RVE homogenisation. *Eng. Comput.* 35, 567–577.
- Özdemir, I., Brekelmans, W.A.M., Geers, M.G.D., 2008. FE2 computational homogenization for the thermo-mechanical analysis of heterogeneous solids. *Comput. Methods Appl. Mech. Eng.* 198, 602–613.
- Pardoen, T., Hutchinson, J.W., 2000. Extended model for void growth and coalescence. *J. Mech. Phys. Solids*.
- Pineau, A., Joly, P., 1991. Local versus global approaches to elastic-plastic fracture mechanics. Application to ferritic steels and a cast duplex stainless steel, in: EGF9.
- Reboul, J., Srivastava, A., Osovski, S., Vadillo, G., 2020. Influence of strain rate sensitivity on localization and void coalescence. *Int. J. Plast.* 125, 265–279.
- Rice, J.R., 1976. The localization of plastic deformation, in: 14th International Congress on Theoretical and Applied Mechanics. pp. 207–220.
- Rudnicki, J.W., Rice, J.R., 1975. Conditions for the localization of deformation in pressure-sensitive dilatant materials. *J. Mech. Phys. Solids* 23, 371–394.
- Salahouelhadj, A., Abed-Meraim, F., Chalal, H., Balan, T., 2012. Application of the continuum shell finite element SHB8PS to sheet forming simulation using an extended large strain anisotropic elastic-plastic formulation. *Arch. Appl. Mech.* 82, 1269–1290.

- Schmid, E., Boas, W., 1950. Plasticity of crystals. Springer US.
- Schwindt, C., Schlosser, F., Bertinetti, M.A., Stout, M., Signorelli, J.W., 2015. Experimental and Visco-Plastic Self-Consistent evaluation of forming limit diagrams for anisotropic sheet metals: An efficient and robust implementation of the M-K model. *Int. J. Plast.* 73, 62–99.
- Signorelli, J.W., Bertinetti, M.A., Roatta, A., 2019. A review of recent investigations using the Marciak-Kuczynski technique in conjunction with crystal plasticity models. *J. Mater. Process. Technol.* 116517.
- Signorelli, J.W., Bertinetti, M.A., Turner, P.A., 2009. Predictions of forming limit diagrams using a rate-dependent polycrystal self-consistent plasticity model. *Int. J. Plast.* 25, 1–25.
- Simo, J.C., 1998. Numerical analysis and simulation of plasticity, in: *Handbook of Numerical Analysis*.
- Suquet, P.M., 1993. Overall potentials and extremal surfaces of power law or ideally plastic composites. *J. Mech. Phys. Solids* 41, 981–1002.
- Swift, H.W., 1952. Plastic instability under plane stress. *J. Mech. Phys. Solids* 1, 1–18.
- Tadano, Y., Yoshida, K., Kuroda, M., 2013. Plastic flow localization analysis of heterogeneous materials using homogenization-based finite element method. *Int. J. Mech. Sci.* 72, 63–74.
- Tchalla, A., Belouettar, S., Makradi, A., Zahrouni, H., 2013. An ABAQUS toolbox for multiscale finite element computation. *Compos. Part B Eng.* 52, 323–333.
- Tekoğlu, C., Hutchinson, J.W., Pardoen, T., 2015. On localization and void coalescence as a precursor to ductile fracture. *Philos. Trans. R. Soc. A Math. Phys. Eng. Sci.*
- Temizer, I., Wriggers, P., 2008. On the computation of the macroscopic tangent for multiscale volumetric homogenization problems. *Comput. Methods Appl. Mech. Eng.* 198, 495–510.
- Teply, J.L., Dvorak, G.J., 1988. Bounds on overall instantaneous properties of elastic-plastic composites. *J. Mech. Phys. Solids* 36, 29–58.
- Terada, K., Hori, M., Kyoya, T., Kikuchi, N., 2000. Simulation of the multi-scale convergence in computational homogenization approaches. *Int. J. Solids Struct.* 37, 2285–2311.
- Terada, K., Kikuchi, N., 2001. A class of general algorithms for mulit-scale analysis of heterogeneous media. *Comput. Methods Appl. Mech. Eng.* 190, 5427–5464.
- Tóth, L.S., Dudzinski, D., Molinari, A., 1996. Forming limit predictions with the perturbation method using stress potential functions of polycrystal viscoplasticity. *Int. J. Mech. Sci.*
- Tvergaard, V., 2015. Study of localization in a void-sheet under stress states near pure shear. *Int. J. Solids Struct.* 75–76, 134–142.
- Tvergaard, V., 2012. Effect of stress-state and spacing on voids in a shear-field. *Int. J. Solids Struct.* 49, 3047–3054.
- Tvergaard, V., 1981. Influence of voids on shear band instabilities under plane strain conditions. *Int. J. Fract.* 17, 389–407.

References

- Tvergaard, V., Needleman, A., 1984. Analysis of the cup-cone fracture in a round tensile bar. *Acta Metall.* 32, 157–169.
- Van Rens, B.J.E., Brekelmans, W.A.M., Baaijens, F.P.T., 1998. Homogenization of the elastoplastic behavior of perforated plates. *Comput. Struct.* 69, 537–545.
- Willis, J.R., 1981. Variational and Related Methods for the Overall Properties of Composites. *Adv. Appl. Mech.* 21, 1–78.
- Wong, W.H., Guo, T.F., 2015. On the energetics of tensile and shear void coalescences. *J. Mech. Phys. Solids* 82, 259–286.
- Wu, P.D., MacEwen, S.R., Lloyd, D.J., Neale, K.W., 2004. Effect of cube texture on sheet metal formability. *Mater. Sci. Eng. A.*
- Yoshida, K., Kuroda, M., 2012. Comparison of bifurcation and imperfection analyses of localized necking in rate-independent polycrystalline sheets. *Int. J. Solids Struct.* 49, 2073–2084.
- Zhu, J.C., Ben Bettaieb, M., Abed-Meraim, F., 2020. Numerical investigation of necking in perforated sheets using the periodic homogenization approach. *Int. J. Mech. Sci.* 166, 105209.
- Zhu, Y.Z., Engelhardt, M.D., Kiran, R., 2018. Combined effects of triaxiality, Lode parameter and shear stress on void growth and coalescence. *Eng. Fract. Mech.* 199, 410–437.